Redox and Nutrient Cycling in the Mesoproterozoic Taoudeni Basin

Kathryn Fiona Husband

A thesis submitted for the degree of Doctor of Philosophy

School of Natural and Environmental Sciences

Newcastle University

December 2019

Abstract

Following the Great Oxidation Event, current evidence suggests that much of the ocean remained anoxic throughout the Proterozoic, with oxygenation in deeper waters only becoming expansive at the end of the Precambrian. Previous models have suggested that the mid-Proterozoic, often known as the "boring billion" owing to an apparent stasis in environmental and evolutionary history, was characterized by pervasive euxinia, in contrast to dominantly ferruginous conditions found both before and after this period. However, more recent studies indicate that ocean redox was highly heterogenous during this "boring billion", with dynamic cycling between oxic, ferruginous and sulphidic states, though data for the mid-Proterozoic remains relatively scarce. Ocean redox conditions are believed to exert a strong control on nutrient cycling, so influencing organic carbon production and burial, and, in turn, environmental oxygen levels. Therefore, in order to understand controls on environmental conditions during a potentially dynamic boring billion, and thus better understand the progression towards a biosphere more suited for animal evolution, detailed studies into oceanic redox chemistry and its influence on nutrient cycling are vital.

This study of Fe-S-C systematics in 3 well preserved cores (S2, S3 and S4) from the 1.1 Ga Taoudeni Basin of Mauritania provides a rare glimpse into evolving redox chemistry during the second half of the "boring billion", for which redox data is currently sparse. Earlier in the succession, where data is limited to S4, euxinia was prevalent in shallow coastal waters. Further up the succession, as sea level rises, euxinia persists in this part of the basin, with fluctuating, mostly anoxic, conditions in the shallower waters of S2. At the highest sea levels encountered in this study ferruginous conditions dominate in S2, while the mid-depths of S3 are oxic, and the likely deeper S4 appears mostly oxic, with possible ferruginous incursions. Following a drop in sea level limited data suggest oxic conditions across the shallower part of the basin. High organic C concentrations, at times exceptionally so, in the middle of the succession in S2 suggest this may have been an area of high productivity. High TOC contents in a fourth core, S1, suggest that, if correct, this area of high productivity could potentially have extended over

200km, or shifted in locus over this distance. However, probable metamorphic alteration associated with a dolerite sill evidenced by presence of AVS and high trace metal concentrations has rendered this core unsuitable for redox analysis. Enhanced organic C burial in S2 is associated with both ferruginous and euxinic conditions, suggesting that the development of euxinic conditions was not simply driven by organic C availability.

P speciation is utilized to provide insight into redox-driven nutrient feedbacks. Results of P speciation suggest extensive drawdown of P in association with organic matter, although a fairly large proportion of total P was not extracted as part of the reactive (that assumed to have been biologically available) fraction. Comparison of TOC/reactive P to the Redfield ratio suggests efficient recycling of P back to the water column under both euxinic and ferruginous conditions, allowing continued high productivity and thus burial of organic C, especially in S2, where recycling of P also appears to have been efficient under oxic conditons. However, in S3 and S4, TOC/reactive P ratios are lower than the Redfield ratio, suggesting efficient trapping of P in the sediment, and suggesting that while very little P was extracted with the Fe oxide fraction, some P drawdown, later retained in other mineral phases, must have been associated with Fe oxides.

This thesis is dedicated to the memory of my mother

Christine Elizabeth Husband

30.01.1952 – 12.02.2017

Acknowledgements

First and foremost, my deepest gratitude goes to both my parents, without whose unwavering support and encouragement this thesis may never have been submitted.

Secondly, I would like to thank all my Supervisors for their support, and in particular, Professor Simon Poulton, for his guidance, support and patience during some challenging years.

I would also like to acknowledge all those who provided technical assistance and advice, both at Newcastle University and in the School of Earth and Environment at the University of Leeds.

And finally, I would like to thank all those who have kept me company in the labs over the years.

Table of contents

Abstract iii

Acknowledgements vii

Table of contents ix

Figures xv

Tables xviii

Chapter 1 1

Introduction 1

1.1 Rationale and thesis outline 1

1.2 Proxies for ocean redox 2

1.2.1 Iron, sulphur and carbon systematics 2

1.2.2 Development of the iron speciation proxy 3

1.3 Oxygenation of the biosphere 7

1.3.1 Oxygen in the atmosphere 7

1.3.2 Ocean redox structure in the Precambrian 8

1.4 Redox driven nutrient cycling 9

1.4.1 The Phosphorus cycle 9

1.4.2 Redox conditions, nutrients and productivity 13

1.4.3 Phosphorus in the Precambrian 14

1.5 The Mesoproterozoic Taoudeni Basin 16

1.5.1 Regional geological setting 16

1.5.2 General stratigraphy 16

1.5.3 The Atar and El Mreiti Groups 18

1.5.4 Siliciclastic provenance 21

1.5.5 Correlations 21

1.5.6 Basin development 22

1.5.7 Sea level history 24

1.5.8 Geochronology 24

Chapter 2 26

Samples and Methodology 26

2.1 Introduction 26

2.2 Sample description and preparation 26

2.2.1 Sample description 26

2.2.2 Depositional model 33

2.2.3 Sample preparation 34

2.3 Elemental analysis 35

2.3.1 Total element analysis 35

2.3.2 Total organic carbon analysis 36

2.3.3 Total carbon, sulphur and nitrogen analysis 36

2.4 Iron speciation 37

2.4.1 Sequential iron extractions 37

2.4.2 Pyrite extraction 38

2.4.3 Boiling HCl extraction 39

2.5 Phosphorus speciation 40

2.6 Isotope analyses 44

2.6.1 Sulphide 44

2.6.2 Organic carbon 44

Chapter 3 45

Ocean redox chemistry recorded in Late Mesoproterozoic sediments from the Taoudeni Basin of Mauritania 45

3.1 Introduction 45

3.2 Results 45

3.2.1 Carbon 45

3.2.1.1 TOC 45

3.2.1.2 Inorganic C 46

3.2.2 Iron speciation 51

3.2.2.1 Fe_{carb} 51

3.2.2.2 Fe_{ox} 51

3.2.2.3 Fe_{mag} 51

3.2.2.4 Fe_{py} 52

3.2.2.5 FeT 52

3.2.3 Sulphur 57

3.2.3.1 Sulphide Sulphur and Total Sulphur 57

3.2.3.2 Sulphur isotopes 57

3.2.4 Aluminium 58

3.2.5 Trace metals 59

3.2.5.1 Manganese 59

3.2.5.2 Molybdenum 60

3.2.5.3 Vanadium 60

3.3 Discussion 64

3.3.1 Redox indicators 64

3.3.1.1 Fe speciation 64

3.3.1.2 Fe/Al 70

3.3.1.3 S isotopes 71
3.3.1.4 Trace metals 74
3.3.2 Spatial and temporal redox reconstruction 84
3.4 Conclusions 91
Chapter 4 92
Phosphorus cycling in a Late Mesoproterozoic sea 92
4.1 Introduction 92
4.2 Results 92
4.2.1 Total Phosphorus 92
4.2.2 Aluminium 97
4.2.3 Organic carbon 98
4.2.4 Phosphorus speciation 99
4.2.4.1 P_{Fe} 99
4.2.4.2 P_{auth} 100
4.2.4.3 P_{det} 101
4.2.4.4 P_{org} 101
4.3.4.5 P_{res} 102
4.3 Discussion 108
4.3.1 Phosphorus pools 108
4.3.2 Reactive phosphorus 109
4.3.3 Phosphorus redox cycling 115
4.3.4 Phosphorus cycling across space and time 125
4.3.5 New insights into phosphorus in the Proterozoic 129
4.4 Conclusions 131

Chapter 5 133

Modification of palaeoredox proxies in core S1 in samples affected by contact metamorphism 133

5.1 Introduction 133

5.2 Results 134

5.2.1 Total organic carbon 134

5.2.2 Iron speciation 137

5.2.2.1 Fe_{carb} 137

5.2.2.2 Fe_{ox} 137

5.2.2.3 Fe_{mag} 138

5.2.2.4 Fe_{AVS} 138

5.2.2.5 Fe_{py} 139

5.2.2.6 Fe_{HCl} 139

5.2.2.7 FeT 140

5.2.3 Aluminium 143

5.2.4 Trace metals in S1 143

5.2.4.1 Chromium 143

5.2.4.2 Copper 144

5.2.4.3 Molybdenum 144

5.2.4.4 Nickel 145

5.2.4.5 Vanadium 145

5.2.4.6 Zinc 146

5.2.5 Trace metals in S2 and S4 150

5.2.5.1 Chromium 150

5.2.5.2 Copper 150

5.2.5.3 Molybdenum 150

5.2.5.4 Nickel 151

5.2.5.5 Vanadium 151

5.2.5.6 Zinc 151
5.3 Discussion 157
5.3.1 Assessment of the use of Fe speciation in the presence of AVS 157
5.3.2 Trace metal patterns in S2 and S4 164
5.3.3 Trace metal patterns in S1 compared to S2 and S4 182
5.4 Conclusions 196
Chapter 6 197
Conclusions 197
Appendix A – S2, S3 and S4 data tables 199
Appendix B – S1 data tables 242
References 270

Figures

Figure 1.1 Proterozoic stratigraphy of the Taoudeni Basin 17

Figure 2.1 Summary geological map of the Taoudeni Basin with approximate core locations 31

Figure 2.2 Summary logs of the four cores 33

Figure 2.3 Sum of sequentially extracted P verses total P extraction 41

Figure 3.1 Depth profiles for C, S and Al in S2 48

Figure 3.2 Depth profiles for C, S and Al in S3 49

Figure 3.3 Depth profiles for C, S and Al in S4 50

Figure 3.4 Depth profiles for Fe pools in S2 54

Figure 3.5 Depth profiles for Fe pools in S3 55

Figure 3.6 Depth profiles for Fe pools in S4 56

Figure 3.7 Depth profiles for trace metals in S2 62

Figure 3.8 Depth profiles for trace metals in S3 62

Figure 3.9 Depth profiles for trace metals in S4 63

Figure 3.10 Depth profiles for Fe redox indicators in S2 66

Figure 3.11 Depth profiles for Fe redox indicators in S3 67

Figure 3.12 Depth profiles for Fe redox indicators in S4 69

Figure 3.13 Distribution of pyrite δ^{34}S data by core 73

Figure 3.14 Mn/Al ratios in cores S2, S3 and S4 79

Figure 3.15 Mo/Al ratios in cores S2, S3 and S4 81

Figure 3.16 V/Al ratios in cores S2, S3 and S4 83

Figure 3.17 FeP/FeHR verses FeHR/FeT plotted by formation 89

Figure 3.18 Redox structure inferred for each formation..... 91

Figure 4.1 Depth plots showing total P, TOC and Al concentratios in S2..... 96

Figure 4.2 Depth plots showing total P, TOC and Al concentratios in S3..... 96

Figure 4.3 Depth plots showing total P, TOC and Al concentratios in S4..... 97

Figure 4.4 Depth plots showing sequentially extracted phosphorus pools in S2..... 106

Figure 4.5 Depth plots showing sequentially extracted phosphorus pools in S3..... 106

Figure 4.6 Depth plots showing sequentially extracted phosphorus pools in S4..... 107

Figure 4.7 Plots of various P pools against Al contents for S2..... 112

Figure 4.8 Plots of various P pools against Al contents for S3..... 113

Figure 4.9 Plots of various P pools against Al contents for S4..... 114

Figure 4.10 Plots of TOC against various P pools for S2 120

Figure 4.11 Plots of TOC against various P pools for S3 122

Figure 4.12 Plots of TOC against various P pools for S4 124

Figure 4.13 P cycling across the basin and through time..... 129

Figure 5.1 Depth profiles for TOC, Al and Fe concentrations in S1..... 137

Figure 5.2 Depth profiles for Fe pools in S1 142

Figure 5.3 Depth profiles for trace metals in S1..... 149

Figure 5.4 Depth profiles for trace metals in S2..... 154

Figure 5.5 Depth profiles for trace metals in S4..... 156

Figure 5.6 Depth profiles for Fe redox indicators in S1 163

Figure 5.7 Crossplots of Cr with Al, TOC and Fe_{py} for S2 (a, b and c) and S4 (d, e and f), plotted by formation 171

Figure 5.8 Crossplots of Cu with Al, TOC and Fe_{py} for S2 (a, b and c) and S4 (d, e and f), plotted by formation 173

Figure 5.9 Crossplots of Mo with Al, TOC and Fe_{py} for S2 (a, b and c) and S4 (d, e and f), plotted by formation 175

Figure 5.10 Crossplots of Ni with Al, TOC and Fe_{py} for S2 (a, b and c) and S4 (d, e and f), plotted by formation 177

Figure 5.11 Crossplots of V with Al, TOC and Fe_{py} for S2 (a, b and c) and S4 (d, e and f), plotted by formation 179

Figure 5.12 Crossplots of Zn with Al, TOC and Fe_{py} for S2 (a, b and c) and S4 (d, e and f), plotted by formation 181

Figure 5.13 Crossplots of Cr with Al, TOC, Fe_{AVS} and Fe_{py} for S1 plotted by formation 185

Figure 5.14 Crossplots of Cu with Al, TOC, Fe_{AVS} and Fe_{py} for S1 plotted by formation 187

Figure 5.15 Crossplots of Mo with Al, TOC, Fe_{AVS} and Fe_{py} for S1 plotted by formation 189

Figure 5.16 Crossplots of Ni with Al, TOC, Fe_{AVS} and Fe_{py} for S1 plotted by formation 191

Figure 5.17 Crossplots of V with Al, TOC, Fe_{AVS} and Fe_{py} for S1 plotted by formation 193

Figure 5.18 Crossplots of Zn with Al, TOC, Fe_{AVS} and Fe_{py} for S1 plotted by formation 195

Tables

Table 2.1 Mean, standard deviation and RSD for total element analysis of S4 82.08 replicates 36

Table 2.2 Summary of iron extraction methods and mean, standard deviation and RSD for replicate samples 40

Table 2.3 Summary of P extraction methods and mean, standard deviation and RSD for replicates of S4 130.02 43

Table 3.1 Mean and SD for TOC and Inorganic C for each core by formation 47

Table 3.2 Mean and SD for Fe pools and Al for each core by formation 53

Table 3.3 S concentrations and isotopic compositions (mean ± 1 SD) for each core by formation 58

Table 3.4 Al and trace metal concentrations (mean ± 1 SD) for each core by formation 59

Table 3.5 Fe redox indicators for each core by formation (mean ± 1 SD) 65

Table 3.6 Fe/Al by formation and redox state for each core (mean ± 1 SD) 71

Table 4.1 Average TOC, Al and P_{total} concentration (mean ± 1 SD) for each core, by formation 94

Table 4.2 Average TOC, Al and P_{total} concentration (mean ± 1 SD) for each core, by formation 103

Table 4.3 Average P pool concentration (mean ± 1 SD) for each core, by redox conditions 104

Table 5.1 Mean and SD for TOC, FeT and Al for S1 135

Table 5.2 Mean and SD for Fe pools in S1 141

Table 5.3 Mean and SD for trace metals in S1 147

Table 5.4 Mean and SD for trace metals in S2 and S4 153

Table A - 1 Sample descriptions for cores S2, S3 and S4.....207

Table A - 2 Carbon and sulphur data for cores S2, S3 and S4.....216

Table A - 3 Total element data for cores S2, S3 and S4.....226

Table A - 4 Fe pools and redox indicators for cores S2, S3 and S4.....236

Table A - 5 P pools for selected samples from cores S2, S3 and S4 241

Table B - 1 Sample descriptions and carbon and sulphur data for core S1.....248

Table B - 2 Total element data for core S1.....255

Table B - 3 Fe pools for core S1.....262

Table B - 4 Redox indicators for core S1.....269

Chapter 1

Introduction

1.1 Rationale and thesis outline

For many years, a vast part of Earth's history has been known as the "boring billion" (e.g. Holland (2006)) owing to an apparent stasis in environmental and evolutionary history (Buick et al., 1995, Brasier and Lindsay, 1998). However, a number of recent studies suggest this period might have been rather more dynamic than that name suggests (Javaux and Lepot, 2018), with evidence of highly heterogenous oceans being a feature of the mid-Proterozoic (Gilleaudeau and Kah, 2015, Sperling et al., 2014, Cox et al., 2016, Planavsky et al., 2018). Although a lot of new data has been published in recent years, controls on ocean chemistry are still poorly understood. This thesis seeks to improve understanding of the links between nutrient availability, specifically phosphorus, and ocean redox chemistry in the Mesoproterozoic Taoudeni Basin. Following an introduction to proxies for redox reconstruction, current knowledge of the oxygenation of the biosphere and the phosphorus cycle will be summarised, and the stratigraphy of the Taoudeni Basin discussed. Chapter 2 provides descriptions of cores used in this study and a discussion of how they fit with existing literature on stratigraphy and environmental setting. Following this, the methods used to study samples are documented. A redox model in which to explore P cycling will be established in chapter 3 and P dynamics will be discussed in chapter 4. Alteration of original depositional signals by post burial events is an issue throughout the geological record, and although the Taoudeni Basin appears to have escaped significant regional metamorphism, localised contact metamorphism due to the emplacement of dolerite sills has the potential to significantly alter the chemistry of rocks such that inferences of depositional conditions are unsound. To this end, Fe-S-C and trace metal systematics in a core that has been subjected to flash pyrolysis will be studied in chapter 5.

1.2 Proxies for ocean redox

The toolkit for assessing ocean redox is becoming ever more extensive, with various trace metal isotope systems now being explored. However, here we focus on an Fe speciation proxy as this is now a well-established method which allows high throughput of samples at relatively low cost, while distinguishing between two important variations on the theme of anoxia – ferruginous and sulphidic conditions – the importance of which will be explored in subsequent sections. In this section, the Fe-S-C systematics underpinning this Fe based proxy will be summarised, along with the development and application of the method.

1.2.1 Iron, sulphur and carbon systematics

Interest in sedimentary pyrite formation dates back more than forty years, and in that time, iron, sulphur and carbon systematics have been extensively studied. Berner (1970) described the basics of pyrite formation in sediments: in the absence of oxygen, organic matter delivered to sediments, along with detrital iron, can be metabolised through anaerobic bacterial sulphate reduction. This process produces H_2S, which reacts with the most reactive forms of Fe to produce FeS. A further reaction between FeS and elemental S (released during the oxidation of some of the H_2S) then forms pyrite. Thus, the formation of pyrite may be limited either by the availability of organic matter, sulphate, or reactive iron (Berner, 1970, Berner, 1984). Observations of differing C/S ratios between freshwater and marine sediments were thought to be a result of low sulphate concentrations in freshwater settings limiting pyrite production (Berner and Raiswell, 1984). In marine environments, it was suggested that organic matter was the major control on pyrite formation in normal (non-euxinic) sediments, while reactive Fe availability limited pyrite formation in euxinic settings (Berner, 1984). That reactive Fe was a major factor was confirmed by Canfield (1989a), who demonstrated that Fe oxide minerals reacted rapidly with sulphide, and their presence precluded the build-up of H_2S in sediment porewaters until they were consumed. In contrast, the Fe in sheet silicates was found to react very slowly with sulphide (Canfield et al., 1992), such that the sulphide produced by sulphate reduction could build up in porewaters, but would be lost by diffusion before significant reaction with silicates occurred. Canfield et al. (1992) concluded that limitations on pyrite

production would depend on the relative rates of sulphate reduction and rates of sulphide reaction with available iron minerals. This conclusion meant that the high degrees of Fe sulphidation observed in euxinic sediments from the Black Sea could not be accounted for by extensive sulphidation of Fe silicate phases (Canfield et al., 1996), and therefore an alternative source of highly reactive iron had to be found. Wijsman et al. (2001) were able to demonstrate that this source was a flux of highly reactive iron from the oxic continental shelf sediments. Dissolved iron lost from shelf areas was transported to deep-sea environments where it could react with water column sulphide and be trapped and deposited in sediments as pyrite.

1.2.2 Development of the iron speciation proxy

The study of Fe-S-C cycling in modern sedimentary environments paved the way for the development of a series of geochemical indicators, namely, C/S, Degree of Pyritisation, Highly Reactive Fe/Total Fe and Total Fe/Aluminium (Raiswell and Canfield, 2012). At first, the focus lay on the roles of carbon and sulphur in the formation of pyrite. Differences between organic carbon to pyrite sulphur ratios under freshwater, normal marine and euxinic marine conditons were identified by Berner and Raiswell (1983) and the C/S technique was developed as a way of distinguishing between freshwater and normal marine rocks (Berner and Raiswell, 1984). However, overlaps in C/S ratios between aerobic, restricted and inhospitable (see below) samples (Raiswell et al., 1988) meant that C/S ratios did not make a good redox indicator.

Degree of Pyritization (DOP) was introduced as a palaeoenvironmental indicator of bottom-water oxygenation by Raiswell et al. (1988), building on a concept developed by Berner (1970) to explore the factors that limit pyrite formation. DOP describes the proportion of reactive iron that has been converted to pyrite and was defined by Berner (1970) as Pyrite Fe/Pyrite Fe + HCl-soluble Fe. HCl-soluble Fe is the iron (including haematite, limnotic goethite and chlorite; Berner, 1970) which can be dissolved by concentrated, boiling HCl (see section 2.4.3), which was thought to extract the iron in compounds most reactive towards H_2S. Raiswell et al. (1988) calibrated DOP using Devonian to Cretaceous sediments that had previously been classified on the basis of palaeoecological and sedimentological criteria. They found that aerobic (deposited in fully oxygenated bottom waters) samples had DOP < 0.42, restricted (deposited in waters with

low oxygen concentrations) samples had a DOP value between 0.46 and 0.80 and inhospitable (little or no oxygen present in bottom waters, H_2S may be present continually or intermittently) samples had a DOP value between 0.55 and 0.93. A boundary at 0.45 separated aerobic from restricted conditions, and although there was an overlap between the latter two categories, Raiswell et al. (1988) showed that a boundary at 0.75 separated over 90 percent of the data.

However, at this point, it was not clear exactly which minerals reacted with dissolved sulphide (i.e. the reactive iron pool), or how quickly (Raiswell and Canfield, 2012). Canfield (1989a) established that oxide minerals (lepidocrocite, ferrihydrite, goethite and haematite) were the most important Fe phases in early diagenetic pyrite formation, while finding little evidence for the involvement of silicate minerals. Further work (Canfield et al., 1992) demonstrated that the iron in sheet silicates reacted with sulphide with a half-life of around 100,000 years. Because this rate of reaction is very much slower than typical rates of sulphide production by sulphate reduction, sulphide would be lost by diffusion before it could react with Fe in silicates to any great extent. The finding of intermediate DOP values at their study site, despite availability of sulphide in the pore waters after Fe oxides were exhausted, led to the conclusion that the boiling HCl extraction was overestimating the reactive iron pool. A comparison of iron extraction methods by Raiswell et al. (1994) found that the boiling HCl extraction did indeed extract significant amounts of iron from some sheet silicates. They also found that a dithionite extraction quantitively dissolved the iron oxides, but had a negligible effect on the silicates responsible for adding to the boiling HCl Fe pool. This study provided reactive iron with a mineralogical definition, and identified an extraction method for its quantification (Raiswell and Canfield, 2012).

Studies of euxinic Black Sea sediments (Canfield et al., 1996) led to the realisation that the pyrite enrichments that were observed were a result of an additional reactive iron source that was separate to the main siliciclastic sediment source. In a study of sediments from a range of modern marine environments, Raiswell and Canfield (1998) discovered that while aerobic continental margin, deep sea and dysaerobic sediments contained similar amounts of highly reactive Fe; Fe_{HR} (dithionite-soluble iron and pyrite iron), poorly reactive Fe; Fe_{PR} (iron soluble in HCl minus that soluble in dithionite) and unreactive iron; Fe_U (total iron minus HCl soluble

iron), samples from euxinic settings were enriched in highly reactive iron due to pyrite being generated in the water column. Raiswell et al. (2001) discussed the Indicator of Anoxicity (IA) as an indicator of water-column anoxia in the Jurassic Kimmeridge Clay. The anoxicity indicator, a ratio also considered by Raiswell and Canfield (1998), was defined as the ratio of pyrite Fe and oxide Fe to total Fe, or FeD+FeP/FeT, where FeD is dithionite-extractable Fe. Following validation of the IA in modern anoxic sediments, they concluded that IA values in the Kimmeridge Clay were consistent with oxygen-restricted biofacies (ORB) classifications. These two studies demonstrated that sediments deposited under oxygenated bottom water generally had IA values < 0.4 while samples from anoxic settings had IA values > 0.5 (with the exception of turbiditic deposits). The studies of modern and Phanerozoic marine sediments by Raiswell and Canfield (1998) and Poulton and Raiswell (2002) allowed thresholds in Fe_{HR}/FeT for oxic ($Fe_{HR} \leq 0.22$) and anoxic ($Fe_{HR} \geq 0.38$) conditions to be determined (Poulton and Canfield, 2011).

More recently, the definition of highly reactive iron has been refined following the realisation that the dithionite extraction excluded from Fe_{HR} minerals such as magnetite, siderite and ankerite, which are important constituents of Proterozoic sediments and would likely have derived from Fe that was highly reactive towards dissolved sulphide (Poulton and Canfield, 2005, Poulton et al., 2004). A new FeHR was therefore defined as $Fe_{carb} + Fe_{ox} + Fe_{mag} + Fe_{py}$, with a sequential extraction scheme (detailed in section 2.4) developed to quantify these pools. Although this proxy was originally developed and calibrated for siliciclastics, it has previously been applied to carbonate-rich sediments (e.g. März et al. (2008) and has now been tested on carbonates (Clarkson et al., 2014). In a study combining new analyses of modern samples that show a wide range of carbonate contents with data from previous calibration studies and from the Pangea database, Clarkson et al. (2014) found that the FeHR/FeT thresholds were generally applicable to carbonate rich sediments. The main exception to this is where Fe concentrations were very low, FeHR/FeT ratios were spuriously high (i.e. over 0.38) in oxic samples. This may be because carbonate rich samples contain less silica and therefore less silicate Fe in the total Fe pool. The majority of oxic samples across a wide range of carbonate contents and with FeT>0.5 wt% plotted close to or below the anoxic threshold of 0.38, while most samples from

anoxic bottom water environments plotted above 0.38, even with very high carbonate concentrations. Clarkson et al. (2014) therefore concluded that the Fe speciation proxy behaves consistently when FeT is >0.5 wt%, which provides a suitable screening criterion when considering whether or not the Fe speciation indicator can be applied to carbonate-rich samples.

FeHR/FeT distinguishes between oxic and anoxic settings, but anoxic conditions could entail free sulphide or free Fe(II) in the water column (Poulton and Canfield, 2005). In order to further distinguish between euxinic and ferruginous anoxic depositional settings, Poulton et al. (2004) introduced the Fe_{py}/FeHR indicator, which describes the extent of pyritization of the highly reactive Fe pool. On the basis of data from the Black Sea (Anderson and Raiswell, 2004) a euxinic threshold of 0.8 was recognized, but subsequent work on Phanerozoic sediments (März et al., 2008) has led to a revised threshold of 0.7 being suggested (Poulton and Canfield, 2011).

An alternative method to the FeHR/FeT ratio for recognising iron enrichments is the FeT/Al ratio. Lyons et al. (2003) found, in a study of sediment cores from the Cariaco Basin, that FeT/Al ratios in euxinic sediments were elevated above a continental baseline recorded in underlying oxic sediments as a result of Fe scavenging during water-column pyrite formation. In order to detect iron enrichments, a base-line is required. A base-line of 0.53 ± 0.11, derived from the mean FeT/Al ratio of Palaeozoic normal marine shales (Raiswell et al., 2008) has been suggested (Raiswell and Canfield, 2012). In their study of samples with a wide range of carbonate contents, Clarkson et al. (2014) obtained a very similar average of 0.55 ± 0.11. This consistency, and a lack of covariation between Fe/Al and carbonate contents led them to conclude that, under oxic conditions, this proxy behaves consistently even when carbonate concentrations are high and FeT and Al are low. However, they note a large relative standard deviation on this ratio, which they attribute to enhanced variability in Al contents, relative to Fe, in lithogenic sediment inputs – sediment supply can be highly variable in terms of chemical composition. They therefore suggest that a local oxic baseline should, where possible, be defined, as have previous studies (Lyons et al., 2003, Poulton et al., 2010). The Fe/Al ratio also does not distinguish between ferruginous and euxinic conditions.

A further limitation of the FeT/Al proxy, and indeed the other palaeoredox indicators, is that iron enrichments resulting from an anoxic water column may be masked by high rates of siliciclastic deposition (Canfield et al., 1996, Lyons et al., 2003, Lyons and Severmann, 2006).

1.3 Oxygenation of the biosphere

1.3.1 Oxygen in the atmosphere

The history of atmospheric oxygen through the Precambrian has been reconstructed using a variety of proxies, including the differential preservation of redox-sensitive elements, sulphur isotope fractionations and the presence in the rock record of banded iron formations (BIFs). A summary by Canfield (2005) suggested that these various forms of evidence point towards low levels of atmospheric oxygen (less than 0.1% PAL (present atmospheric level)) in the Archean, with an oxygenation of the Earth's surface at around 2.45 Ga known as the Great Oxidation Event. Following this is an apparent return to low oxygen conditions between 2.0 and 1.8 Ga. After 1.8 Ga, atmospheric oxygen levels were estimated to have been in the range of 5% to 18% PAL (Canfield and Teske, 1996) with apparently little change during this time (the 'boring billion'). A further increase in oxygen levels occurred towards the end of the Proterozoic, which has been described as a Neoproterozoic Oxygenation Event (Shields-Zhou and Och, 2011). While low oxygen levels prior to the GOE seem to be well established (Lyons et al., 2014, Poulton, 2017), subsequent atmospheric oxygen dynamics remain poorly constrained. Current evidence suggests that O_2 levels likely fluctuated (e.g. (Canfield et al., 2013). A low marine sulphate reservoir, inferred from sulphur isotope data, has been suggested to indicate low levels of atmospheric oxygen (Kah et al., 2004, Kah and Bartley, 2011). Chromium isotope data has been also been used to track fluctuations in Proterozoic oxygen levels (Frei et al., 2009) and recent studies have suggested maximum mid-Proterozoic O_2 levels of 0.1% PAL (Planavsky et al., 2014), which is supported by a recent reconstruction of Precambrian phosphorus availability and accompanying modelling (Reinhard et al., 2017). However, Zhang et al. (2016) have proposed atmospheric oxygen levels > 4% PAL for the Mesoproterozoic on the basis of a model of marine carbon – oxygen cycle dynamics.

1.3.2 Ocean redox structure in the Precambrian

There are a number of models for the response of the oceans to atmospheric oxygen changes. Early models suggested that the end of BIF deposition (thought to indicate iron-rich oceans) at 1.8 Ga was due to oxidation of the deep ocean (Holland, 1984). Holland has since cited the absence of marine manganese deposits throughout the subsequent 'boring billion' as evidence for a mildly oxygenated deep ocean (Holland, 2006). In contrast, Canfield (1998) suggested that anoxic bottom waters persisted long after the end of BIF deposition and that sulphide was responsible for precipitating iron from the deep ocean. These sulphidic (euxinic) conditions were proposed to have continued until the second big rise in atmospheric oxygen during the Neoproterozoic. Use of iron speciation and sulphur isotope compositions on sediments from the 1.8 Gyr Animikie group, Canada (Poulton et al., 2004) and on Mesoproterozoic carbonaceous shales from the McArthur Basin, northern Australia (Shen et al., 2002) provided evidence of euxinic conditions.

However, more recently it has been suggested that ferruginous conditions continued to dominate in the deep oceans through the Proterozoic, with euxinia confined to continental margins and epicontinental seas. An extension of the study on the 1.8 Gyr Animikie group to include cores from progressively more distal locations has addressed the problem of a previous lack of spatial and temporal resolution (Poulton et al., 2010). These data indicate a stratified ocean, with oxic shallow waters, euxinic mid-depth waters and deep ferruginous waters, with euxinic conditions extending at least 100km from the shoreline. A similar redox structure has been reported for the Ediacaran (635-542 Ma) Doushanto Formation of China (Li et al., 2010). Widespread ferruginous conditions below the mean storm wave base are also reported by Canfield et al. (2008), who suggest that deep ferruginous waters were not just associated with Neoproterozoic glaciations, as previously thought, but were a general feature of late Neoproterozoic oceans. Indeed, ferruginous oceans are now thought to have been a major feature of anoxic events throughout the Earth's history (Poulton and Canfield, 2011). In recent years, much more data for the mid-Proterozoic has been published leading to suggestions of widespread iron-rich conditions at this time (Planavsky et al., 2011) and a Mesoproterozoic iron formation has been identified (Canfield et al., 2018). New evidence also suggests a high degree

of heterogeneity and dynamic cycling between different redox conditions during the mid-Proterozoic (e.g. (Gilleaudeau and Kah, 2015, Sperling et al., 2014, Cox et al., 2016, Planavsky et al., 2018)).

Organic matter loading has been cited as a control on redox conditions. For example, Sperling et al. (2014) suggested that very low TOC contents were the key to maintenance of oxic conditions found in a Mesoproterozoic succession from Russia while Cox et al. (2016) suggested that sulphidic conditions in the Mesoproterozoic Roper Seaway developed as a result of high organic carbon loading. In a study of a Neoproterozoic record of a shift between ferruginous and euxinic conditions, Johnston et al. (2010) proposed that higher organic carbon production could push a system from ferruginous conditions to euxinia. They suggested that where oxygen had been depleted, and free Fe was available, dissimilatory Fe reducers would outcompete sulphate reducers until reactive Fe^{3+} was exhausted. Only at this point, if sufficient TOC remained, could sulphate reducers produce enough H_2S for it to build up in the water column. Poulton and Canfield (2011), however, argue that the relative fluxes of Fe and S to the ocean exert a major control on the balance between ferruginous and euxinic conditions. An example of this has been presented by Guilbaud et al. (2015), where an inferred transition to ferruginous conditions was suggested to be a result of an increased Fe flux to the oceans relative to S due to changes in weathering regime and sulphate being sequestered by intracontinental evaporites.

1.4 Redox driven nutrient cycling

1.4.1 The Phosphorus cycle

An essential nutrient, thought to limit primary production on geological timescales (Tyrrell, 1999), there has been much interest in phosphorus cycling. The main source of P to the oceans is riverine input of P derived from continental weathering, and ultimately this P will be removed through burial in sediments (Ruttenberg, 1993, Delaney, 1998, Benitez-Nelson, 2000). Four removal mechanisms have been identified, namely, burial with organic matter, absorption and precipitation with clays and Fe oxyhyrdoxide particles, phosphorite burial and hydrothermal

processes (Benitez-Nelson, 2000, Delaney, 1998, Froelich et al., 1982). Following deposition, P may be released to porewaters through the reduction of ferric oxyhydroxides and from organic matter decomposition (Krom and Berner, 1981). This P can be released back to the water column, or be incorporated into authigenic phases (Delaney, 1998). Continental margin sediments may be a significant sink for reactive P in the ocean (Filippelli, 1997).

In work on volcanogenic sediments from the East Pacific Rise, Berner (1973) demonstrated that phosphate was removed from sea water by adsorption to volcanogenic sediments, a process that has also been confirmed in other studies (e.g. (Feely et al., 1991, Feely et al., 1998, Wheat et al., 1996)). Evidence for the trapping of P by Fe has also been found in continental margin settings (Slomp et al., 1996b). Once in the sediment, it was found that phosphate was released to pore waters upon the reduction of poorly crystalline iron oxides and subsequently either readsorbed or released to the overlying water. Phosphorus recycling and burial has been shown to be influenced by redox conditions. Mort et al. (2010) studied porewater and sediment samples from the Baltic Sea where redox conditions currently range from oxic, through seasonally hypoxic to almost permanent euxinia. They found strong surface enrichments in Fe-oxide bound P at oxic and seasonally hypoxic sites, but not at anoxic sites, with P being released back to the water column during periods of hypoxia. Ultimately though, they found that little Fe-oxide bound P was preserved at depth. In contrast, März et al. (2008) found that P was dominantly bound to Fe oxides in black shales from the Cretaceous during non-euxinic anoxic periods. Their data demonstrated strong drawdown of P at these times, in comparison to the intervening euxinic phases. Drawdown of P associated with Fe oxides under ferruginous conditions has also been implicated in the enrichment of P in phosphatic Cambrian carbonates (Creveling et al., 2014). Meanwhile, work in a modern ferruginous setting has demonstrated that carbonated green rust, formed below the chemocline by the reduction of ferrihydrite, may be even more effective than Fe oxides at scavenging nutrients such a phosphorus (Zegeye et al., 2012).

A much discussed matter in the study of ocean P cycling is the idea that P can be preferentially regenerated from organic matter in relation to C. Comparisons of buried organic matter C_{org}/P_{org} ratios to the Redfield ratio, generally accepted to be 106:1 (Redfield, 1963), have been used to

demonstrate this. An investigation into organic C to organic P ratios in marine sediments by Ingall and Van Cappellen (1990) revealed a systematic variation with sedimentation rate. With the assumption that preferential regeneration of phosphorus relative to carbon took place during oxic respiration, they explained high C/P ratios at intermediate sedimentation rates as being the result of the preferential release of P during incomplete organic matter degradation. Low C/P residual organic matter at sites of very slow sedimentation rates were explained as being the residual P-enriched organic phases left behind after extensive organic matter oxidation, while low C/P ratios at high sedimentation rates resulted from the good preservation of organic matter with Redfield ratios of C to P due to rapid burial. Further investigations revealed a possible role for redox in the organic C/P ratios preserved in the sedimentary record. Ingall et al. (1993) found average ratios of 150 in bioturbated (therefore oxic) shales and 3900 for closely associated laminated (therefore anoxic) shales. High C/P ratios in laminated sediments were suggested to be the result of extensive regeneration of P from sedimentary organic matter and enhanced preservation of organic C relative to the oxic sediments, which they recognised as being a mechanism for burying large quantities of organic C whilst sustaining further productivity. This hypothesis has been supported by studies of modern settings (Ingall and Jahnke, 1994, Ingall and Jahnke, 1997). Work by Slomp et al. (2002) on Mediterranean sapropels has also shown enhanced regeneration of P relative to organic C, which they suggest was largely due to the enhanced release of P from organic matter during sulphate reduction, in comparison to the more efficient retainment of P by aerobic organisms. Further work on sapropels demonstrated that both sedimentation rate and exposure to oxygen exerted control on the relative burial rates of P and organic C (Slomp et al., 2004). Slomp et al. (2004) also suggested that it was the changing burial efficiency of C_{org}, rather than P_{org}, that controlled the ratio, with much higher C_{org}/P_{org} ratios under euxinic conditions being the result of enhanced C_{org} burial.

Phosphorite deposits constituting significant Phanerozoic P sinks had long been known about (Froelich et al., 1982) when the formation of apatite was identified in modern Mexican continental margin sediments (Jahnke et al., 1983). Evidence of apatite formation in settings not traditionally associated with phosphorite formation led Ruttenberg and Berner (1993) to

conclude that apatite formation was a more important P sink than had previously been recognised. An increase in the authigenic apatite reservoir with depth, mirrored by a decrease in organic P suggested to them that continued apatite formation during early diagenesis was occurring at the expense of organic P – in other words, phosphorus was being transferred from one reservoir to another in a process described as "sink-switching". Work by Slomp et al. (1996a) demonstrated that Fe-bound P was also being redistributed to authigenic apatite during early diagenesis. They also reported that the cycling of P between Fe-bound P and pore water phosphate at the redox interface created conditions that were favourable for apatite formation, and that Fe-bound P acted as an intermediate between organic P and apatite. High contributions of apatite to the total reactive P burial flux supported the assessment by Ruttenberg and Berner (1993) that apatite had a globally important role in P burial. This transfer of P to an apatite sink has been identified in a number of other studies (e.g. (Filippelli and Delaney, 1996, Mort et al., 2010)). Anderson et al. (2001) suggested that the efficient transfer of organic P to authigenic minerals means that $C_{organic}/P_{reactive}$ ratios should be used alongside $(C/P)_{org}$ ratios when assessing the geochemical behaviour of sedimentary P.

More recent studies have demonstrated the role of redox in the balance of phosphorus sinks. On the basis of a reactive-transport model, Tsandev et al. (2012) found that burial of authigenic calcium associated P minerals (Ca-P), organic P (org P) and iron-bound P (Fe-P) was affected by water column oxygenation and organic matter (OM) loading such that authigenic Ca-P burial was favoured under high OM fluxes and very low or high oxygen. Where oxygen is low and OM fluxes are intermediate to high, org P burial is promoted, while Fe-P is preserved only when oxygen levels are high and OM fluxes low.

In order to better understand P burial and diagenesis, Ruttenberg (1992) developed a sequential extraction method (SEDEX) to quantify five sedimentary P reservoirs. Although it was only standardised for application to modern settings, adapted versions have been successfully applied to ancient sequences (e.g. März et al. (2008)). However, some studies have shown that care must be taken in using this method for very old rocks. A key advantage of the SEDEX procedure was that it discriminated between detrital apatite and authigenic apatite, the importance of this being that authigenic apatite is a sink for reactive P whereas detrital apatite

would not have been reactive in the water column, and therefore not bioavailable. Through a combination of petrological observation and application of the SEDEX technique, Creveling et al. (2014) demonstrated that, while a large proportion of extracted P from their Cambrian drill core material was operationally defined as detrital, much of it was likely to have been authigenic in origin. This was thought to be a result of increasing crystallinity of authigenic phosphorus minerals (Shemesh, 1990) during burial diagenesis (Creveling et al., 2014), and such a transformation of authigenic apatite had previously been suspected in a Miocene succession (Filippelli et al., 1995, Föllmi et al., 2005). Despite this complication, P speciation in Proterozoic deposits, likely to be highly crystalline, should provide a valuable new insight into Precambrian P cycling (see section 1.4.3).

1.4.2 Redox conditions, nutrients and productivity

The work of Ingall and others (Ingall et al., 1993, Ingall and Jahnke, 1994) led to the suggestion of a positive feedback loop that linked ocean anoxia, enhanced P regeneration and marine productivity, whereby oxygen depletion as a result of eutrophication enhances P regeneration, thus stimulating biological productivity. Enhanced primary production would increase rates of respiration, intensifying water column anoxia and therefore increasing benthic P release. A second mechanism involving prevention of drawdown of phosphate by ferric oxyhyroxides under anoxic conditions was also suggested. This model was further devoloped to incorporate a negative feedback mechanism that prevents runaway anoxia (Van Cappellen and Ingall, 1994, Van Cappellen and Ingall, 1996); burial of more organic carbon leads to more oxygen being released to the atmosphere, which subsequently will increase dissolved oxygen concentrations in seawater.

There are, however, circumstances where P may be retained under anoxic conditions. März et al. (2008) demonstrated in a study of Cretaceous black shales that while strong phosphorus regeneration occurred under anoxic, sulphidic (i.e. euxinic) conditions, enhanced P burial occurred under anoxic, non-sulphidic (i.e. ferruginous) conditions as a result of scavenging and/or incorporation of P by Fe (oxyhydr)oxide particles. Ferruginous conditions may not always lead to enhanced P burial though. In a study of black shales from the Cretaceous Tarfaya

shelf, Poulton et al. (2015) found evidence of extensive P recycling under ferruginous conditions. They suggested that porewater sulphide generation was sufficient to remobilise sequestered P back to the water column through the reduction of Fe oxides and preferential release of P during bacterial sulphate reduction of organic matter.

1.4.3 Phosphorus in the Precambrian

Whilst a number of detailed studies have been conducted on phosphorus cycling in Phanerozoic successions, research in the Precambrian has largely focussed either on the study of rare Palaeoproterozoic and Neoproterozoic phosphorites, or on approaching the question of what oceanic concentrations of dissolved phosphate might have been. Estimations of this have been obtained through experimental study of the interactions between P and Fe, and with silica, and modelling, with published empirical data from Precambrian rocks limited to P/Fe ratios from iron formations and hydrothermal deposits (Planavsky et al., 2010), and total P concentrations from shales (Reinhard et al., 2017).

On the basis of what was known about adsorption of phosphorous on to iron oxides in the modern ocean, and P and Fe content of Archean and early Proterozoic banded iron formations (BIFs), Bjerrum and Canfield (2002) suggested that oceanic orthophosphate concentrations would have been around 10-25% of present day levels, thus limiting rates of photosynthesis, carbon burial, and in turn, atmospheric oxygen concentrations. However, this conclusion was disputed by Konhauser et al. (2007), who argued that higher silica levels in the Archean ocean would effectively compete with phosphate for sorption sites, such that ferrihydrite would not have been the major sink for phosphate that Bjerrum and Canfield had suggested. Konhauser et al. concluded that Archean ocean phosphate levels could have been on a par with modern oceans, with a "phosphate crisis" leading to a reduction in productivity being unlikely. The time frame over which P/Fe ratios in iron-oxide-rich sedimentary rocks were used to estimate the oceanic phosphate reservoir was then extended up to the Quaternary by Planavsky et al. (2010). Taking into account changes in the silica cycle, they concluded that P/Fe ratios suggested very high marine phosphate concentrations in the Cryogenian following the glaciations at that time. This is more than five times higher than their estimates for the Phanerozoic. Prior to those high

Cryogenian values, they suggest that phosphate concentrations could have been equivalent to the Phanerozoic, but are likely to have been somewhat higher.

A study by Jones et al. (2015) returned estimates of early Earth phosphate concentrations to the order of magnitude first suggested by Bjerrum and Canfield (2002). Jones et al. argued that the experiments conducted by Konhauser et al. (2007) did not sufficiently reflect the complexity of sea water, and demonstrated through their own experiments an important role for Ca^{2+} and Mg^{2+} ions in the sorption of phosphorus by iron oxides, leading them to estimate that Precambrian BIFs recorded seawater phosphorus concentrations 18 to 58 times lower than in modern oceans, thus reviving the idea of an "early Earth phosphorus crisis".

As well as producing rather different interpretations of phosphorus dynamics in the Precambrian, this approach is also limited by notable gaps in the data due to a lack of suitable rocks for this sort of analysis. Particularly noticeable is the dearth of data for the Mesoproterozoic. These issues have recently been addressed by Reinhard et al. (2017), who compiled a large data set from existing literature and from new analyses which span the last 3.5 billion years of marginal marine siliciclastic deposition. Their approach was to use bulk P content to track broad changes in authigenic P burial, and they found that there was an increase in the variability and mean P content of shales from the Cryogenian onwards, compared to earlier in the Precambrian. They note that more than 95% of Precambrian samples have concentrations of P that fall within the expected range of detrital P for modern marine sediments and average upper continental crust, implying that P concentrations recorded during much of the Precambrian largely record detrital P inputs, while the increased mean and variability in P concentrations from the Cryogenian onwards reflects a shift to more authigenic P inputs to the sedimentary record. They interpret this as evidence for P biolimitation before about 700 – 800 Ma, which they propose might have resulted in primary producers having elemental stochiometries that diverged strongly from the Redfield ratio, due to an Fe-based nutrient P trap.

1.5 The Mesoproterozoic Taoudeni Basin

1.5.1 Regional geological setting

The Taoudeni Basin is situated on the West African craton, which consists of an Archaen-Palaeoproterozoic basement and a number of sedimentary basins (Villeneuve and Cornée, 1994). The Taoudeni Basin, which covers about 2 million square km, is bounded to the north/northwest and to the south by the basement of the Reguibat and Leo shields. The basement, cratonised mainly during the Eburnean orogeny at ~ 2000 Ma (Deynoux et al., 2006) is considered to have been tectonically stable since 1700 Ma (Villeneuve and Cornée, 1994), except for intrusions linked to the Central Atlantic Magmatic Province and the opening of the North Atlantic during the Late Triassic (Verati et al., 2005, Rooney et al., 2010). Resulting from the Pan-African (late Neoproterozoic) and Hercynian (~ 300 Ma) tectonic events, the Pan-African and Mauritanide fold belts form the eastern and western boundaries of the Taoudeni Basin (Bronner et al., 1980, Villeneuve and Cornée, 1994). The geodynamic evolution of the basin between 1100 and 300 Ma was apparently controlled by two main factors: more recently (since ~ 650 Ma) the Pan-African orogenic event gave elasticity to the craton allowing subsidence rates of 15 m/Ma, while prior to this, subsidence rates were generally low but highly variable as a result of local occurrences of heavy material (ferruginous quartzite associated with aluminous gneisses) increasing the density of the lower crust (Bronner et al., 1980).

1.5.2 General stratigraphy

Sedimentary deposits form a thin cover (on average 3km) over distances of 1000 – 1500 km across the Taoudeni Basin, stretching, on the northern margin, from the Adrar region of Mauritania to Grizim in Algeria. The sedimentary cover of the Taoudeni Basin has been divided into five Sequences (Bertrand-Sarfati et al., 1991) or four Supergroups (Villeneuve, 2005), which record deposition in shallow marine and continental environments (Benan and Deynoux, 1998) from the Middle Proterozoic until the Mesozoic-Cenozoic. Resting unconformably on the basement, the first sequence consists of Middle to Late Proterozoic deposits. During the Pan-African collision, the craton experienced minor tilting and erosion. The glacial deposits (the Jbeliat Group in the Adrar region) that begin Supergroup 2 rest with an erosional and

slightly angular unconformity upon Supergroup 1 or directly upon the basement and can be traced in outcrop nearly continuously across 1300 km from Mauritania to Algeria (Arnaud et al., 2011). Supergroup 3 is made up of Ordovician and Silurian deposits, Supergroup 4 consists of Devonian and Carboniferous strata and a fifth sequence consists of Meso-Cenozoic continental sedimentation (Bertrand-Sarfati et al., 1991).

Trompette (1973) subdivided Supergroup 1 into three groups on the basis of lithology (Figure 1.1). The lowermost Char Group, 0-300 m thick, lies unconformably on the Reguibat shield and consists of fluvial to marine siliciclastic deposits (Benan and Deynoux, 1998, Deynoux et al., 2006). Separated by another unconformity, the overlying 700m thick (Deynoux et al., 2006) Atar Group, with which this thesis is concerned, consists of stromatolitic carbonates and mixed siliciclastic and carbonate facies (Bertrand-Sarfati and Moussine-Pouchkine, 1988). It is mostly marine, except for the lowermost formation. The Atar Group is unconformably overlain by the Assabet el Hassaine Group, 300 up to 1300 m thick, which consists of fine-grained siliciclastic marine deposits (Deynoux et al., 2006).

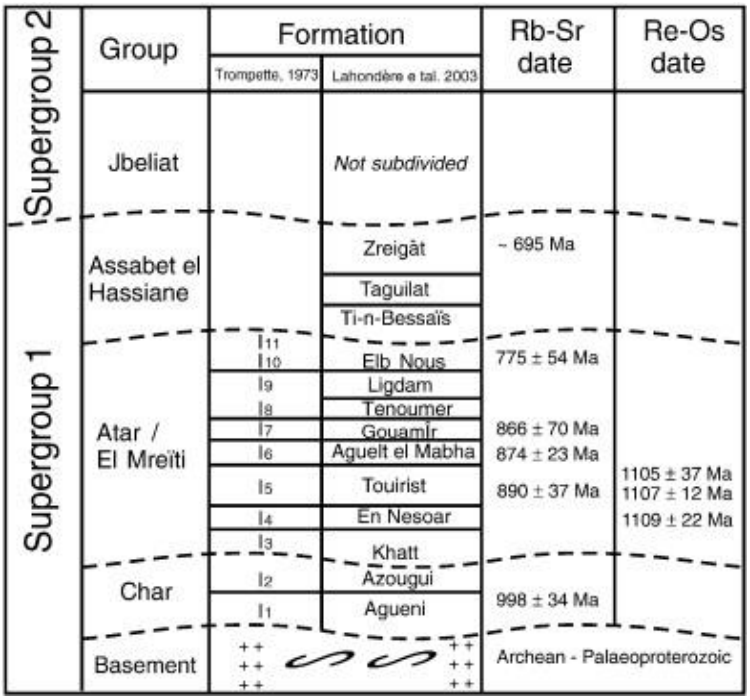

Figure 1.1 Proterozoic stratigraphy of the Taoudeni Basin, from Rooney et al. (2010).

1.5.3 The Atar and El Mreiti Groups

The type section for the Atar Group was described from outcrops occurring in the Adrar region of Mauritania (near Atar) by Trompette (1973). It consists of ten formations; I3 to I12. This study focuses on the lower 4 of these formations.

I3 (also known as Foum Chor), the basal formation of the Atar Group, sits unconformably on both the underlying eroded Char Group and the basement rock of the Reguibat Shield (Kah et al., 2012). Kah et al. (2012) report I3 to consist of fining upward, coarse- to medium-grained fluvial and marginal marine sandstones. A more detailed facies analysis of the base of the Atar Group from sections in the Adrar region (Benan and Deynoux, 1998) suggests that the Foum Chor Formation (I3) represents an estuarine setting. This conclusion comes from the observation that fluvial deposits in the lower part of the unit pass laterally and vertically into coastal- and tide-dominated shallow marine deposits. In their representative composite section, this formation consists of a fluvial succession moving into coastal plain facies then tide-dominated shallow marine deposits (consisting of sequences of large-scale sandstone beds and sheet-like sandstone-siltstone alternations, interpreted to be tidal sand bars and sand flats, possibly representing alternation between subtidal and intertidal deposition) which are truncated by an erosional surface and overlain by further fluvial deposits. Benan and Deynoux (1998) note lateral variation in facies associations, with an absence of the lower fluvial deposits and a considerably thicker coastal and shallow marine succession in the northern-most of the three composite sections presented.

The overlying I4 Formation marks a transition to a more dominantly marine environment (Gilleaudeau and Kah, 2013b) across the northern part of the basin. The I4 formation consists of interbedded siltstone and shale with increasing carbonate contents towards the top of the formation (Kah et al., 2012) and intervals of black shale (Gilleaudeau and Kah, 2013b), interpreted to mark a transgression (Gilleaudeau and Kah, 2015).

The boundary between the I4 and I5 formations is apparently gradational and poorly defined, but, in two cores, R2 and R4 from near Atar (Martín-Monge et al., 2016), Gilleaudeau and Kah

(2015) identify the boundary as a major transgressive surface that marks the beginning of a series of open marine stromatolitic reefs. (Bertrand-Sarfati and Moussine-Pouchkine, 1985, Kah et al., 2009). These reef units alternate with siltstones and black shales. The formation is interpreted to have been deposited in an open marine setting (Gilleaudeau and Kah, 2013b), with possible water depths of 80 – 100m (Bertrand-Sarfati and Moussine-Pouchkine, 1985, Kah et al., 2009). Three distinct reefs are recognized, the onset of each being marked by the appearance of herringbone carbonate cement. Herringbone carbonate is apparently restricted to deep-basin environments and extensive precipitation of this through the third reef is suggested to be evidence of the persistence of deeper-water (not quantified here) environments (Kah et al., 2012).

An abrupt change to thinly bedded carbonate marks the start of the I6 Formation. Wave ripples and intraclastic, flat pebble conglomerates suggest tidal to storm-dominated shallow marine environments (Kah et al., 2012). I6 further consists of a fining-upward succession of shallow marine sandstone, siltstone and shale which is interpreted to represent a return to siliciclastic-dominated deposition that marks an abrupt loss of accommodation space across the basin. Scattered stromatolitic bioherms occur in the lower part of the formation, while bright white, massively-bedded limestone that has been interpreted to be calcitized gypsum is found in the upper part of the formation indicating a shallow marine, but restricted, environment (Gilleaudeau and Kah, 2013a, Kah et al., 2012). A major transgressive surface marks the transition to I7, which sees a return to open-marine limestone deposition. Gilleaudeau and Kah (2013a) cite abundant columnar and branching stromatolites as evidence of dominantly subtidal marine conditions.

Strata in the north-central Taoudeni Basin, which can be correlated with the Atar Group, are referred to as the El Mreiti Group. A shift in facies apparently occurs somewhere between Atar and Tenoumer, an area largely covered by Holocene sand dunes. Gilleaudeau and Kah (2013a) report that the transition from Atar to El Mreiti facies is marked by a reduction in synoptic relief of stromatolites, and eventual restriction of their growth, thinning of depositional packages and increased clay content within carbonate facies. Intermittent Proterozoic outcrops to the south of Zouerat, which can be correlated with the Atar Group in the Adrar region, are considered by

Kah et al. (2012) to exhibit El Mreiti facies which continue eastward to El Mreiti. The nomenclature (Lahondère et al., 2003) for the formations that make up the El Mreiti group is detailed in Figure 1.1. Atar-like facies reappear further to the east in western Algeria. Gilleaudeau and Kah (2015) consider the Atar Group to be pericratonic deposits on the western craton edge and the El Mreiti Group to be epicratonic deposits on the craton interior.

The basal formation of the El Mreiti Group, the Khatt Formation, is described by Kah et al. (2012) and Gilleaudeau and Kah (2015) as consisting mainly of medium- to coarse-grained fluvial to marginal marine sandstone, siltstone and shale, with evidence such as wind-ripples and halite casts in silty layers suggesting that parts of the formation were deposited as marine tidal flats.

The overlying En Nesoar Formations consists of shale and mudstone, which Gilleaudeau and Kah (2013b) report to be tidally influenced. As in I4, carbonate contents increases in the upper part of the formation. Limestones have alternating pale and dark cm-thick laminae and columnar stromatolites. Kah et al. (2012) describe wavy lamination, clayey interstromatolitic material and the absence of dessication features, and interpret the deposition of the En Nesoar Formation as being in shallow subtidal marine environments.

The base of the Touirist Formation is marked by a prominent flooding surface and a thin stromatolitic unit (20 – 150 cm thick). This is overlain by thin-bedded clayey carbonate interbedded with organic-rich black shale (Kah et al., 2012).

The Aguelt el Mabha and Gouamir formations consist of siltstone and shale with variable carbonate content. In the Aguelt el Mabha Formation, carbonate is found in thin lenses within shales, while massively bedded carbonates interpreted to be calcitized evaporites are found in the Gouamir Formation (Gilleaudeau and Kah, 2013a). The Tenoumer Formation apparently sees a return to open marine carbonate deposition (Gilleaudeau and Kah, 2015).

Gilleaudeau and Kah (2015) subdivide clastic deposits into three types of marine environment (this model does not include the Khatt and I3 formations). Their Environment I is the most

proximal, and consists of the wave-influenced siltstone and shale of the epicratonic Aguelt el Mabha Formation. Environment II is considered more distal on the basis of lower silt content and intermittent evidence for wave energy, and describes the epicratonic En Nesoar and Touirist Formations and the lower part of the pericratonic I4 formation. The upper part of I4, and all of I5 are described by Environment III, which consists of finely laminated shale with no evidence for wave energy.

1.5.4 Siliciclastic provenance

There is limited information available about the source of terrigenous siliciclastic inputs. Earlier studies suggested that siliciclastics were transported from outside of the craton and (Bertrand-Sarfati and Moussine-Pouchkine, 1985), but in a study of detrital zircons, Nicoll et al. (2010) found that the ages of zircons found in the Char and Atar Groups indicate provenance from the local granitic and gneissic basement. In terms of flow direction, some palaeocurrent data has been published. Trompette (1969) reports that elongated stromatolite reefs have a constant direction of elongation. This is north-northeast to northeast and is apparently consistent with palaeocurrent direction deduced from a variety of sedimentological features found in the interbedded siliciclastic sediment.

1.5.5 Correlations

With a lack of biostratigraphy or well constrained dating (radiometric dating is limited to a small number of Rb-Sr analyses (Clauer, 1976, Clauer, 1981, Clauer et al., 1982) and three Re-Os dates (Rooney et al., 2010)) options, correlations of Proterozoic strata across the West African Craton have relied on recognition of unconformities (Trompette, 1994) and of marker beds, in particular, stromatalites (Bertrand-Sarfati and Trompette, 1976). Bertrand-Sarfati and Trompette (1976) identified seven units that could be traced between widespread locations, from the Adrar region across the northen edge of the basin to the other side of the craton in Algeria. More recently, however, it has been reported that only one stromatolitic horizon can be identified in both the western (Atar Group) and central (El Mreiti Group) basin (Teal and Kah, 2005).

With the exception of a recent publication (Martín-Monge et al., 2016), the Khatt Formation is generally correlated to I3, the En Nesoar Formation to I4 and the Tourist Formation to I5 (e.g. Rooney et al., 2010, Kah et al., 2012, Beghin et al., 2017a&b).

Kah et al. (2012) identify a regional flooding surface within 20 m of the base of the I5 Formation and at the base of the Touirist Formation, represented by the first appearance of coniform stromatolites with herringbone carbonate cement. They consider this stratigraphic tie-point, along with $\partial^{13}C_{carb}$ data, to support the correlation of these two units. A second stratigraphic tie-point identified by Kah et al. (2012) correlates the bases of the I6 and Aguelt el Mabha Formations and is marked by a transition from deeper to shallower marine environments, indicating a loss of accommodation space. This is in contrast to previous interpretations that the Aguelt el Mabha Formation was deposited in a depression constructed by reef growth in I5, which had no lateral correlative unit in the Atar Formation (Bertrand-Sarfati and Moussine-Pouchkine, 1992). However, reinterpretation of growth morphology in reef units in I5 led Kah et al. (2009) to conclude that reef growth wouldn't have created the intracratonic depression that would be required for this to be the case. More recently, on the basis of similar redox conditions and the presence of a microfossil in I5 otherwise only observed in the most proximal facies of the El Mreiti Group, Beghin et al. (2017a) have suggested that part of I5 may be correlative with the Aguelt el Mabha Formation. The possibility that I5 is coeval with both the Touirist and Aguelt el Mabha Formations has previously been noted by Lahondère et al. (2003).

1.5.6 Basin development

Moussine-Pouchkine and Bertrand-Sarfati (1997) describe the setting for the deposition of the lower part of the Atar Group (which encompasses all of the formations with which this study is concerned) as being a huge, flat cratonic area. Shallow marine siliciclastic sequences that grade into red shales and carbonates are found in the Adrar region, while in the Hank region (around El Mreiti) marine to aeolian sequences are seen, overlain transgressively by tidal carbonates with minor silicicastics. Moussine-Pouchkine and Bertrand-Sarfati (1997) report that overlying Conophyton-Jacutophyton-Baicalia biostromes occur in western and eastern parts, but growth stopped towards the middle Hank, where marls and bituminous shales filled a large, restricted

basin. Later, further stromatolitic biostromes occurred over both the Conophyton-Jacutophyton-Baicalia biostromes and the marls. Overall, it has been interpreted that depositional facies indicate a shallowing of environments towards the interior of the West African Craton. It is reported, however, that there isn't a great deal of difference in the thickness of epicratonic (clayey-carbonate and shale facies deposited on broad, shallow-water epicratonic platform) and pericratonic (predominantly stromatolitic facies deposited on shallow-water cratonic margins) deposits (Kah et al., 2012, Gilleaudeau and Kah, 2013a). There are no detailed reconstructions of basin profile available in the published literature, but Gilleaudeau and Kah (2013a) provide a summary of the development of the basin during the deposition of the Atar and El Mreiti Groups. During the deposition of the first two formations, the contrast in total thicknesses of the two groups (~ 160 m and ~ 60 m for the Atar and El Mreiti groups respectively) is interpreted as stratigraphic condensation and sedimentary bypass in intracratonic regions (Gilleaudeau and Kah, 2013a). The first stromatolitic reef in I5 and a thin stromatolitic unit near to the base of the the Touirist Formation mark flooding of the craton interior. Gilleaudeau and Kah (2013a) interpret the lesser stratigraphic thickness of the Touirist Formation compared to the I5 Formation as being the result of rapid growth of offshore reefs in the Atar region, which filled up available accommodation space. Differences in accommodation space, and thus depositional water depth, were therefore smaller during the deposition of the I5 and I6 formations in the Atar region and the Aguelt el Mabha, Gouamir and Tenoumer formations in intracontinental areas. Differences is facies between I6 and the Aguelt el Mabha and Gouamir formations are interpreted to reflect distance from terrigenous sources and progressive loss of wave energy (Gilleaudeau and Kah, 2013a). An added complexity in considering basin profile is that stromatolitic bioherms would have altered sea floor shape, and may have acted as barriers to water circulation (Moussine-Pouchkine and Bertrand-Sarfati, 1997, Lottaroli et al., 2009). However, further examination of stromatolite biostromes and observation of the juxtaposition of high- and low- relief forms (indicating different levels of energy during growth and therefore distinct depositional environments) have led to the conclusion that it is unlikely that Atar Formation stromatolite build-ups would have formed regional barriers to wave or current energy (Kah et al., 2009).

1.5.7 Sea level history

Gilleaudeau and Kah (2015) present a relative sea level history for the Atar and El Mreiti strata (fig. 2, Gilleaudeau and Kah 2015) which will be applied to this study. Gilleaudeau and Kah (2015) suggest there is a general shallowing up through the I3/Khatt Formations, although they state that I3 is a fining-up succession while Benan and Deynoux (1998) identify a series of coarsening upwards packages, but interpret most of I3 to be a single transgressional half cycle truncated by an overlying fluvial deposits. Moving up through the I4/En Nesoar Formation, water depth increases, with a gradational transition from Environment type II to III in I4 (Gilleaudeau and Kah, 2015). Sea level reaches a highstand at the base of the I5/Touirist Formations which is maintained through most of the formation, although detailed study of reef growth (Kah et al., 2009, Bertrand-Sarfati and Moussine-Pouchkine, 1988) has been used to suggest repeated sea-level fluctuation from below to above wave base during the deposition of I5 (Kah et al., 2012). During the growth of columnar stromatolites, a depth of 50 – 100 m below wave base is estimated (Craig et al., 2013, Bertrand-Sarfati and Moussine-Pouchkine, 1988). The intervening siliciclastic deposition is suggested to have occurred below wave base while walled bioherms and storm deposits occur above wave base. Towards the top of the I5/Touirist Formations there is an abrupt transition to shallower marine conditions, with a regional sequence boundary marking the base of the I6/Aguelt el Mabha Formations (Kah et al., 2012). Gilleaudeau and Kah (2015) suggest a gradual deepening of the environment up through the I6/Aguelt el Mabha Formations.

1.5.8 Geochronology

The age of the Proterozoic successions in the Taoudeni Basin was originally constrained by Rb-Sr illite and glauconite geochronology undertaken on a number of formations from Supergroup 1 which suggested ages from 998 ± 34 Ma for the Char group to ~ 695 Ma for the Assabet el Hassaine Group, with a consistent decrease in age through the stratigraphic column (Clauer, 1976, Clauer, 1981, Clauer et al., 1982). Clauer (1981) obtained an age of 890 ± 37 Ma for the Atar Group. However, more recent Re-Os geochronology has yielded ages of 1107 ± 12 Ma, 1109 ± 22 Ma and 1105 ± 37 Ma for the Atar Group (Rooney et al., 2010), moving the deposition of the Atar Group from the Neoproterozoic to the Mesoproterozoic. Although one

of the two cores used in the Re-Os dating has been altered as a result of contact metamorphism, Rooney et al. (2010) consider that the close agreement in ages from both immature and overmature organic rich shales suggests that Re-Os ORS systematics were not significantly affected by flash pyrolysis associated with this contact metamorphism. They suggest that the ~ 200 million year discrepancy between these two isotopic systems is a result of the Rb-Sr geochronology recording diagenetic events possibly associated with the Pan African Collision, rather than the depositional age of the Atar Group. The Mesoproterozoic ages obtained from Re-Os geochronology are also consistent with carbon isotope data that suggests an age of 1.1 - 1.2 Ma (Teal and Kah, 2005, Kah et al., 2012).

Chapter 2

Samples and Methodology

2.1 Introduction

This chapter details the samples used in this study in the context of existing literature on the depositional environments encountered in this succession and the methods used to analyse those samples.

2.2 Sample description and preparation

2.2.1 Sample description

Around 400 samples were obtained from 4 cores (S1 (23° 28′ 60 N/7° 52′ 0 W), S2 (22° 43′ 0 N/9° 37′ 0 W) (locations from Rooney et al. (2010)), S3 and S4) drilled in 2004 by the oil and gas company Total through the Atar/El Mreiti Groups at the north-western edge of the Taoudeni Basin, in Mauritania, as shown in Figure 2.1. The main focus of this study was on shale horizons, although some carbonate-rich samples were also analysed. Figure 2.2 shows summary stratigraphic logs of the four cores (Total, unpublished), plus zones where samples were taken. Formation boundaries come from an unpublished, confidential report (Reconnaissance géologique de la roche-mère méso-néoprotérozoïque sur la bordure nord du basin de Taoudeni, Mauritanie, BRGM). S1, S2 and S3 are reported to belong to the El Mreiti Group while S4 is described in terms of the Atar Group. This report shows a detailed correlation scheme for the cores based on identification of sequence stratigraphic boundaries and comparison with outcrop sections, but discussion in this thesis will be limited to using formation boundaries for correlation. The BRGM report sequence stratigraphic correlation scheme shows a number of cycles of sea level change within formations, but broadly speaking there is a general deepening trend for the lower part of the succession, and a general shallowing trend towards the top of the Touirist Formation, consistent with published literature. However, in contrast to Kah et al, this

report considers the upper part of I5 in S4 to be equivalent to the Aguelt el Mabha Formation in cores S1, S2 and S3.

Lithologies sampled for the four cores are summarised below. Descriptions of each sample (except for those received as powders) are to be found in appendices 1 (S2, S3 and S4) and 2 (S1).

S2 cuts through five formations (Khatt, En Nesoar, Touirist, Aguelt el Mabha and Gouamir), but only three of these are sampled in this study. Beghin et al. (2017a) report that the Khatt Formation in this core consists mainly of grey, green and brown silty to sandy shale interbedded with medium-grained sandstone. They observed cross-bedding (hummocks, ripples and waves) and gutter casts. No samples from that formation were available for this study however. Samples from towards the base of the En Nesoar Formation consist of laminated grey to black shales, some of which are silty and contain occasional mica grains. Pyrite is visible in some samples. A couple of samples used in this study contain greater than 1 wt% inorganic carbon; these will be described here as calcareous shales. Occasional ripples, gutter casts and wavy bedding were noted by Beghin et al. (2017a) in the En Nesoar Formation. Sampling in the Tourist Formation focussed on dominantly shale horizons, although there are some calcareous samples and occasional carbonate rich samples ($\geq$ 6 wt% inorganic C – these will distinguished in data plots with open symbols). The Touirist Formation shales sampled are largely dark grey to black and in many, lamination can be discerned. This is mostly planar, but some wavy, disrupted lamination and cross-lamination is observed. Clayey limestones/dolomites and carbonates also occur in this formation (Beghin et al., 2017a). Only four samples from the Aguelt el Mabha Formation were available. Three of these are calcareous, varying in colour from greenish to reddish grey. Wavy and lenticular layers can be seen. The fourth, carbonate rich sample consists of lenticular cream carbonate bodies interbedded with grey shale. Beghin et al. (2017) report that the Aguelt el Mabha Formation consists maily of red, brown and green carbonate-containing shale or clayey limestone, mudstone and fine-grained siltstone. They observed gutter casts, ripples and lenticular calcareous bodies or planar stromatolites.

S3 mainly intersects the Aguelt el Mabha Formation, with a few metres of the Touirist Formation at the bottom of the core and the beginning of the Gouamir Formation recognised at the top. All samples in this study from the Touirist Formation were received as powders and so cannot be described in detail. Inspection of unpublished core photographs suggests most of the samples are of greenish grey shale interbedded with cream coloured, lenticular carbonate bodies. Some samples are calcareous - presumably those including some of the cream carbonate. S3 170.73 is from a laminated light to dark grey section. A small number of samples from the Aguelt el Mabha Foramtion were also available to this study. Four samples from ~ 123 – 124 m depth are pale to dark grey laminated shales. The other samples, from 59 – 62 m, consist of laminated fine sandstones and silty shales ranging from grey to black in colour. Some are micaceous and all contain at least 0.5 wt% inorganic C.

S4 reportedly covers three formations in the Atar Group: I3, I4 and I5. Samples from the I3 Formation at the base of the core consist of micaceous, laminated silty and sandy shales. Some samples contain sand bodies and mud drapes and lenticular and flaser bedding (Reineck and Wunderlich, 1968) can be observed. Laminations can also be wavy and irregular. A roughly 2 m thick dolerite sill interrupts the I3 Formation within the bottom 5 m of the core. Above this continue grey to black micaceous shales and silty shales. Laminations can be observed through much of the formation, sometimes wavy, irregular or disrupted. Lenticular sand bodies are also present. Pyrite is visible in places, as is probable Fe carbonate (siderite or ankerite). Following a gap in sampling, shales of the I4 Formation are sampled between 140 and 120 m depth. These shales are laminated and vary in colour from greenish grey to black. Uneven lamination, disruption to lamination and some cross lamination is observable. There is often visible mica, but grains are generally small and sparser than is seen in samples from the I3 Formation. Visible pyrite occurs quite frequently, in irregular layers, lenses and grains. Samples from the I5 Formation mainly come from two parts of the core. At around 90 m depth shales are generally calcareous and laminated with lighter beds (possibly more carbonate rich) sometimes forming lenticular bodies in grey shale. Visible mica grains can be seen. At around 80 m, shales are mostly black. Where observed, lamination is generally planar and parallel. Again, mica is present. In a couple of samples where inorganic C > 1 wt%, brownish orange grains are present

and the sample doesn't react with 5 vol. % HCl – high Fe_{carb} contents in these samples suggest that this is likely to be an iron carbonate such as siderite or ankerite. Inorganic C is very low in the rest of the shales in this part of the core.

S1 intersects four formations (En Nesoar, Touirist, Aguelt el Mabha and Gouamir) and a dolerite sill. Samples from S1 analysed in this study cover two formations – the En Nesoar and Touirist formations. Two samples from the dolerite sill that cuts through the En Nesoar Formation in this core are also analysed for comparison. The core reaches down to somewhere in the En Nesoar Formation. Samples from the bottom ~ 6m of the core consist of carbonates ranging in colour from white to dark greenish grey. Some are stromatolitic, others are carbonate breccias. Overlying these are dark grey to black shales which acid testing and a range in Al contents (down to ~ 2 wt%) suggest contain varying amounts of carbonate. Some contain visible Fe sulphide. The remainder of the En Nesoar Formation consists of finely laminated black shales, which are interrupted by a dolerite sill of roughly 30 m thick. A number of these samples contain minor white veining (including probable calcite, but also a white mineral that does not react to 5 vol.% HCl) which was avoided when taking sections of samples for crushing. There are more black shales at the base of the overlying Tourist Formation. Between 80.86 and 75.53 m the black shales contain varying amounts of carbonate, as evidenced by low Al contents and reaction to 5 vol.% HCl. Black and dark grey laminae are visible in places, and also whitish grains elongated perpendicular to the core edge. Iron sulphide is visible in a number of these samples. Above this, the core records further deposition of black shales, many samples containing visible Fe sulphide. Fine lamination is visible in places and may be present through more of the section, but a lack of variation in colour makes lamination difficult to discern.

On the basis of mineral assemblage analysis of shale, it is thought that the Atar/El Mreiti Groups have not undergone regional metamorphism, and post depositional temperatures are likely not to have exceeded 100°C on a basin-wide scale (Rooney et al., 2010). However, evidence of contact metamorphism and hydrothermal alteration has been found in some parts of the Taoudeni Basin, thought to be associated with Jurassic dolerite intrusions (Girard et al., 1989). Girard et al. (1989) reported that petrographic and fluid inclusion data provide evidence for diagenesis at temperatures of 135-170°C in samples collected from the Assabet el Hassiane

Group, which overlies the Atar Group. Their data set included samples from a location 60 km northeast of Atar, where there are apparently no significant dolerite outcrops. There are, however, dolerite intrusions in both cores S1 and S4, approximately 30 m and 2 m thick respectively. A more recent study by Rooney et al. (2010) reports that shales from S1, described as baked black, are overmature while shales from S2 are marginally mature with respect to thermal maturity of hydrocarbons. There is no such data published for shales from S3 or S4. Rooney et al. (2010) present a model of contact conditions suggesting that for shale at the contact with the sill, temperatures would have been around 550-650°C while away from the contact the shales of S1 would have experienced a peak temperature of around 288°C. Apparently shales from S1 and S2 have similar compositions except for the presence of pyrrhotite in S1. Rooney et al. (2010) report, on the basis of X-ray diffractometry, a mineral assemblage for cores S1 and S2 of quartz, kaolinite, illite, feldspar and minor amounts of pyrite/pyrrhotite.

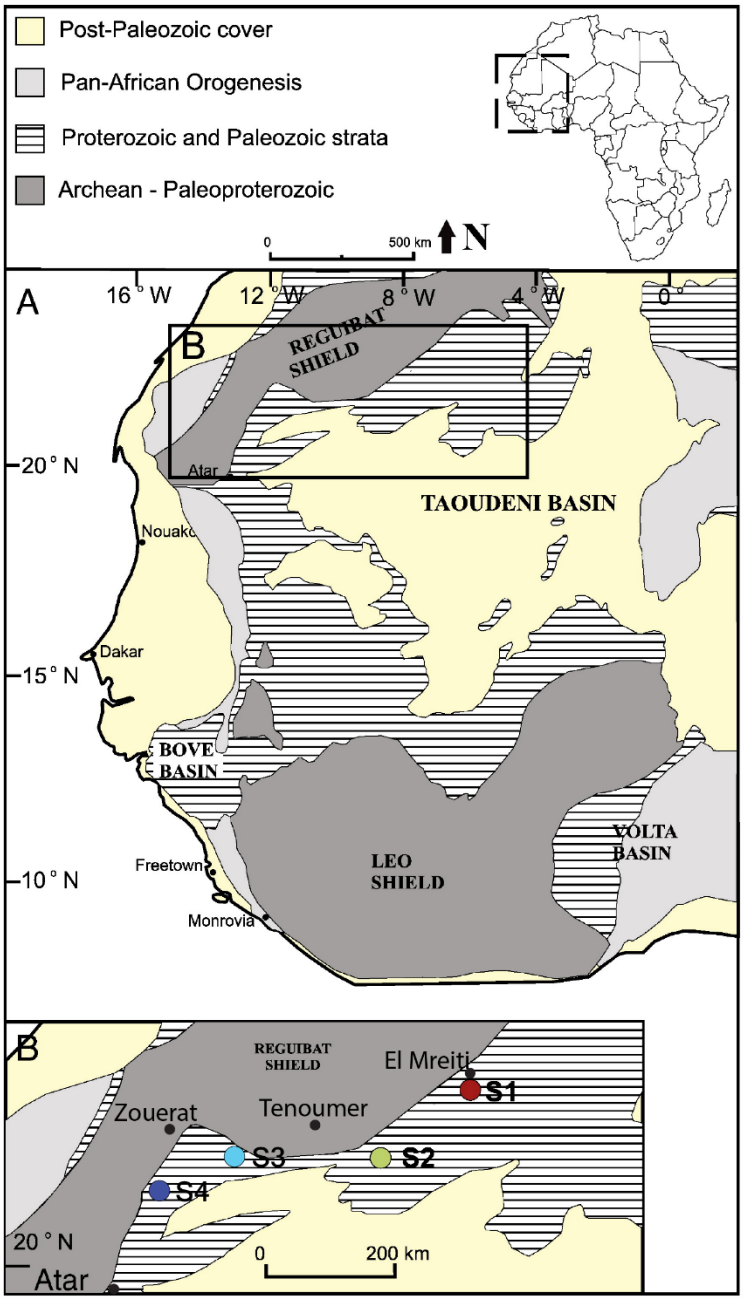

Figure 2.1 Summary geological map of the Taoudeni Basin with approximate core locations, adapted from Rooney et al. (2010)

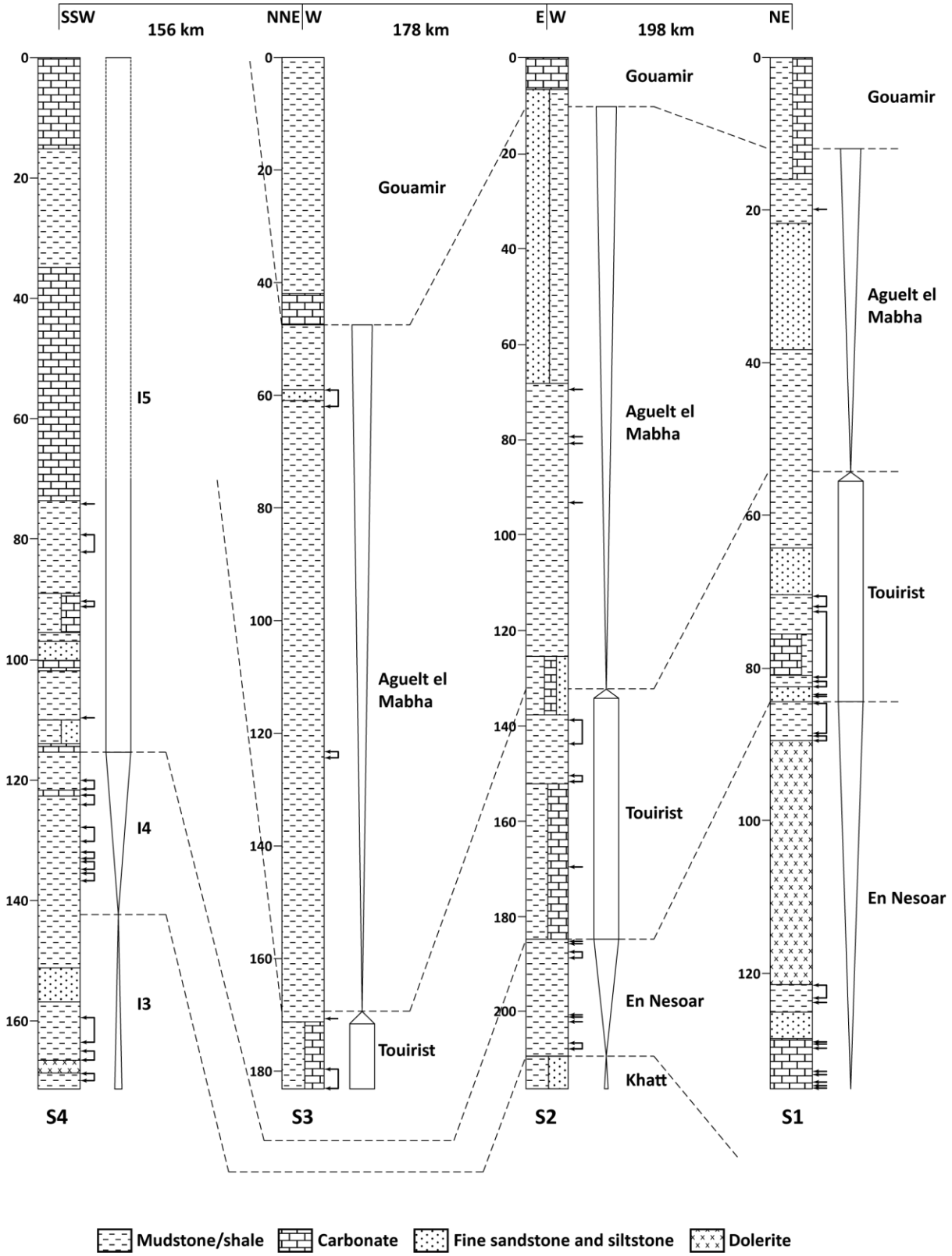
SSW
156 km
NNE
W
178 km
E
W
198 km
NE
I5
I4
I3
Gouamir
Aguelt el Mabha
Touirist
En Nesoar
Khatt
S4
S3
S2
S1
Mudstone/shale
Carbonate
Fine sandstone and siltstone
Dolerite

Figure 2.2 Summary logs of the four cores, adapted from unpublished Total documents. Lithologies shown are the dominant lithology, although more variation is apparent on cm scales in some samples. Formation boundaries are from an unpublished confidential report. Relative sea level history is from Gilleaudeau and Kah (2015). Arrows indicate horizons in the core that were sampled, with single arrows indicating single samples and bracketed arrows indicating a number of samples.

2.2.2 Depositional model

The depositional model that will be used in this study is as follows:

The basal formation of the Atar/El Mreiti Groups is represented in this study only by the more distal S4 core (although data from the Khatt Formation in core S2 from Beghin et al. (2017) will also be considered). Although previous studies suggest the I3 Formation was deposited under laterally and temporally variable fluvial to shallow marine environments, with an estuarial setting proposed (Benan and Deynoux, 1998), core S4 is located north of the extent of these studies (the composite sections of Benan and Deynoux (1998) suggest that facies become more distal towards the north). Sedimentological features such as mud drapes, lenticular and flaser bedding and gutter casts are consistent with deposition on tidal flats under intertidal to subtidal conditions (Daidu et al., 2013). Hummocky cross stratification has also been recognised in this formation (BRGM report), which is considered to be structure formed on the shoreface and shelf by waves (Dott Jr and Bourgeois, 1982). These features, along with the micaceous nature of the deposits, are consistent with transitions between the shallow marine wave-dominated and tide-dominated facies described by Benan and Deynoux (1998). Recent literature suggests that these marine conditions did extend east of Atar towards El Mreiti at times during the deposition of the I3/Khatt Formations. The environment was more dominantly marine during the deposition of the I4/En Nesoar formations, with a deepening of depositional environment up core. This is seen in both cores S2 and S4 as deposits are generally finer grained and the occurrence of features such as cross-stratification and gutter casts (occurring in higher energy i.e. shallower environments) is less common. The more proximal S1 and S2 cores were likely deposited intermittently below wave base or below fair weather but not below storm wave base (Gilleaudeau and Kah (2015) are not clear whether intermittent evidence for wave energy implies fluctuations in sea level or storm events), with some tidal influence. Deposition in the

lower portion of I4 in S4 is also shallow marine, intermittently influenced by wave energy, but gradually transitions to a depositional setting where shales are permanently below wave base. This persists in the I5/Touirist Formation, with a suggestion of open marine conditions (Conophyton type columnar stromatolites are observed in two carbonate horizons in S4 (BRGM report), while sediments recorded in S3, S2 and S1 probably continued to be deposited in waters shallow enough for the wave base to intermittently impinge on the sediment-water interface (Gilleaudeau and Kah, 2015). In the absence of detailed reconstructions of basin profile, S3 is assumed to be intermediate in depth between S2 and S4. Sea level reaches a highstand at the base of the I5/Touirist Formation and is relatively stable through most of it, until a rapid loss of accommodation space just below the I6/Aguelt el Mabha Formation. Only the Aguelt el Mabha Formation is represented in this study, with samples from S2 and S3. Deposition in the Aguelt el Mabha Formation was apparently above wave base, implying shallower conditions than in the En Nesoar or Tourist Formations, as evidenced by the abundant occurrence of gutter casts and ripples in the Aguelt el Mabha Formation noted by Beghin et al. (2017a). Although Beghin et al. (2017a) have suggested that part of the I5 Formation in S4 is correlative with the Aguelt el Mabha Formation, shale samples in this study are all from beneath the upper Conophyton bed (BRGM report). Therefore, it is here considered that, while the upper part of the I5 Formation in core S4 may correlate with the Aguelt el Mabha Formation, it is likely that the part of the I5 Formation sampled for this study is correlative with the Touirist Formation in core S2.

2.2.3 Sample preparation

Some samples were received as powders, but most were received as sectors of core slices of varying thickness (ranging from ~ 2 mm to 5 cm) labelled with single core depths to the nearest centimetre. A subsection of each sample was removed using a saw and crushed to a fine powder using a Tema Laboratory Disc Mill.

2.3 Elemental analysis

2.3.1 Total element analysis

Total element concentrations were determined by a HNO_3-$HClO_4$-HF extraction. Approximately 100 mg of sample was weighed into a porcelain crucible and ashed overnight at 550 ˚C. The sample was then washed into a Teflon beaker using 5 mL of concentrated nitric acid, to which 2 mL concentrated hydrofluoric acid and a couple of drops of perchloric acid were added. This was evaporated off overnight, at 70˚C. 2 mL of boric acid was then added and evaporated off, to convert insoluble aluminium hexafluorates to soluble forms of Al. The resulting precipitate was dissolved in 5 mL of 50 % hydrochloric acid and transferred to a volumetric flask, which was made up to volume with deionised water. Total Fe (FeT) was measured by Atomic Absorption Spectrometry (AAS) and total Al, Cr, Cu, Mn, Mo, Ni, P, V and Zn were measured using Inductively Coupled Plasma Optical Emission Spectroscopy (ICP-OES, Varian Vista-MPX). The reproducibility of these extractions is shown in Table 2.1.

Element	Mean ± SD	RSD %
Al	12.10 ± 0.19 wt%	1.6
Cr	153.25 ± 4.44 ppm	2.9
Cu	53.81 ± 3.46 ppm	6.4
Fe	2.64 ± 0.13 wt%	4.8
Mn	48.62 ± 3.26 ppm	6.7
Mo	31.82 ± 4.69 ppm	14.7
Ni	55.34 ± 4.33 ppm	7.8
P	230.52 ± 26.97 ppm	11.7
V	146.27 ± 4.46 ppm	3.0
Zn	85.26 ± 6.42 ppm	7.5

Table 2.1 Mean, standard deviation and RSD for total element analysis of S4 82.08 replicates

2.3.2 Total organic carbon analysis

Approximately 100 mg of sample was weighed into a porous crucible, to which 1 mL of 4 mol/L hydrochloric acid was added, to remove carbonates. Once the acid had drained away, the crucible and sample were dried at 65˚C in an oven for 16 to 24 hours. The samples were then analysed on a Leco CS244 Carbon/Sulphur Analyser, which has a general reproducibility of < 5 %.

2.3.3 Total carbon, sulphur and nitrogen analysis

Approximately 1.5 mg of untreated sample was weighed into tin cups and then analysed for concentrations of carbon, sulphur and nitrogen using an Elementar Pyrocube elemental analyser. Replicates of the standard B2160, certified as N: 0.66 wt%, C: 7.89 wt%, S: 0.84 wt%,

were measured after approximately every 12 samples, giving RSDs of 5.17 %, 1.34 % and 9.16 %, and accuracies of 101.07 %, 99.26 % and 100.97 % respectively.

2.4 Iron speciation

The Fe speciation technique of Poulton and Canfield (2005) was used to assess redox conditions. In this technique, different operationally defined pools of iron are identified. These include Fe associated with carbonate minerals (e.g., siderite; Fe_{carb}), iron (oxyhydr)oxides (e.g., goethite and hematite; Fe_{ox}), magnetite (Fe_{mag}), acid volatile Fe sulphides (Fe_{AVS}) and pyrite (Fe_{py}). The non-sulphidized pools are quantified in a sequential extraction, while pyrite (Fe_{py}) and acid volatile sulphide Fe (Fe_{AVS}) are determined from a separate extraction (see below). Redox conditions are assessed by considering the ratio of highly reactive iron (FeHR) to total iron (FeT, as determined in the total element analysis), FeHR/FeT, where FeHR is the sum of Fe_{carb}, Fe_{ox}, Fe_{mag} and Fe_{py}, and the ratio of sulphidized iron (FeP, the sum of Fe_{py} and Fe_{AVS}), to highly reactive iron, FeP/FeHR (see Chapter 1 for full details). Fe_{AVS} is not included in the calculation of FeHR, since Fe_{AVS} is quantitatively removed during the sequential Fe extraction stages (and hence would otherwise be included twice as FeHR; Poulton et al., 2010). The iron extraction techniques used are described below and summarised in Table 2.2. A further boiling HCl extraction (Berner, 1970, Raiswell et al., 1988) was applied to samples from S1 to establish Fe_{HCl} in order to allow the use of the DOP indicator (see section 5.3.1).

2.4.1 Sequential iron extractions

Approximately 75 mg of sample was weighed into a centrifuge tube. Fe associated with carbonates (Fe_{carb}), e.g., siderite, was extracted with 10 mL of 1 M sodium acetate solution, adjusted to a pH of 4.5 with acetic acid, at 50˚C, for 48 hours. Samples were centrifuged for 3 minutes at 4000 rpm and the supernatant decanted, diluted and kept for analysis.

Iron (oxyhydr)oxides (Fe_{ox}), e.g., goethite and hematite, were extracted from the remaining sample with 10 mL of sodium dithionite solution (50 mg/L, buffered to pH 4.8 with 0.35 M acetic acid and 0.2 M sodium citrate) for 2 hours at room temperature. Samples were

centrifuged for 3 minutes at 4000 rpm and the supernatant decanted, diluted and kept for analysis.

Magnetite (Fe_{mag}) was extracted with a 0.2 M ammonium oxalate/0.17 M oxalic acid solution for 6 hours at room temperature. Samples were centrifuged for 3 minutes at 4000 rpm and the supernatant decanted, diluted and kept for analysis.

Fe concentrations for each fraction were measured on an AAS. Replicate extractions gave an RSD of 7.8 % for Fe_{carb}, 2.7% for Fe_{ox} and 4.5 % for Fe_{mag}, as shown in Table 2.2.

2.4.2 Pyrite extraction

Acid volatile sulphide Fe (Fe_{AVS}) and pyrite (Fe_{py}) were determined gravimetrically via the acid and chromous chloride distillation techniques of Canfield et al. (1986). Between 0.5-1.5g of sample was weighed out into a glass reaction vessel with three ground glass fittings. This was placed over a heating element and attached to a condenser, which fed into a trap consisting of a test tube with 0.5 mL 1 M $AgNO_3$, filled to approximately two thirds with deionised water. Nitrogen was bubbled through the flask through the second opening, and the third was stoppered except for when the extractants were added. To extract any AVS, 8 mL of 50% HCl was added using a syringe, and the heat turned on so that the acid was boiling. Any hydrogen sulphide gas liberated from the decomposition of AVS rises through the condenser to the test tube, where it reacts with the silver nitrate to produce a black precipitate of silver sulphide. If, after 10-15 minutes of sample boiling, a precipitate had started to form in the trap, the reaction was allowed to continue for an hour (or longer in a few cases, where, after an hour, precipitate was still forming in the trap) to fully extract AVS from the sample, with further $AgNO_3$ added if necessary. The trap was then replaced before extraction of pyrite started. If no such precipitate had formed after 10-15 minutes then it was assumed that no measurable AVS was present.

Following the AVS extraction, 16 mL of 1 M chromous chloride was added to the reaction vessel and the sample kept at boiling point for an hour (or, in some cases, longer, if precipitate was still forming after an hour), with more $AgNO_3$ being added to the trap if necessary.

The precipitate was filtered on to a cellulose nitrate membrane filter and the precipitate weighed. The concentration of S in AVS and in pyrite in the sample was calculated from the weight of the silver sulphide precipitate, and from this, the concentration of Fe was then calculated assuming the stoichiometries of FeS and FeS_2, respectively. The precipitate was kept for sulphur isotope analysis. Replicate extractions gave an RSD of 9.0 % for Fe_{py}, as shown in Table 2.2. Fe_{AVS} was generally below detection in most samples except those from S1.

2.4.3 Boiling HCl extraction

Approximately 50 mg of sample was weighed into a test tube. 5mL of concentrated HCl was added and, over a Bunsen burner, the sample was brought to boiling point over 1 minute and boiled vigorously for a further minute. The reaction was quenched with deionised water and the solution and remaining sediment transferred to a volumetric flask. Fe concentrations were measured on an AAS and replicate extractions gave an RSD of 3.0 %.

Extraction pool	Extraction method	Replicated Sample	Mean ± SD (wt%)	RSD %
Fe_{carb}	10 mL 1 M sodium acetate at pH 4.5 for 48 hours at 50˚C.	S4 122.88	0.67 ± 0.05	7.8
Fe_{ox}	10 mL sodium dithionite solution at pH 4.8 for 2 hours at room temperature.	S4 122.88	0.13 ± 0.00	2.7
Fe_{mag}	0.2 M ammonium oxalate/0.17 M oxalic acid solution for 6 hours at room temperature.	S4 122.88	0.11 ± 0.00	4.5
Fe_{AVS}	8 mL 50% HCl at boiling point for 15 minutes – 1 hour.	S2 143.86	0.00 ± 0.00	N/A
Fe_{py}	16 mL 1 M chromous chloride for 1 hour at boiling point.	S2 143.86	0.84 ± 0.07	9.0
Fe_{HCl}	5mL conc. HCl boiled for 2 minutes.	S1 71.65	3.00 ± 0.06	2.0
FeT	Ashed overnight at 550 ˚C. 5 mL conc. HNO_3, 2 mL conc. HF and a couple of drops of $HClO_4$ evaporated off overnight at 70˚C. 2 mL boric acid evaporated off overnight.	S4 82.08	2.64 ± 0.13	4.8

Table 2.2 Summary of iron extraction methods and mean, standard deviation and RSD for replicate samples

2.5 Phosphorus speciation

Phosphorus speciation was determined via the technique of Ruttenberg (1992), adapted for ancient sediments (Marz et al., 2008; 2014; Creveling et al., 2014). This procedure separates P into four operationally defined pools: 1) Fe-bound P (P_{Fe}); 2) authigenic/biogenic apatite plus $CaCO_3$-bound P (P_{auth}); 3) detrital apatite plus other inorganic P (P_{det}); and 4) organic P (P_{org}).

Comparisons between the sum of these pools and total P, as determined by the total element analysis, suggested that not all P had been extracted by the sequential phosphorus speciation procedure (Figure 2.3), and so an additional step was added to extract any residual phosphorus (P_{res}). By including P_{res}, P recovery increased from ~ 80 % to ~ 90 %.

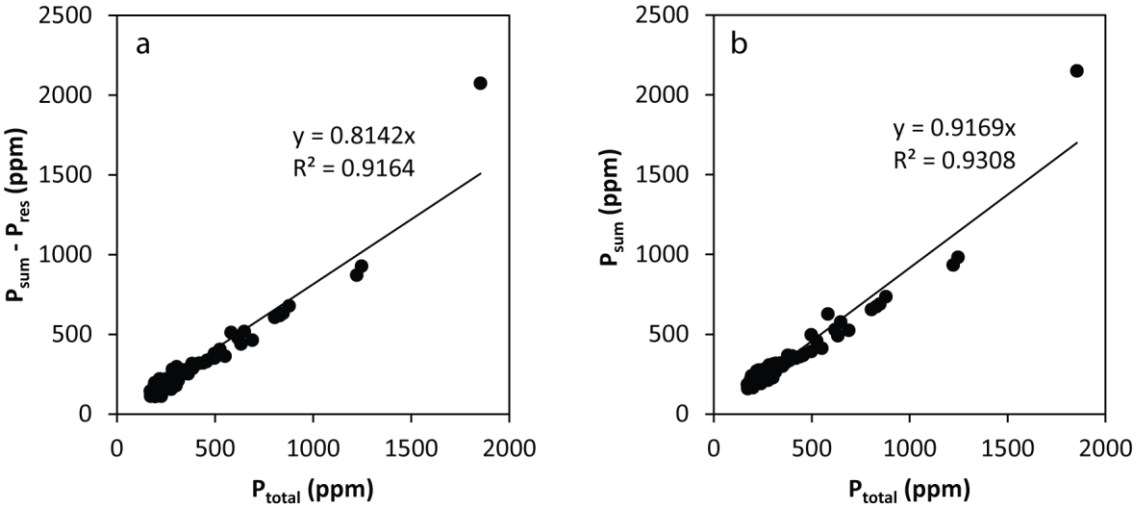

Figure 2.3 Sum of sequentially extracted P verses total P extraction, without residual P (a) and with residual P (b)

The phosphorus extraction techniques used are described below and summarised in Table 2.3, along with RSD values for each pool.

Around 100 samples were selected to represent a range of well-defined redox conditions (oxic, ferruginous and euxinic) across cores S2, S3 and S4, and for each sample 150-200 mg was weighed into a centrifuge tube. Iron-bound phosphorous (P_{Fe}) was extracted with 10 mL of citrate-dithionite-bicarbonate (CDB) solution (0.3 M sodium citrate/ 1 M sodium bicarbonate/ 0.14 M sodium dithionite, pH 7.6) for 8 hours at room temperature. The sample was then centrifuged, and a sub-sample of the supernatant was taken for analysis before the rest was discarded. The sample was washed twice for 2 hours with 5 mL of 1 M magnesium chloride solution to extract any phosphorus that had readsorbed to sediment in the previous step. A sub-sample of the supernatant from each wash was kept for analysis.

Authigenic apatite, plus carbonate associated phosphorus and biogenic apatite, (P_{auth}) was extracted with 10 mL of 1 M sodium acetate solution (buffered to pH 4 with acetic acid) for 6 hours at room temperature. The sample was then centrifuged, and a sub-sample of the supernatant was taken for analysis before the rest was discarded. The sample was washed twice for 2 hours with 5 mL of 1 M magnesium chloride solution.

Detrital apatite (plus any other inorganic P) (P_{det}) was extracted with 10 mL of ~1 M HCl for 16 hours at room temperature. The sample was then centrifuged, and a sub-sample of the supernatant was taken for analysis before the rest was discarded. The sample was washed twice for 2 hours with 5 mL of 1 M magnesium chloride solution.

The sample was then transferred to a porcelain crucible and ashed at 550˚C for a minimum of 2 hours. The sample was transferred back to its centrifuge tube and organic phosphorus (P_{org}) was extracted with 10 mL of 1 M HCl for 16 hours at room temperature. The sample was then centrifuged, and a sub-sample of the supernatant was taken for analysis before the rest was discarded.

Finally, any remaining phosphorus (here termed residual phosphorus, P_{res}) was extracted using the three acid (HNO_3-$HClO_4$-HF) total digestion method. The sample was transferred from the centrifuge tube into a Teflon beaker using 5 mL of concentrated nitric acid, to which 2 mL concentrated hydrofluoric acid and a couple of drops of perchloric acid were added. This was evaporated off overnight, at 70˚C. 2 mL of boric acid was then added and evaporated off, to convert insoluble aluminium hexafluorates to soluble forms of Al. The resulting precipitate was dissolved in 5 mL of 50 % hydrochloric acid and transferred to a volumetric flask, which was made up to volume with deionised water.

With the exception of P_{Fe} (which was analysed by ICP-OES, Varian Vista-MPX), the sequential P extracts, including washes, were analysed immediately following the extraction, with a UV/VIS Spectrophotometer (Thermo Electron Corporation Genesys 6). Phosphorus concentrations were determined colourimetrically, using the molybdate blue method. Replicate extractions gave an RSD of 20.8 % for P_{Fe}, 13.0 % for P_{auth}, 5.8 % for P_{det}, 3.5 % for P_{org} and

4.0 % for P_{res}. When various pools are added together, $P_{reactive}$ has an RSD of 2.4 % and P_{sum} has an RSD of 1.7 %.

Extraction pool	Extraction method	Mean ± SD (ppm)	RSD %
P_{Fe}	10 mL 0.3 M sodium citrate/ 1 M sodium bicarbonate/ 0.14 M sodium dithionite at pH 7.6 for 8 hours at room temperature	0.15 ± 0.03	20.8
P_{auth}	10 mL 1 M sodium acetate solution buffered to pH 4 with acetic acid for 6 hours at room temperature	25.85 ± 3.37	13.0
P_{det}	10 mL ~1 M HCl for 16 hours at room temperature	3.39 ± 0.20	5.8
P_{org}	Ashed at 550˚C for a minimum of 2 hours. 10 mL 1 M HCl for 16 hours	133.52 ± 4.71	3.5
P_{res}	5 mL conc. HNO_3, 2 mL conc. HF and a couple of drops of $HClO_4$ evaporated off overnight at 70˚C. 2 mL boric acid evaporated off overnight.	55.01 ± 2.19	4.0
$P_{reactive}$	Sum of P_{Fe}, P_{aut} and P_{org} (biologically available)	159.52 ± 3.481	2.4
P_{sum}	Total of sequentially extracted pools	217.92 ± 3.78	1.7

Table 2.3 Summary of P extraction methods and mean, standard deviation and RSD for replicates of S4 130.02

2.6 Isotope analyses

2.6.1 Sulphide

Samples of silver sulphide, from the quantification of pyrite Fe by chromous chloride distillation, were weighed into tin cups containing a vanadium pentoxide catalyst and were sent to Iso-Analytical for analysis. These were combusted and the isotope composition of the resultant SO_2 was measured by Elemental Analysis – Isotope Ratio Mass Spectrometry (EA-IRMS) in order to calculate $\delta^{34}S_{V\text{-}CDT}$. Replicates of two barium sulphate standards were run. IA-R061 (an in-house standard), with an excepted value of 20.33 ‰, had an accuracy of 99.71 % and an RSD of 0.9 %, and IAEA-SO-5 9 (an inter-laboratory standard), with an accepted value of 0.50 ‰, had an accuracy of 77.12 % and an RSD of 50.9 %.

2.6.2 Organic carbon

Samples were treated twice with 3 mL of 25% HCl to remove carbonates. The remaining sample was washed with deionised water and dried. Samples were then weighed into tin cups for isotopic analysis on an Isoprime continuous flow mass spectrometer coupled to an Elementar Pyrocube elemental analyser. Repeat extractions of S4 80.45 gave a mean $\delta^{13}C_{VPDB}$ of -29.78 ± 0.21 ‰, giving an RSD of 0.7 %.

Chapter 3

Ocean redox chemistry recorded in Late Mesoproterozoic sediments from the Taoudeni Basin of Mauritania

3.1 Introduction

This chapter will detail Fe-S-C and trace metal systematics for cores S2, S3 and S4. S1 will be dealt with in a separate chapter as some of the geochemical data suggest that S1 has undergone significant contact metamorphism probably associated with the ~30 m dolerite sill that interrupts the core. Although S4 also contains a dolerite sill, it is only ~2 m thick and the surrounding sedimentary deposits do not show the same geochemical evidence for alteration as seen in S1. Data for the formations sampled from S2, S3 and S4 is summarised in tables 3.1 and 3.2, and core depth profiles of the data are shown in figures 3.1 to 3.6. Full data tables are to be found in Appendix A.

3.2 Results

3.2.1 Carbon

3.2.1.1 TOC

TOC is highly variable across the 3 cores, with the highest concentrations (up to 34.3 wt%) being found in S2 in the Touirist Formation (Table 3.1; Figure 3.1). Samples from the En Nesoar Formation in S2 also show high TOC values, with a maximum of 16.7 wt%. TOC does not fall below 0.1 wt% in the Touirist and En Nesoar formations in S2, and is generally greater than 1 wt%, with mean values of 10.27 wt% and 6.87 wt% respectively, as shown in Table 3.1. In contrast TOC is very low in the Aguelt El Mabha Formation in S2, with the highest value being 0.05 wt%, although it should be noted that only 4 samples were analysed from this formation (Figure 3.1). Similarly, in S3 (see Table 3.1; Figure 3.2) the lowest TOC

concentrations are of this order, and TOC does not go above 1 wt%. The maximum for the Touirist Formation in S3 (0.80 wt%) is greater than for the Aguelt El Mabha Formation (0.28 wt%) but the average TOC for both formations in S3 is similar, and low.

In S4, TOC is more abundant than in S3, but concentrations are still fairly low, ranging between 0.10 and 2.35 wt% across the three formations sampled in this core (Table 3.1; Figure 3.3). TOC concentrations are similar across all three formations, with I4 (equivalent to the En Nesoar Formation) having the highest average, but I5 (Touirist) having the highest maximum and the greatest range in TOC.

3.2.1.2 Inorganic C

Inorganic carbon concentrations are generally fairly low as sampling was focused on shale horizons. The samples with the highest concentrations of inorganic carbon are found in the Aguelt el Mabha Formation in S2 and the Touirist Formation in S3, with averages of 5.08 ± 2.06 wt% and 2.24 ± 2.17 wt% respectively (Table 3.1; Figure 3.1 and Figure 3.2). The most carbonate rich sample is in S2, at 8.03 wt%. While inorganic carbon contents in the Touirist Formation in S2 go up to 7.41 wt%, the majority of samples analysed had < 1 wt%, giving an average of 1.29 ± 1.88 wt%. Almost all samples from the En Nesoar Formation in S2 had < 1 wt% inorganic C, giving an average of 0.63 ± 1.03 wt%. All samples analysed from the Aguelt El Mabha Formation in S3 were fairly low in inorganic C, with an average of 0.59 ± 0.31 wt%, compared with an average of 2.24 ± 2.17 wt% and a maximum of 5.56 wt% for the Touirist Formation in S3. S4 is the core lowest overall in inorganic C (Figure 3.3), with only one sample from the I3 Formation and just a few samples from the I5 Formation having > 1 wt%, giving averages for the I3, I4 and I5 formations of 0.44 ± 0.32 wt%, 0.22 ± 0.08 wt% and 0.71 ± 0.84 wt% respectively.

Core	Formation	TOC wt%	Inorganic C wt%
S2	Aguelt el Mabha (I6)	0.04 ± 0.01	5.08 ± 2.06
	Touirist (I5)	10.27 ± 8.81	1.29 ± 1.88
	En Nesoar (I4)	6.87 ± 4.84	0.63 ± 1.03
S3	Aguelt El Mabha (I6)	0.10 ± 0.08	0.59 ± 0.31
	Touirist (I5)	0.17 ± 0.21	2.24 ± 2.17
S4	I5 (Touirist)	0.56 ± 0.41	0.71 ± 0.84
	I4 (En Nesoar)	1.02 ± 0.26	0.22 ± 0.08
	I3 (Khatt)	0.75 ± 0.16	0.44 ± 0.32

Table 3.1 Mean and SD for TOC and Inorganic C for each core by formation

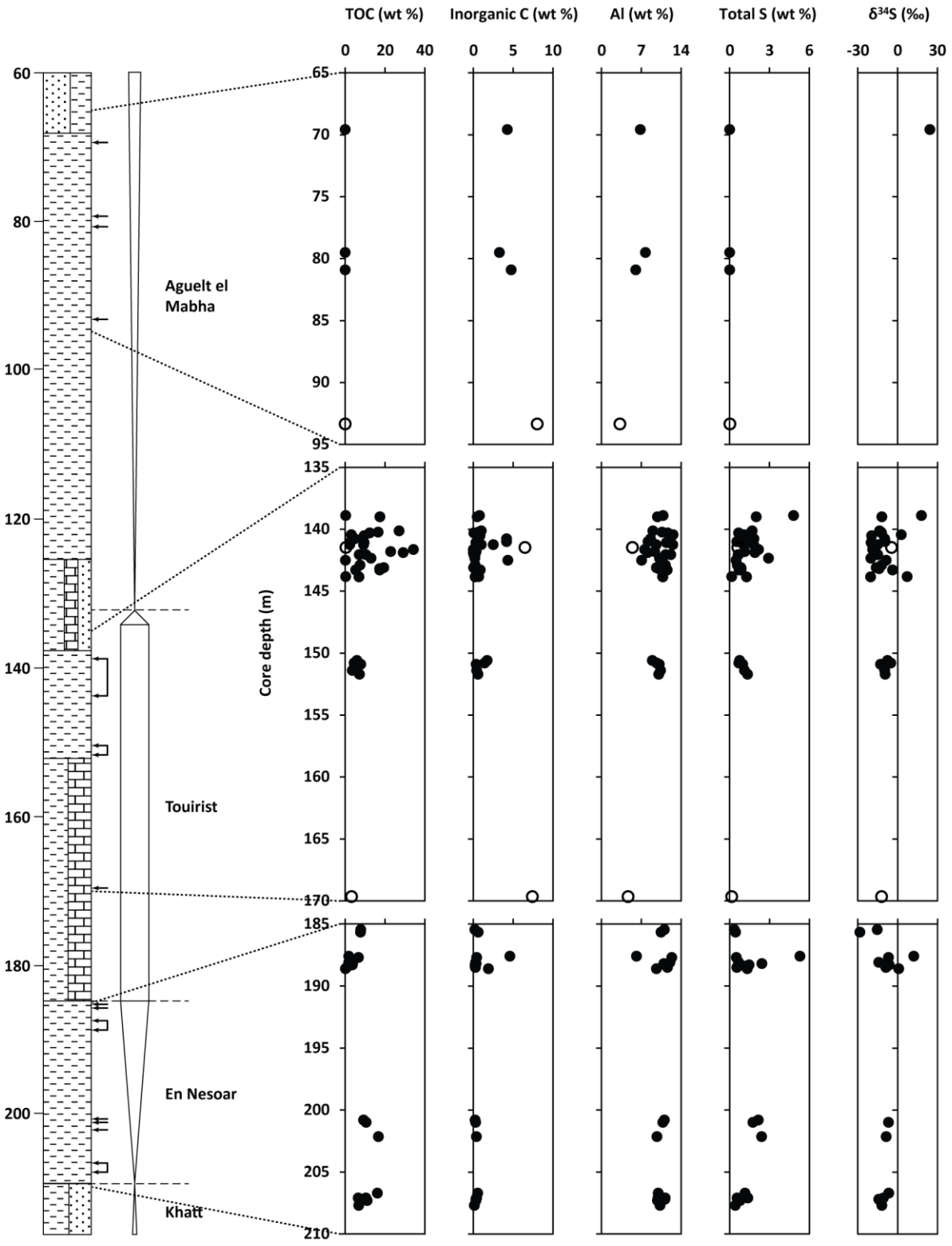

Figure 3.1 Depth profiles for C, S and Al in S2 Open circles indicate carbonate-rich samples.

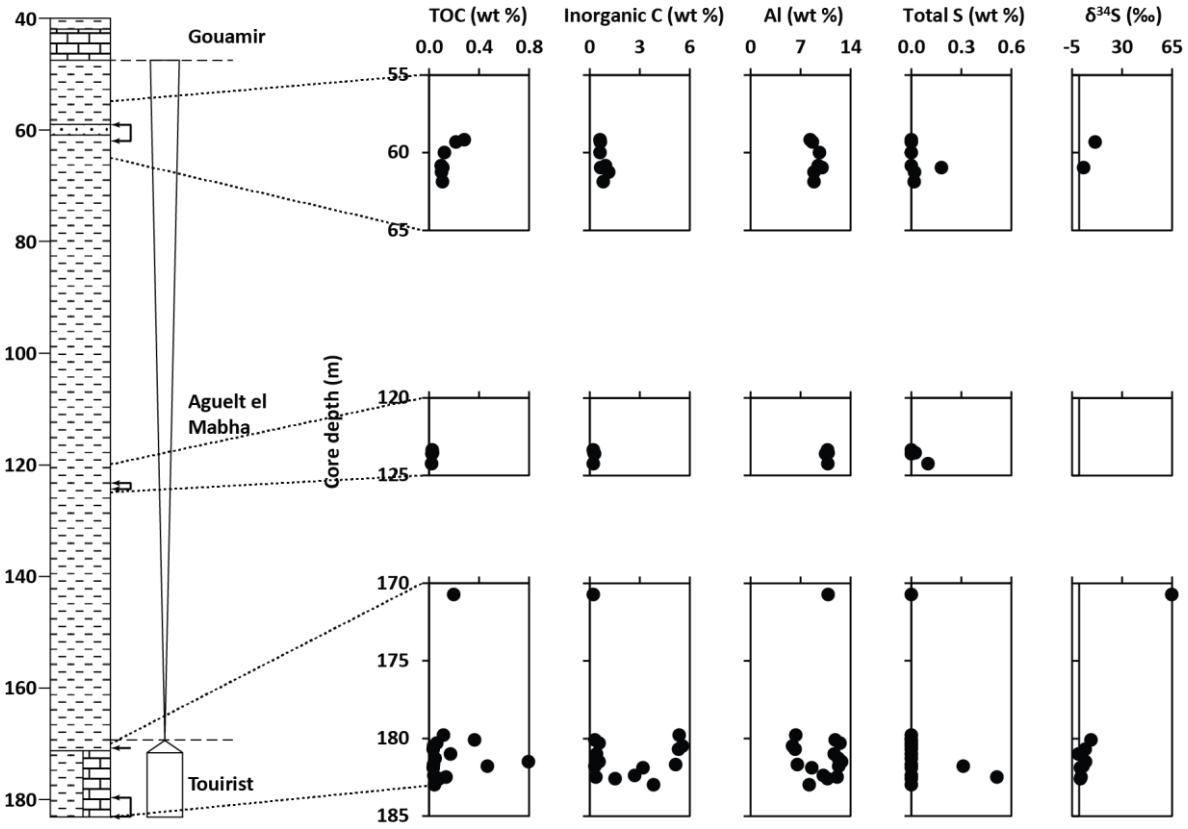

Figure 3.2 Depth profiles for C, S and Al in S3

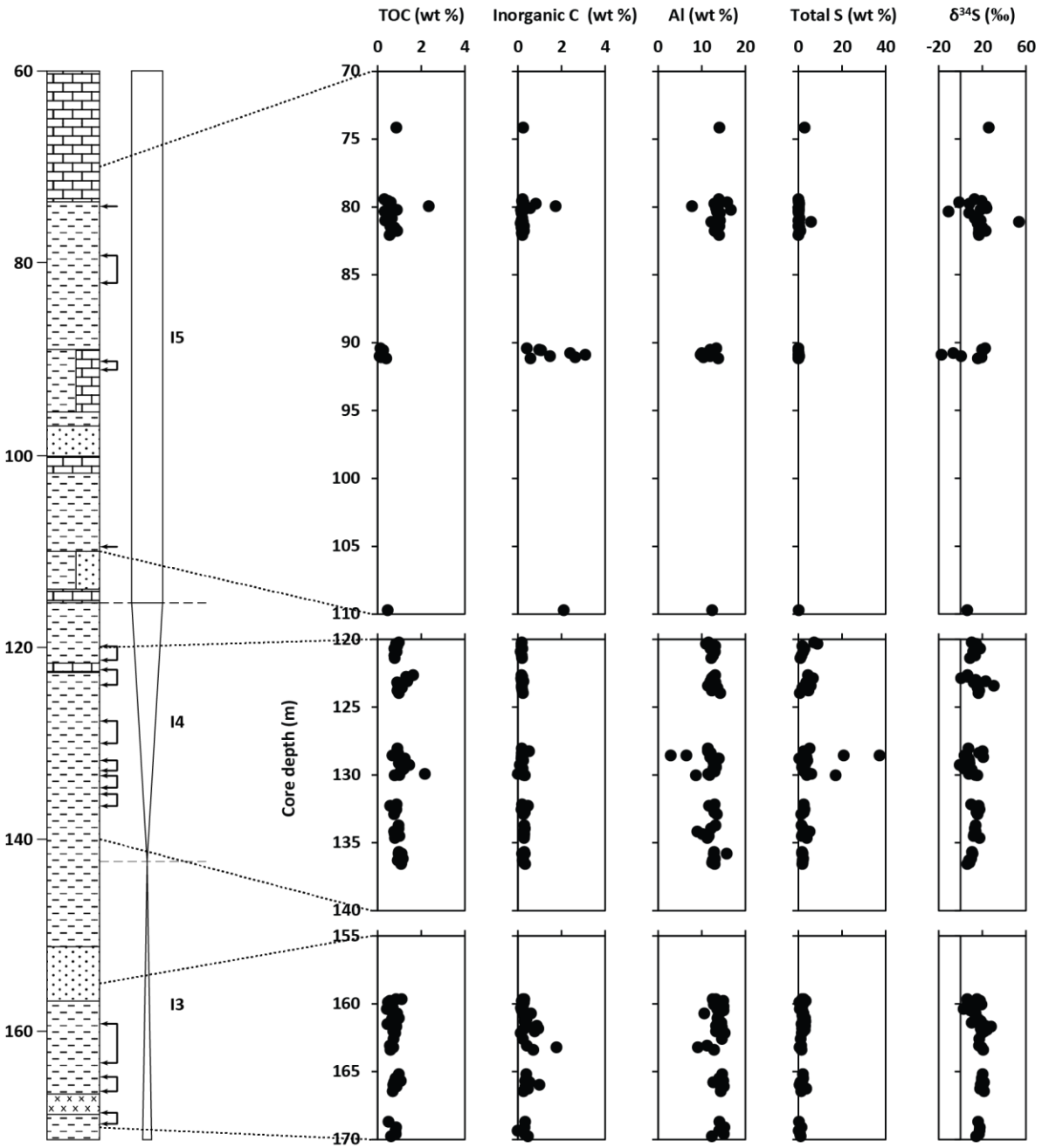

Figure 3.3 Depth profiles for C, S and Al in S4

3.2.2 Iron speciation

3.2.2.1 Fe_{carb}

On average, the highest concentrations of Fe_{carb} are seen in S4, as shown in Table 3.2, with an average across all formations sampled of 0.54 ± 0.52 wt %. Fe_{carb} is also more variable in S4, ranging from 0.07 – 3.66 wt%. Least variation is seen in S3, with averages of 0.25 ± 0.05 and 0.40 ± 0.06 wt% for the Touirist and Aguelt El Mabha formations. Concentrations of Fe_{carb} are more varied in S2, but considerably lower in range than that seen in S4, with averages of 0.28 ± 0.12, 0.43 ± 0.16 and 0.17 ± 0.23 wt% for the En Nesoar, Touirist and Aguelt El Mabha formations respectively, and a maximum of 0.88 wt%.

3.2.2.2 Fe_{ox}

In contrast to Fe_{carb}, the lowest concentrations of Fe_{ox} are found in S4, with an average of 0.06 ± 0.03 wt% across the three formations sampled. Fe_{ox} is similarly low in S2 in the En Nesoar and Touirist formations (0.07 ± 0.03 and 0.07 ± 0.02 wt% respectively), but 2 samples from the Aguelt El Mabha Formation have more than 1 wt% Fe_{ox}. Similar concentrations are seen in the middle of the Aguelt El Mabha Formation in S3, but towards the top of this formation, Fe_{ox} concentrations are only slightly higher than generally seen in S2 and S4, giving an average of 0.37 ± 0.39 wt% for the Aguelt El Mabha Formation in S3. Samples from the Touirist Formation mostly have concentrations of Fe_{ox} below 0.1 wt%, with an average of 0.15 ± 0.18 wt%.

3.2.2.3 Fe_{mag}

On average, the lowest concentrations of Fe_{mag} are seen in S2, with an average of 0.11 ± 0.07 wt%. The En Nesoar Formation in S2 has the lowest concentration of Fe_{mag}, with an average of 0.06 ± 0.03 wt% and a maximum of 0.12 wt%. The Touirist and Aguelt el Mabha formations in S2 are more comparable with the Touirist Formation in S3 and the I3 and I4 formations in S4 in terms of average concentration, as shown in Table 1.5, but formations in S4 have greater ranges, with maximums of 1.13 and 0.64 wt% in I3 and I4 respectively (in contrast to 0.36 wt% in the Touirist Formation of S3 and 0.21 and 0.26 wt% in the Touirist and Aguelt El Mabha

formations of S2). The Aguelt El Mabha Formation in S3 has the greatest average concentration of Fe_{mag} (0.45 ± 0.11 wt%), while the I5 Formation in S4 has the greatest variability, with a maximum of 3.70 wt%, and an average concentration of 0.39 ± 0.63 wt%.

3.2.2.4 Fe_{py}

Concentrations of Fe_{py} are highest in S4, with an overall average of 2.20 ± 3.53 wt% and maximums of 2.87 wt%, 30.83 wt% and 5.56 wt% for the I3, I4 and I5 formations respectively. In contrast, the average for S3 is 0.05 ± 0.12, while the average across S2 is 0.74 ± 0.68 wt%. All cores contain samples with very little or no Fe_{py}, but while very few samples from S4 have < 0.1 wt% Fe_{py}, almost all samples from the Touirist and Aguelt el Mabha formations in S3 contain < 0.1 wt%, in many cases only trace amounts, insufficient for obtaining $\delta^{34}S$ measurements. Similarly, in the samples analysed from the Aguelt El Mabha Formation in S2, the highest concentration of Fe_{py} was 0.004 wt%. In the Tourist and En Nesoar formations however, only one sample had a concentration of < 0.1 wt%. The maximum for the En Nesoar Formation in S2 was 1.96 wt%, with an average of 0.72 ± 0.54 wt%, and the maximum for the Touirist Formation was 3.93 wt%, with an average of 0.84 ± 0.74 wt%.

3.2.2.5 FeT

On average, S4 has the highest concentrations of FeT, with a mean of 4.92 ± 4.16 wt%, while S3 and S2 have means of 4.34 ± 1.05 wt% and 3.12 ± 0.94 wt% respectively (figures 1.8 - 1.10). S4 is also the most variable core, with an overall range of 1.00 - 36.12 wt% FeT. The highest concentrations are found in the I4 Formation, with a mean of 6.77 ± 5.20 wt%, while the I5 Formation has an average of 4.07 ± 3.15 wt% and a maximum of 19.55 wt%. The I3 Formation has an average of 3.10 ± 1.37 wt%, similar to all 3 formations sampled from S2. FeT is least variable in S3, with means of 3.75 ± 0.69 wt% and 5.21 ± 0.87 wt% for the Touirist and Aguelt El Mabha formations respectively.

Core	Formation	Fe_{carb} wt %	F_{ox} wt %	Fe_{mag} wt %	Fe_{py} wt %	FeT wt %	Al wt %
S2	Aguelt El Mabha (I6)	0.17 ± 0.23	0.67 ± 0.72	0.20 ± 0.12	0.00 ± 0.00	3.09 ± 1.45	5.98 ± 1.94
	Touirist (I5)	0.43 ± 0.16	0.07 ± 0.02	0.13 ± 0.05	0.84 ± 0.74	3.10 ± 0.81	9.91 ± 1.86
	En Nesoar (I4)	0.28 ± 0.12	0.07 ± 0.03	0.06 ± 0.03	0.72 ± 0.54	3.15 ± 1.08	10.59 ± 1.32
S3	Aguelt El Mabha (I6)	0.40 ± 0.06	0.37 ± 0.39	0.45 ± 0.11	0.01 ± 0.01	5.21 ± 0.87	9.74 ± 0.93
	Touirist (I5)	0.25 ± 0.05	0.15 ± 0.18	0.17 ± 0.08	0.08 ± 0.15	3.75 ± 0.69	9.96 ± 2.57
S4	I5 (Touirist)	0.46 ± 0.66	0.06 ± 0.03	0.39 ± 0.63	0.44 ± 1.04	4.07 ± 3.15	13.09 ± 1.76
	I4 (En Nesoar)	0.62 ± 0.47	0.07 ± 0.03	0.21 ± 0.10	3.71 ± 4.87	6.77 ± 5.20	12.09 ± 1.89
	I3 (Khatt)	0.49 ± 0.47	0.04 ± 0.02	0.15 ± 0.26	1.54 ± 0.77	3.10 ± 1.37	13.77 ± 1.30

Table 3.2 Mean and SD for Fe pools and Al for each core by formation

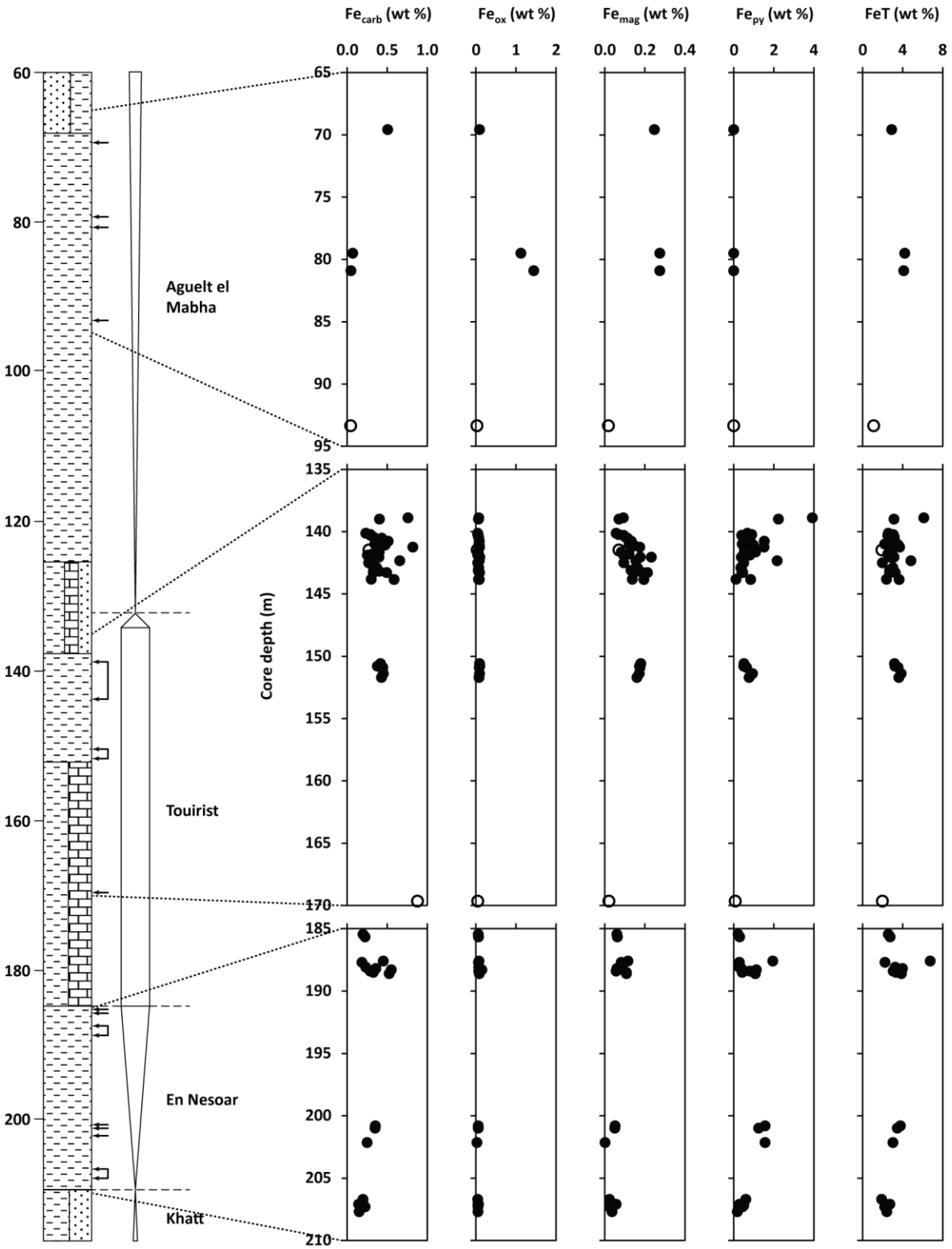

Figure 3.4 Depth profiles for Fe pools in S2 Open circles indicate carbonate-rich samples.

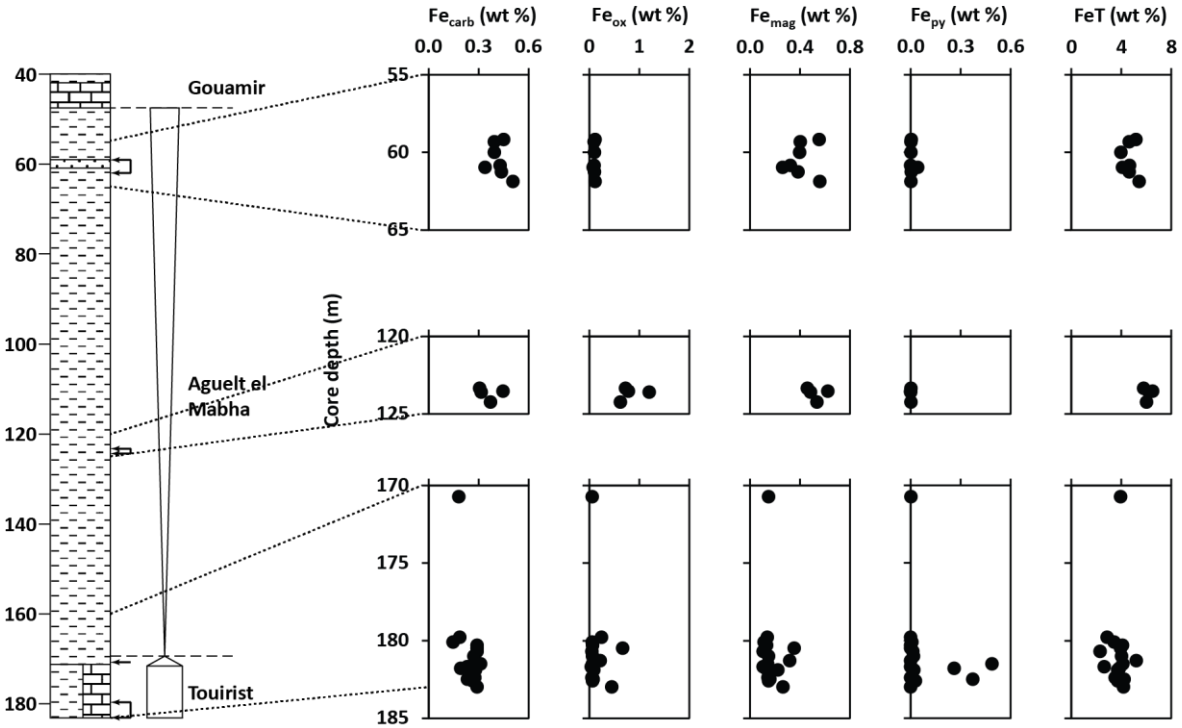

Figure 3.5 Depth profiles for Fe pools in S3

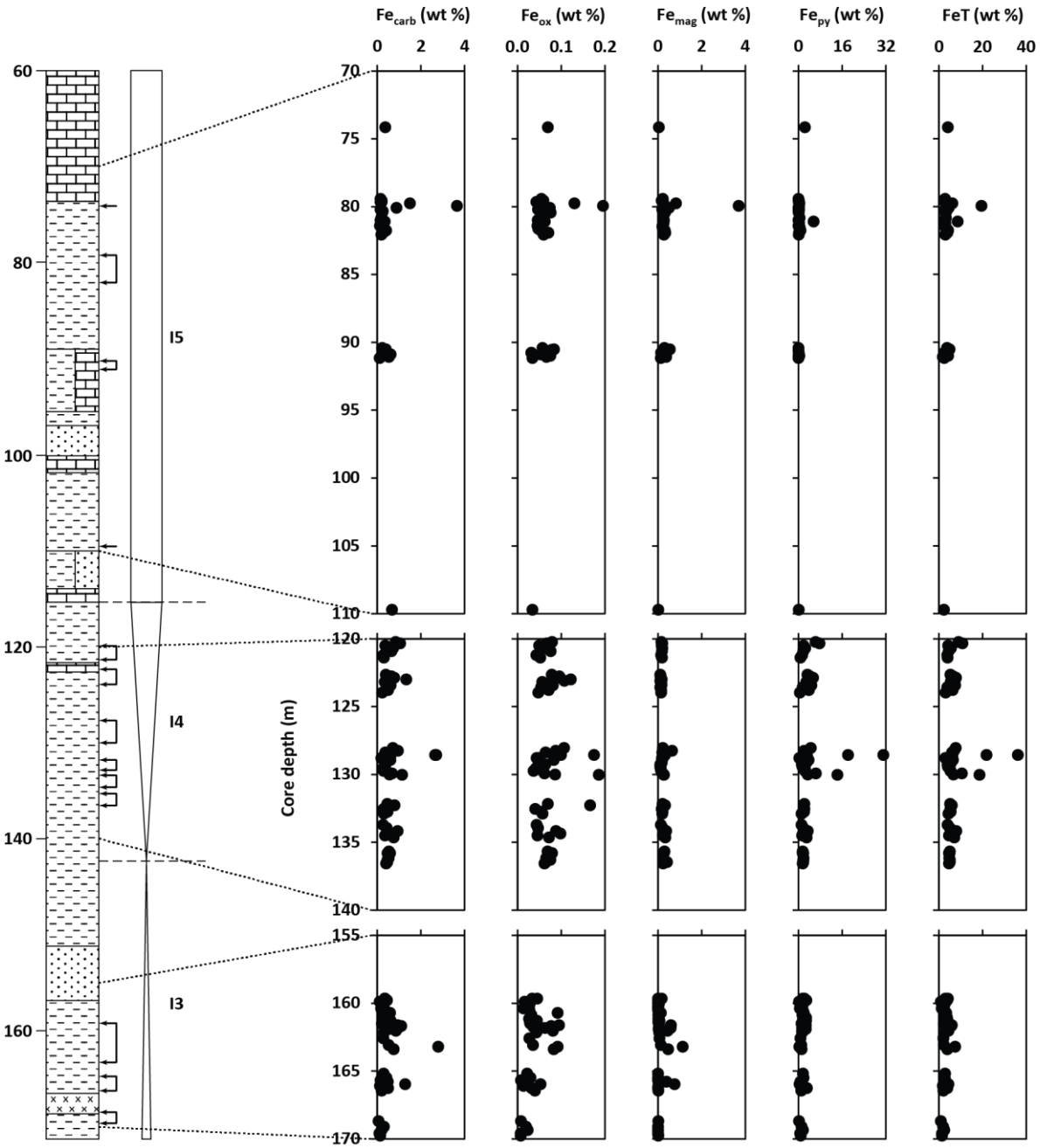

Figure 3.6 Depth profiles for Fe pools in S4

3.2.3 Sulphur

3.2.3.1 Sulphide Sulphur and Total Sulphur

On average, measurements for sulphide sulphur and for total sulphur match closely - they are within 1 standard deviation for the sulphide sulphur repeat (0.07 wt%) for both formations in S3, the Aguelt El Mabha Formation in S2 and the I3 and I5 formations in S4. There is also a fairly good match (within 2 SD) for the I4 Formation in S4. However, there is some discrepancy between sulphide sulphur and total sulphur measurements for the En Nesoar and Touirist formations in S2, suggesting that a significant proportion of the sulphur in several samples from these formations in this core is not bound in pyrite, or any other Fe sulphide (only unmeasurable traces of AVS were found in a very small number of samples from these cores), and may instead be present as organic S, given the high TOC contents of some of these units (Figure 3.1).

3.2.3.2 Sulphur isotopes

In S2 $\delta^{34}S$ is largely negative, with an average of -9.19 ± 8.21‰ for the En Nesoar Formation and -10.64 ± 8.39‰ for the Touirist Formation, with a range up to 12.31 and 17.92‰ respectively (Figure 3.1). The one measurement from the Aguelt El Mabha Formation is slightly higher than this, at 24.44‰. In contrast to S2, measurements of $\delta^{34}S$ in S3 and S4 are largely positive (figures 3.2 – 3.3). In S3 the averages for the Touirist and Aguelt El Mabha formations are 9.75 ± 20.89‰ and 7.26 ± 5.61‰. In S4, the averages for the I3, I4 and I5 formations are 17.19 ± 5.19‰, 11.82 ± 5.78‰ and 14.55 ± 13.18‰ respectively. The maximums in both S3 and S4 are much higher than for S2, at 65.00‰ in S3 and 53.57 ‰ in S4, although in both cases these are single measurements more than 25‰ higher than the next highest measurements. Minimums for S2, S3 and S4 are -28.54‰, -0.36‰ and -17.42‰ respectively.

Core	Formation	Sulphide wt%	Total S wt%	$\delta^{34}S$ (‰)
S2	Aguelt El Mabha (I6)	0.00 ± 0.00	0.01 ± 0.01	24.44 (1 sample)
	Touirist (I5)	0.97 ± 0.85	1.22 ± 0.89	-10.64 ± 8.39
	En Nesoar (I4)	0.83 ± 0.62	1.35 ± 1.17	-9.19 ± 8.21
S3	Aguelt El Mabha (I6)	0.01 ± 0.01	0.03 ± 0.06	7.26 ± 5.61
	Touirist (I5)	0.09 ± 0.18	0.10 ± 0.24	9.75 ± 20.89
S4	I5 (Touirist)	0.50 ± 1.20	0.49 ± 1.13	14.55 ± 13.18
	I4 (En Nesoar)	4.26 ± 5.59	4.35 ± 5.75	11.82 ± 5.78
	I3 (Khatt)	1.77 ± 0.89	1.80 ± 0.91	17.19 ± 5.19

Table 3.3 S concentrations and isotopic compositions (mean ± 1 SD) for each core by formation

3.2.4 Aluminium

On average, the largest concentrations of Al are seen in S4, with a mean across the 3 formations sampled of 12.88 ± 1.83 wt% (figures 3.1 – 3.3). The greatest range in Al concentrations is also seen in S4, with a minimum of 2.87 wt% and a maximum of 16.68 wt%. The Aguelt El Mabha Formation in S2 is the lowest in Al, with a mean of 5.98 ± 1.94 wt%, while the Touirist and En Nesoar formations in S2 have average Al concentrations of 9.91 ± 1.86 and 10.59 ± 1.32 wt%. Similar to the latter two formations in S2, the Tourist Formation in S3 has a mean of 9.96 ± 2.57 wt% and the Aguelt El Mabha Formation a mean of 9.74 ± 0.93 wt%. Generally, Al content is enriched relative to average shale (Turekian and Wedepohl, 1961).

Core	Formation	Al (wt%)	Mn (ppm)	Mo (ppm)	V (ppm)
S2	Aguelt El Mabha (I6)	5.98 ± 1.94	733 ± 162	0.95 ± 1.69	76 ± 14
	Touirist (I5)	9.91 ± 1.86	411 ± 543	7.50 ± 5.26	155 ± 101
	En Nesoar (I4)	10.59 ± 1.32	221 ± 171	6.10 ± 3.27	207 ± 112
S3	Aguelt El Mabha (I6)	9.74 ± 0.93	752 ± 460	2.16 ± 1.76	101 ± 15
	Touirist (I5)	9.96 ± 2.57	1225 ± 1046	6.65 ± 3.05	93 ± 28
S4	I5 (Touirist)	13.09 ± 1.76	106 ± 112	4.48 ± 2.17	124 ± 19
	I4 (En Nesoar)	12.09 ± 1.89	103 ± 75	4.79 ± 2.99	132 ± 25
	I3 (Khatt)	13.77 ± 1.30	123 ± 226	5.08 ± 1.54	126 ± 19

Table 3.4 Al and trace metal concentrations (mean ± 1 SD) for each core by formation

3.2.5 Trace metals

3.2.5.1 Manganese

Manganese concentrations vary widely, with a minimum of 20 ppm the I3 Formation of S4 and a maximum of 4044 ppm in the Touirist (I5) Formation of S3. Samples from S2 are generally depleted in Mn relative to average shale (Turekian and Wedepohl, 1961), especially in the En Nesoar (I4) Formation, where the average concentration is 221 ± 171 ppm (Table 3.4). Greater variation in the Touirist Formation (I5), where there are a few enriched samples (Figure 3.7), gives an average of 411 ± 543 ppm, while the four samples from the Aguelt el Mabha Formation (I6) are close to average shale, with a mean of 733 ± 162 ppm. The highest concentrations of Mn are seen in samples from S3, with averages of 1225 ± 1046 and 752 ± 460 ppm for the Touirist (I5) and Aguelt el Mabha (I6) formations respectively – note the greater variability in the Touirist (I5) Formation (Figure 3.8). Apart from one sample in I3, shale from S4 is generally

much depleted in Mn (Figure 3.9) relative to average shale, with an average across the three formations of 110 ± 147 ppm.

3.2.5.2 Molybdenum

Molybdenum is slightly enriched relative to average shale (Turekian and Wedepohl, 1961) in most samples, but generally not significantly so (see figures 3.7 – 3.9). In S2, the greatest concentrations occur in the Touirist (I5) Formation, with an average of 7.50 ± 5.26 ppm and a maximum of 21.00 ppm (Table 3.5). The average for the En Nesoar (I4) Formation is only slightly lower at 6.10 ± 3.27 ppm, while a mean of 0.95 ± 1.69 ppm for the Aguelt el Mabha (I6) Formation suggests a slight depletion relative to average shale. Similarly, Mo concentrations in the Aguelt el Mabha (I6) are close to average shale with a mean of 2.16 ± 1.76 ppm while there appears to be a slight enrichment in the Touirist (I5) Formation with an average of 6.65 ± 3.05 ppm. Mo is generally slightly enriched in S4, but averages for the I4 and I5 formations are slightly lower than for the equivalent formations in S2 and S3 (En Nesoar and Touirist formations), being 4.79 ± 2.99 and 4.48 ± 2.17 ppm respectively. The average for the I3 Formation is only slightly higher than for the other two formations sampled from S4, at 5.08 ± 1.54 ppm.

3.2.5.3 Vanadium

Vanadium concentrations are largely similar to average shale (Turekian and Wedepohl, 1961), with some enrichment in the lower part of the En Nesoar (I4) Formation and in some samples form the Touirist (I5) Formation in S2 and slight depletion apparent in samples form the Aguelt el Mabha (I6) Formation in cores S2 and S3 and the Touirist Formation in S3 (figures 3.7 – 3.9). Average V concentration for the Aguelt el Mabha (I6) Formation in S2 is 76 ± 14 ppm as opposed to 155 ± 101 and 207 ± 112 ppm for the Touirist (I5) and En Nesoar (I4) formations respectively (table 1.7). There is less difference between formations in S3 and S4 with overall averages of 96 ± 23 and 128 ± 22 ppm.

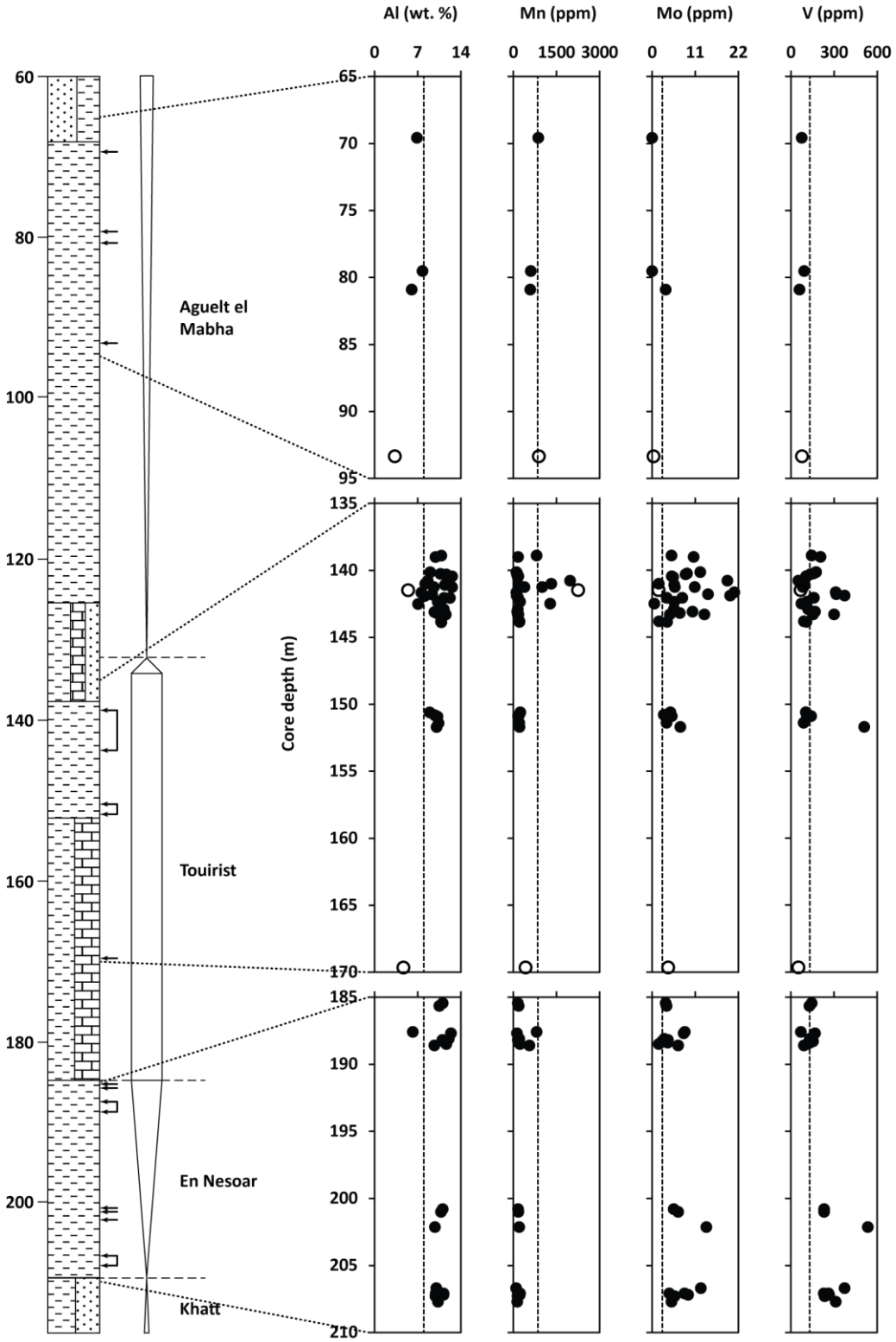
Al (wt. %)
Mn (ppm)
Mo (ppm)
V (ppm)
0 7 14
0 1500 3000
0 11 22
0 300 600
Aguelt el Mabha
Touirist
En Nesoar
Khatt
Core depth (m)
60
80
100
120
140
160
180
200
65
70
75
80
85
90
95
135
140
145
150
155
160
165
170
185
190
195
200
205
210

Figure 3.7 Depth profiles for trace metals in S2 – open circles indicate carbonate-rich samples and dashed lines indicate average shale (Turekian and Wedepohl, 1961)

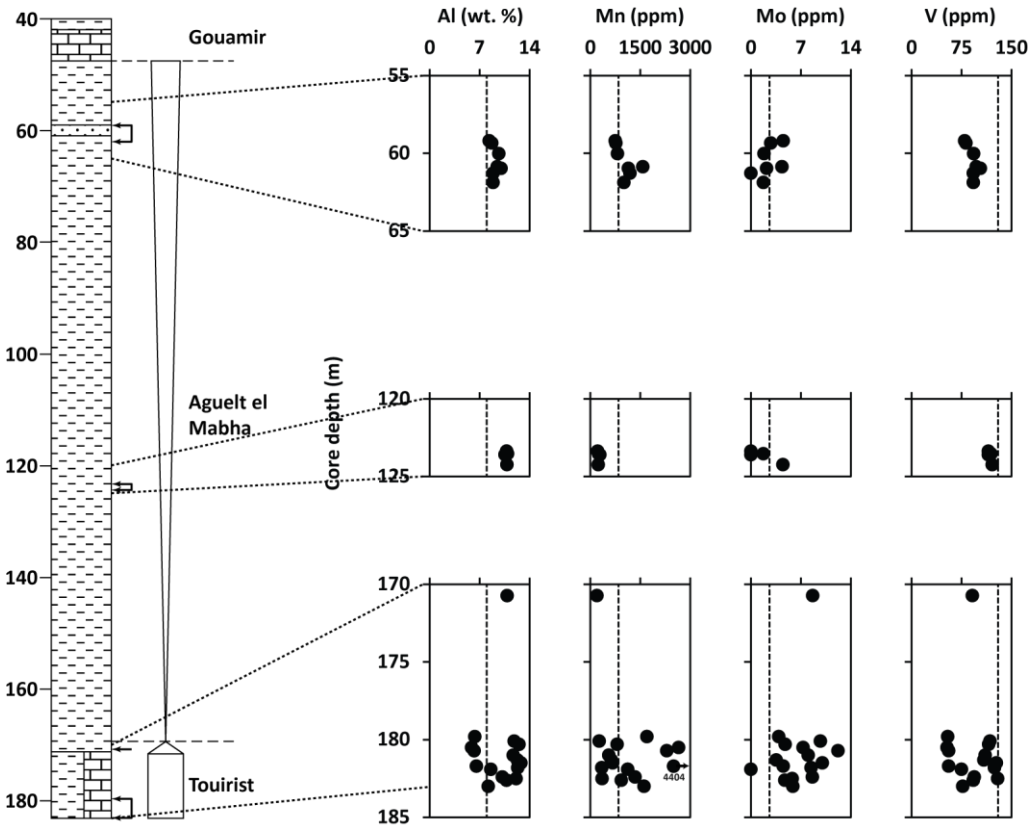

Figure 3.8 Depth profiles for trace metals in S3 – dashed lines indicate average shale (Turekian and Wedepohl, 1961)

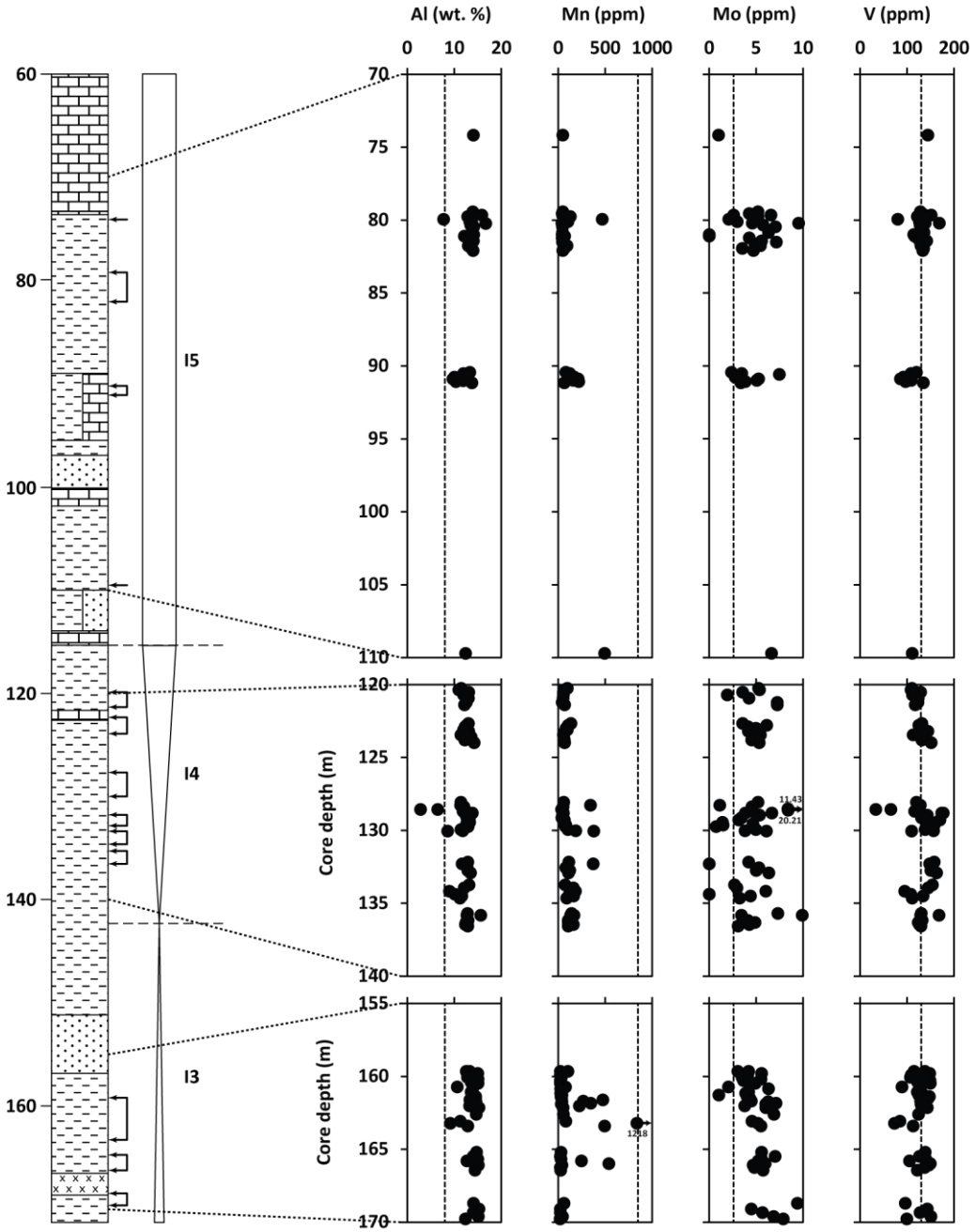

Figure 3.9 Depth profiles for trace metals in S4 – dashed lines indicate average shale (Turekian and Wedepohl, 1961)

3.3 Discussion

3.3.1 Redox indicators

The main focus in interpreting depositional redox conditions will be the FeHR/FeT and FeP/FeHR indicators, as together these have the potential to distinguish between oxic, ferruginous and euxinic water masses (Poulton and Canfield, 2011). Supporting Fe/Al, $\delta^{34}S$ and redox sensitive trace metal concentration data will also be presented, with a view to resolving redox associations of samples which have equivocal FeHR/FeT ratios (between 0.22 and 0.38) which may represent either oxic or anoxic conditions.

3.3.1.1 Fe speciation

Although some samples contain a lot of carbonate (up to 8.03 wt% inorganic C), all samples contain at least 1 wt% FeT. Therefore, on the basis of the study by Clarkson et al. (2014), there can be confidence in the Fe speciation results for all samples in this study, regardless of carbonate contents.

Shales from S2 show a wide range of FeHR/FeT ratios, from 0.08 to 0.89. Only four samples show clear evidence for deposition under oxic conditions (Figure 3.10) with averages for FeHR/FeT (Table 3.5) in all three formations somewhat greater than the Phanerozoic average of 0.14 ± 0.08 for marine shales deposited under oxic conditions (Poulton and Raiswell, 2002). While many samples, especially in the Touirist (I5) Formation, show clear evidence of deposition under anoxic conditions, there is also a significant proportion of samples with equivocal values for FeHR/FeT, especially in the En Nesoar (I4) Formation.

In previous redox studies Fe/Al ratios have been used to identify authigenic enrichments in sediments being deposited under anoxic conditions, but relative to average shale (Lyons and Severmann, 2006) both the En Nesoar (I4) and Touirist (I5) formations appear depleted with mean Fe/Al ratios of 0.32 ± 0.20 and 0.32 ± 0.08 as opposed to 0.5. This is perhaps not surprising as the results show that Al concentrations are generally greater than average shale concentrations (Turekian and Wedepohl, 1961) in the En Nesoar (I4) and Touirist formations.

Therefore, a local oxic baseline would need to be established to detect enrichments implying deposition under an anoxic water column. In contrast, the four samples from the Aguelt el Mabha (I6) Formation have similar Al concentrations to average shale, and give an average Fe/Al ratio of 0.50 ± 0.15, suggesting that there may have been a change in terriginous Fe/Al input over time (see further discussion in Section 3.3.1.2).

Of the clearly anoxic samples, most have FeP/FeHR ratios < 0.70, as do all equivocal samples, indicating that anoxic conditions were dominantly ferruginous, with occasional euxinic excursions in both the En Nesoar (I4) and Tourist (I5) formations. FeP/FeHR ratios are very low in the Aguelt el Mabha (I6) Formation, with an average of 0.01 ± 0.02.

Core	Formation	FeHR/FeT	FeP/FeHR	Fe/Al
S2	Aguelt El Mabha (I6)	0.29 ± 0.15	0.01 ± 0.02	0.50 ± 0.15
	Touirist (I5)	0.46 ± 014	0.52 ± 0.16	0.32 ± 0.08
	En Nesoar (I4)	0.35 ± 0.13	0.58 ± 0.14	0.32 ± 0.20
S3	Aguelt El Mabha (I6)	0.23 ± 0.05	0.01 ± 0.02	0.54 ± 0.07
	Touirist (I5)	0.17 ± 0.06	0.10 ± 0.17	0.39 ± 0.09
S4	I5 (Touirist)	0.30 ± 0.14	0.25 ± 0.22	0.35 ± 0.42
	I4 (En Nesoar)	0.60 ± 0.16	0.75 ± 0.10	0.78 ± 1.71
	I3 (Khatt)	0.71 ± 0.13	0.72 ± 0.18	0.23 ± 0.13

Table 3.5 Fe redox indicators for each core by formation (mean ± 1 SD)

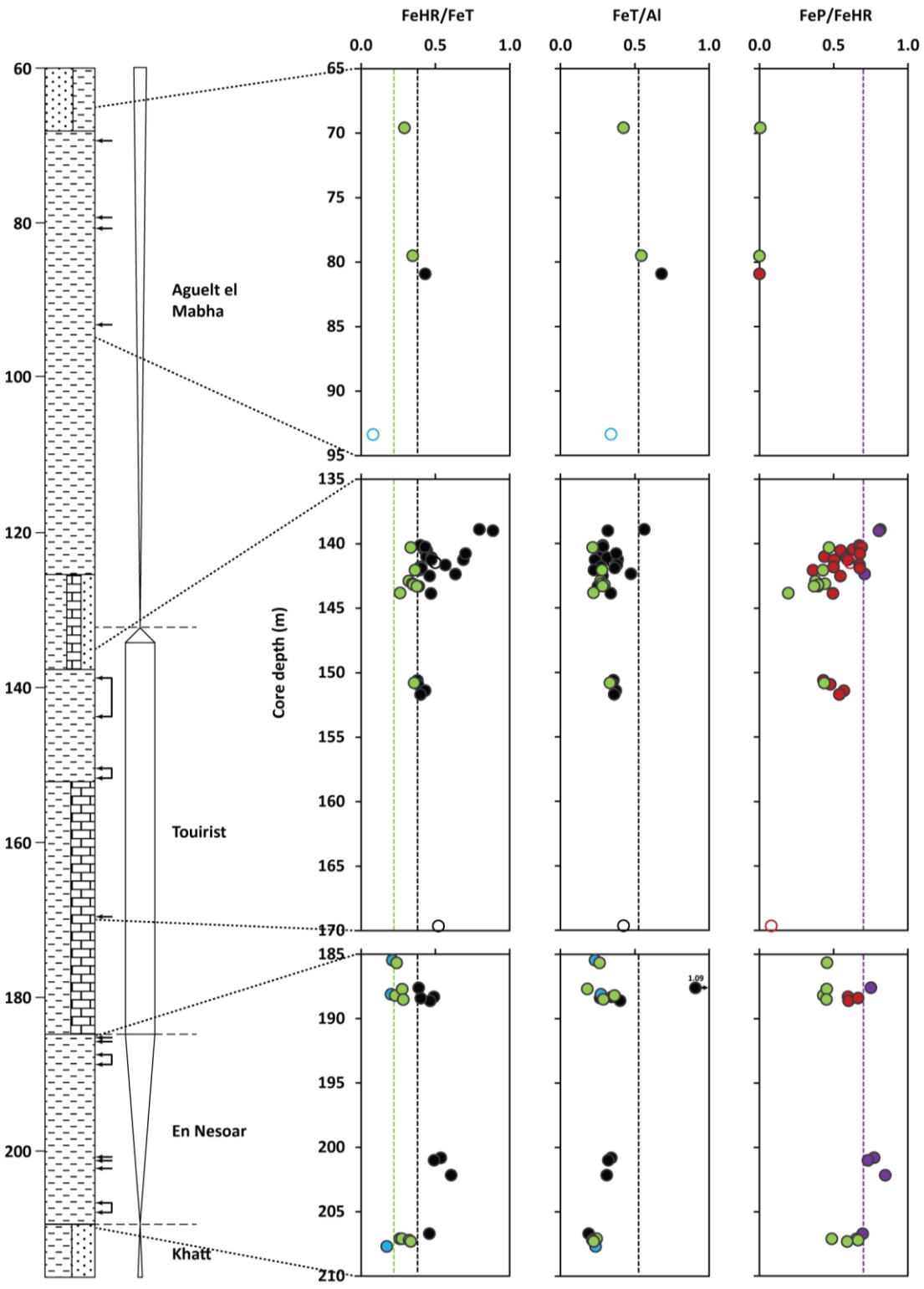

Figure 3.10 Depth profiles for Fe redox indicators in S2. Blue markers indicate oxic samples, green equivocal, black undifferentiated anoxic, red ferruginous and purple euxinic. Open circles indicate

carbonate-rich samples. The blue dotted line represents FeHR/FeT=0.22, the green FeHR/FeT=0.38, the black Fe/Al=0.5 and the purple FeP/FeHR=0.7.

FeHR/FeT ratios in S3 are much closer to Phanerozoic average shale, with means of 0.17 ± 0.06 and 0.23 ± 0.05 for the Touirist (I5) and Aguelt el Mabha (I6) formations respectively. Most samples analysed are clearly oxic, with the few equivocal samples having generally very low FeP/FeHR ratios (Figure 3.11). FeT/Al ratios are on average very similar to the equivalent formations in S2.

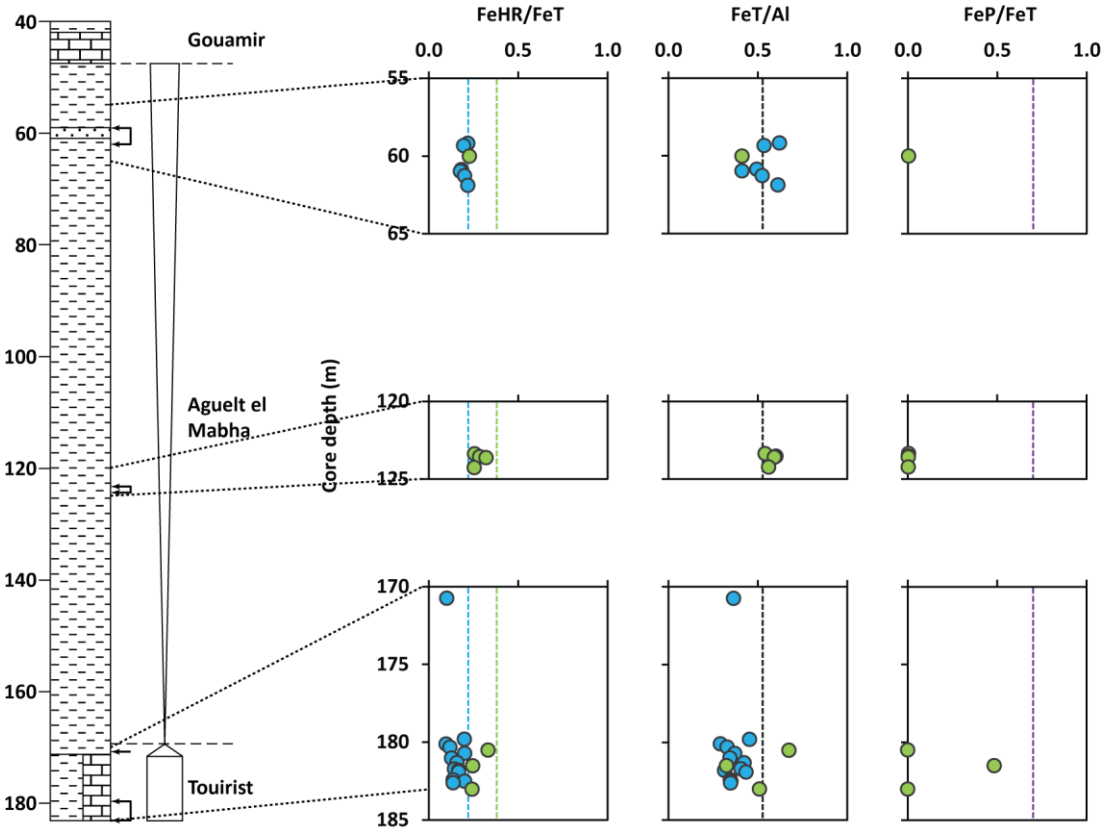

Figure 3.11 Depth profiles for Fe redox indicators in S3. Blue markers indicate oxic samples, green equivocal, black undifferentiated anoxic, red ferruginous and purple euxinic. The blue dotted line represents FeHR/FeT=0.22, the green FeHR/FeT=0.38, the black Fe/Al=0.5 and the purple FeP/FeHR=0.7.

FeHR/FeT ratios in S4 are largely clearly anoxic in the lower two formations sampled (Figure 3.12), with averages of 0.71 ± 0.13 and 0.60 ± 0.16 in the I3 and I4 formations. FeHR/FeT

ratios in I5 are much lower, with an average of 0.30 ± 0.14. Many samples have FeHR/FeT ratios < 0.22 suggesting deposition under an oxic water column while a small number of samples with FeHR/FeT > 0.38 provide clear evidence of occasional anoxic episodes. The average Fe/Al ratio for the I5 Formation is similar to that of the equivalent Touirist Formation in S3 and S2 (Table 3.6). Half of the anoxic samples have Fe/Al ratios suggesting some authigenic enrichment, while the equivocal samples have Fe/Al ratios similar to the oxic samples. The three equivocal samples in the I4 Formation are all at the lower end of the range of Fe/Al values for this formation, while some anoxic samples show significant enrichment in Fe, giving an average of 0.78 ± 1.71. While this average is skewed by some exceptionally Fe rich samples, a shift in Fe/Al ratios from the underlying I3 formation is apparent (Figure 3.12), where the average is 0.23 ± 0.13.

FeP/FeHR ratios are high in I3 and I4, with averages of 0.72 ± 0.18 and 0.75 ± 0.10 respectively, suggesting dominantly euxinic conditions during shale deposition in these formations. FeP/FeHR ratios < 0.7 suggest conditions were ferruginous at times, although in many cases, especially in the I4 Formation, FeP/FeHR ratios are close to 0.7, and hence could represent euxinic depositional conditions. A couple of euxinic incursions are evident in the I5 Formation, but the other four clearly anoxic samples and all of the equivocal samples have FeP/FeHR ratios considerably lower, giving an overall average of 0.25 ± 0.22, implying that most possible anoxic episodes were ferruginous.

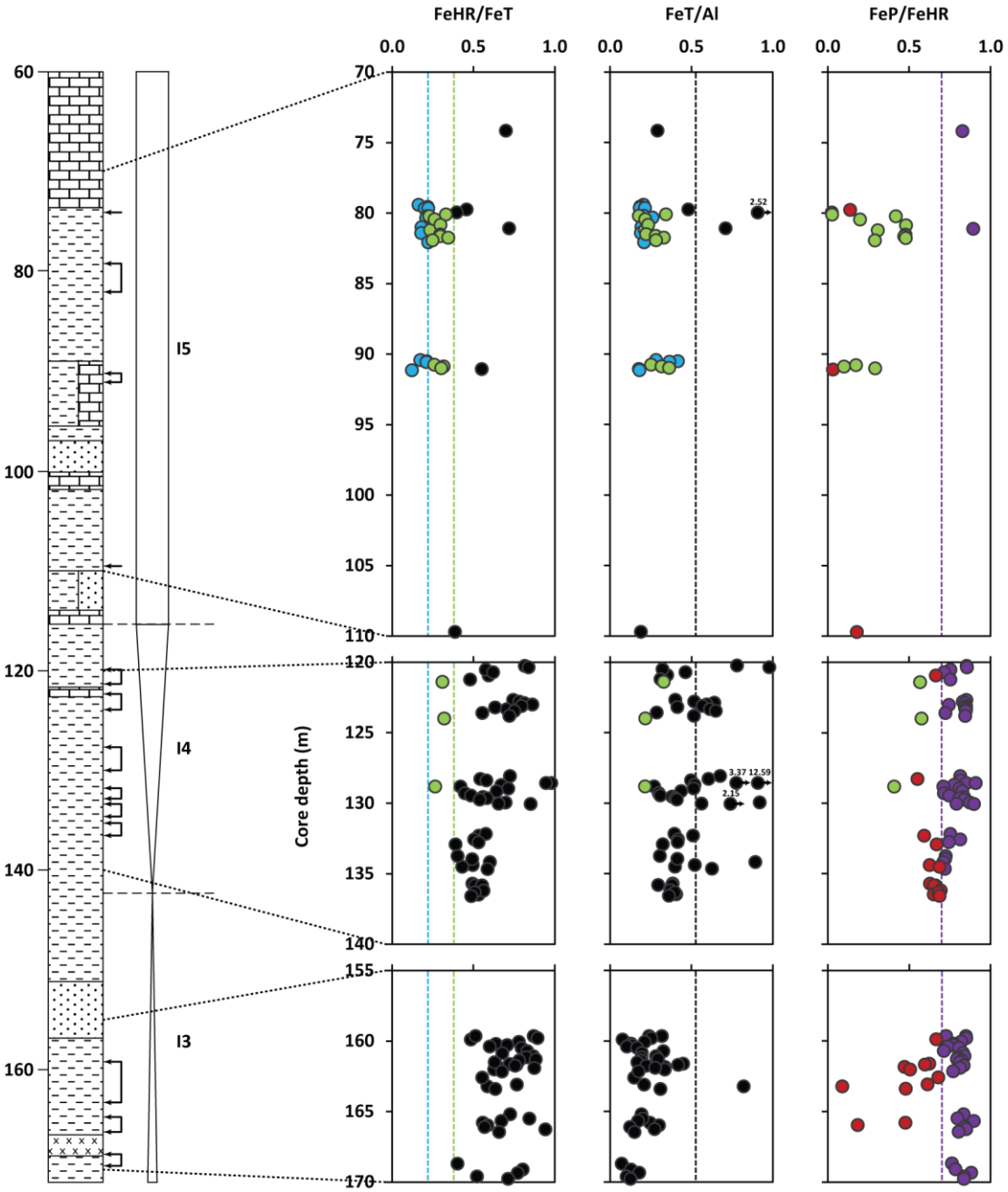

Figure 3.12 Depth profiles for Fe redox indicators in S4. Blue markers indicate oxic samples, green equivocal, black undifferentiated anoxic, red ferruginous and purple euxinic. The blue dotted line represents FeHR/FeT=0.22, the green FeHR/FeT=0.38, the black Fe/Al=0.5 and the purple FeP/FeHR=0.7.

3.3.1.2 Fe/Al

Although work by Clarkson et al. (2014) suggests that Fe/Al ratios should be applicable even at higher carbonate contents, the generally higher Al concentrations than those found in average shales mean that 0.53 is not a suitable baseline from which to assess whether equivocal samples are enriched in Fe or not. Limited provenance studies suggest that siliciclastics in the Char and Atar Groups were likely sourced from the local granitic and gneissic basement (Nicoll et a., 2010), but Bronner et al. (1980) report the presence of hyperaluminous and ferruginous horizons, which could potentially have been a source of variation in the lithogenic Fe/Al inputs. Evidence indicating shifts in Fe/Al ratios over time suggests that an oxic baseline from which to assess enrichments in equivocal samples would need to be established for each formation.

In the En Nesoar Formation in S2 average Fe/Al for oxic samples is 0.25 ± 0.02, as opposed to averages of 0.34 ± 0.07 and 0.45 ± 0.36 for ferruginous samples (Table 3.6), implying a slight enrichment in Fe in anoxic samples. Although there is overlap in the ranges of Fe/Al for oxic, equivocal and anoxic samples, an almost identical FeT/Al average for oxic and equivocal samples might suggest that the equivocal samples were deposited under oxic conditions. Although no oxic samples are available for comparison in the equivalent I4 Formation in S4, an average of 0.25 ± 0.07 for equivocal samples is comparable with oxic samples in S2, and somewhat lower than the average for ferruginous and euxinic samples from S4, indicating that brief periods of oxygenation may have occurred during the deposition of I4 in S4.

In the I5 Formation in S4, the average Fe/Al ratio for equivocal samples is 0.28 ± 0.05, which is similar to an average of 0.23 ± 0.07 for oxic samples and rather lower than the averages for ferruginous and euxinic samples (although it should be noted that these averages are based on a small number of samples with highly variable Fe content), suggesting that on the whole equivocal samples were probably deposited under oxic conditions. There are no definitively oxic samples to compare with in the equivalent Touirist Formation in S2, but an average of 0.27 ± 0.04 for equivocal samples is not much lower than the average for ferruginous samples in this part of the core, which is lower than the oxic average for the Touirist Formation in S3. On

average equivocal samples in S3 are enriched in Fe relative to oxic ones, but there are only three samples.

In the Aguelt el Mabha (I6) Formation, the two equivocal samples have Fe/Al ratios intermediate between the oxic sample and the ferruginous sample, and similar to averages for both oxic and equivocal samples in the same formation in S3.

Core	Formation	Fe/Al Oxic	Fe/Al Equivocal	Fe/Al Ferruginous	Fe/Al Euxinic
S2	Aguelt El Mabha (I6)	0.34	0.48 ± 0.08	0.68	-
	Touirist (I5)	-	0.27 ± 0.04	0.32 ± 0.06	0.45 ± 0.12
	En Nesoar (I4)	0.25 ± 0.02	0.25 ± 0.06	0.34 ± 0.07	0.45 ± 0.36
S3	Aguelt El Mabha (I6)	0.53 ± 0.08	0.54 ± 0.08	-	-
	Touirist (I5)	0.37 ± 0.05	0.50 ± 0.18	-	-
S4	I5 (Touirist)	0.23 ± 0.07	0.28 ± 0.05	0.84 ± 1.13	0.5 ± 0.3
	I4 (En Nesoar)	-	0.25 ± 0.07	0.41 ± 0.09	0.94 ± 2.02
	I3 (Khatt)	-	-	0.33 ± 0.20	0.19± 0.07

Table 3.6 Fe/Al by formation and redox state for each core (mean ± 1 SD)

3.3.1.3 S isotopes

$\delta^{34}S$ data shows little relationship with redox conditions or formation for each core, but variation from lighter to heavier isotopic values from S2 to S3 to S4 is apparent when the data are split into 5‰ bins (Figure 3.13) for each core. These results are entirely consistent with the redox model developed from Fe speciation data (see Section 3.3.2). Lighter $\delta^{34}S$ values in S2

are consistent with mostly diagenetic pyrite formation within the sediment with a non-limited sulphate supply e.g. Canfield and Teske (1996). Heavier $\delta^{34}S$ in S4 is consistent with greater utilization of water column sulphate in a dominantly euxinic environment e.g. Shen et al. (2002), while the spread in pyrite sulphur isotope composition is consistent with fluctuations between euxinic and ferruginous conditions, whereby euxinic and ferruginous samples have differing sulphate availability.

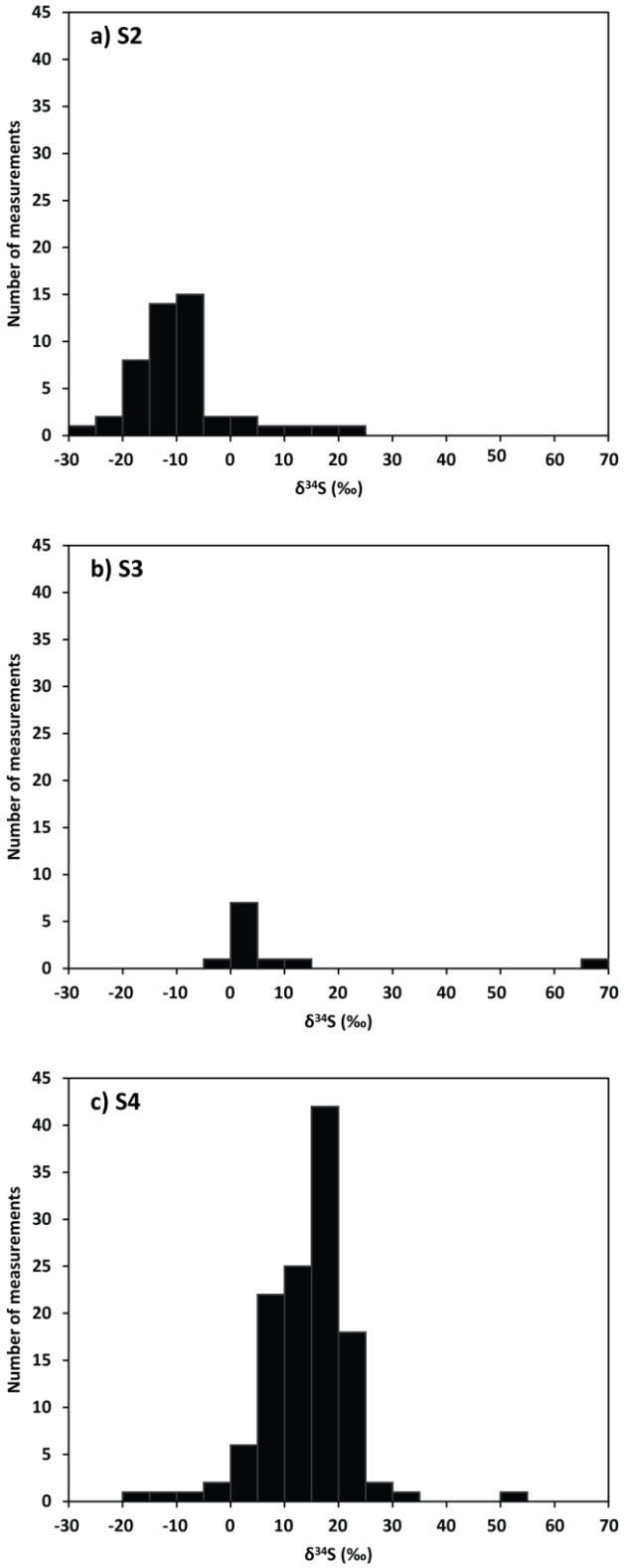

Figure 3.13 Distribution of pyrite $\delta^{34}S$ data by core

3.3.1.4 Trace metals

In order to account for variation in carbonate and organic carbon content, trace metal data is normalised to Al content in figures 3.14 – 3.16. For Al normalised Mn and Mo, patterns of enrichment or depletion relative to average shale are much the same as for absolute concentrations of these metals. Some of the variability in V is reduced by normalisation to Al.

In S4 all but one sample show depletion in Mn relative to average shale, suggesting that in the deeper basin there was no significant Mn drawdown, which is not unexpected in the I3 and I4 formations, where conditions were consistently anoxic. However, some enrichment might be expected in I5 where redox conditions fluctuated between oxia and anoxia. Manganese occurs as Mn^{3+} and Mn^{4+} in insoluble oxyhydroxides in oxygenated waters, but in oxygen deficient settings, it is more soluble, existing in a lower oxidation state (Mn^{2+}). Consequently, where oxic and anoxic conditions are juxtaposed, such as at the chemocline, cycling of Mn occurs (Calvert and Pedersen, 1996). This can lead to concentration of Mn at the chemocline which can be precipitated as Mn oxides under oxygenated conditions and dissolved and reprecipitated as Ca-rich rhodochrosite under anoxic conditions (Huckriede and Meischner, 1996). Some enrichment, and high variability, is seen in the Touirist (I5) Formation in both S2 and S3, suggesting that sediment deposition in shallower parts of the basin at this time was close to a fluctuating chemocline leading to Mn precipitation with Fe oxides under periodic oxic conditions followed by conversion to rhodochrosite under anoxic conditions (Huckriede and Meischner, 1996). Consistent with this as a mechanism of enrichment is presence of higher concentrations of Mn in more carbonate rich samples. The enrichment and variability seen in the Touirist Formation is reduced in the shallower Aguelt el Mabha (I6) Formation, with Mn/Al comparable with average shale. The lack of enrichment in Mn in S4, even in the I5 formation where redox conditions fluctuated, in contrast to enrichment seen in the Touirist Formation in cores S2 and S3 suggests that drawdown of Mn was limited to shallower, epicratonic settings. Gilleaudeau and Kah (2013a, 2015) made similar observations.

The behaviours of Mo and V are influenced by ocean redox conditions, with enrichments in these trace metals associated with anoxia (Tribovillard et al., 2006). In oxic conditions, V exists

as vandate ions, but under reducing conditions it is reduced to a form which can be removed to the sediment in organometallic ligands or by surface adsorption processes (Calvert and Pedersen, 1993, Algeo and Maynard, 2004, Tribovillard et al., 2006). Where H_2S is present in the water column, V is further reduced, and can then become more enriched in sediment when it is taken up by geoporphyrins or precipitated as solide oxide or hydroxide phases (Algeo and Maynard, 2004, Tribovillard et al., 2006). Under oxic conditions, Mo exists as a low reactivity molybdate ion. Under reducing, but non-sulphidic conditions, Mo can be taken up by organic carbon and by pyrite forming below the sediment-water interface, but such accumulation is apparently limited (Algeo and Maynard, 2004). However, where sufficient H_2S is available in the water column, molybdate is converted to particle-reactive thiomolybdates (Helz et al., 1996). Theses ions can then be scavenged in the water column by Fe sulphide minerals and organic matter, potentially leading to sedimentary Mo concentrations of tens to hundreds of ppm (Lyons et al., 2009). The differing sensitivities of V and Mo to redox conditions have been used to differentiate between anoxic conditions without and with H_2S in the water column - V enrichment without significant Mo enrichment is indicative of anoxic conditions without H_2S in the water column, with further enrichment occurring where H_2S is available, while Mo is enriched mainly under sulphidic conditions (Algeo and Maynard, 2004, Tribovillard et al., 2006). However, studies of sedimentary Mo concentrations in euxinic settings have shown that enrichments may be muted where persistent sulphidic sinks and restricted resupply of Mo to the water body suppresses the size of the oceanic Mo reservoir (Algeo and Lyons, 2006, Scott et al., 2008).

Mo/Al ratios in S4 are generally comparable with average shale, except for two enriched samples with particularly high pyrite contents. This lack of enrichment in mostly euxinic samples from the deeper basin is indicative of constant Mo drawdown under anoxic conditions in a restricted basin (Algeo and Lyons, 2006, Scott et al., 2008). Muted enrichment under all redox conditions in S2 and S3 relative to roughly contemporaneous samples from S4 suggests there may be some drawdown of the terrestrial Mo input before it can reach the deeper parts of the basin. Similar patterns were also observed by Gilleaudeau and Kah (2013b).

Similarly to Mo/Al ratios, V/Al ratios in S4 show no enrichment in the deeper basin, consistent with continual drawdown of V under anoxic conditions in a restricted basin. V/Al ratios in S3 are very similar. Some enrichment in V is apparent in both the En Nesoar (I4) and the Touirist Formations and probably indicates drawdown of riverine V input under both ferruginous and euxinic conditions in shallower environments.

Unfortunately for refining redox interpretations of samples for which FeHR/FeT proved equivocal, Mn, Mo and V concentrations show a lot of overlap between oxic and anoxic conditions as defined by FeHR/FeT ratios. Although Fe/Al ratios for equivocal samples from the I4 formation are relatively low, Mn/Al, Mo/Al and V/Al ratios all fall in line with the surrounding ferruginous and euxinic samples, so these equivocal samples cannot be convincingly labelled as oxic. The same is true for trace metals in the equivalent En Nesoar Formation in S2, but there at least is some clear evidence for oxic excursions here in the FeHR/FeT data, and average Fe/Al values suggest equivocal samples are more likely to have been deposited under oxic conditions.

Similarity in Mn/Al, Mo/Al and V/Al ratios for oxic and equivocal samples from the I5/Touirist Formations in S3 and S4, as well as low Fe/Al ratios in S4 relative to anoxic samples indicates that equivocal samples were probably oxic, although again there is overlap in trace metal abundances between oxic and anoxic samples in S4. Although the greatest enrichments seen in the Touirist Formation in S2 are limited to ferruginous samples, Mn/Al, Mo/Al and V/Al ratios of equivocal samples do overlap with those for ferruginous and euxinic samples, and FeT/Al ratios of equivocal samples do not significantly differ from those of ferruginous samples, making it difficult to discern the most likely depositional conditions for these samples.

As in the Touirist (I5) Formation in S3, samples from the Aguelt el Mabha (I6) Formation show similar trace metal distributions, as well as having very similar Fe/Al. This, together with a lack of any evidence of anoxic conditions, suggests that the equivocal samples were most likely deposited under oxic conditions. The data for samples from the Aguelt el Mabha (I6) Formation in S2 is more ambiguous – Fe/Al ratios are intermediate between the one oxic and the one

ferruginous sample analysed, Mn/Al and V/Al ratios are closer to the ferruginous sample and Mo/Al ratios closer to the oxic sample.

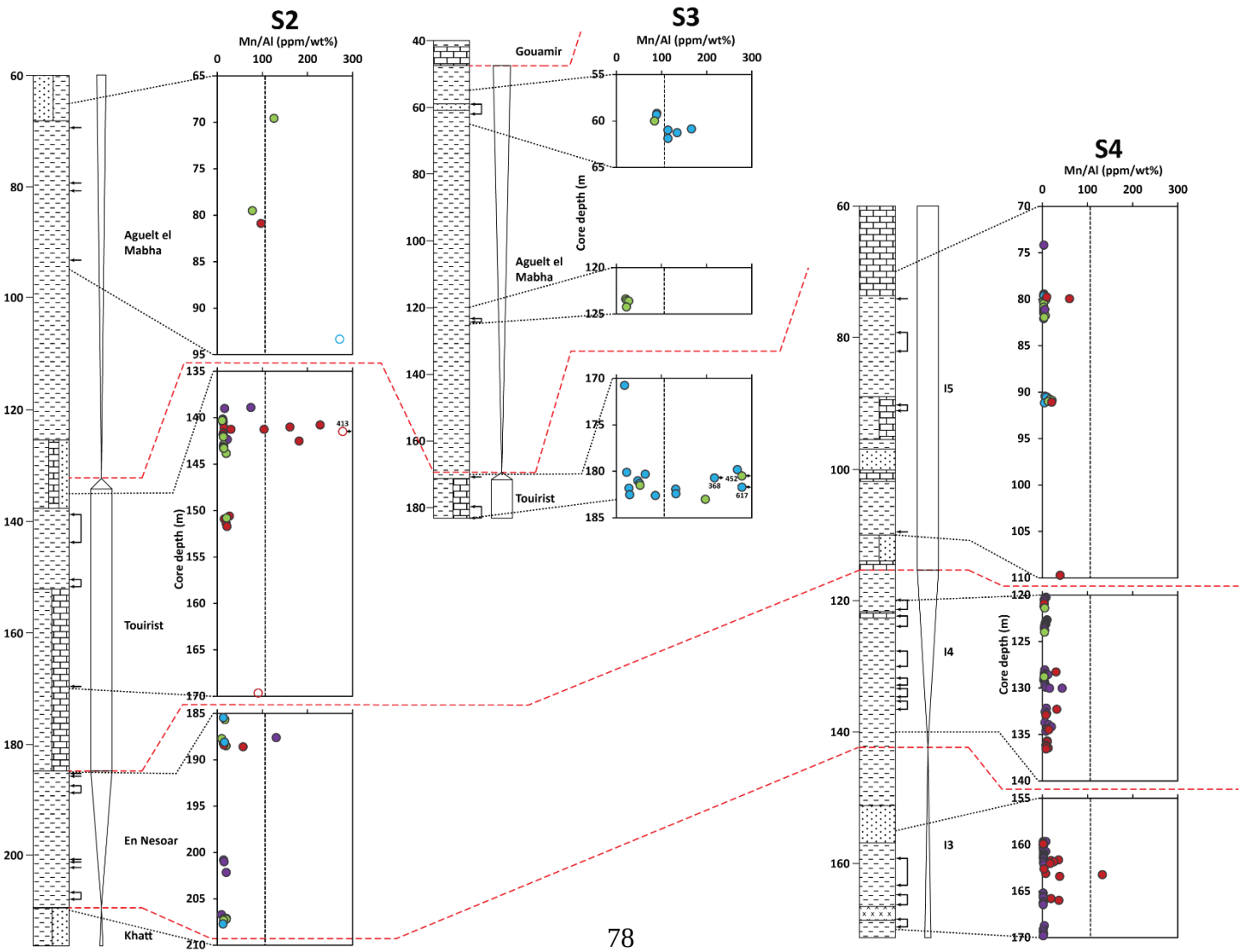
S2
Mn/Al (ppm/wt%)
0
100
200
300
Aguelt el Mabha
Touirist
En Nesoar
Khatt
Core depth (m)
413
S3
Gouamir
Aguelt el Mabha
Touirist
Core depth (m
368
452
617
S4
Mn/Al (ppm/wt%)
I5
I4
I3
Core depth (m)

Figure 3.14 Mn/Al ratios in cores S2, S3 and S4. Open circles indicate carbonate-rich samples. Vertical dotted lines indicate average shale values taken from Turekian and Wedepohl (1961).

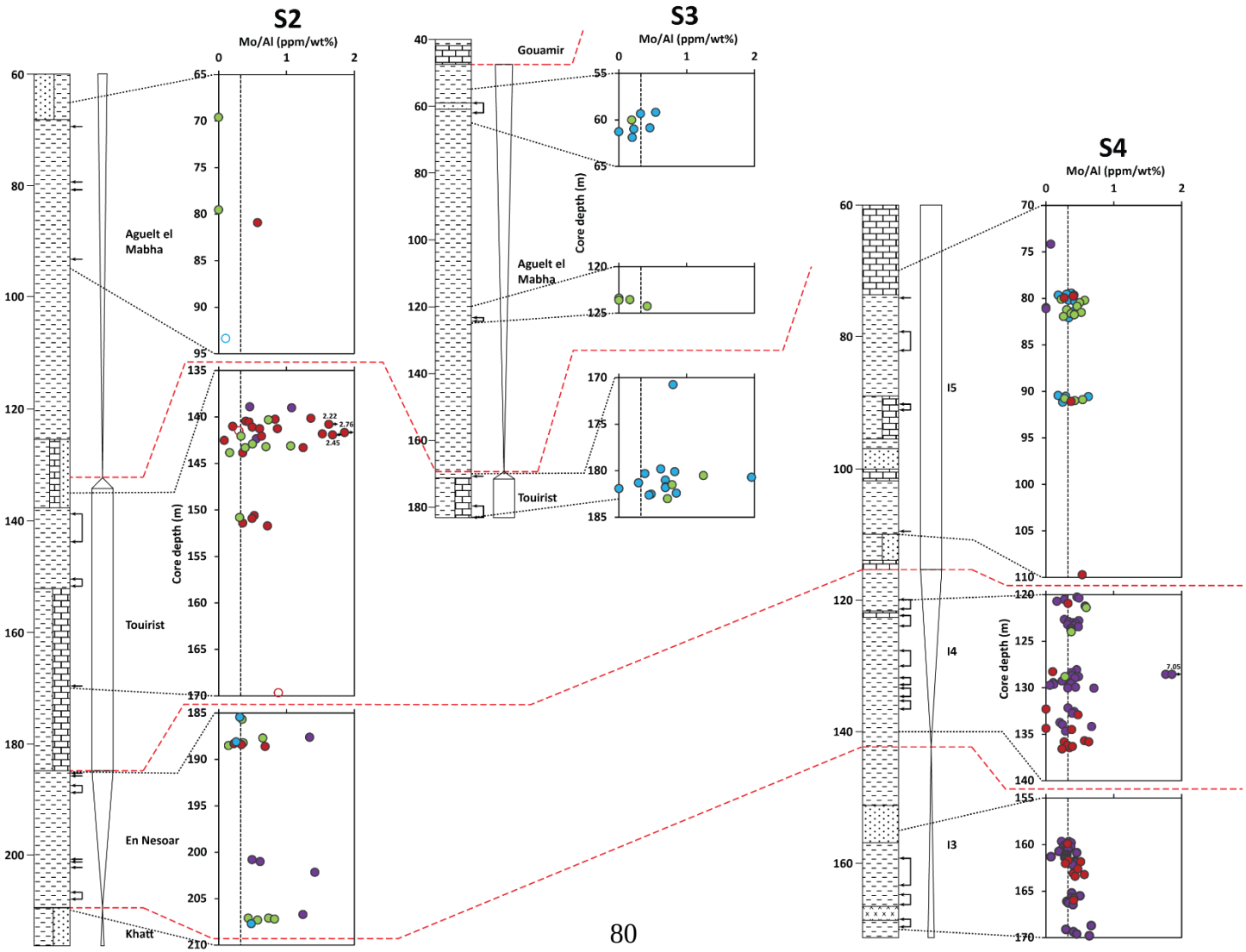
S2
Mo/Al (ppm/wt%)
Aguelt el Mabha
Touirist
En Nesoar
Khatt
Core depth (m)
S3
Gouamir
Aguelt el Mabha
Touirist
S4
I5
I4
I3

Figure 3.15 Mo/Al ratios in cores S2, S3 and S4. Vertical dotted lines indicate average shale values taken from Turekian and Wedepohl (1961).

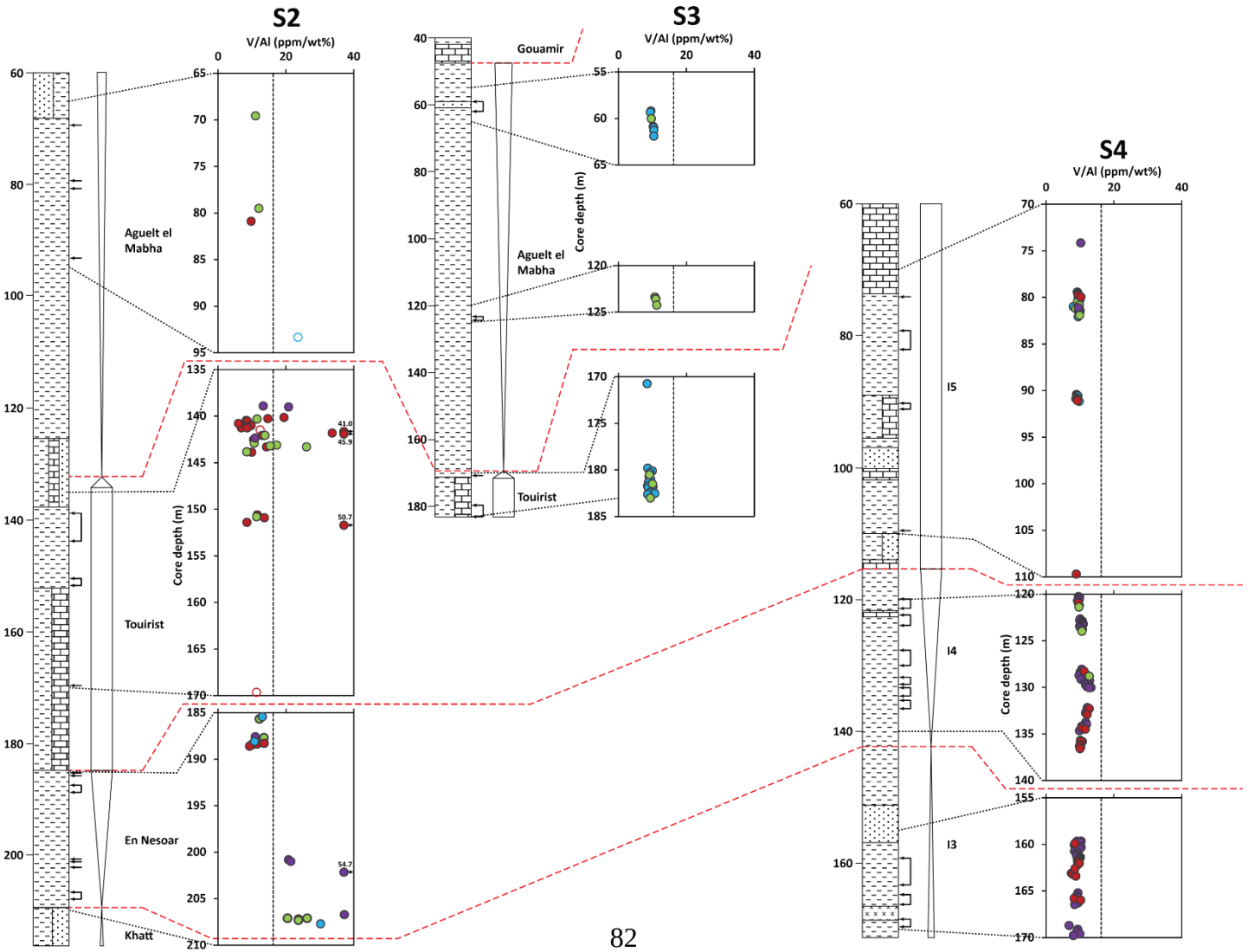
S2
V/Al (ppm/wt%)
0
20
40
Aguelt el Mabha
Touirist
En Nesoar
Khatt
Core depth (m)
41.0
45.9
50.7
54.7
S3
V/Al (ppm/wt%)
Gouamir
Aguelt el Mabha
Touirist
Core depth (m)
S4
V/Al (ppm/wt%)
I5
I4
I3
Core depth (m)

Figure 3.16 V/Al ratios in cores S2, S3 and S4. Vertical dotted lines indicate average shale values taken from Turekian and Wedepohl (1961).

3.3.2 Spatial and temporal redox reconstruction

Fe speciation and supporting S isotope and redox sensitive trace metal data suggest that redox conditions in the Taoudeni Basin were spatially highly heterogeneous and rapidly fluctuating during the deposition of the Atar/El Mreiti Group, with temporal variability in the redox structure of the basin. A plot of FeP/FeHR against FeHR/FeT (Figure 3.17) clearly shows that in S4 there was a shift from dominantly euxinic conditions in the I3 and I4 formations to a more oxidised deeper basin in I5, despite an increase in sea level. Meanwhile in S2 there is a move to greater enrichment in highly reactive Fe going from the En Nesoar (I4) Formation to the Touirist (I5) Formation. Conditions in the Touirist (I5) Formation in S3, and the Aguelt el Mabha (I6) Formation in S2 and S3 are indicated to be persistently oxic, with very little pyrite formation.

Figure 3.18 shows a schematic reconstruction of redox structure in the Taoudeni Basin through time. Here, a different approach is taken to reconstructing redox structure than that taken in other recent publications on the Taoudeni Basin (Gilleaudeau and Kah, 2015, Beghin et al., 2017a). Gilleaudeau and Kah (2015) considered redox structure in terms the three depositional environments they identified, while Beghin et al. (2017a) view redox structure in the context of a marine transgression and a marine regression. Both these approaches assume a stratified basin throughout the deposition of the Atar/El Mreiti Group. In this study, an attempt to reconstruct redox structure in a series of time slices, based on formation, is made. In the absence of detailed reconstructions of basin profile on a formation by formation basis, a simplified, generalised profile is shown, similar to those shown by Gilleaudeau and Kah (2015) and Beghin et al. (2017a).

Data in this study suggests that deposition of the I3 Formation took place in shallow waters, under highly reducing sulfidic conditions, with occasional ferruginous intervals. Ferruginous intervals may have been the result of fluctuations in a chemocline between free Fe^{2+} and free H_2S in the water column. This formation was not represented in S2 or S3 and so redox conditions in more proximal areas is uncertain, but it is generally assumed that the sea surface was oxidised as it is thought that the atmosphere was sufficiently oxygenated by this time to

allow diffusion of oxygen into surface waters. Two samples from the Khatt Formation close to El Mreiti suggest that that is indeed the case (Gilleaudeau and Kah, 2015). However, data from Beghin et al. (2017a) suggests that the Khatt Formation in S2 was likely deposited under generally anoxic, ferruginous conditions. One possibility is a change in redox conditions between the localities' samples, with the samples in the Beghin et al. (2017a) study being from slightly deeper water, which would fit with a stratification model. However, this discrepancy could well be a result of sampling of different time intervals – the samples of Beghin et al. (2017) come from close to the base of the overlying En Nesoar Formation, while stratigraphic logs suggest that Gilleaudeau and Kah (2015) sampled lower down in the Khatt Formation. Beghin et al. (2017a) note that a ferruginous signal in the Khatt Formation, deposited in an environment with high wave energy, is surprising as they would, at this time in Earth history, have expected oxic conditions in such proximal environments. They speculate local enrichments in highly reactive iron due to proximity to the source could explain this signal without requiring anoxia. However, data presented in this thesis demonstrates that over 300 km away in S4, the intertidal to subtidal shallow marine sediments in I3 were also deposited under an anoxic water column, fluctuating between ferruginous and euxinic conditions. Therefore, it seems the most likely explanation for a dominantly anoxic signal is that shallow waters were indeed anoxic at this time. Possibly, this could be a period of particularly low atmospheric oxygen levels, but work to reconstruct atmospheric oxygen levels at this time would be required to further explore this. Overall, data in this study and from Beghin et al. (2017a) supports a model whereby, while there may be a thin layer of oxygenated waters at the top of the water column, a ferruginous layer exists within intertidal to subtidal depths. In the more distal, craton edge location of S4, slightly deeper waters are dominantly euxinic, with fluctuations to ferruginous conditions occurring as a result of fluctuations in a chemocline between free Fe^{2+} and free H_2S in the water column.

Figures 3.10 and 3.12 suggest that euxinia persisted in the more distal part of the basin as sea level rose in the I4/En Nesoar Formation, while redox conditions in shallower waters fluctuated between oxic, ferruginous and euxinic conditions, indicating that deposition in S2 was

occurring close to a fluctuating chemocline. Thus, a stratified redox structure as shown in Figure 3.18 is still apparent.

During deposition of the I5/Touirist Formation, when sea level was at its highest, evidence from this study suggests that towards the craton edge, in likely deeper waters, the basin was mostly oxic, with possible ferruginous intervals and very occasional euxinic incursions. Intermediate depths from further up the formation in S3 were also oxic. However, in shallower waters, closer to the centre of the craton, represented by S2, the water column was mostly anoxic and ferruginous. This suggests the development of an oxygen minimum zone in a largely oxygenated basin. This contrasts with data from Gilleaudeau and Kah (2015), who found that shale units in I5 of the Atar Group were anoxic and dominantly euxinic, while the Touirist Formation in the El Mreiti Group showed dominantly euxinic conditions. They view the transition from oxic to euxinic conditions as mirroring a transition from above to below wave base, consistent with a stratified redox model. This is not however consistent with the results presented here, or in the data covering a small number of samples from S4 in the study of Beghin et al. (2017a). Beghin et al (2017a) suggest that this could be explained by correlating the samples analysed from the I5 Formation in S4 with the Aguelt el Mabha Formation in S2, rather than the Touirist Formation, thus maintaining the stratification model. This seems unlikely however for the data presented in this chapter because the samples from S4 analysed in this study come from between Conophyton beds, and no sedimentary features indicating deposition in the shallower conditions above wave base that are represented by the Aguelt el Mabha Formation (e.g. cross-stratification, gutter casts) are observed. Figure 3.17 shows a clear shift to more oxidising conditions in the I5 Formation compared to the I3 and I4 formations, which sedimentary features suggest were deposited under higher energy, and therefore, likely, shallower waters. Both the I5 Formation in S4 and the Touirist Formation in S3 suggest a more oxidising environment in comparison to the Touirist Formation in S2. As the literature discussed in the introduction and sample description sections suggest that, at this time, waters were most likely deeper at the craton edge, an oxygen minimum zone, as shown in Figure 3.18 as a ferruginous wedge, seems more consistent with this data than a stratified redox structure. It is possible that the data from Gilleaudeau and Kah (2015) for the I5 Formation does not show

evidence of oxidising conditions due to sampling covering different time intervals, but it is most likely further evidence of spatial heterogeneity. Possibly, their results indicate another oxygen minimum zone to the south of core S4, with a euxinic wedge rather than a ferruginous wedge due to the greater water depths and further distance from continental Fe sources in comparison to the location of core S2.

Following a drop in sea level at the top of the I5/Touirist Formation, data here suggests that conditions recorded in S3 remained oxic in the Aguelt el Mabha Formation, with a limited number of samples showing some variation in redox still occurring in S2, closest to the centre of the craton. Data from Gilleaudeau & Kah (2015) indicates oxic depositional conditions for the Aguelt el Mabha Formation, while Beghin et al (2017a) find evidence for fluctuations between oxic and ferruginous environments in S2. As S3 is likely more distal (although not necessarily deeper due to filling of accommodation space during the deposition of the I5/Touirist Formation (Gilleaudeau and Kah, 2013a), but oxic, whereas evidence for anoxia is still present in S2, it seems likely that an oxygen minimum zone persists during the deposition of the I6/Aguelt el Mabha formation. Intermittent oxic conditions in S2 suggest however that this oxygen minimum zone could be waning. A lack of I6 in S4 means that more distal conditions are uncertain.

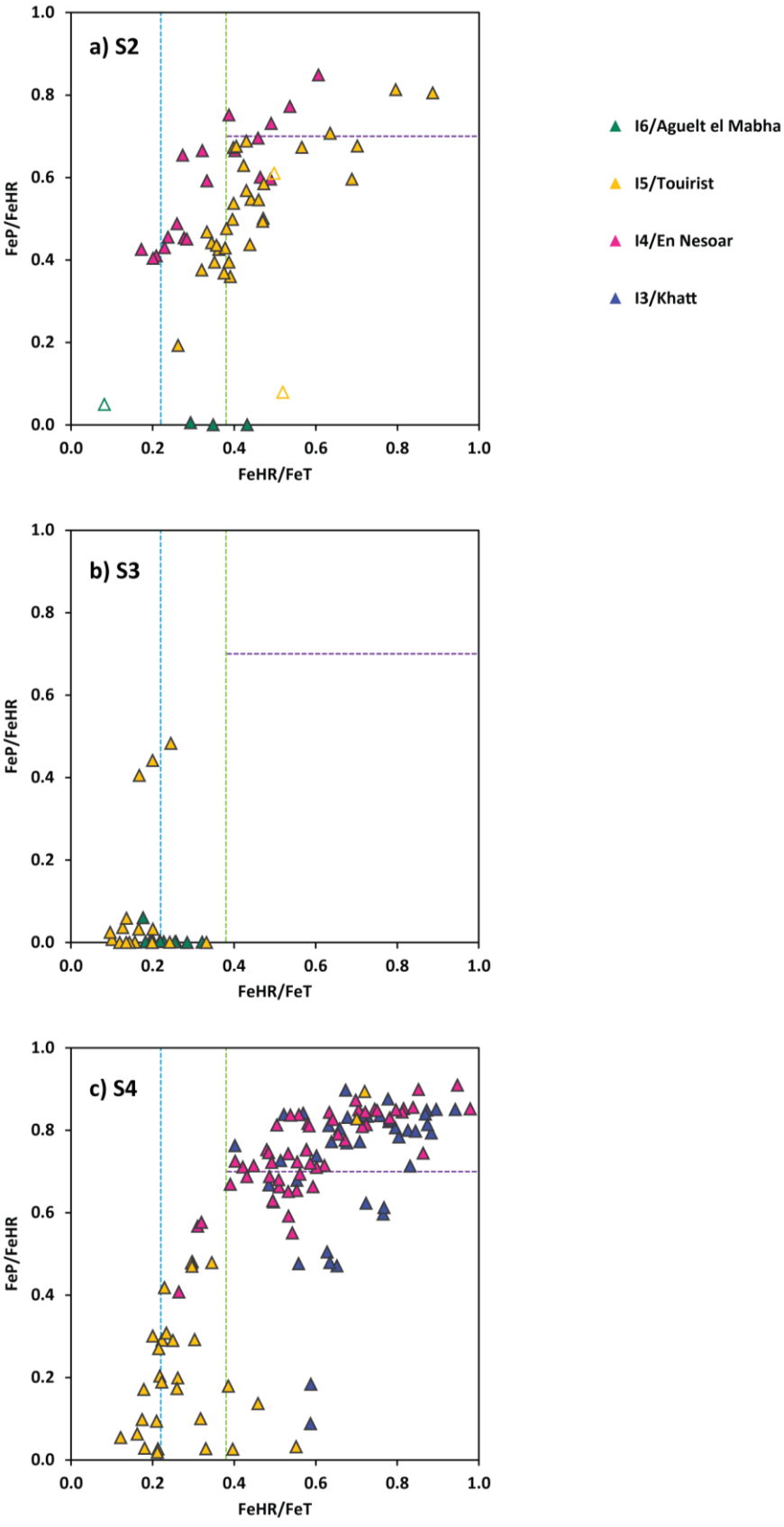
a) S2
b) S3
c) S4
FeP/FeHR
FeHR/FeT
0.0
0.2
0.4
0.6
0.8
1.0
I6/Aguelt el Mabha
I5/Touirist
I4/En Nesoar
I3/Khatt

Figure 3.17 FeP/FeHR verses FeHR/FeT plotted by formation Open triangles indicate carbonate-rich samples.

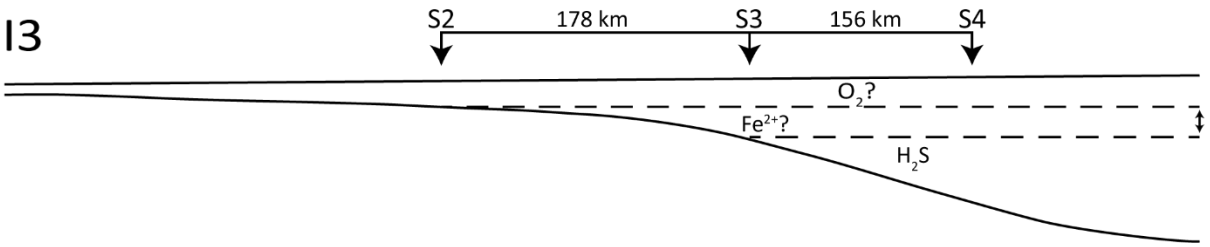
I3
S2
178 km
S3
156 km
S4
O2?
Fe2+?
H2S

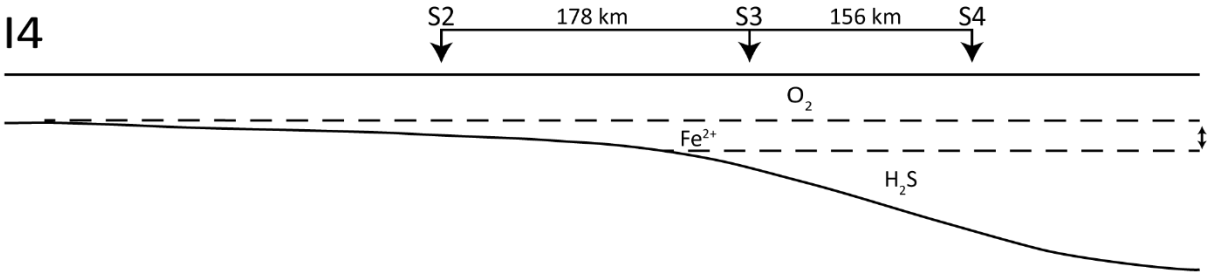
I4
S2
178 km
S3
156 km
S4
O2
Fe2+
H2S

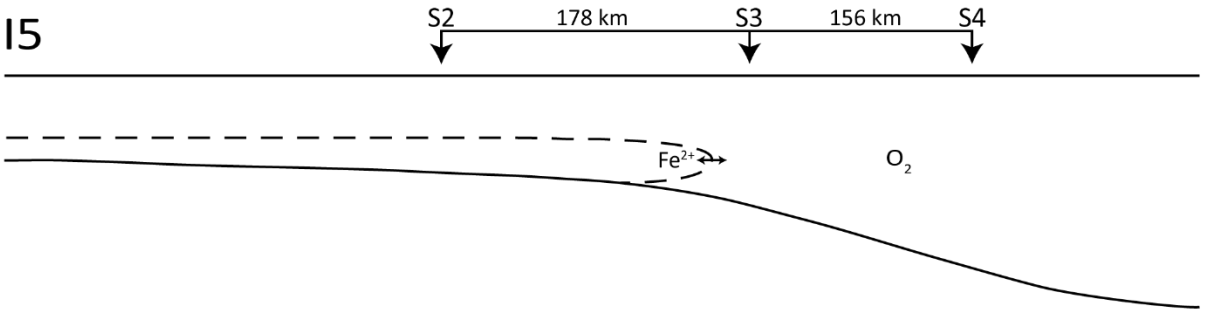
I5
S2
178 km
S3
156 km
S4
Fe2+
O2

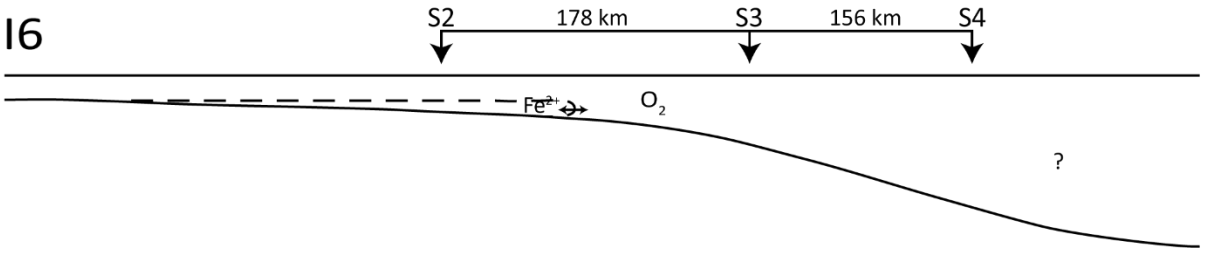
I6
S2
178 km
S3
156 km
S4
Fe2+
O2
?

Figure 3.18 Redox structure inferred for each formation sampled, using additional data from Beghin et al (2017a). Note that vertical scale is exaggerated compared to horizontal scale (the greatest estimated depth for the Atar Group being 50 – 100m below wave base (Bertrand-Sarfati and Moussine-Pouchkine, 1988)).

3.4 Conclusions

Reconstruction of redox conditions using the FeHR/FeT and FeP/FeHR indicators, supported by Fe/Al, S isotope and Mn, Mo and V concentration data, as recorded in 3 cores from the Mesoproterozoic Taoudeni Basin, suggests that redox conditions varied both spatially and temporally. Despite increasing water depth, an initially highly reducing sulphidic basin became largely oxygenated over time, with the exception of an oxygen minimum zone in shallower waters associated with high organic carbon fluxes. Following a drop in sea level, the oxygen minimum zone likely decreased in size.

Chapter 4

Phosphorus cycling in a Late Mesoproterozoic sea

4.1 Introduction

This chapter will examine the cycling of phosphorus, a key nutrient to life on Earth and thought to be the limiting factor in primary production over geological time scales (Tyrrell, 1999), thus imparting a possible major control on the chemical evolution of the biosphere. Research in recent years has shown that whether P is retained in sediment or regenerated to the water column (and therefore available for further organic matter production) can depend on local redox conditions, while local redox conditions are in turn (at least in part) influenced by organic matter availability (Ingall et al., 1993, Ingall and Jahnke, 1994). Thus, the interplay between P cycling and redox conditions may strongly influence oxygen availability and hence the habitability of the biosphere (Van Cappellen and Ingall, 1994, 1996).

In this chapter, overall P concentrations will be compared for different redox conditions and locations within the Taoudeni Basin, normalising to Al to take account of widely varying carbonate and organic carbon contents. Inferences about P cycling between the water column and sediment in different parts of the basin, and at different times will be made by looking at ratios of P to Al, and to TOC. Through the utilisation of a P speciation technique the forms in which P is stored in the rock, and in what forms it was likely delivered to the precursory sediment, will be considered.

4.2 Results

4.2.1 Total Phosphorus

Total P (plus TOC and Al) averages for each core are presented in Table 4.1. Total P varies over two orders of magnitude, ranging from 68 to 8915 ppm. Only five samples have P

concentrations greater than 1000 ppm, while the vast majority are depleted in P relative to average shale (Turekian and Wedepohl, 1961), as can be seen in figures 4.1 - 4.3.

In S2 total P ranges from 187 to 1247 ppm, with an overall average of 433 ± 249 ppm. The greatest variability is found in the Touirist (I5) Formation, with a mean of 525 ± 281 ppm. While a number of samples in the Touirist (I5) Formation have P_{total} > 500 ppm, only one sample in the En Nesoar (I4) Formation does, giving an average for this formation of 311 ± 103 ppm. The four samples from the Aguelt el Mabha (I6) Formation were all at the lower end of the range for this core, with an average of 246 ± 44 ppm. When split by redox, ferruginous samples have the highest average P_{total} but show a very similar range to euxinic samples. Of the two samples with P_{total} > 1000, one is ferruginous, the other euxinic. All the oxic and equivocal samples fall within this range, with similar averages for oxic, equivocal and euxinic samples. Only a few samples, all found in the Touirist (I5) Formation, have P_{total} greater than average shale – the majority of these are ferruginous, along with one euxinic and one equivocal, but likely ferruginous sample.

All samples from S3 fall below the total P concentration for average shale, with an overall average of 334 ± 106 ppm. Greater variability is seen in the Tourist (I5) Formation, which has an average of 397 ± 93 ppm. With an average of 242 ± 22, P_{total} for the Aguelt el Mabha (I6) Formation in S3 is very similar to the same formation in S2. All of these samples are oxic or equivocal, with the equivocal samples likely also deposited under an oxygenated water column (see discussion in Chapter 3).

The overall average P_{total} for S4 is 374 ± 947 ppm, suggesting rather more variability than in S2 (or, indeed, S3). However, inspection of the Total P plots suggests that variability is actually much more restrained in S4 when compared to the Touirist (I5) Formation in S2, with only occasional extreme values of P_{total} bringing the mean and standard deviation up (removing the three samples over 1000 ppm gives a mean of 244 ± 60 ppm). Only three samples, one from each of the three sampled formations, have P_{total} > 1000 ppm. All other samples have P_{total} lower than average shale. The bulk of the samples in all three formations (I3, I4 and I5) fall within the range 175 to 275 ppm, with an overall range of 68 to 8916 ppm. Averages are 259 ± 74,

229 ± 56 and 252 ± 38 ppm for the I3, I4 and I5 Formations respectively (excluding extreme values – see Table 4.1).

Core	Formation	TOC (wt%)	Al (wt%)	P_{total} (ppm)
S2	Aguelt El Mabha	0.04 ± 0.01	5.98 ± 1.94	246 ± 44
	Touirist	10.27 ± 8.81	9.91 ± 1.86	525 ± 281
	En Nesoar	6.87 ± 4.84	10.59 ± 1.32	311 ± 103
S3	Aguelt El Mabha	0.10 ± 0.08	9.74 ± 0.93	242 ± 22
	Touirist	0.17 ± 0.21	9.96 ± 2.57	397 ± 93
S4	I5	0.56 ± 0.41	13.09 ±1.76	252 ± 38[a]
	I4	1.02 ± 0.26	12.09 ± 1.89	229 ± 56[b]
	I3	0.75 ± 0.16	13.77 ± 1.30	259 ± 74[c]

Table 4.1 Average TOC, Al and P_{total} concentration (mean ± 1 SD) for each core, by formation. Some anomalous results are excluded from the averages and standard deviations: [a] excludes S4 79.95, 8916 ppm; [b] excludes S4 136.46, 6173 ppm; [c] excludes S4 163.22, 1853 ppm.

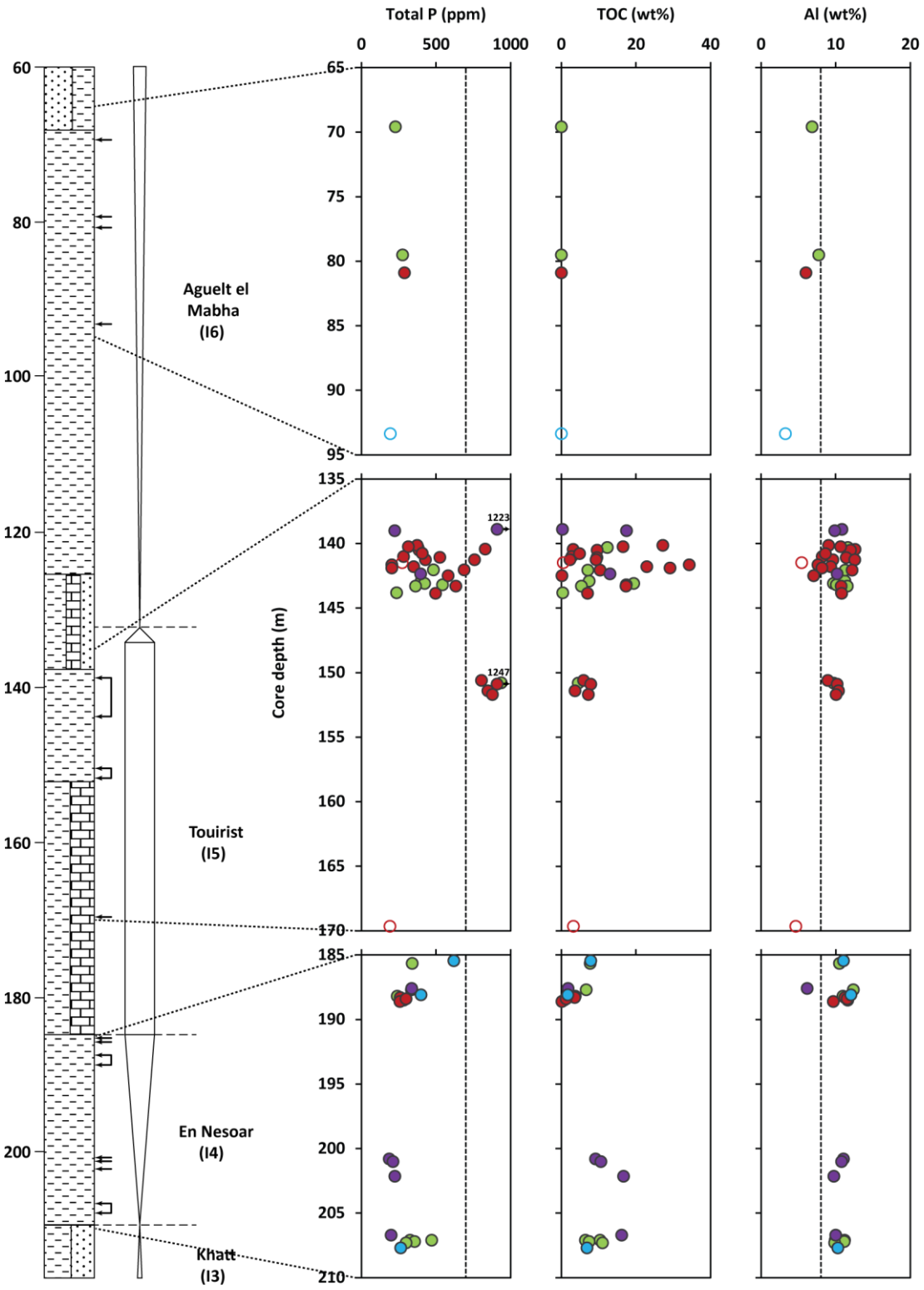
Total P (ppm)
TOC (wt%)
Al (wt%)
Core depth (m)
Aguelt el Mabha (I6)
Touirist (I5)
En Nesoar (I4)
Khatt (I3)
1223
1247

Figure 4.1 Depth plots showing total P, TOC and Al concentratios in S2. Dotted lines indicate average shale values (Turekian and Wedepohl, 1961). Samples are colour coded by redox, with blue for oxic, red for ferruginous, purple for euxinic and green for equivocal samples. Open circles indicate carbonate-rich samples.

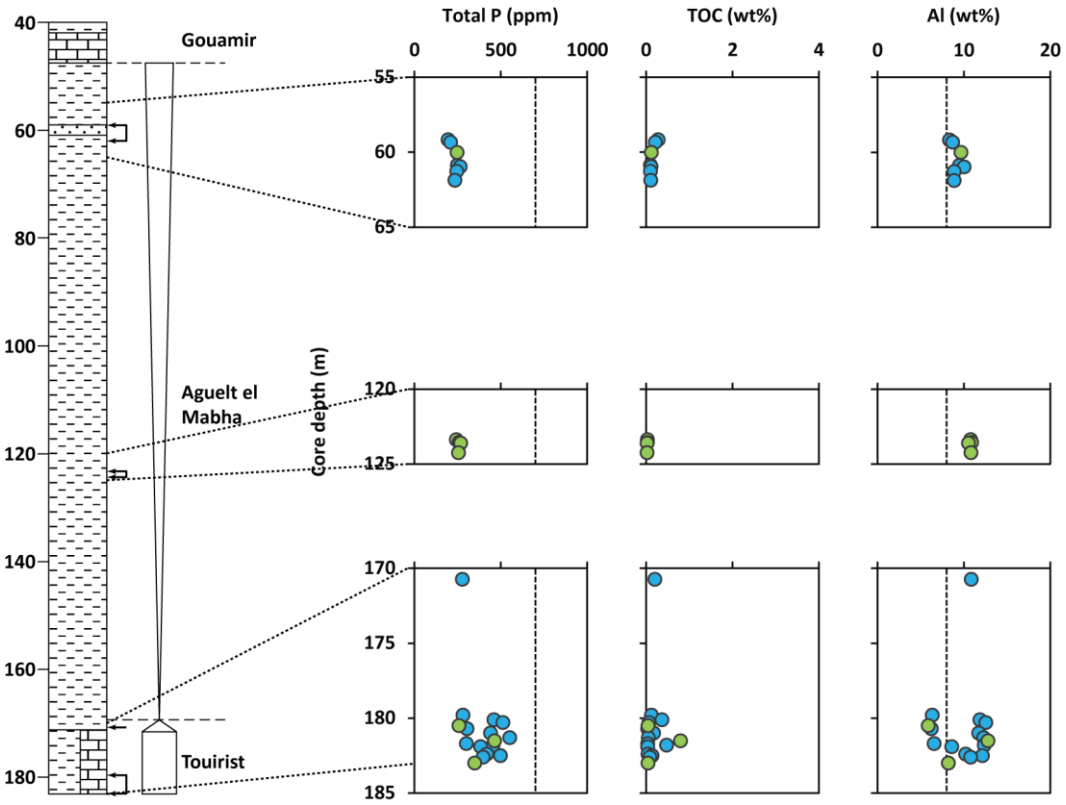

Figure 4.2 Depth plots showing total P, TOC and Al concentratios in S3. Dotted lines indicate average shale values (Turekian and Wedepohl, 1961). Samples are colour coded by redox, with blue for oxic and green for equivocal samples.

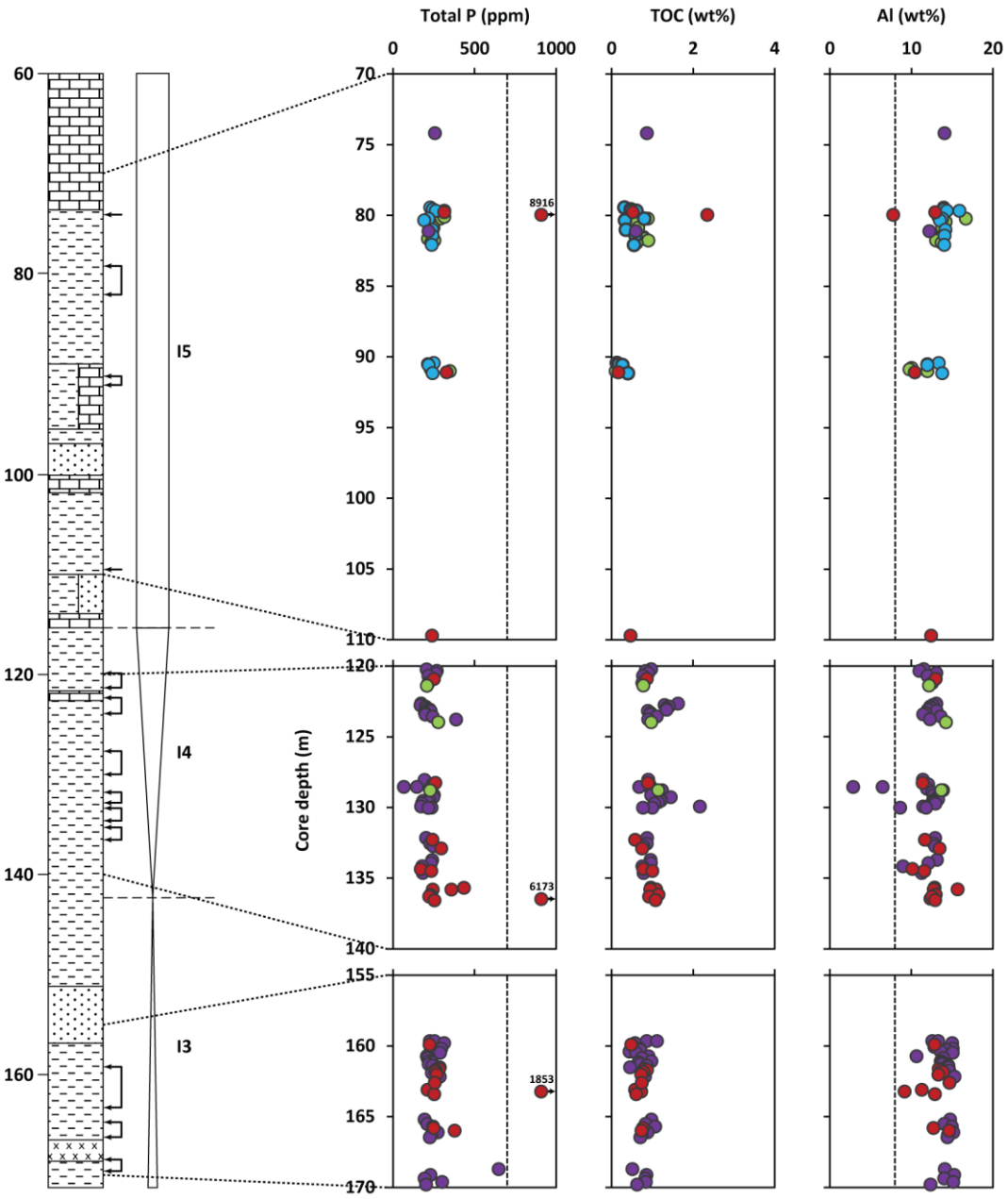

Figure 4.3 Depth plots showing total P, TOC and Al concentratios in S4. Dotted lines indicate average shale values (Turekian and Wedepohl, 1961). Samples are colour coded by redox, with blue for oxic, red for ferruginous, purple for euxinic and green for equivocal samples.

4.2.2 Aluminium

Although Al has already been discussed in Chapter 3, it will briefly be mentioned here too. On average, Al concentrations are greatest in S4, with means of 13.77 ± 1.30, 12.09 ± 1.89 and

13.09 ± 1.76 wt% for the I3, I4 and I5 formations respectively. Samples from S4 also show the greatest range in Al contents, from 2.87 wt% in I4 to 16.68 wt% in I5. Figure 4.3 suggests that, on the whole, Al concentrations are slightly lower in the I4 Formation and the lower I5 Formation than in the I3 Formation or higher up in the I5 Formation, but almost all samples have Al concentrations 2 - 6% greater than average shale.

Except for in the Aguelt el Mabha (I6) Formation, most samples from S2 have Al concentrations greater than average shale, with means of 10.59 ± 1.32, 9.91 ± 1.8 and 5.98 ± 1.94 wt% for the En Nesoar (I4), Touirist (I5) and Aguelt el Mabha (I6) formations respectively. Averages for various redox conditions vary over less than a percent, except for the equivocal group, which has the highest mean (10.46 ± 1.38 wt%).

In S3, the mean concentration for the Touirist (I5) Formation is 9.96 ± 2.57 wt%, while for the Aguelt el Mabha (I6) Formation it is 9.74 ± 0.93 wt%, which doesn't suggest the same drop in Al concentrations as seen between these two formations in S2. However, Figure 4.3 shows that there is a split in Al concentrations in the Touirist (I5) Formation (likely reflecting varying carbonate contents), with values in the Aguelt el Mabha (I6) Formation being intermediate, and just above average shale. Variation in Al concentration seems to parallel total P in S3.

4.2.3 Organic carbon

The highest concentrations of organic carbon are found in S2, with averages of 6.87 ± 4.84 and 10.27 ± 8.81 wt% in the En Nesoar (I4) and Touirist (I5) formations, and maximums of 16.70 and 34.30 wt% respectively. Figure 4.1 suggests a slight shift in TOC concentrations in the En Nesoar (I4) Formation, with a range of 6.50 to 16.70 wt% in the lower part, and 0.14 to 7.90 wt% in the upper part. High TOC is found in samples deposited under ferruginous as well as euxinic conditions – indeed, the four highest TOC concentrations are found in ferruginous samples in the Touirist (I5) Formation. There are also a couple of apparently oxic samples with TOC contents exceeding 5 wt% in the En Nesoar (I4) Formation, while the other oxic sample in that formation has a TOC contents within the range of the stratigraphically close by anoxic and equivocal samples. There are no definitively oxic samples in the more variable Touirist (I5)

Formation to compare with anoxic samples. Equivocal samples are found through most of the range of the anoxic samples, except for the four highest. In contrast to the lower two formations, the four samples from the Aguelt el Mabha Formation are very low in TOC, with an average of 0.04 ± 0.01 wt%. Across the core, on average TOC concentrations are highest under euxinic conditions, but only just, with a mean of 10.67 ± 6.63 wt% for euxinic samples and 9.22 ± 9.62 wt% for ferruginous samples. The four oxic samples meanwhile have an average of 4.14 ± 3.84 wt%.

TOC contents are low in S3, with means of 0.17 ± 0.21 and 0.10 ± 0.08 for the Touirist (I5) and Aguelt el Mabha (I6) formations respectively. Although the Tourist (I5) Formation has a slightly higher average, this is because of just three samples with TOC > 0.3 wt%, the maximum being 0.80 wt%, as opposed to a maximum of 0.28 wt% in the Aguelt el Mabha (I6) Formation. There are no clearly anoxic samples in either formation, and results discussed in Chapter 3 suggest that the equivocal samples are likely oxic.

Concentrations of organic C in S4 are greater than in S3, with several, mostly in the I4 Formation, exceeding 1 wt%. However, with a maximum of 2.35 wt % (in I5) measured in this study, S4 has far less organic C than S2. Averages for the I3, I4 and I5 formations are 0.75 ± 0.16, 1.02 ± 0.26 and 0.56 ± 0.41 wt% respectively. Because most of the samples analysed from I5 are oxic or equivocal, while almost all samples from I4 and I3 are anoxic, it is difficult to directly compare TOC in oxic verses anoxic samples. It is however noticeable that average TOC roughly halves going from I4 to I5. Across the whole core, oxic samples have the lowest mean TOC contents, at 0.42 ± 0.19 wt%. Euxinic samples have the highest mean, of 0.92 ± 0.28 wt%, but the average for ferruginous samples is not much lower, at 0.84 ± 0.37 wt%.

4.2.4 Phosphorus speciation

4.2.4.1 P_{Fe}

In all samples, very little Fe oxide associated P was extracted. In a number of samples P_{Fe} was below detection, and in most of the remaining samples concentrations recorded are very close

to the limit of detection (0.2 mg/L, samples analysed at x10 dilution) for the ICP-OES (note - results for this pool were obtained by a different analytical method to the other four pools, owing to interference by the extractant for P_{Fe} with the photometric method used to quantify the other pools, hence a 10 time dilution was required). The maximum, of 14 ppm, is found in an oxic sample from the I5 Formation of S4, closely followed by 13 ppm for a euxinic sample from the Touirist (I5) Formation of S2. Averages for each core by formation and by redox conditions are shown in tables 4.2 and 4.3, but P_{Fe} is insignificant in all samples, meaning that comparisons between cores, formations and redox states is of limited value.

4.2.4.2 P_{auth}

P_{auth} is most variable and generally higher in S2, with means of 54 ± 59, 154 ± 92 and 121 ± 25 ppm for the En Nesoar (I4), Touirist (I5) and Aguelt el Mabha (I6) formations respectively, and a range of 10 - 342 ppm. The equivalent formations sampled in S3 have concentrations somewhat lower, with means of 56 ± 26 and 30 ± 5 ppm for the Touirist (I5) and Aguelt el Mabha (I6) formations and a range of 24 - 115 ppm. Likewise, in S4 the I4 and I5 formations average at 24 ± 6 and 42 ± 14 ppm, while I3 has a mean of 30 ± 33 ppm. The overall range for S4 is 11 - 157 ppm. An increase in average P_{auth} contents going from the En Nesoar/I4 to the Touirist/I5 Formation is seen in both S2 and S4, while a decrease going from the Touirist/I5 to the Aguelt el Mabha/I6 Formation is seen in both S2 and S3. There is also a decrease in average P_{auth} concentrations going from I3 to I4 in S4, although the means are the same within 1 standard deviation.

No obvious pattern relating P_{auth} concentrations and redox conditions is apparent. An overall average of 136 ± 89 ppm for ferruginous samples in S2, in contrast to 93 ± 65 ppm for oxic samples and 77 ± 114 for euxinic samples, suggests that more P_{auth} was formed or retained in sediments under ferruginous conditions, but these averages include the Touirist (I5) Formation, where P_{auth} is highest (maximum 342 ppm), and nearly all samples are ferruginous. In the En Nesoar (I4) Formation in S2 (Figure 4.4), the two ferruginous samples are lower in P_{auth} than surrounding oxic samples, and in S4, oxic samples have the highest concentration of P_{auth} on

average, but within 1 standard deviation of the means for ferruginous and euxinic samples (Table 4.3). In both S2 and S4, P_{auth} is on average lowest in euxinic samples.

4.2.4.3 P_{det}

As with P_{auth}, the highest concentrations and greatest variability in P_{det} is generally seen in the Touirist (I5) Formation in S2, with the notable exception of the 1943 ppm found in one sample from the I3 Formation in S4. On the whole, P_{det} is somewhat lower in S4 than in S2 or S3, with means of 27 ± 52 (not including the previously mentioned sample), 6.1 ± 5.8 and 24 ± 23 ppm for the I3, I4 and I5 formations respectively, in contrast to means of 143 ± 48 and 58 ± 61 ppm for the Touirist (I5) and Aguelt el Mabha (I6) formations in S3 and 60 ± 44, 195 ± 132 and 72 ± 11 ppm for the En Nesoar (I4), Touirist (I5) and Aguelt el Mabha (I6) formations in S2. Again, as for P_{auth}, a decrease in P_{det} concentrations going from the I3 Formation to the I4 Formation, an increase from the En Nesoar/I4 Formation to the Touirist/I5 Formation, and a decrease from the Touirist/ I5 Formation to the Aguelt el Mabha Formation, is apparent.

Averages for samples by redox state in each core suggest that P_{det} is highest in sediments which were deposited under ferruginous conditions (Table 4.3), while there is little difference between euxinic and oxic samples within the same core. Figures 4.4 and 4.6 largely support this, although the two ferruginous samples in the En Nesoar (I4) Formation have very similar concentrations to stratigraphically close oxic samples – the higher overall average for ferruginous samples is heavily influenced by ferruginous samples from the Touirist (I5) Formation, where there are no oxic samples with which to compare. The two highest values for P_{det}, at 1943 and 474 ppm, are from ferruginous samples, and in the I5 Formation in S4 two of the three ferruginous samples have P_{det} contents higher than stratigraphically nearby oxic and euxinic samples.

4.2.4.4 P_{org}

In contrast to P_{auth} and P_{det}, P_{org} is highest in S4, with averages of 137 ± 26, 118 ± 26 and 139 ± 18 ppm for the I3, I4 and I5 formations respectively, and a range of 78 - 195 ppm. In S3

means are 97 ± 34 and 86 ± 14 ppm for the Touirist (I5) and Aguelt el Mabha (I6) formations, with a range of 50 – 180 ppm, while in S2 averages for P_{org} are 103 ± 12, 106 ± 25 and 36 ± 21 ppm for the En Nesoar (I4), Touirist (I5) and Aguelt el Mabha (I6) formations, with a range of 21 – 141 ppm. Similarly to P_{auth} and P_{det}, the averages suggest a decrease in P_{org} concentrations going from the I3 Formation to the I4 Formation, an increase from the En Nesoar/I4 Formation to the Touirist/I5 Formation, and a decrease from the Touirist/ I5 Formation to the Aguelt el Mabha Formation (although the differences are small in some cases).

The results do not indicate any clear relationship between P_{org} concentrations and redox conditions. Average P_{org} in S2 is highest for euxinic samples and lowest for oxic samples; the opposite is the case in S4 (see Table 4.3). Figures 4.4 and 4.6 suggest that within formations, P_{org} is similar for all redox conditions.

4.3.4.5 P_{res}

With the exception of P_{Fe}, P_{res} is on average the smallest pool in S2 and S3 – it does however constitute a significant pool in almost all samples, and is on average the second largest pool in S4. P_{res} is also overall the least variable pool except for P_{Fe}, with a range of 10 – 119 ppm. Although the maximum is found in the Touirist Formation of S2, P_{res} is on average highest in S4, with means of 59 ± 13, 57 ± 16 and 56 ± 10 ppm for the I3, I4 and I5 formations respectively. Averages in S3 are a bit lower, at 35 ± 12 and 46 ± 5 ppm for the Touirist (I5) and Aguelt el Mabha (I6) formations. Means for S2 are 52 ± 4.3, 57 ± 25 and 19 ± 13 ppm for the En Nesoar (I4), Touirist (I5) and Aguelt el Mabha (I6) formations respectively.

As for P_{org}, the results do not suggest a link between P_{res} contents and redox conditions. Figures 4.4 and 4.6 show that within formations, P_{res} is similar for all redox conditions – indeed, the two formations where all three redox conditions have been identified (En Nesoar (I4) in S2 and I5 in S4) are the least variable in P_{res}. Averages are very similar for oxic, ferruginous and euxinic samples in S4 (56 ± 6.2, 56 ± 15 and 59 ± 14 ppm respectively).

Core	Formation	P_{Fe} ppm	P_{auth} ppm	P_{det} ppm	P_{org} ppm	P_{res} ppm
S2	Aguelt El Mabha	4.5 ± 4.5	121 ± 25	72 ± 11	36 ± 21	19 ± 13
	Touirist	2.0 ± 3.5	154 ± 92	195 ± 132	106 ± 25	57 ± 25
	En Nesoar	1.2 ± 2.1	54 ± 59	60 ± 44	103 ± 12	52 ± 4.3
S3	Aguelt El Mabha	0.5 ± 0.8	30 ± 5.4	58 ± 61	86 ± 14	46 ± 4.8
	Touirist	2.1 ± 3.2	56 ± 26	143 ± 48	97 ± 34	35 ± 12
S4	I5	2.9 ± 4.2	42 ± 14	24 ± 23	139 ± 18	56 ± 10
	I4	0.5 ± 0.6	24 ± 6	6.1 ± 5.8	118 ± 26	57 ± 16
	I3	1.4 ± 2.3	30 ± 33	27 ± 52 [a]	137 ± 26	59 ± 13

Table 4.2 Average TOC, Al and P_{total} concentration (mean ± 1 SD) for each core, by formation. Some anomalous results are excluded from the averages and standard deviations: [a] excludes S4 163.22, 1943 ppm.

Core	Redox	P_{Fe} ppm	P_{auth} ppm	P_{det} ppm	P_{org} ppm	P_{res} ppm
S2	Oxic	1.5 ± 3.0	93 ± 65	90 ± 36	91 ± 35	45 ± 18
	Ferruginous	1.6 ± 2.3	136 ± 89	171 ± 119	101 ± 27	56 ± 25
	Euxinic	3.3 ± 5.3	77 ± 114	88 ± 164	107 ± 17	51 ± 10
S3	Oxic	1.5 ± 2.7	46 ± 24	111 ± 56	93 ± 28	39 ± 11
S4	Oxic	2.7 ± 4.3	43 ± 14	15 ± 8.8	147 ± 14	56 ± 6.2
	Ferruginous	1.4 ± 2.5	33 ± 12	34 ± 23 [a]	132 ± 30	56 ± 15
	Euxinic	1.2 ± 2.3	27 ± 27	14 ± 41	126 ± 24	59 ± 14

Table 4.3 Average P pool concentration (mean ± 1 SD) for each core, by redox conditions. Some anomalous results are excluded from the averages and standard deviations: [a] excludes S4 163.22, 1943 ppm.

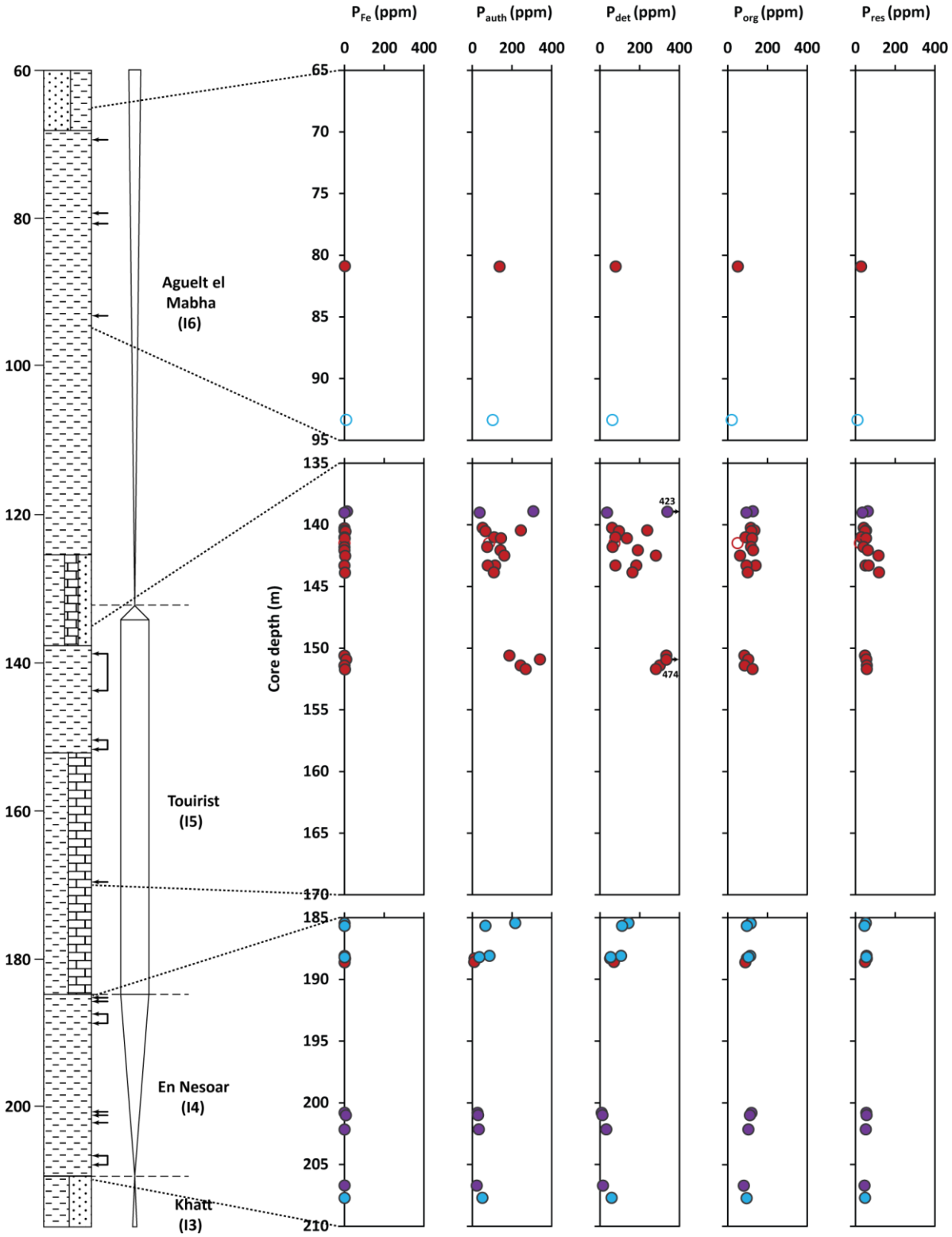
P_Fe (ppm)
P_auth (ppm)
P_det (ppm)
P_org (ppm)
P_res (ppm)
0 200 400
Core depth (m)
Aguelt el Mabha (I6)
Touirist (I5)
En Nesoar (I4)
Khatt (I3)
423
474

Figure 4.4 Depth plots showing sequentially extracted phosphorus pools in S2. Samples are colour coded by redox, with blue for oxic, red for ferruginous and purple for euxinic samples. Open circles indicate carbonate-rich samples.

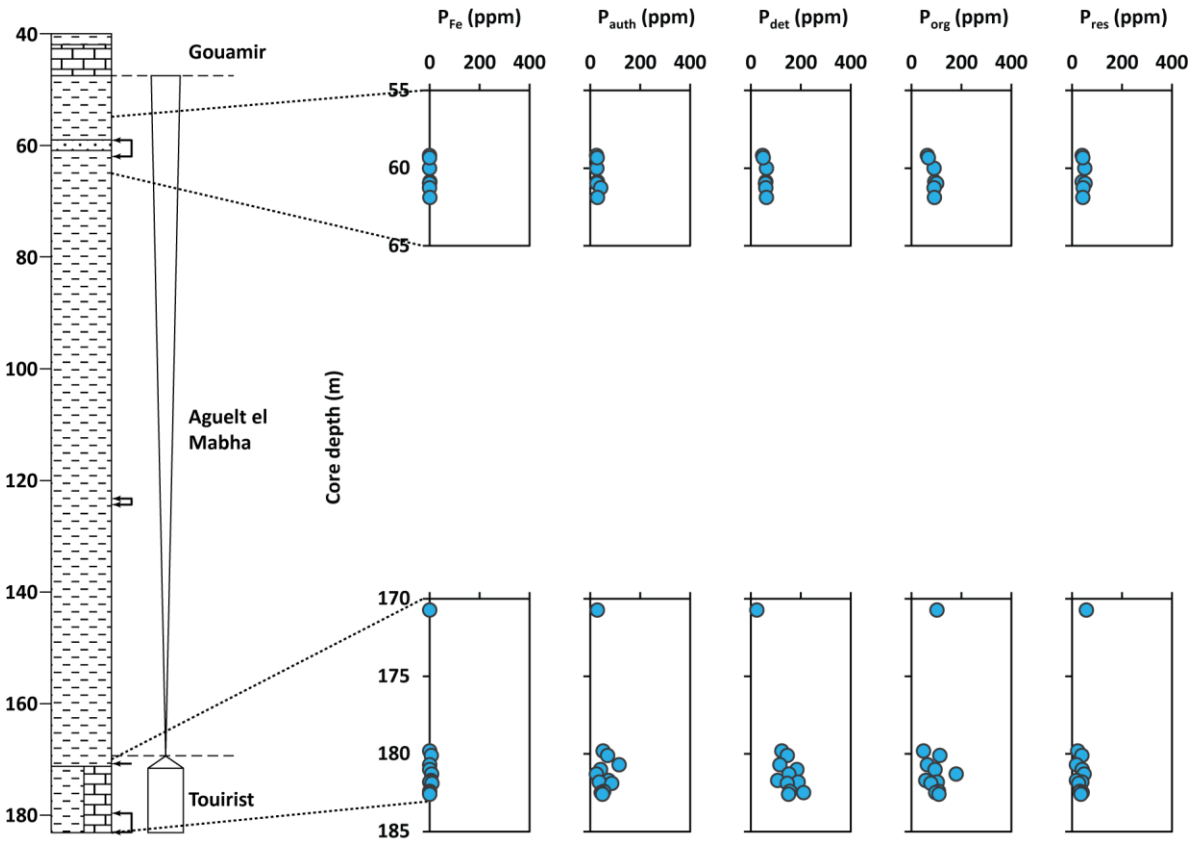

Figure 4.5 Depth plots showing sequentially extracted phosphorus pools in S3. Samples are colour coded by redox, with blue for oxic samples.

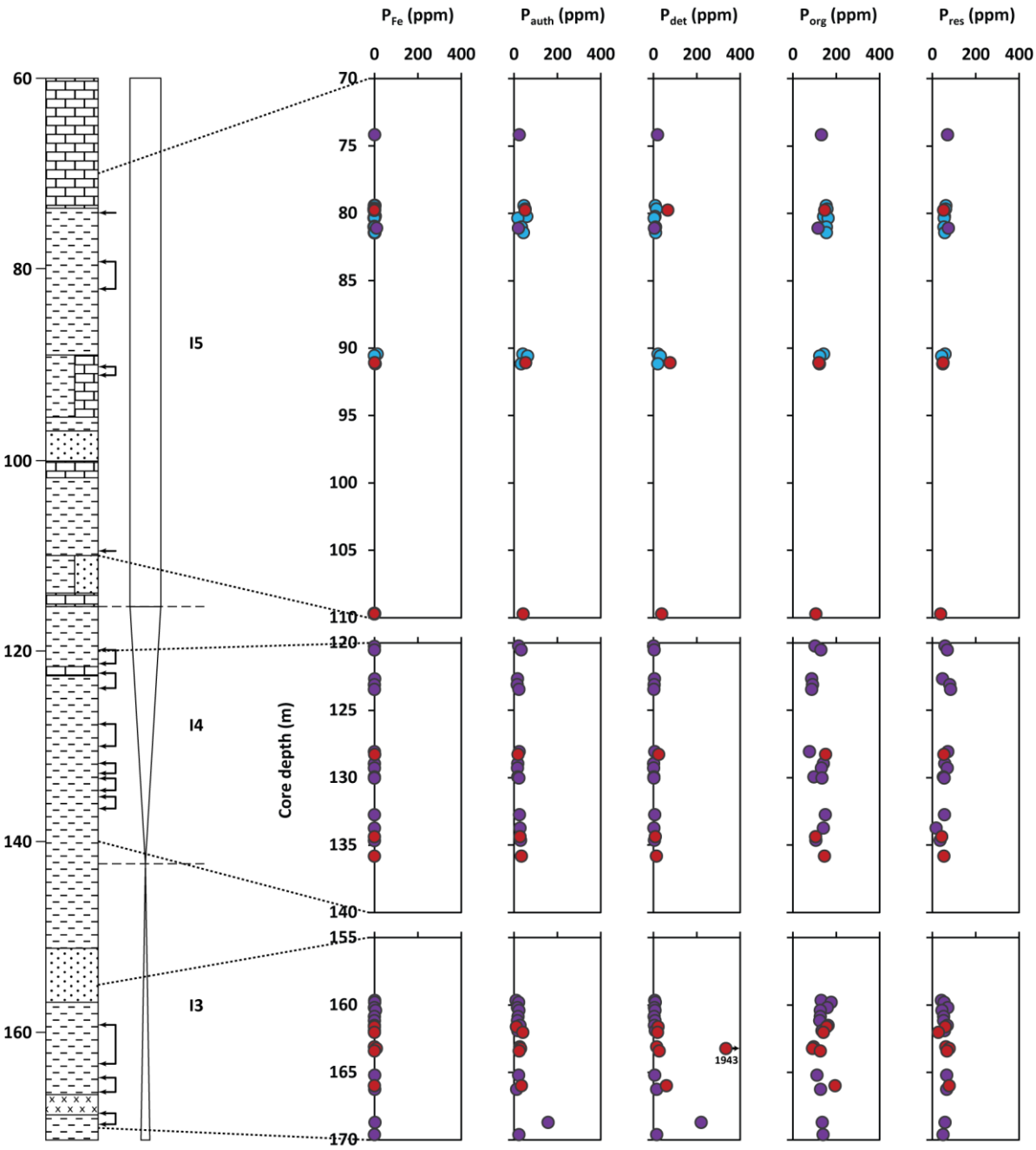

Figure 4.6 Depth plots showing sequentially extracted phosphorus pools in S4. Samples are colour coded by redox, with blue for oxic, red for ferruginous and purple for euxinic samples.

4.3 Discussion

4.3.1 Phosphorus pools

The results show that in all formations sampled from S4, and under oxic, ferruginous and euxinic conditions, P_{org} is the dominant P sink, accounting for, on average 55 ± 11 % of phosphorus sequentially extracted, with only two samples (both of which contain unusually high P_{det} concentrations for S4) falling below 40%. The second largest pool is generally P_{res} (24 ± 8 %), followed by P_{auth} (12 ± 5 %), with P_{det} mostly being the smallest pool (8 ± 1 %) except for P_{Fe}.

Results are more mixed for S2 and S3. In S3, P_{org} is the largest pool in the Aguelt el Mabha Formation, constituting 39 ± 3 % of P_{sum}, followed by P_{det} (26 ± 1 % of P_{sum}), P_{res} (21 ± 2 %) and P_{auth} (14 ± 2 %). The Touirist Formation in S3 is rather more variable, but on average, P_{det} is the largest pool, forming 42 ± 11% of P_{sum}, followed by P_{org} (29 ± 11 %), then P_{auth} (17 ± 9 %). This change in proportions is mainly a result of higher concentrations of P_{auth} and P_{det} in the Touirist Formation relative to the Aguelt el Mabha Formation in S3.

In S2, P_{org} is the dominant pool in the En Nesoar Formation, but only the third largest pool in the Touirist Formation, constituting 41 ± 10 % and 25 ± 11 % of P_{sum} respectively. However, in terms of whole rock concentrations, P_{org} is actually very similar in these two formations, the main difference between the two formations being an increase in P_{auth} and P_{det} contributions to P_{sum} in the Touirist Formation. Consequently, in the Touirist Formation, P_{auth} and P_{det} constitute 29 ± 7 and 34 ± 10 % of P_{sum} respectively, as opposed to 17 ± 10 and 20 ± 11 % in the En Nesoar Formation. This may be strongly influenced by redox – the samples from the Touirist Formation are predominantly ferruginous, while the En Nesoar Formation is mostly oxic or euxinic. Noticeably, P_{auth} and P_{det} are lower in euxinic than in oxic samples in this formation. Only two samples were analysed from the Aguelt el Mabha Formation for S2 – one oxic, one ferruginous – but they showed very similar results, with P_{auth} being the largest pool, forming 48 ± 3 % of P_{sum}, followed by 29 ± 3 % for P_{det} and 14 ± 5 % for P_{org}. When split by redox, P_{org} is the dominant pool under euxinic conditions (44 ± 15 % of P_{sum}), followed by P_{res} (21 ± 8 %),

P_{auth} (18 ± 8 %) and P_{det} (16 ± 15 %). Under oxic conditions, P_{org}, P_{auth} and P_{det} are fairly equal, at 29 ± 11 %, 28 ± 14 % and 28 ± 5 % of P_{sum} respectively. P_{det} is the largest pool under ferruginous conditions, being 33 ± 9 % of P_{sum}, followed by P_{auth} (27 ± 11 %) and P_{org} (25 ± 11 %).

4.3.2 Reactive phosphorus

In the original sedex procedure developed by Ruttenberg (2003), P_{Fe}, P_{auth} and P_{org} constitute the reactive P pools buried in sediments. However, as discussed in the introduction, Creveling et al. (2014) have shown, through a combination of petrographic and geochemical techniques, that in very ancient rocks, the P_{auth} pool is only partially extracted in the Na acetate step, with the rest likely extracted in the step designed to quantify detrital phosphorus. It is possible, therefore, that in this study of billion year old rocks, the true reactive P contents of the samples analysed falls between P_{react} and $P_{react+det}$. Whilst the proportion of the extracted detrital P pool that is truly detrital cannot easily be quantified, it might be expected that a detrital P input would scale with aluminium contents, as Al is thought to be unreactive in a sedimentary context. Therefore, a good, positive correlation, or lack thereof, might indicate whether most of the P_{det} pool is truly detrital, or if part of it should actually be considered to have been bioavailable at the time of deposition.

Also to be taken into consideration in this study is the residual phosphorus, P_{res}, which was extracted in an additional step added on to the sequential phosphorus speciation procedure. Given the difficulty in extracting this portion of P, we assume that it represents particularly crystalline, unreactive P from detrital mineral inputs, and therefore forms part of the detrital phosphorus pool. Thus, the maximum value for detrital P would be $P_{det+res}$. However, if, as discussed above, some of the extracted P_{det} actually includes phosphorus that was, at the time of deposition, part of the authigenic P pool, the true detrital P content of these samples will fall between P_{res} and $P_{det+res}$.

In order to assess whether or not the sequentially extracted P_{det} pool truly represents the detrital P content in these samples, P_{sum}, P_{det}, P_{res} and $P_{det+res}$ were plotted against Al concentrations for

each core, by formation (figures 4.7 - 4.9). For S2, a fairly good correlation between P_{res} and Al is apparent for both the En Nesoar/I4 and Touirist/I5 formations, with R^2 values of 0.49 and 0.57 respectively (two samples, from depths of 142.5 and 143.86 m, are excluded from the line of best fit for the Touirist Formation as they appear on visual inspection to be somewhat anomalous – they are not excluded from the lines of best fit in the other plots as they do not appear to constitute a departure from a trend in those plots). As only two samples from the Aguelt el Mabha/I6 Formation were analysed in the sequential P extraction, a correlation cannot be established, but both data points do lie close to the line of best fit for the underlying Touirist/I5 Formation. In contrast, there is a very poor correlation between P_{det} and Al, especially in the Touirist/I5 Formation. The correlation between Al and $P_{det+res}$, and P_{sum}, is also poor. This would suggest that, while P_{res} is likely of detrital origin, much of the P_{det} pool is actually not truly detrital, and should therefore be included in the reactive P pool when considering P cycling between the sediment and water column at the time of deposition.

Similarly in S3, good correlations between P_{res} and Al are evident in both the En Nesoar/I5 (the sample from 170.73m depth in S3 is excluded from the line of best fit as it shows a clear departure from the trend set by the other points, and is over 9 m above the others, which are all within three metres of one another) and Aguelt el Mabha/I6 formations. However, unlike in S2, Al also correlates well with P_{det}, with the best R^2 value for the Aguelt el Mabha/I6 Formation being for $P_{det+res}$ verses Al. It is therefore likely that the detrital pool for S3 is best estimated as $P_{det+res}$, while a contribution from P_{det} to P_{react} is not likely to be significant. It should be noted, however, that a good correlation also exists between P_{sum} and Al. As P_{sum} consists, on average, of roughly 50% $P_{det+res}$ in both formations, this correlation between P and Al clearly isn't simply a function of detrital mineral deposition.

Any sort of positive correlation between Al and supposedly detrital P completely breaks down in S4, with the best R^2 value (0.51) being for a line of best fit which suggests a negative correlation between P_{det} and Al and, in contrast to S2 and S3, there is a poor correlation between P_{res} and Al in all formations sampled (even when the sample from 163.22 m depth, which contains an exceptional amount of P_{det} in comparison to other samples in this study, is removed from the line of best fit). This could be a reflection of the fact that S4 is the most distal core. As

detrital P generally resides in relatively dense igneous and metamorphic minerals, it might be expected that such P would be deposited in more proximal locations, while Al rich clay minerals would have remained suspended in the water column longer, to be deposited more distally – it was earlier noted that, on average, Al concentrations are higher in S4 than in S3 or S2. However, the R^2 value is reduced to 0.20 if the sample with the lowest Al/ highest P_{det} concentrations is removed, and while the Al content of samples from S4 is generally higher than in S2, P_{res} content is similar in the two cores in equivalent formations. A lack of correlation between P_{res} and Al means that it is not obvious that P_{res} is detrital. P_{det} is generally low in S4, so, even if part of this pool belongs with P_{auth}, it would only constitute a minor contribution to P_{react}.

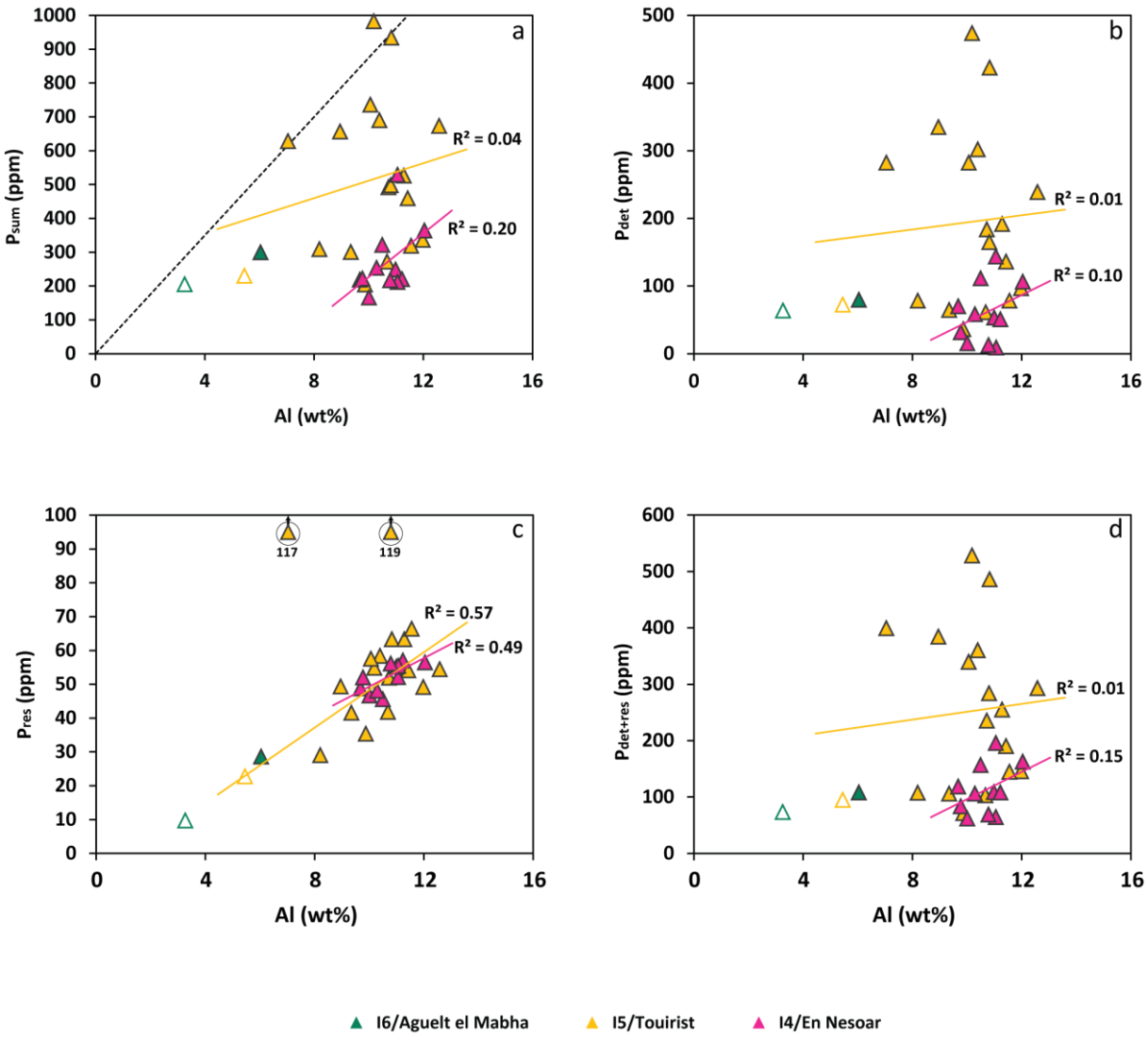

Figure 4.7 Plots of various P pools against Al contents for S2. Data points and lines of best fit are colour coded according to formation, with pink for the En Nesoar/I4 formation, yellow for the Touirist/I5 formation and green for the Aguelt el Mabha/I6 formation. Open triangles indicate carbonate-rich samples. The black dotted line on the first plot indicates average shale total P and Al. Circled points have been omitted from line of best fit calculations, as discussed in the text.

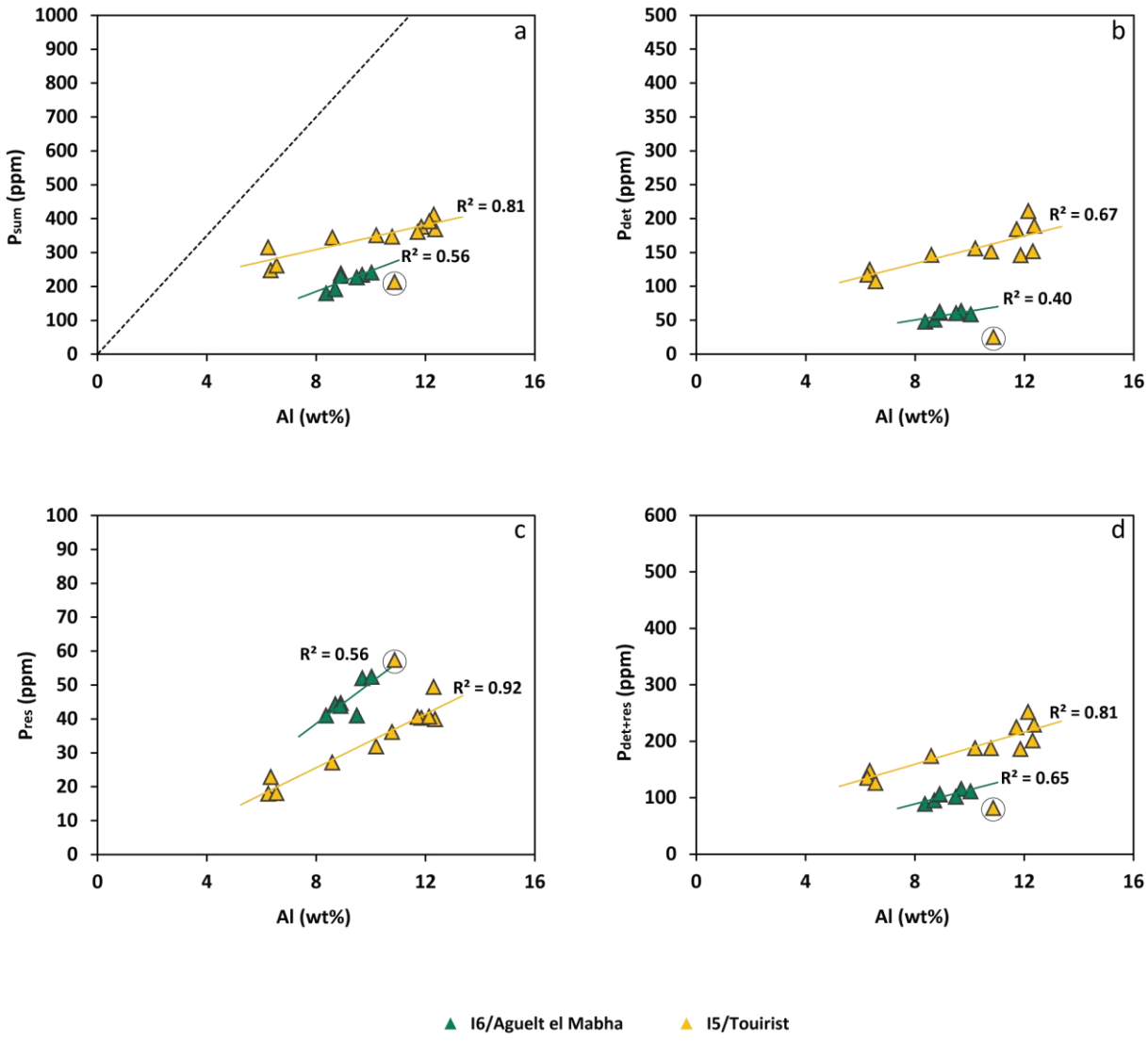

Figure 4.8 Plots of various P pools against Al contents for S3. Data points and lines of best fit are colour coded according to formation, with yellow for the Touirist/I5 formation and green for the Aguelt el Mabha/I6 formation. The black dotted line on the first plot indicates average shale total P and Al. Circled points have been omitted from line of best fit calculations, as discussed in the text.

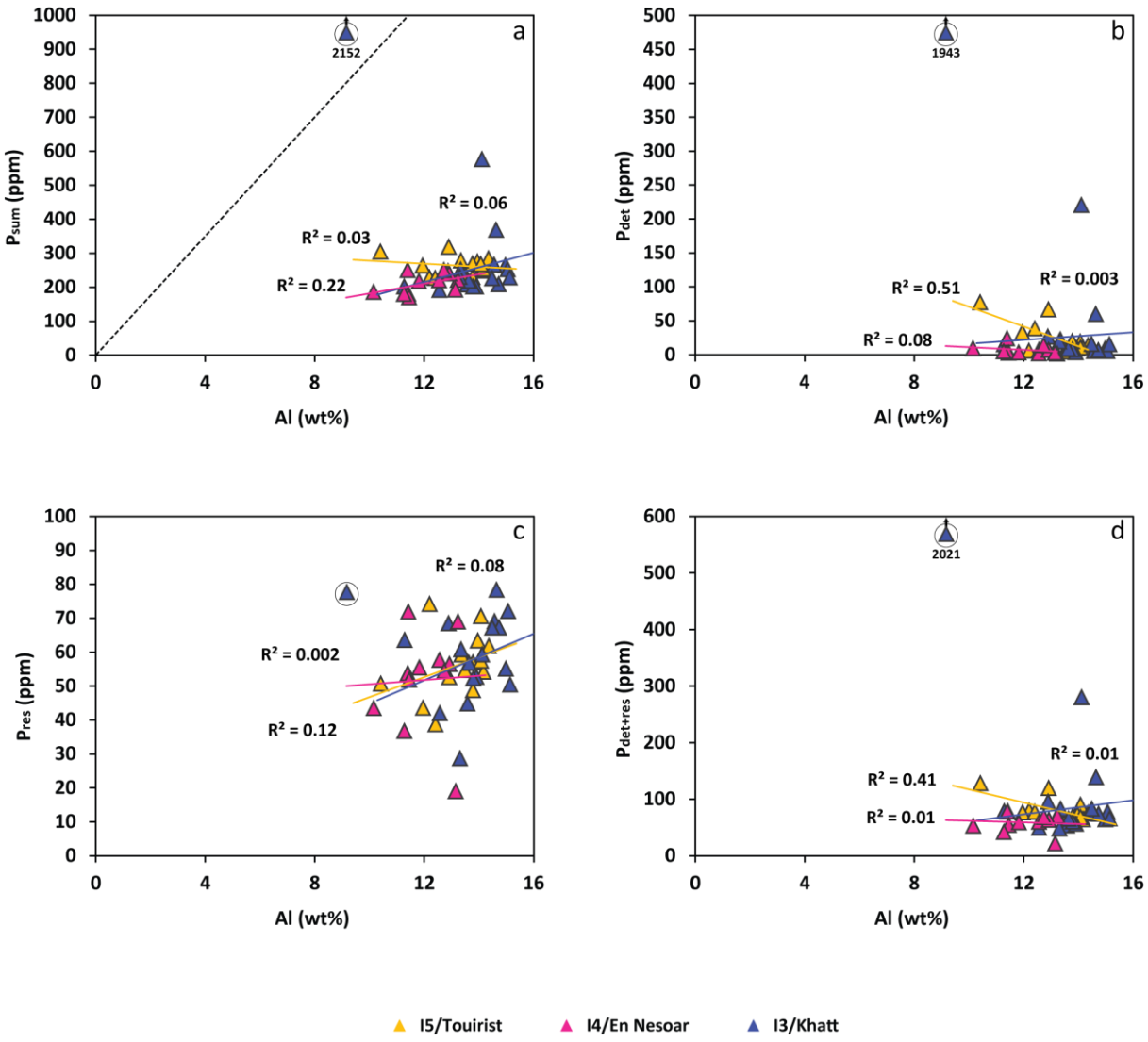

Figure 4.9 Plots of various P pools against Al contents for S4. Data points and lines of best fit are colour coded according to formation, with blue for the I3/Khatt formation, pink for the I4/En Nesoar formation and yellow for the I5/Touirist formation. The black dotted line on the first plot indicates average shale total P and Al. Circled points have been omitted from line of best fit calculations, as discussed in the text.

4.3.3 Phosphorus redox cycling

Figures 4.10 - 4.12 show TOC verses various P pools for the three cores, S2, S3 and S4, in the context of the Redfield ratio. Extensive research on the fate of organic matter in the ocean has shown that under certain conditions, phosphorus is preferentially released from organic matter compared to carbon, therefore making it available to fuel further primary productivity (Ingall et al., 1993, Ingall and Jahnke, 1994). Making the assumption that the original organic matter produced during photosynthesis would have had a molar TOC:P_{org} ratio close, on average, to 106:1, the level of phosphorus recycling taking place can be evaluated by comparing TOC:P_{org} ratios to the well-established Redfield ratio, with ratios above 106 implying preferential release of P from organic matter. However, because sink-switching may occur in the sediment, phosphorus originally delivered in organic matter may be retained in the sediment in authigenic minerals, rather than diffusing back into the water column. Consideration of only TOC:P_{org} ratios would therefore give a misleading impression of the extent to which P might have been made available to fuel further primary productivity (Anderson et al., 2001) It is therefore also useful to consider the whole reactive P pool in relation to TOC, which, in this study, likely also includes some of the P_{det} pool.

In S2, molar TOC:P_{org} ratios (1172 ± 840, 1553 ± 1298 and 3080 ± 1944 for oxic, ferruginous and euxinic samples respectively, maximum of 5154) which far exceed the Redfield ratio (106) in the majority of samples from all redox environments (Figure 4.10a) suggests extensive remobilisation of phosphorus from organic matter. Interestingly, although TOC is highly variable (0.00 – 1.91 mol/100g (to 2 dp; organic carbon was detectable in all samples)), P_{org} mostly falls in a rather narrow range (0.00026 – 0.00046 mol/100g). This narrow range for P_{org} is unlikely to be a detection issue. P_{org} was measured by UV/VIS which detects P concentrations on the order of 1 ppm. One possibility is that this narrow range in P_{org} is indicative of a recalcitrant part of the organic P pool that is not accessible to microbes. The six samples (also covering all three defined types of redox environment) which fall on or below the Redfield ratio are the lowest in TOC and four of these are also particularly low in P_{org} (<0.00021 mol/100g). However, as can be seen in Figure 4.10b, once P_{auth} is taken into account as part of P_{react}, these four samples move into the same range as occupied by the rest for P_{react}, suggesting that while

they are unusually low in P_{org}, they are not that low in P overall. With the exception of the one euxinic sample falling below the Redfield ratio, euxinic samples show little shift in figures 4.10b and 4.10c, suggesting that most retained P is in the organic fraction, and little is converted to authigenic P. It can therefore be concluded that under euxinic conditions, P is efficiently recycled to the water column. In contrast, figures 4.10b and 4.10c show that relatively high proportions of P were extracted in the P_{auth} and P_{det} pools in most ferruginous and some oxic samples, suggesting that either organic P was converted and stored in other forms, or delivered in association with Fe (hydr)oxides, then trapped in authigenic minerals. Although very little P_{Fe} was extracted in this study, and Fe_{ox} is generally low (< 0.1 wt%), studies in modern settings suggest that it is likely that under ferruginous conditions, P would be exported to the sediment in association with minerals such as green rust (Zegeye et al., 2012).

Despite this evidence of trapping of P in authigenic minerals, Figure 4.10d shows that TOC:P ratios (371 ± 271, 449 ± 528 and 1507 ± 910 for oxic, ferruginous and euxinic conditions respectively) remain well above the Redfield ratio for most samples even when all phosphorous, reactive or not, is taken into account. This suggests extensive recycling of P, even under ferruginous and oxic conditions, fuelling the high productivity implied by some exceptionally high TOC concentrations. Previous studies of P dynamics in anoxic water columns (März et al., 2008) have suggested that P is retained under ferruginous conditions in association with Fe oxides. With barely measurable quantities of P associated with Fe oxides being extracted, the results of the present study do not suggest this. This could be explained by the high input of organic carbon fuelling sulphate reduction, making sulphide available in the sediment to reduce Fe oxides, thus releasing adsorbed phosphorus. Whilst some of this, along with P released from organic matter, may have been retained in the sediment in authigenic phosphorus minerals, figures 4.10b and 4.10c suggest that a large proportion was returned to the water column.

In contrast, in S3, further from the source of nutrients, all samples analysed (all of which are oxic) fall on or below the Redfield ratio, suggesting no remobilisation of organic bound phosphorus (Figure 4.11a) relative to organic carbon. Instead, there is evidence of enrichment of P relative to the Redfield ratio in a number of samples, with an overall average TOC:P_{org} ratio for S3 of 43 ± 34. Such low ratios have been observed before in studies of organic carbon

and organic phosphorus in modern marine sediments. Ingall and Van Cappellen (1990) reported C/P ratios down to 49 ± 28 in settings with low sedimentation rates, which they concluded was the result of near complete oxidation of organic matter leaving behind a phosphorus enriched residue. However, Anderson et al. (2001) have suggested that $(C/P)_{organic}$ ratios below the Redfield ratio may simply be an artefact of low TOC concentrations being close to method detection limits. Samples from S3 do have low TOC concentrations, mostly below 0.2 wt%.

Further reactive phosphorus was retained in the sediment as P_{auth} (Figure 4.11b). Given that the closeness of TOC:P_{org} ratios to the Redfield ratio implies a lack of preferential release of P from organic matter, this authigenic component was most likely derived from an input of P associated with Fe oxides. It is likely that these Fe oxides would not have been rapidly reduced, because low productivity (TOC is very low in S3) would have limited organic carbon supply, and therefore sulphide supply (Fe_{py} is also very low in S3), preventing the escape of P back to the water column, thus allowing P to become incorporated into authigenic minerals such as apatite. A further shift to the right in Figure 4.11c indicates a considerable P_{det} fraction, particularly in samples from the Touirist Formation (see Figure 4.8b) – it is unclear whether this is the result of a greater detrital input or if part of the authigenic pool was extracted with P_{det} and this therefore indicates increased input and/or retainment of P originally associated with Fe oxides during the deposition of the Touirst Formation.

For S4, Figure 4.10a clearly shows that TOC:P_{org} ratios are highest under euxinic conditions (204 ± 118), suggesting a greater degree of P recycling relative to TOC under euxinic conditions than under ferruginous or oxic conditions (133 ± 47 and 72 ± 35). Assuming that the Redfield ratio is an appropriate approximation for results of primary productivity at this time, some mobilisation of P from the organic fraction is evident in most ferruginous samples (133 ± 47), but under oxic conditions, a mean of 72 ± 35 suggests that organic P was retained in its original sink. As in S2, the TOC verses P_{react} and $P_{react+det}$ (figures 4.12b and 4.12c) plots illustrate the increased P_{auth} and P_{det} inputs seen under ferruginous and oxic conditions when compared to euxinic conditions. As the TOC:P_{org} ratio for most oxic, and some ferruginous samples, is already below the Redfield ratio, the further decrease in TOC:P ratio when P_{auth} is taken into account suggests, like in S3, that at least some of this P_{auth} derives from P delivered to the

sediment in association with Fe oxides. Figure 4.12d shows that with all P taken into account, all oxic and ferruginous samples fall on or below the Redfield ratio, but there is still evidence for some remobilisation of P under euxinic conditions, where the mean TOC:P_{sum} ratio is 114 ± 64.

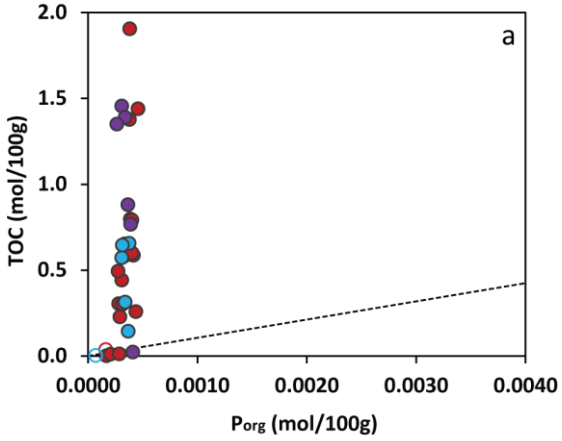
a
TOC (mol/100g)
2.0
1.5
1.0
0.5
0.0
0.0000
0.0010
0.0020
0.0030
0.0040
Porg (mol/100g)

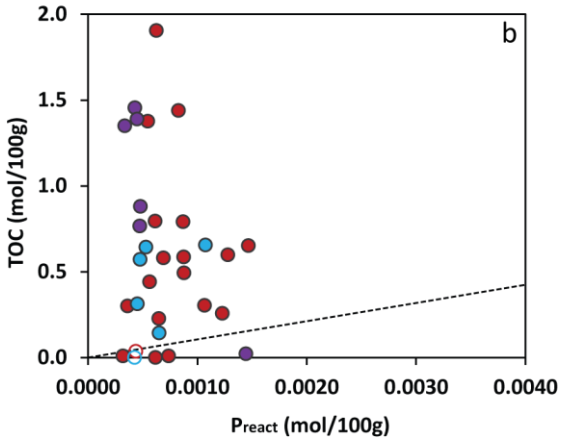
b
TOC (mol/100g)
2.0
1.5
1.0
0.5
0.0
0.0000
0.0010
0.0020
0.0030
0.0040
Preact (mol/100g)

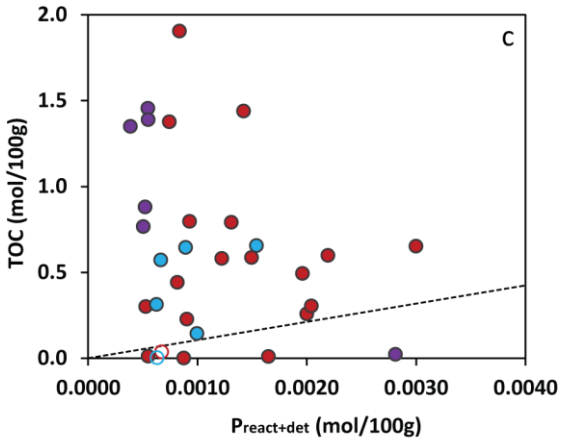
c
TOC (mol/100g)
2.0
1.5
1.0
0.5
0.0
0.0000
0.0010
0.0020
0.0030
0.0040
Preact+det (mol/100g)

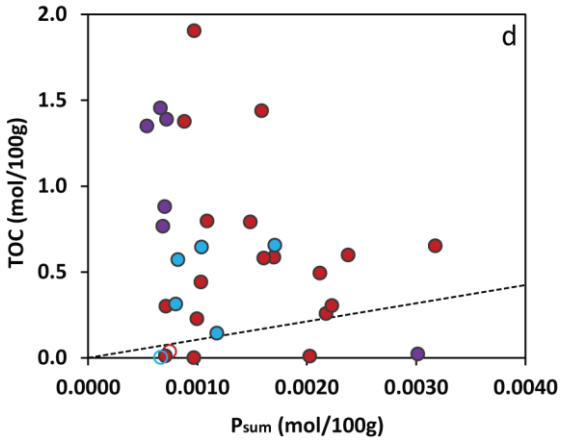
d
TOC (mol/100g)
2.0
1.5
1.0
0.5
0.0
0.0000
0.0010
0.0020
0.0030
0.0040
Psum (mol/100g)

Figure 4.10 Plots of TOC against various P pools for S2. Data points are colour coded according to redox, with blue for oxic, red for ferruginous, and purple for euxinic samples. Open circles indicate carbonate-rich samples. The black dotted line indicates the Redfield Ratio of 106:1.

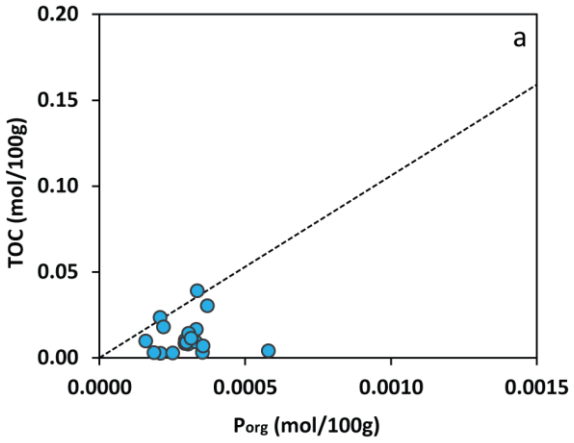
a
TOC (mol/100g)
0.20
0.15
0.10
0.05
0.00
0.0000
0.0005
0.0010
0.0015
Porg (mol/100g)

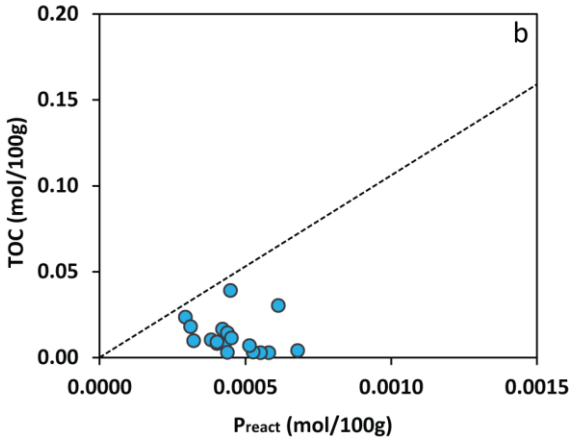
b
TOC (mol/100g)
0.20
0.15
0.10
0.05
0.00
0.0000
0.0005
0.0010
0.0015
Preact (mol/100g)

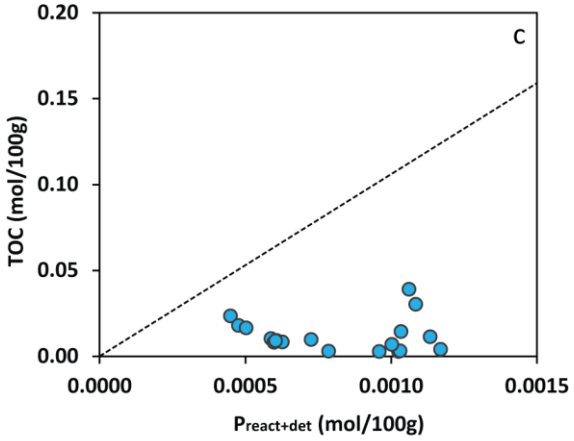
c
TOC (mol/100g)
0.20
0.15
0.10
0.05
0.00
0.0000
0.0005
0.0010
0.0015
Preact+det (mol/100g)

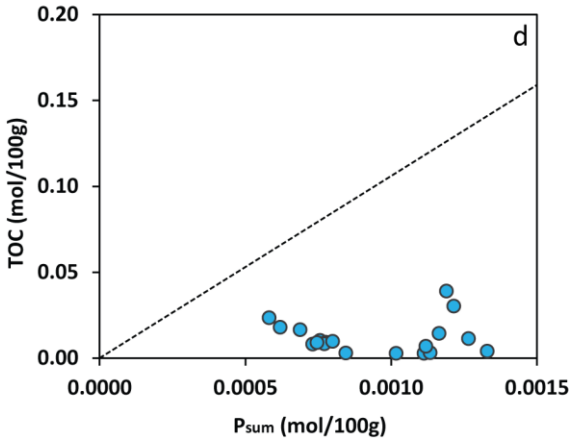
d
TOC (mol/100g)
0.20
0.15
0.10
0.05
0.00
0.0000
0.0005
0.0010
0.0015
Psum (mol/100g)

Figure 4.11 Plots of TOC against various P pools for S3. Data points are colour coded according to redox, with blue for oxic samples. The black dotted line indicates the Redfield Ratio of 106:1.

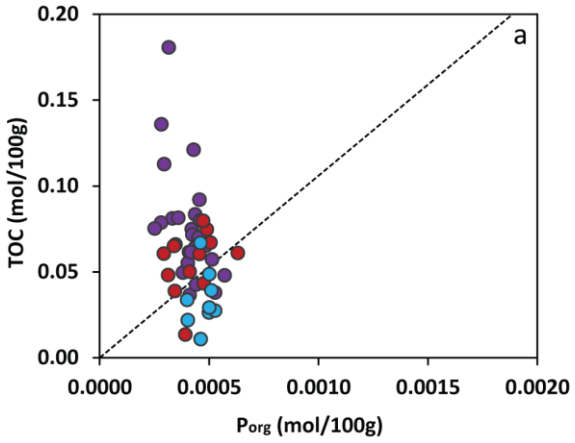
a
TOC (mol/100g)
0.20
0.15
0.10
0.05
0.00
0.0000
0.0005
0.0010
0.0015
0.0020
Porg (mol/100g)

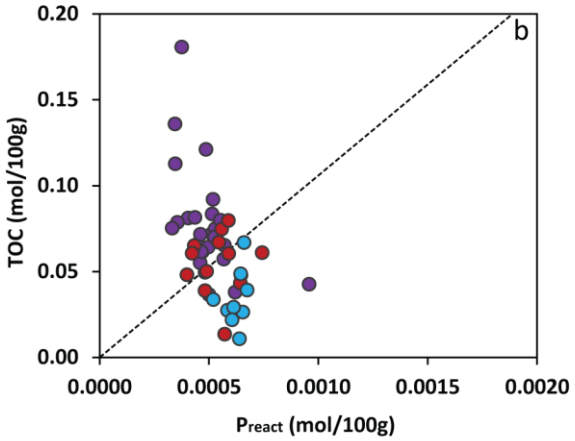
b
TOC (mol/100g)
0.20
0.15
0.10
0.05
0.00
0.0000
0.0005
0.0010
0.0015
0.0020
Preact (mol/100g)

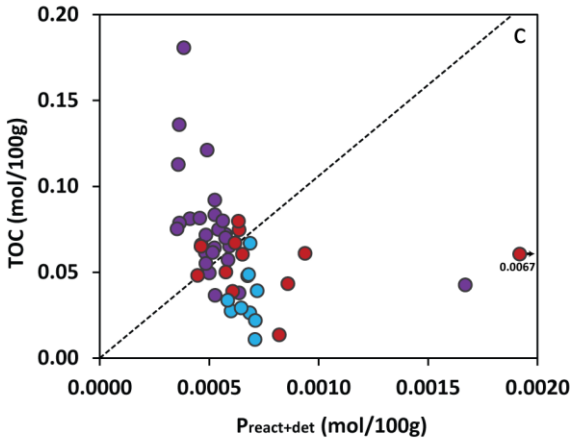
c
TOC (mol/100g)
0.20
0.15
0.10
0.05
0.00
0.0067
0.0000
0.0005
0.0010
0.0015
0.0020
Preact+det (mol/100g)

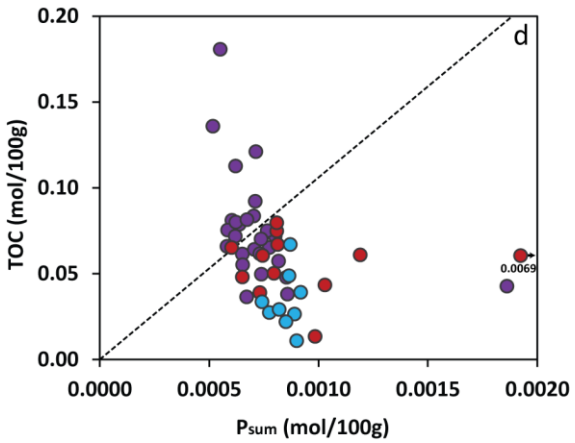
d
TOC (mol/100g)
0.20
0.15
0.10
0.05
0.00
0.0069
0.0000
0.0005
0.0010
0.0015
0.0020
Psum (mol/100g)

Figure 4.12 Plots of TOC against various P pools for S4. Data points are colour coded according to redox, with blue for oxic, red for ferruginous, and purple for euxinic samples. The black dotted line indicates the Redfield Ratio of 106:1.

4.3.4 Phosphorus cycling across space and time

As well as demonstrating a redox control on phosphorus cycling, or perhaps because of this, carbon/phosphorus dynamics show changes across the Taoudeni Basin, and through time (Figure 4.13). Redox data suggests that the basin was largely anoxic during the deposition of the I3/Khatt and I4/En Nesoar formations. The deeper basin (S4) was predominantly euxinic, but with some waxing and waning of ferruginous conditions, while there was a mix of oxic, ferruginous and euxinic conditions in shallower waters (S2). Considerably greater amounts (6-7 times) of TOC are preserved in the shallower basin, and TOC:P_{org}, TOC:P_{react} and TOC:$P_{react+det}$ ratios in S2 (1971 ± 1528, 1399 ± 1211, 1136 ± 1079) are much higher than in S4 (258 ± 124, 213 ± 104, 205 ± 102 for I4) suggesting a greater degree of recycling of P to the water column, especially under euxinic conditions, thus potentially maintaining high productivity and high organic C burial in more central parts of the craton. A moderate degree of recycling to the water column is, however, also apparent in S4, assuming fresh organic matter with Redfield stoichiometry.

During the deposition of the I5/Touirist Formation, organic C burial is increased in S2, where the water column is predominantly ferruginous with occasional euxinic excursions, but decreased in S4, where oxic conditions are prevalent. TOC concentrations are also very low in S3, which is between S2 and S4 and shows no evidence of anoxia. TOC:P_{org} ratios at or below the Redfield ratio in S3 and S4 suggest efficient trapping of P in the sediment and even lower TOC:P_{react} ratios indicate a P_{Fe} flux to the sediment, whilst high TOC:P_{org}, TOC:P_{react} and TOC:$P_{react+det}$ ratios in S2 (1849 ± 1458, 980 ± 1032, 668 ± 796) imply efficient recycling of P to the water column despite the likely additional flux of P associated with green rust.

The I6/Aguelt el Mabha Formation is not represented in S4, but results from both S2 and S3 show a decrease in both TOC and P concentrations. Low TOC/P_{org} and TOC/P_{react} ratios suggest efficient trapping of P in the sediment. Possibly this is the result of a decreased continental P flux following a drop in sea level.

TOC content is noticeably higher in S2 compared to S3 or S4. Debate as to what controls organic carbon concentrations in sedimentary rocks has been ongoing for a number of decades. Much of this has focussed on whether TOC rich sediments are the result of elevated primary productivity or enhanced preservation (Tyson, 2005, Piper and Calvert, 2009, Pedersen and Calvert, 1990, Arthur and Sageman, 1994). Preservation of organic matter has often been linked to anoxia, with studies showing that oxygen exposure is strongly negatively correlated to organic carbon burial efficiency (Hartnett et al., 1998). It has also been shown that sulphate reduction and oxic respiration oxidise equal amounts of organic carbon in nearshore sediments (Canfield, 1989b, Jørgensen, 1982), but at lower sedimentation rates, oxic respiration becomes more important. An explanation for this is that efficient decomposition of certain compounds requires presence of particular oxygen-respiring organisms (Canfield, 1989b). Other authors, however, consider high primary production to be the first-order control on the accumulation of organic-rich deposits (Pedersen and Calvert, 1990). Pedersen and Calvert (1990) noted that euxinic sediments in the modern black sea are not particularly enriched in organic matter, but a saproprel rich in organic carbon was deposited in the Holocene under oxic conditions. Similarly, in this study, pervasive anoxia in the I3 and I4 formations is accompanied by fairly low organic carbon concentrations (means of 0.75 ± 0.16 and 1.02 ± 0.26 wt% respectively) while some samples from S2 that have been shown to be oxic by Fe speciation have TOC concentrations exceeding 5 wt%. It is increasingly recognised that controls on organic matter contents are more of complex interplay between various factors such as sedimentation rates, microbial metabolism and relative sea-level change than a simple end-member model like production verses preservation (Sageman et al., 2003, Rimmer et al., 2004) being involved, with the circumstances of deposition being important (Canfield, 1994). A more detailed discussion of these factors is beyond the scope of this thesis, but with such high TOC concentrations in S2, it is likely that, regardless of the influence of preservation factors, primary productivity was elevated in S2 compared to S3 and S4.

The apparent rather low productivity in S3 and S4, when compared to S2, could be explained by the greater distance from the nutrient source. Although there is evidence for extensive recycling of P in S2, a lot of the continental P supply may have been sequestered at more

proximal locations, towards the centre of the craton, hence progressively lower P concentrations in S3 and S4 compared to S2.

As a shallow epeiric sea, the Taudeni Basin was likely far removed from hydrothermal inputs so Fe, like P, and S, would have been supplied from the land. During the deposition of the lower two formations (I3/Khatt and I4/En Nesoar), redox data suggests that the basin was predominantly euxinic, with occasional oxic excursions which show enhanced authigenic P burial (see Figure 4.4) relative to anoxic samples in the shallower part of the basin. In the deeper basin, similar TOC values for ferruginous and euxinic samples suggest that TOC was probably not controlling the style of anoxia, with relative supplies of Fe and S a more likely candidate. Lower rates of TOC burial in the deeper basin suggest lower productivity, although this could also be a result of a high degree of organic matter breakdown, consuming oxygen and maintaining anoxia. The I5/Touirist Formation sees a transition to a largely oxygenated deep basin, with a ferruginous wedge closer to land. One possibility is that with continentally derived P available to drive primary productivity and therefore organic C production, oxygen was consumed in the water column and therefore anoxia was maintained in the shallower part of the basin (S2). With large quantities of organic C still reaching the sediment, enhanced sulphide production from sulphate reduction would have allowed efficient recycling of P from organic matter and reduction of Fe oxides to the water column, maintaining high productivity. However, as P would gradually have been sequestered in more proximal locations, along with the continental Fe supply, more oxic waters were able to develop during the deposition of the I5/Touirist formation in S4, where the phosphorus that did reach the location of S4 was mostly retained, thus likely further restricting productivity.

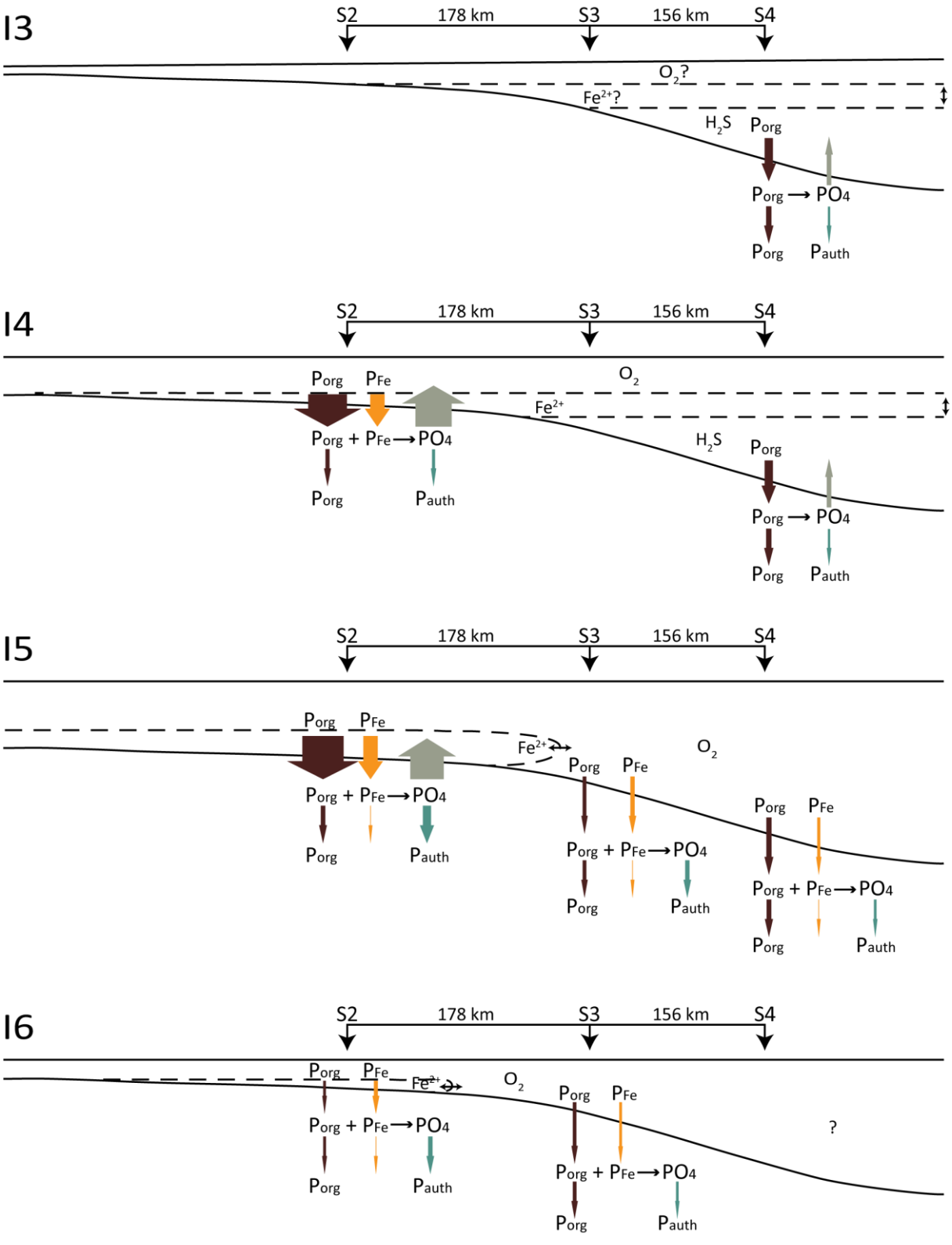
I3
S2
178 km
S3
156 km
S4
O2?
Fe2+?
H2S
Porg
Porg → PO4
Porg
Pauth
I4
S2
178 km
S3
156 km
S4
Porg
PFe
O2
Fe2+
Porg + PFe → PO4
Porg
Pauth
H2S
Porg
Porg → PO4
Porg
Pauth
I5
S2
178 km
S3
156 km
S4
Porg
PFe
Fe2+
O2
Porg + PFe → PO4
Porg
Pauth
Porg
PFe
Porg + PFe → PO4
Porg
Pauth
Porg
PFe
Porg + PFe → PO4
Porg
Pauth
I6
S2
178 km
S3
156 km
S4
Porg
PFe
Fe2+
O2
Porg + PFe → PO4
Porg
Pauth
Porg
PFe
Porg + PFe → PO4
Porg
Pauth
?

Figure 4.13 P cycling across the basin and through time. Coloured arrows show movement of various P pools between the sediment and the water column. Size of arrow is roughly indicative amount of P being transferred, but not to scale. I3 (Khatt) shows flux of P_{org} to the sediment with burial of P_{org} and P_{auth}, with some recycling of PO_4 to the water column. There is no P data for the Khatt Formation. I4 (En Nesoar) shows continuation of this P cycle at S4, but in contrast, in the En Nesoar Formation in S2, there are large fluxes of P_{org}, and also some P_{Fe}, to the sediment. Some burial occurs as P_{org} and P_{auth} (with very minor amounts of P being buried in association with Fe oxides), but a large proportion of the P flux to the sediment is recycled to the water column as PO_4. In I5 (Touirist), a high level of input and recycling continues to occur in S2, while inputs to S3 and S4 are much smaller. There is little evidence for recycling of P from S3 and S4, with P_{org} influxes being buried, and P_{Fe} influxes largely being retained as P_{auth} and very minor amounts of P_{Fe}. There is no data for I6 (Aguelt el Mabha) for the S4 location, but S3 shows a very similar picture to in the Touirist Formation, except there is no evidence for any retention of P in association with Fe oxides. Limited data in S2 suggests that P fluxes are reduced in the Aguelt el Mabha Formation to levels similar to those seen in S3, with no evidence for P recycling to the water column.

4.3.5 New insights into phosphorus in the Proterozoic

Analysis of TOC contents and phosphorus speciation in three cores covering four formations from the Atar Group of the 1.1 Ga Taoudeni Basin demonstrates, for the first time, that redox-promoted P recycling occurred during the mid-Proterozoic, and could potentially have been a major control on organic carbon production and burial, and therefore on oxygen supply to the biosphere. The most recent estimates of phosphorus availability during the Precambrian (Jones et al., 2015; Reinhard et al., 2017) suggest that before the Cryogenian, primary productivity may have been severely limited by P availability. With an overall mean of 0.04 ± 0.03 wt%, total P concentrations from the Taoudeni Basin are very similar to the average of 0.051 ± 0.003 wt% for pre-Cryogenian deposits presented by Reinhard et al.(2017), while only two samples exceed their average of 0.209 ± 0.023 wt% for samples younger than 720 Myr old (Cryogenian, Ediacaran and Phanerozoic). Reinhard et al. (2017) interpret this shift in mean "bulk" P, as well as the increase in variability seen in younger samples, as a shift from predominantly detrital P deposition in the earlier Precambrian to P deposition that includes a large and variable authigenic component from the late Precambrian onwards, noting that more than 95 % of Precambrian samples fall within the expected detrital range. With an average total P of 0.04 ± 0.03 wt%, the samples from the Taoudeni Basin would presumably fall into this group. However, P speciation has shown that much of the P preserved in the rocks of the Atar Group

is actually either organic or authigenic in origin. P_{org} and P_{auth} combined account for up to a maximum of 89% of P_{sum}, with a mean for P_{react}/P_{sum} across the 3 cores of 0.60 ± 0.12. In samples from S2 where P_{react}/P_{sum} falls below 50%, much of the remaining P was extracted as P_{det}, but in S2, while P_{res} correlates well the Al content, interpreted to be a measure of detrital input, P_{det} does not, suggesting that at least part of this pool consists of recrystallized authigenic P. Consequently, an even higher proportion of P_{sum} could be considered to have been non-detrital in origin. These results therefore demonstrate that, in the Taoudeni Basin at least, locally variable authigenic enrichments of P were a feature of the P cycle during the Mesoproterozoic. Low overall concentrations suggest that both reactive and detrital P might have been present in the ocean in lower concentrations than in more recent geological history.

Despite more restricted P availability, large quantities of organic carbon could still be buried if P is preferentially regenerated from organic matter and returned to the water column to drive further primary productivity. And this is precisely what analysis of S2 demonstrates. High $TOC:P_{org}$, $TOC:P_{react}$ and $TOC:P_{react+det}$ ratios in the En Nesoar (I4) and Touirist (I5) formations imply a depletion in P relative to C in the organic matter preserved in the core, and that much of the released P was effectively recycled to the water column instead of being trapped in the sediment in authigenic minerals. Although the highest ratios are seen in anoxic samples, this occurred under all redox conditions probably due to high porewater sulphide concentrations stimulated by high TOC inputs. In contrast, at more distal locations closer to the edge of the craton (S3 and S4), production and/or preservation of organic matter was much more limited. An overall drop in P concentrations across the basin implies a reduced supply of P in more distal locations, presumably as some of the continental source was sequestered closer to land. $TOC:P_{org}$ and $TOC:P_{react}$ ratios at or below the Redfield ratio suggest that, under oxic conditions, P was efficiently trapped in the sediment. Moderately high $TOC:P_{org}$ ratios recorded under euxinic conditions, and, to a lesser degree, ferruginous conditions, suggest a degree of P regeneration, but to a far smaller extent than in S2. $TOC:P_{react}$ ratios for ferruginous samples do however indicate that much of the P released from organic matter was trapped in authigenic minerals rather than being released back to the water column.

These conclusions assume that organic matter was being produced with a Redfield stoichiometry. It has, however, been suggested that an assumption that the Redfield ratio has been constant throughout Earths history may be erroneous. Planavsky (2014) argued that a combination of stoichiometric plasticity in cyanobacteria, presumed to be the dominant primary producer for much of the Precambrian, and P stress resulting from a deep sea ferric iron phosphorus trap in predominantly ferruginous oceans, would have led to far higher C:P ratios than seen in modern oceans. Reinhard et al (2017) incorporate a maximum ratio of 400 in the model they use to explore their observations of sedimentary phosphorus abundances through time. If such a C:P ratio is realistic for fresh organic matter produced in the Taoudeni Basin during the mid-Proterozoic, then almost no samples from S4 show evidence for preferential mineralisation of organic P. However, with a number of samples exceeding 1000 for TOC:P_{org} and TOC:P_{react}, results from S2 still provide strong evidence for phosphorous regeneration. A higher original C:P ratio would also mean that a lot of samples from S4 showed evidence for P_{org} enrichment relative to TOC, a result for which there is currently no clear explanation. It seems unlikely that it would be a consequence of TOC concentrations being close to the limit of detection, as it includes samples with TOC contents exceeding 1 wt%. Variation in community structures under different redox conditions, as suggested by Beghin et al. (2017a), could however have led to variations in fresh organic matter stoichiometry across the basin, depending on the relative proportions of eukaryotes to prokaryotes.

4.4 Conclusions

Phosphorus speciation suggests that much of the phosphorus in samples from cores S2, S3 and S4 would have been bioavailable at the time of deposition. It is stored mainly in the P_{org} and P_{auth} pools, with very little being found in association with Fe oxides. It is, however, likely that some P was delivered to the sediment in association with Fe minerals alongside that that reached the sediment in organic matter. P_{det} is also a significant pool in a number of samples, particularly in S2 but also in S3. Supposedly detrital in origin, the P_{det} pool in this sequential extraction is generally assumed not to have been bioavailable. However, other studies have shown that in ancient rocks, this might not always be true because authigenic P minerals may not be fully

extracted in the Na acetate step. A lack of correlation between P_{det} and Al in S2 is here interpreted to be evidence that at least part of the P_{det} pool in this study belongs with the P_{auth} pool and so should be included in the sum of reactive pools.

Examination of carbon to phosphorus ratios suggests that in S3 and S4, where TOC concentrations are quite low, there is little evidence for organic P regeneration from the sediment to the water column under oxic conditions, while P was likely delivered to sediment in association with Fe oxides and trapped in authigenic P minerals. In S4, TOC:P_{org} ratios above the Redfield ratio suggest some remobilisation of P from organic matter particularly during periods of euxinia, but also to some extent under ferruginous conditions. In contrast, in the En Nesoar and Touirist formations in S2, TOC:P_{org} ratios are generally far in excess of the Redfield ratio, suggesting extensive remineralization of P from organic matter in comparison to carbon under oxic and ferruginous, as well as euxinic, conditions. TOC:P ratios generally remain above the Redfield ratio in all redox conditions, even when all extracted P is included, indicating extensive regeneration of P to the water column. It is suggested that continentally derived P may have driven high primary productivity in shallower waters at the centre of the craton. Consumption of oxygen during the breakdown of organic matter likely maintained anoxia in the water column while a large organic carbon flux to the sediment could have stimulated high rates of sulphide production through sulphate reduction, thus allowing efficient recycling of P from organic matter and reduction of Fe oxides. Regeneration of P to the column could then have maintained high productivity. A lower flux of P to likely deeper waters towards the craton edge could have restricted primary productivity. Efficient trapping of P in sediments would likely have further restricted primary productivity, and therefore organic carbon production, allowing oxic waters to develop.

These results demonstrate that redox influenced P cycling, similar to that seen in modern and Phanerozoic settings, was also occurring in the Proterozoic. They also show that, although total P concentrations are low, this does not necessarily imply a lack of authigenic P enrichment of a largely detrital P input to the sediment. Instead, it seems that detrital P inputs were reduced compared to more recent geological history, and both deposition and regeneration of bioavailable P was occurring.

Chapter 5

Modification of palaeoredox proxies in core S1 in samples affected by contact metamorphism

5.1 Introduction

The results for core S1 are presented separately because the presence of AVS and high concentrations of trace metals found in S1 suggest that this core has undergone potentially significant metamorphism. Given the presence of a ~ 30 m thick dolerite sill, this is perhaps not unexpected. In this chapter, the ramifications of such an intrusion for redox proxies are considered. Is it possible to recover information about depositional conditions in successions that have been altered in this way? Of importance to this study is how the effects of metamorphism can be recognised, since a dolerite sill is also present in S4. The samples analysed from S1 include both black shales and carbonates, from above and below the sill.

Although the Proterozoic sedimentary cover of the Taoudeni Basin has escaped regional metamorphism, with estimates of post-depositional temperatures of < 100°C, intrusions related to the opening of the Atlantic Ocean, and associated circulation of hot fluids, are reported to have caused contact metamorphism and hydrothermal alteration (Girard et al., 1989). Rooney et al. (2010) report that the organic rich shales in S1 are "baked black" 20m above and 5m below a 30m thick dolerite sill and can be classified as being overmature, in contrast to the shales of S2, which are marginally mature. They conclude that this is a result of flash pyrolysis having occurred during the emplacement of the dolerite sill in S1, resulting in maturation and expulsion of hydrocarbons. Similar data for S4, which contains a much smaller dolerite intrusion (< 2m thick) is not available, but, unlike for S1, organic walled microfossils were recoverable from S4 in the I3 Formation, approximately 5m above the sill (Beghin et al., 2017b). It was, however, noted that, while in general preservation of organic-walled microfossils and microbial mats (extracted from S2, S3 and S4) is "exquisite", this was not the case in the I3 and I4 Formations of S4 (Beghin et al., 2017a).

The metamorphic grade of shales from S1 is apparently difficult to quantify due to a lack of index minerals. Rooney et al. (2010) found that S1 shales had compositions similar to S2 shales (quartz, kaolinite, illite, feldspar, pyrite), but with added pyrrhotite, reported to be a common mineral in metamorphosed graphitic rocks. They suggest that at the contact, the ORS of S1 might have experienced temperatures of 550 – 650 °C but convective and/or conductive cooling led to peak temperatures of ~288 °C through the rest of the altered shale.

5.2 Results

5.2.1 Total organic carbon

Total organic carbon concentrations are high throughout the sampled parts of the En Nesoar and Touirist Formations in S1, with an overall average of 10.79 ± 8.70 wt% (Table 5.1). The highest TOC concentrations occur in the En Nesoar Formation, either side of the dolerite sill, reaching a maximum of 38.50 and 37.05 wt% above and below respectively. Figure 5.1 suggests a sharp increase in TOC at the margins of the dolerite sill, although the En Nesoar Formation is generally very rich in organic carbon above the sill, with a mean of 18.70 ± 7.77 wt% and a range of 6.80 – 38.50 wt%. Below the sill, although the mean is 15.80, there is a drop from 37.05 to 0.48 wt% TOC in just over a metre. The stromatolitic carbonates at the base of the core are low in TOC, generally < 0.1 wt%. The sampled part of the Touirist Formation is more consistent, with an average of 7.14 ± 2.91 wt% and a range of 1.11 – 16.93 wt% - carbonate-rich samples (identified through acid testing and Al contents) do not show any marked difference in TOC in this formation.

Formation	TOC wt%	FeT wt%	Al wt%
Touirist	7.14 ± 2.91	3.47 ± 4.23	7.99 ± 4.61
En Nesoar above sill	18.90 ± 7.77	2.64 ± 2.27	9.75 ± 1.59
Dolerite sill	0.03 ± 0.01	7.81 ± 0.06	8.12 ± 0.00
En Nesoar below sill	10.64 ± 14.04	3.95 ± 4.47	5.15 ± 3.50
En Nesoar All	15.80 ± 11.21	3.13 ± 3.30	8.03 ± 3.33
All except dolerite	10.79 ± 8.70	3.33 ± 3.86	8.01 ± 4.11

Table 5.1 Mean and SD for TOC, FeT and Al for S1

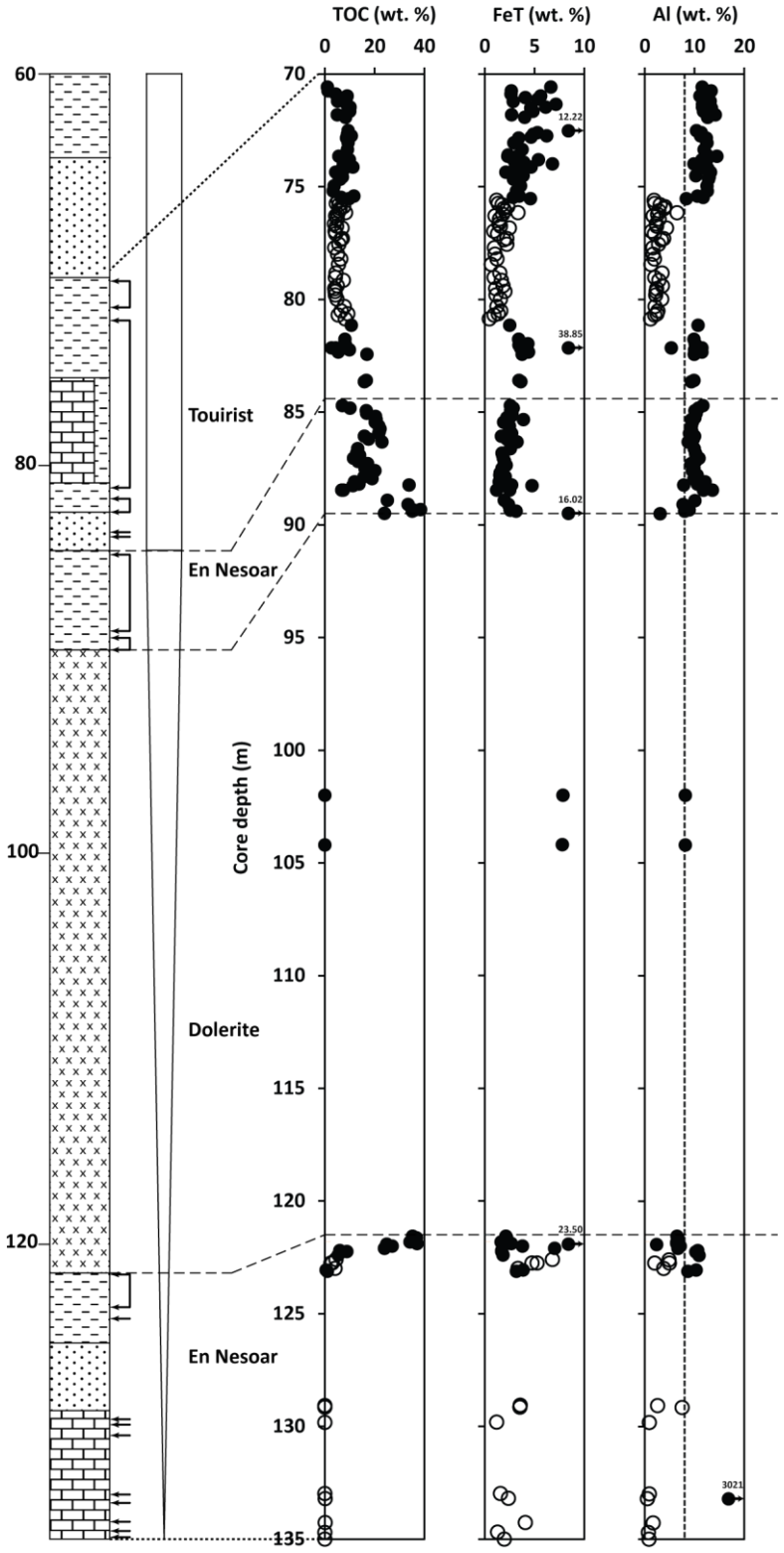
TOC (wt. %)
FeT (wt. %)
Al (wt. %)
0 20 40
0 5 10
0 10 20
Core depth (m)
Touirist
En Nesoar
Dolerite
En Nesoar
12.22
38.85
16.02
23.50
3021

Figure 5.1 Depth profiles for TOC, Al and Fe concentrations in S1 Open circles indicate carbonate-rich samples.

5.2.2 Iron speciation

5.2.2.1 Fe_{carb}

Fe_{carb} concentrations range between 0.16 and 13.22 wt% with an overall mean (not including dolerite) of 1.38 ± 1.51 wt% (Table 5.2). The mean for the Touirist Formation is 1.40 ± 1.32 wt%, with most samples falling into a definable trend (Figure 5.2). Between 70 and 75 m core depth, concentrations generally sit between 1 and 3 wt%. At around 75.5 m, where samples become carbonate-rich, there is a drop in Fe_{carb} to values typically in the range of 0.2 – 0.5 wt%, between 76 and 80 m depth. Concentrations increase back to 1 – 2 wt% in underlying carbonate-poor/free rock. The overall average for the Touirist Formation is 1.40 ± 1.32 wt%. In general, with the exception of the sample apparently encased by dolerite, Fe_{carb} concentrations decrease slightly down the En Nesoar Formation towards the dolerite sill, giving a mean of 1.21 ± 0.98 wt %. Below the dolerite sill, the widest range in Fe_{carb} contents is seen, with an average of 1.62 ± 2.56 wt %. With the exception of the maximum of 13.22 wt% at 121.92 m depth, a similar range is seen for both the black shales and the stromatolitic carbonates that occur in the En Nesoar Formation below the sill.

5.2.2.2 Fe_{ox}

Fe_{ox} concentrations are, on the whole, lower than Fe_{carb}, with an overall average (not including dolerite) of 0.71 ± 0.79 wt%. With the exception of a few iron-rich samples, Fe_{ox} is generally greatest in the upper part of the Touirist Formation, typically around 1 wt%. As for Fe_{carb}, a drop is seen at approximately 75.5 m depth (in the carbonate-rich rock), to around 0.3 wt%, followed by a slight increase at around 80 m, giving a mean for the Touirist Formation of 0.83 ± 0.71 wt%. Again, like for Fe_{carb}, Fe_{ox} concentrations generally decrease in the En Nesoar Formation towards the dolerite sill. Directly below the sill, Fe_{ox} is quite variable, ranging from

5.80 wt % (the maximum for the core) in the black shales down to 0.08 wt% in the carbonates. Overall, the mean for the En Nesoar Formation is 0.53 ± 0.86 wt%.

5.2.2.3 Fe_{mag}

On average, Fe_{mag} is the smallest Fe pool, with an overall mean (except dolerite) of 0.17 ± 0.29 wt%. The majority of samples fall below 0.2 wt%, with occasional exceptions up to a maximum of 2.82 wt% (in the Touirist Formation). Clusters of samples with slightly higher Fe_{mag} concentrations occur in the En Nesoar Formation just above and below the dolerite sill, and at around 77 m depth, in the carbonate-rich part of the Touirist Formation. Fe_{mag} is, however, the largest Fe pool extracted from the dolerite sill, with a mean for the two samples of 0.90 ± 0.20 wt%.

5.2.2.4 Fe_{AVS}

Fe_{AVS} is the most variable pool, with an overall mean of 1.05 ± 2.49 wt% and a range of 0.00 - 27.89 wt%. On average, this constitutes 20% of extracted reactive Fe, which is striking considering that Fe_{AVS} was undetectable in the other three cores. Most samples fall into the range of 0 – 3 wt%, and the depth profile shows similarities to those for Fe_{carb} and Fe_{ox}, albeit with a bit more scatter. In the upper and lower parts of the sampled Touirist Formation most samples contain more than 0.5 wt %, but for most of the carbonate-rich portion (between 76 and 80.7 m depth), Fe_{AVS} concentrations are typically < 0.05 wt%, giving an overall average of 1.06 ± 3.03 wt%. The En Nesoar Formation is a little less variable, with an overall mean of 1.03 ± 1.48 wt%. Fe_{AVS} concentrations in the En Nesoar Formation vary most just above and below the dolerite sill. As well as being a significant constituent of the black shales in much of the sampled part of the core, Fe_{AVS} is also present in considerable quantities in the carbonates at the base of the succession. Fe_{AVS} was virtually undetectable in the dolerite.

5.2.2.5 Fe_{py}

With a mean of 0.64 ± 0.75 wt%, Fe_{py} is, on average, a smaller pool than Fe_{AVS}. Particularly noticeable is the low concentration of Fe_{py} in the carbonates at the base of the core. Pyrite is detectable here, but in much smaller quantities than the rest of the core (with the exception of the dolerite). The overlying black shales are the most variable in pyrite contents, with a range of 0.027 – 6.24 wt%, giving the En Nesoar Formation below the dolerite sill a mean of 0.58 ± 1.30 wt%. Above the sill, with the exception of sample S1 89.5 (3.09 wt%), Fe_{py} concentrations in the En Nesoar Formation are fairly consistent, with a mean of 0.37 ± 0.46 wt% and ranging between 0.02 and 0.62 wt%. Pyrite is generally more abundant in the overlying Touirist Formation, with a number of samples exceeding 1 wt% Fe_{py}, giving an average of 0.78 ± 0.60 wt%. Although there are few samples with Fe_{py} <0.1 wt % in the 75 - 80 m depth interval, Fe_{py} does not show the same persistent drop as seen for Fe_{carb}, Fe_{ox} and Fe_{AVS}.

5.2.2.6 Fe_{HCl}

The profile for Fe_{HCl} shows some similarities to those for Fe_{carb}, Fe_{ox} and Fe_{AVS}. With an overall mean of 2.43 ± 3.03 wt%, Fe_{HCl} constitutes, on average, 73 % of FeT. Below the sill, Fe_{HCl} ranges between 0.91 and 19.39 wt%, with a mean of 2.84 ± 3.79 wt%. The highest concentrations occur in the shales close to the dolerite contact, but even in the carbonates, Fe_{HCl} can exceed 3 wt%. Above the sill, the average for the En Nesoar Formation is 1.80 ± 1.95 wt%. With the exception of a couple of samples, including the one closest to the dolerite, there is a general trend of increasing Fe_{HCl} concentrations towards the contact with the Touirist Formation. This trend continues into the Touirist Formation until a drop to generally lower concentrations, mostly between 0.3 and 1.5 wt%, at around 81m depth. Above 75.6 m, Fe_{HCl} is generally between 2 and 6 wt%. Overall, the Touirist Formation has mean of 2.61± 3.19 wt% and a maximum of 28.13 wt%.

5.2.2.7 FeT

The overall average for FeT is 3.33 ± 3.86 wt%. The range is wide (see Figure 5.1), from 0.44 to 38.85 wt%, although only one sample falls below 0.5 wt% (the lower limit suggested by Clarkson et al. (2014) as appropriate for utilisation of Fe based redox proxies in carbonate-rich samples) and only four samples exceed 8 wt%. These are the same four samples that show unusually (relative to other samples in S1) high concentrations in some or all of the Fe pools extracted. As is the case for all the Fe pools, FeT is on average higher in the En Nesoar Formation below the dolerite than above it, with means of 3.95 ± 4.47 and 2.64 ± 2.27 wt% respectively. This is a result of the greater concentrations of Fe found in some of the samples found directly beneath the sill. The FeT contents of the carbonates at the base of the core fall within a very similar range to almost all the black shale samples from just above the dolerite. There is a slight increase in FeT, very similar to that seen in Fe_{carb}, at the start of the Touirist Formation, followed by a decrease in concentrations to typically between 1 and 2 wt% from 80.86 to 75.6 m depth, where the rock is carbonate-rich. Above this, FeT ranges from 2 to 7 wt%, giving the Touirist Formation a mean of 3.47 ± 4.23 wt%. For comparison, FeT is higher in the dolerite than in most other samples, with a mean of 7.81 ± 0.06 wt%. Only ~ 20 % of this was extracted in the individual Fe pools, suggesting most of the iron in the dolerite resides in Fe phases not targeted by this set of extractions.

Formation	Fe_{carb} wt %	F_{ox} wt %	Fe_{mag} wt%	Fe_{AVS} wt%	Fe_{py} wt%	Fe_{HCl} wt%
Touirist	1.40 ± 1.32	0.83 ± 0.71	0.15 ± 0.31	1.06 ± 3.03	0.78 ± 0.60	2.61 ± 3.19
En Nesoar above sill	1.21 ± 0.98	0.44 ± 0.57	0.15 ± 0.20	0.89 ± 1.21	0.37 ± 0.46	1.80 ± 1.95
Dolerite sill	0.62 ± 0.15	0.27 ± 0.01	0.90 ± 0.20	0.00 ± 0.01	0.04 ± 0.03	3.01 ± 0.00
En Nesoar below sill	1.62 ± 2.56	0.68 ± 1.21	0.27 ± 0.31	1.28 ± 1.84	0.58 ± 1.30	2.84 ± 3.79
En Nesoar All	1.36 ± 1.74	0.53 ± 0.86	0.19 ± 0.25	1.03 ± 1.48	0.45 ± 0.87	2.19 ± 2.81
All except dolerite	1.38 ± 1.51	0.71 ± 0.79	0.17 ± 0.29	1.05 ± 2.49	0.64 ± 0.75	2.43 ± 3.03

Table 5.2 Mean and SD for Fe pools in S1

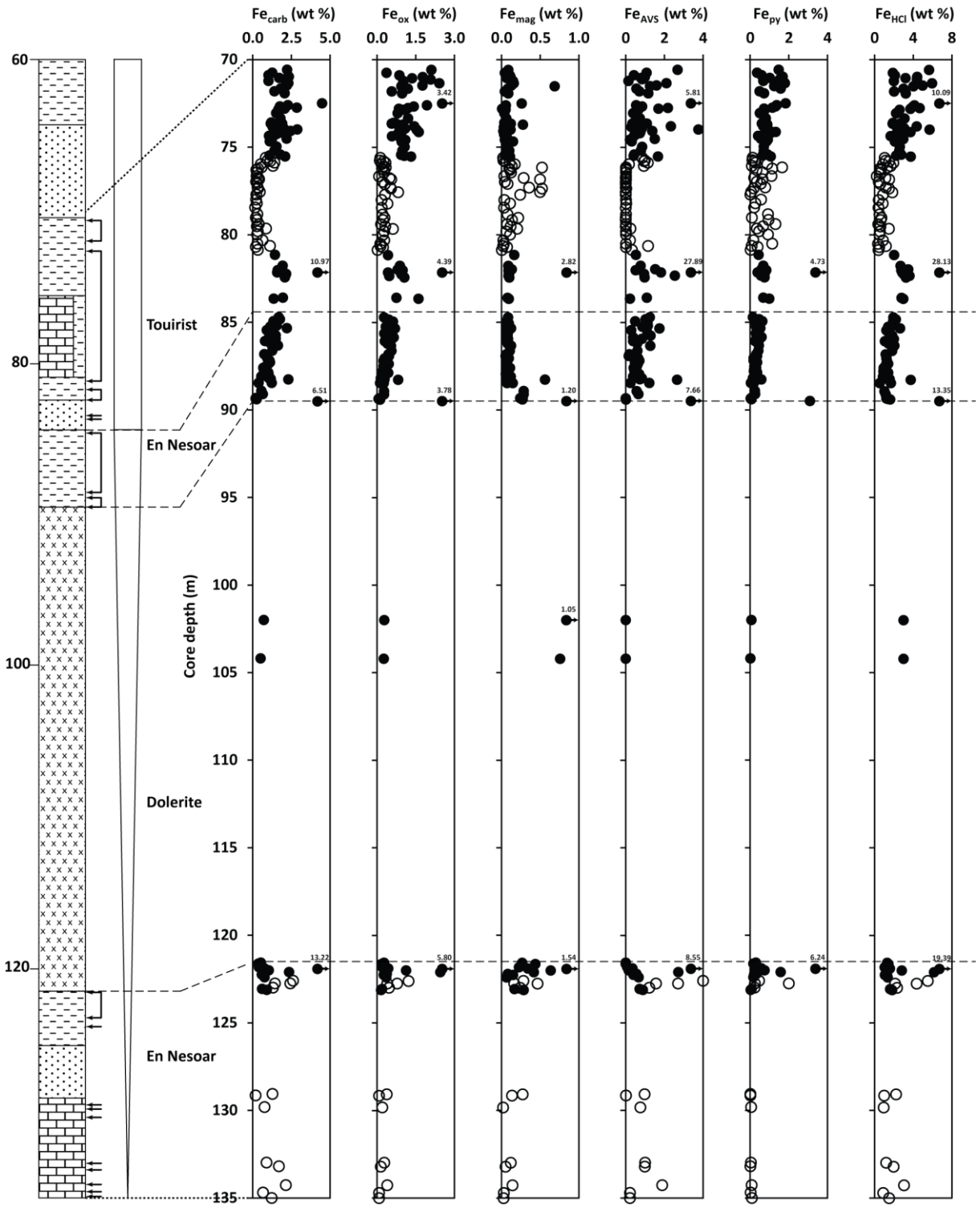

Figure 5.2 Depth profiles for Fe pools in S1 Open circles indicate carbonate-rich samples

5.2.3 Aluminium

With a mean of 8.01 ± 4.11 wt% (Table 5.1), Al concentrations are very close to average shale (80000 ppm (Turekian and Wedepohl, 1961)), although there is quite some variation, with a range of 0.50 to 14.46 wt%. Unsurprisingly (average carbonate being 4200 ppm), the lowest Al concentrations, mostly < 1 wt%, are seen in the stromatolitic carbonates at the base of the core. The black shales just below the dolerite mostly cluster around the average shale line (Figure 5.1), giving an overall mean of 5.15 ± 3.50 wt % for the En Nesoar Formation below the sill. The majority of samples in the En Nesoar Formation above the sill exceed the average shale value of 8 wt%, giving a mean of 9.75 ± 1.59. Although the Touirist Formation has a mean very close to average shale, three well defined sections with differing Al contents can be discerned, which match quite closely to the changes in Fe concentrations described in section 5.2.2. Below a depth of 80.86 m, all measured samples, except the one containing an exceptional amount of Fe, have Al concentrations between 9 and 11.5 wt%. Between 80.86 and 75.6 m depth, where acid testing suggests that the rock is carbonate-rich, most samples fall in the range 1 – 4 wt % Al. In the rest of the sampled Touirist Formation, all have Al concentrations greater than average shale, typically between 10 and 14 wt%.

5.2.4 Trace metals in S1

5.2.4.1 Chromium

Chromium concentrations vary in the core in a very similar way to aluminium (see figures 5.1 and 5.3). Although, on average (89 ± 63 ppm, Table 5.3), Cr concentrations beneath the dolerite sill are very close to average shale (90 ppm), there is an increase to around 200 ppm at the dolerite margin, with most shale and carbonate samples a metre or more below the sill falling below average shale (but above an average carbonate value of 11ppm (Turekian and Wedepohl, 1961)). In the rest of the En Nesoar Fomation above the sill, most samples are enriched in Cr relative to average shale, with a mean of 224 ± 36 ppm. Cr concentrations are lower in the Touirist Formation (122 ± 63 ppm), with a clear split between samples which fall above average

shale below 80.86 m and above 75.6 m depth, and carbonate-rich samples depleted relative to average shale in between.

5.2.4.2 Copper

Below the dolerite sill, with a mean of 50 ± 72 ppm, samples are mostly depleted or close to average shale (45 ppm), whilst above the sill, the vast majority of samples are enriched compared to average shale, with means of 122 ± 33 and 135 ± 85 ppm for the En Nesoar and Touirist Formations respectively. Although the carbonates at the base of the core are very low in copper (0 – 8 ppm), this is in keeping with an average carbonate value of 4 ppm (Turekian and Wedepohl, 1961). Only four of the shale samples significantly exceed average shale (>100 ppm). All samples in the En Nesoar Formation above the sill are, however, enriched relative to average shale, falling between 60 and 200 ppm. There is a slight general increase in Cu concentrations toward the boundary with the Tourist Formation. With the exception of S1 121.92, the most enriched samples (>200 ppm) are found in the Touirist Formation (maximum 408 ppm), mostly towards the top of the sampled part of the core, where variation is also generally the greatest. There is a dip in Cu concentrations in the middle of the formation, in the same carbonate-rich region as for Cr, but not quite so clearly defined.

5.2.4.3 Molybdenum

For most of the En Nesoar Formation beneath the dolerite sill, Mo concentrations are close to the average shale value of 2.6 ppm, with Mo being absent, or undetectable, in some of those samples, particularly the carbonates (average carbonate being 0.4 ppm (Turekian and Wedepohl, 1961)). There is a sudden increase to concentrations >20 ppm between 122.2 and 122.1 m depth. Above the sill, all samples are enriched relative to average shale, many very considerably so, with means of 19.3 ± 8.5 and 29.8 ± 17.7 ppm for the En Nesoar and Touirist Formations respectively. There is an initial decrease upcore from a maximum for the En Nesoar Formation above the dolerite of 38.9 ppm at the sill margin. This is followed by a general increase in Mo concentrations towards the boundary with the overlying Touirist Formation. As for copper, Mo concentrations are generally highest towards the top of the sampled part of the

core, reaching a maximum of 79.1 ppm. Variation is also greatest here, with the maximum within half a metre of the second lowest concentration for the Touirist Formation. Between 82.34 and 74.26 m, where samples are mostly carbonate-rich, Mo concentrations are generally a little lower, and fall within a narrower range compared to samples just above and below this section.

5.2.4.4 Nickel

The depth profile for Ni shows some similar characteristics to those of Cu and Mo. At the base of the core, the carbonates are low in Ni (between 10 and 40 ppm), although this is actually consistent with an average carbonate value of 20 ppm. A couple of the shales beneath the dolerite sill also fall within this range, but most at least match the average shale value of 68 ppm, with the samples closest to the sill being enriched in Ni, up to 338 ppm, and showing a similar profile to Mo. In the En Nesoar Formation above the sill, samples are routinely enriched in Ni relative to average shale, with most concentrations >100 ppm and a mean of 187 ± 60 ppm. A slight dip in concentrations at about 87 m depth is evident in the profile (Figure 5.3) with a genral increase in Ni concentrations towards the boundary with the Touirist Formation. Ni concentrations in the Touirist Formation are more varied, with a range of 41 to 551 ppm and a mean of 192 ± 119 ppm. Initially, the Touirist Formation is somewhat enriched in Ni, but concentrations drop to being mostly close to average shale (but above average carbonate) between 80.86 and 75.6 m depth. Ni concentrations generally increase upcore, reaching a maximum at 70.98 m (also the maximum for Cu and Mo). The Ni depth profile above the dolerite sill is very similar to that of Cu.

5.2.4.5 Vanadium

Much of S1 is enriched in vanadium, some samples significantly so, with an overall average of 714 ± 497 ppm and a maximum of 2137 ppm. Even at the bottom of the core, where some samples are low in V relative to average shale (130 ppm), most carbonate containing samples have V concentrations at least three times higher than average carbonate (20 ppm). As for Mo and Ni, shales are enriched in V just below the dolerite sill, with the closest samples ranging

between 600 and 1500 ppm. Above the sill, V concentrations decrease away from the contact, from 941 to 210 ppm. V concentrations become more variable, with a general increase towards the start of the Touirist Formation, giving a mean for the En Nesaor Formation above the sill of 514 ± 239 ppm. Following initially very high values (>1000 ppm), V concentrations drop to comparatively low (typically 400 – 600 ppm) levels until around 77.5 m depth, where concentrations become more variable, with a general increase upcore, reaching a maximum of 2137 ppm. The overall mean for the Touirist Formation is 907 ± 51 ppm, nearly seven times average shale.

5.2.4.6 Zinc

Zn concentrations are generally low at the base of the core, mostly between average shale (95 ppm) and average carbonate (20 ppm), with a mean of 90 ± 165 ppm. This average is increased considerably by two samples with rather higher Zn concentrations (420 and 764 ppm), neither of which showed any noticeable enrichment in other trace metals. While concentrations do increase slightly towards the dolerite sill, shales close to the contact are not enriched in Zn like they are in some other trace metals. Above the sill, samples are largely enriched in Zn relative to average shale, with averages of 228 ± 125 ppm and 366 ± 242 ppm for the En Nesoar and Tourist Formations respectively. The En Nesoar Formation shows a range of 71 ppm at the sill contact to 698 ppm towards the top of the formation. Zn concentrations are quite variable throughout the Touirist Formation, particularly above ~77.5 m. In contrast to some other trace metals, carbonate-rich samples don't display quite such a noticeable difference in distribution of Zn values when compared with underlying and overlying rock.

Formation	Cr ppm	Cu ppm	Mo ppm	Ni ppm	V ppm	Zn ppm
Touirist	122 ± 63	135 ± 85	29.8 ± 17.7	192 ± 119	907 ± 513	366 ± 242
En Nesoar above sill	224 ± 36	122 ± 33	19.3 ± 8.5	187 ± 60	514 ± 239	228 ± 125
Dolerite sill	196 ± 62	129 ± 3	1.5 ± 2.2	91 ± 10	284 ± 2	92 ± 2
En Nesoar below sill	89 ± 63	50 ± 72	11.4 ± 16.9	89 ± 93	338 ± 413	90 ± 165
En Nesoar All	173 ± 81	95 ± 62	16.3 ± 12.8	150 ± 88	448 ± 324	176 ± 155
All except dolerite	144 ± 75	118 ± 78	24.1 ± 17.1	174 ± 108	714 ± 497	286 ± 229

Table 5.3 Mean and SD for trace metals in S1

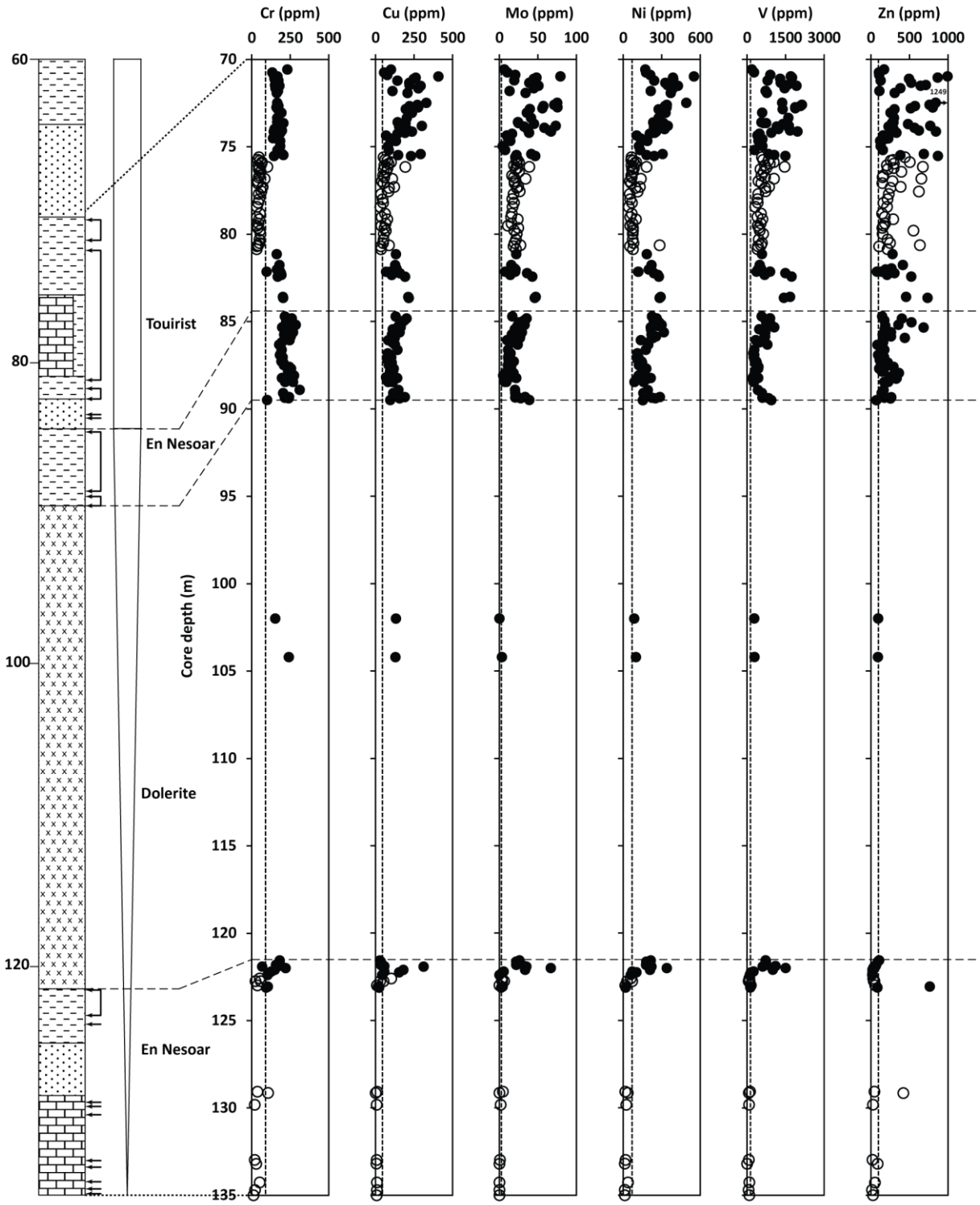
Cr (ppm)
0 250 500
Cu (ppm)
0 250 500
Mo (ppm)
0 50 100
Ni (ppm)
0 300 600
V (ppm)
0 1500 3000
Zn (ppm)
0 500 1000
1249
Touirist
En Nesoar
Dolerite
En Nesoar
Core depth (m)
60
80
100
120
70
75
80
85
90
95
100
105
110
115
120
125
130
135

Figure 5.3 Depth profiles for trace metals in S1. Vertical dotted lines indicate average shale values taken from Turekian and Wedepohl (1961). Open circles indicate carbonate-rich samples.

5.2.5 Trace metals in S2 and S4

5.2.5.1 Chromium

In both S2 and S4, Cr concentrations are mostly at or slightly above average shale (90 ppm), with the greatest enrichments (up to 392 ppm) seen towards the base of the En Nesoar (I4) Formation in S2. The mean for the En Nesoar Formation in S2 is 198 ± 95 ppm, compared to 135 ± 26 ppm in the equivalent I4 Formation in S4 (Table 5.4). In the Touirist/I5 Formation, concentrations are slightly higher in S4, with a mean of 151 ± 8 ppm compared to 120 ± 27 in S2. The I3 Formation in S4, which has been intruded by a small dolerite sill, has average Cr concentrations of 127 ± 20 ppm, similar to the overlying I4 Formation. There is little evidence for enrichment or depletion depending on redox setting, although in parts of both cores where redox conditions seem to cycle between oxic and ferruginous, oxic samples show marginally higher concentrations (see figures 5.4 and 5.5).

5.2.5.2 Copper

While in S2 Cu concentrations are generally at or above average shale (45 ppm), S4 is largely depleted in Cu. Means for the Touirist (I5) and En Nesoar (I4) formations in S2 are 74 ± 6 ppm and 84 ± 4 ppm respectively, with maximums of 146 and 194 ppm. In S4, the I5 Formation has an average Cu concentration of 22 ± 12 ppm, and the I3 Formation an average of 24 ± 14 ppm. The I4 Formation has a higher mean, of 47 ± 52 ppm, but this is increased by higher concentrations (up to 316 ppm) in a few euxinic samples. However, most euxinic samples fall within a similar range to ferruginous ones.

5.2.5.3 Molybdenum

Mo concentrations are generally comparable to average shale in both S2 and S4. S2 shows some evidence for muted enrichments, with several samples, mostly in the Touirist Formation, exceeding 10 ppm. Averages are slightly higher in S2 than in S4, with means of 7.5 ± .3 and 6.1 ± 3.3 ppm for the Touirist and En Nesoar formations in S2 compared to 4.5 ± 2.2 and 4.8 ±

3.0 for the equivalent formations in S4 (I5 and I$). The I3 Formation in S4 is very similar to the two formations above, having a mean of 5.1 ± 1.5 ppm.

5.2.5.4 Nickel

Modest enrichments in Ni relative to average shale are evident in S2, particularly towards the top of the Touirist (I5) and the bottom of the En Nesoar (I4) formations, with overall means for the two formations of 107 ± 48 and 123 ± 62 ppm respectively. Ni concentrations are generally lower in S4, with a lot of samples slightly depleted relative to average shale. The I4 Formation has marginally higher Ni concentrations, with a mean 71 ± 43 ppm, compared to 56 ± 17 and 49 ± 17 ppm in the I5 and I3 formations.

5.2.5.5 Vanadium

V concentrations generally cluster around average shale in S2 and S4, with some enrichments occurring in S2 in both the En Nesoar (I4) and Touirist (I5) formations. On average, V concentrations are slightly elevated above average shale, with means of 207 ± 112 ppm for the En Nesoar (I4) Formation and 155 ± 101 ppm for the Touirist (I5) Formation. The means for S4 are very close to average shale, being 126 ± 19, 132 ± 25 and 124 ± 1 ppm for the I3, I4 and I5 formations respectively.

5.2.5.6 Zinc

With the exception of a small number of euxinic samples, S4 is generally depleted in Zn. The highest concentrations occur in the I4 Formation, giving a mean of 149 ± 249 ppm. With only a couple of samples slightly exceeding average shale, the I3 Formation is the most depleted, with an average of 48 ± 21 ppm. With most samples at or just below average shale, the I5 Formation has a mean of 75 ± 55 ppm. On average, the equivalent formations in S2 are slightly enriched in Zn compared to S4, and average shale, with means of 128 ± 188 and 302 ± 308 for the Touirist (I5) and En Nesoar (I4) formations respectively. However, most samples cluster

around average shale with just a few samples being particularly enriched in Zn (>500 ppm), mostly at the base of the En Nesoar Formation.

Core	Formation	Cr ppm	Cu ppm	Mo ppm	Ni ppm	V ppm	Zn ppm
S2	Touirist	120 ± 27	74 ± 36	7.5 ± 5.3	107 ± 48	155 ± 101	128 ± 188
	En Nesoar	198 ± 95	84 ± 42	6.1 ± 3.3	123 ± 62	207 ± 112	302 ± 308
S4	I5	151 ± 28	22 ± 12	4.5 ± 2.2	56 ± 17	124 ± 19	75 ± 55
	I4	135 ± 26	47 ± 52	4.8 ± 3.0	71 ± 43	132 ± 25	143 ± 249
	I3	127 ± 20	24 ± 14	5.1 ± 1.5	49 ± 17	126 ± 19	48 ± 21

Table 5.4 Mean and SD for trace metals in S2 and S4

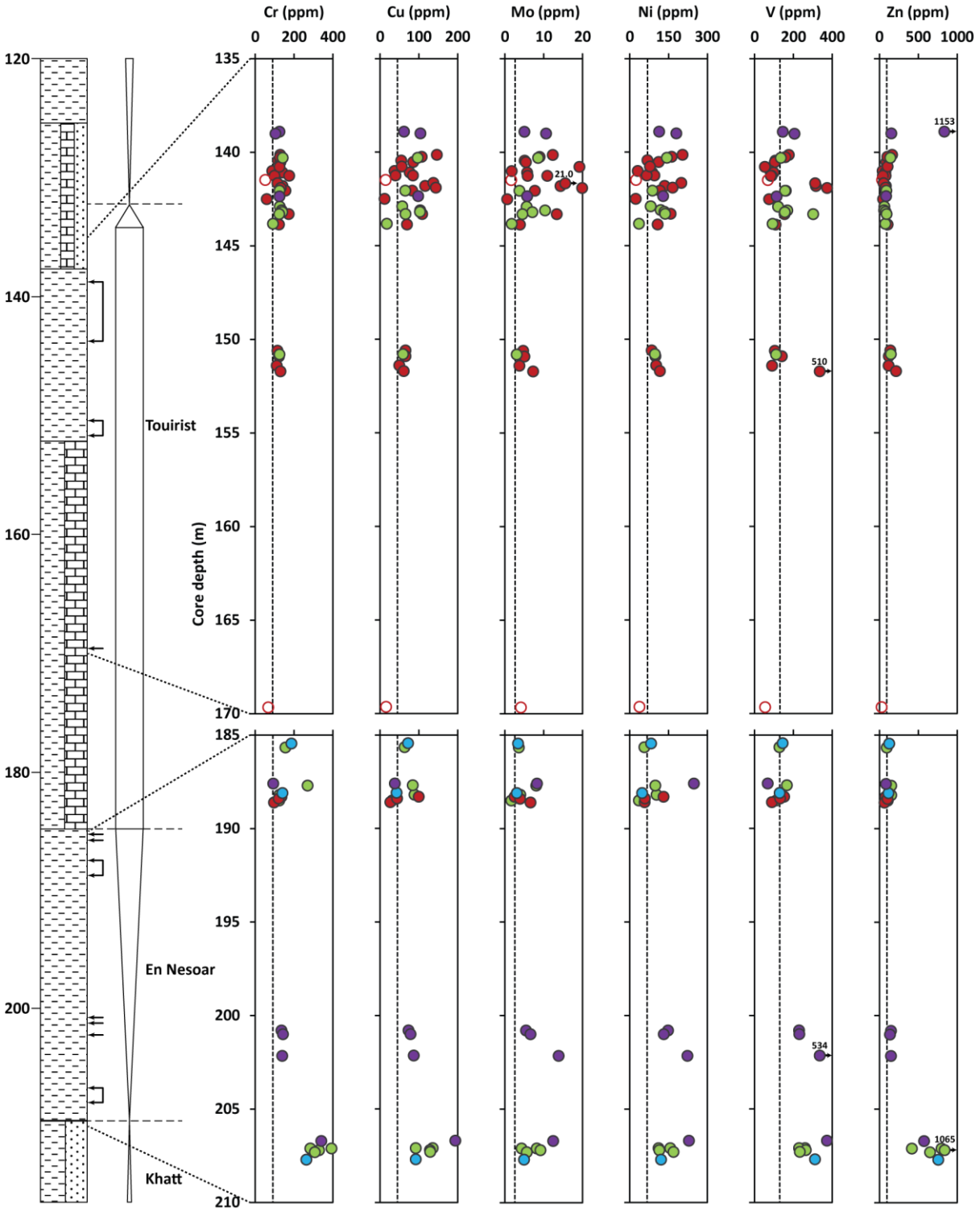

Figure 5.4 Depth profiles for trace metals in S2. Vertical dotted lines indicate average shale values taken from Turekian and Wedepohl (1961). Colour of points indicates water column redox conditions at time of

depostion, with blue being oxic, green, equivocal, red, ferruginous and purple, euxinic. Open circles indicate carbonate-rich samples.

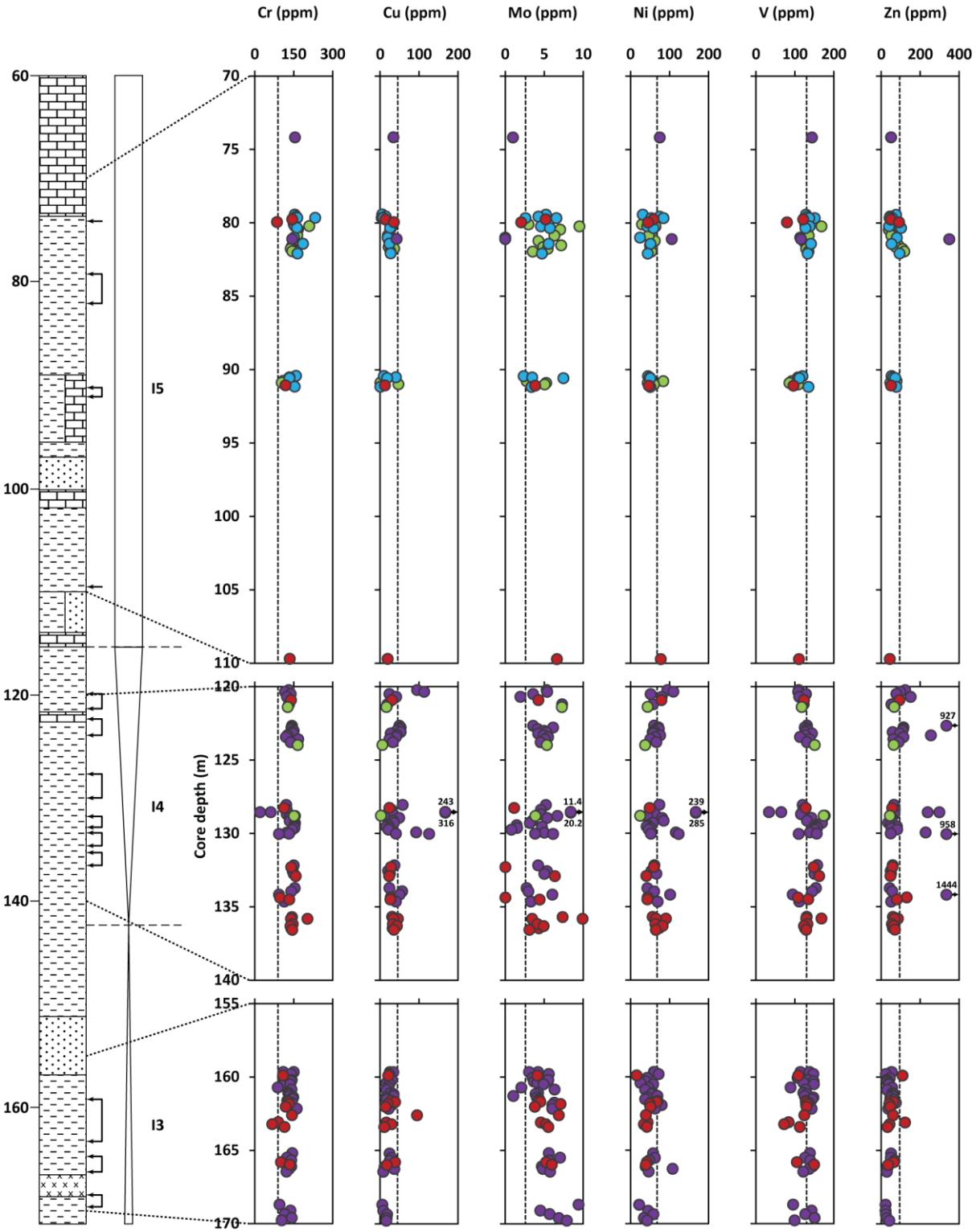

Figure 5.5 Depth profiles for trace metals in S4. Vertical dotted lines indicate average shale values taken from Turekian and Wedepohl (1961). Colour of points indicates water column redox conditions at time of depostion, with blue being oxic, green, equivocal, red, ferruginous and purple, euxinic.

5.3 Discussion

5.3.1 Assessment of the use of Fe speciation in the presence of AVS

In the initial calculation of FeHR/FeT, Fe_{AVS} is included, such that FeHR = Fe_{carb} + Fe_{ox} + Fe_{mag} + Fe_{py} + Fe_{AVS}. The first plot in Figure 5.6 demonstrates the problem with this, as FeHR/FeT exceeds 1 for most samples above the sill, and many below. FeHR/FeT ratios reach as high as 1.85, and the overall average is 1.12 ± 0.28. This is a result of Fe_{AVS} being extracted twice – by acid distillation and with the sequential phases. In a test on one sample of fine-grained coastal sediment Poulton and Canfield (2005) found that the pH 4.5 acetate extraction, intended to target carbonate Fe, also fully extracted AVS. Although the method has only been tested on freshly precipitated AVS, Poulton et al. (2010) did find in a study of 1.8 Gyr old rocks that AVS was quantitatively extracted as part of the sequential extractions. It is not however clear whether this is universally the case for Fe_{AVS} minerals, especially where they may be highly crystalline. In neither study is the composition of AVS more precisely defined – AVS can be complex and variable and includes more than one mineral previously observed in sediments e.g. greigite and mackinawite (Rickard and Morse, 2005). Evidence for incomplete Fe_{AVS} recovery during the sequential extractions might be found if Fe_{AVS} concentrations obtained from acid distillation exceeded the sum of the sequential extractions (Fe_{seq}), but this is the case for only one sample out of 155 in this study: S1 82.15 B. This sample has a particularly high Fe_{AVS} concentration of 27.89 wt%, compared to 18.17 wt % for Fe_{seq}. If Fe_{AVS} is only partially extracted with the sequential phases, the second plot, where FeHR = Fe_{carb} + Fe_{ox} + Fe_{mag} + Fe_{py}, can only provide a minimum for FeHR/FeT ratios. This definition of FeHR does produce more believable FeHR/FeT ratios, with an average of 0.87 ± 0.20 and a maximum of 1.25, but is of little use if the degree to which Fe_{AVS} has been extracted with the sequential phases is unknown.

All of the highly reactive, non-sulphidic phases, and Fe_{AVS}, can be quantitatively extracted in a boiling 12 N HCl extraction (Berner, 1970, Raiswell et al., 1994, Poulton and Canfield, 2005), and this extraction produces a considerably better result for the sample S1 82.15 B, with Fe_{HCl} being 28.13 wt%. However, the FePRS (poorly reactive sheet silicates) pool is also partially extracted in this procedure and consequently, the third plot in Figure 5.6, where FeHR = Fe_{HCl} + Fe_{py}, provides an upper limit for FeHR/FeT. This actually gives broadly similar results (average 0.89 ± 0.16) to

the previous plot except for a somewhat higher minimum (0.29 as opposed to 0.12). A crossplot of these two variations of FeHR/FeT produces a line of best fit with the equation y = 0.70x + 0.28 and an R^2 value of 0.79. However, as the FeHR/FeT indicator has not been calibrated for a FeHR value including Fe_{PRS}, it is not possible to use this to identify depositional redox conditions.

There is, however, an alternative, in the form of the Degree of Pyritization, or DOP, where DOP = Pyritic Iron/Pyritic Iron + HCl-soluble Fe (Berner, 1970, Raiswell et al., 1988). Work by Raiswell et al. (1988) on sediments from the Devonian to Cretaceous which had been classified on the basis of palaeoecological and sedimentological criteria, provided the following categories for DOP values, with suggested boundaries (as shown in Figure 5.6) set at 0.45 and 0.75:

DOP < 0.42 – Aerobic (deposited in fully oxygenated bottom waters)

0.46 < DOP < 0.80 – Restricted (deposited in waters with low oxygen concentrations)

0.55 < DOP < 0.93 – Inhospitable (little or no oxygen present in bottom waters, H_2S may be present continually or intermittently)

This can be extended to include Fe_{AVS} (Lyons and Severmann, 2006), where DOP = Fe_{py} + Fe_{AVS}/ Fe_{py} + Fe_{HCl} (termed degree of sulphidisation, DOS, by Boesen and Postma (1988)).

On the basis of the DOP parameter, the majority of samples from S1 were deposited under restricted conditions, with a large number apparently from aerobic environments, and only a few deposited under inhospitable conditions. This contrasts with all variations of FeHR/FeT, which all suggest that almost all samples were deposited under anoxic conditions, mostly ferruginous according to a plot of Fe(S)/FeHR (Fe_{py} + Fe_{AVS}/ Fe_{carb} + Fe_{ox} + Fe_{mag} + Fe_{py} + Fe_{AVS}) as shown in Figure 5.6 (although it has been shown that intermediate DOP values are possible under euxinic conditions where there is rapid accumulation of siliciclastics (Lyons and Severmann, 2006)). However, as FeHR will be overestimated, Fe(S)/FeHR ratios may be underestimated to varying degrees, depending on Fe_{AVS} concentrations and the extent to which Fe_{AVS} was extracted with the sequential phases. Interestingly, the DOP plot bears a strong resemblance to Fe(S)/FeHR (a crossplot of DOP verses Fe(S)/FeHR having a line of best fit with the equation y = 1.38x - 0.03 and

an R^2 value of 0.78), although DOP values are generally higher and more varied. Noticeably, both these plots show a sudden drop in samples immediately above or below the dolerite sill, with the exception of sample S1 89.5, which is separated from the rest of the overlying sedimentary column by a thin band of dolerite. This is also evident in the three versions of FeHR/FeT.

The above discussion highlights the inadequacies of the Fe speciation method when high concentrations of Fe_{AVS} are present – FeHR may not be determined with any degree of certainty and although minimum and maximum FeHR/FeT ratios could be calculated, it is difficult to relate these to depositional conditions due to a lack of calibration for FeHR/FeT ratios defined in these alternative ways. DOP therefore needs to be used instead in such circumstances.

A second issue to be taken into account here is whether or not it is appropriate to apply Fe-based redox proxies to this core, given that estimated temperatures (Rooney et al., 2010) of between ~288 °C (through most of the succession) and 650 °C (at the sill margins) mean that metamorphic alteration is likely to have occurred. Suggestive of this is the presence of pyrrhotite as established by XRD analysis by Rooney et al. (2010). Pyrrhotite has previously been reported in contact metamorphic aureoles (e.g. Gillett (2003)), but is apparently uncommon in marine sediments (Cornwell and Morse, 1987, Rickard and Morse, 2005, Rickard and Luther, 2007). Pyrrhotite is an acid volatile sulphide (Cornwell and Morse, 1987), so it reasonable to assume that the Fe_{AVS} pool extracted from S1 consists of pyrrhotite and is therefore metamorphic in origin. A lack of measurable AVS in the other 3 cores (some samples from S2 produced some precipitate during acid distillation, but this generally produced a stain on the filter paper that was not detectable by weighing, and no visible sign of AVS was apparent in samples from S3 and S4) supports the conclusion that Fe_{AVS} in S1 was a result of contact metamorphism during the emplacement of a dolerite sill.

A number of mechanisms for the formation of pyrrhotite have been proposed, as discussed by Gillett (2003). The mechanism Gillet favoured for the particular system he was investigating was in situ formation of pyrrhotite by the reaction of pyrite, magnetite and organic matter during metamorphic heating, even at temperatures < 200 °C. Pyrrhotite formation has also been attributed to desulphidisation at high temperature where S was lost as H_2S, or to the extraction of ferrous iron from silicates by the addition of sulphur (both of which would imply an open system).

Direct conversion of pyrite to pyrrhotite is also apparently possible at higher temperatures (~ 200 °C in graphitic rocks), with S either being lost in an open system, or reacting with a sink such as Fe from silicates to form further pyrrhotite in a closed system.

Elucidating the exact mechanism responsible for pyrrhotite formation in S1 is difficult based on the data presented here, but some observations based on Fe-speciation can be made. It is known that pyrite can be thermally decomposed to pyrrhotite, which may ultimately be oxidised to haematite or magnetite (e.g. Pelovski and Petkova (1999), Hu et al. (2006)). In an investigation of sill emplacement in Jurassic sedimentary deposits on the Isle of Skye, Yallup et al. (2013) identified evidence for the thermal decomposition of pyrite and production of pyrrhotite within 80 cm of a 3 m thick dolerite sill. Within a few cm of the contact, they observed magnetite which they concluded was a product of the oxidation of pyrrhotite. As noted earlier, in core S1 there is a drop in Fe(S)/FeHR and in DOP for the samples at the margins of the sill, which could be a result of the breakdown of pyrite and transfer of released S away form the sill. With the exception of S1 89.5, which, being encased in dolerite, might approximate to a closed system, the samples closest to the sill are noticeably depleted in Fe_{py} and have low concentrations of Fe_{AVS} compared to samples ~ 0.3 m away from the sill margins. Concomitant with this is a spike in Fe_{mag}. It therefore seems likely that, in S1, there was thermal decomposition of pyrite to pyrrhotite at the sill margins, with subsequent oxidation to magnetite occurring. However, observation of textural relationships would be needed to confirm this. Investigation of the S isotope compositions of the pyrite and pyrrhotite might also be informative (Kajiwara et al., 1981, Yamamoto, 1984).

Despite this likely production of magnetite, a decrease in the proportion of FeHR, however it is defined, to FeT, is apparent in this zone, which implies that Fe here exists in some other mineral that is not extracted by any of the techniques applied in this study. This could be the result of an unusually high (for this core) Fe_U input during deposition, or FePRS that has not been extracted by boiling HCl (Fe-bearing silicates are only partially soluble by this technique (Raiswell et al., 1994)), but given the proximity to high temperatures, it seems quite possible that it is another metamorphic Fe mineral, as yet unidentified.

Fe_{py} is generally low in the En Nesoar Formation above the sill, with concentrations on average half those in the overlying Touirist Formation. This does not seem to be related to depositional constraints, as Fe_{py} is very similar in these two formations in S2. It might, therefore, be taken as evidence for the breakdown of pyrite to pyrrhotite in the En Nesoar Formation of S1, with accompanying release of S. It has been found that the presence of carbonaceous material catalyses the breakdown of pyrite, allowing the reaction to occur at lower temperatures that it might otherwise do (Lambert, 1973, Hall, 1986). High TOC concentrations found in the in S1 could therefore have contributed to pyrite breakdown in the En Nesoar Formation, beyond the sill margins. Comparison between S1 and S2 suggests that, even with a minimum estimate for FeHR/FeT that might not include all Fe_{AVS}, rather more Fe resides in the FeHR fraction in S1 than in S2 in the En Nesoar formation (mean FeHR/FeT of 0.81 ± 0.20 verses 0.35 ± 0.13). This could be a result of S, which was released from the conversion pyrite to pyrrhotite, extracting Fe from silicates (Tracy and Robinson, 1988, Andrews and Ripley, 1989), thereby reducing the FePRS pool and increasing the FeHR pool.

Fe_{AVS} is also present in large quantities in some parts of the Touirist Formation in S1, but, given very similar Fe_{py} concentrations in this formation in S1 and S2, it seems likely that pyrrhotite in the Touirist Formation was not derived from pyrite, but was the result of S mobilised from the En Nesoar Formation reacting with Fe from silicates. Veining observed in this core is evidence of fractures which could have allowed transport of S up through the sedimentary deposits. As in the En Nesoar Formation, FeHR/FeT values are much higher in S1 than in S2 (0.96 ± 0.11 verses 0.46 ± 0.14) despite similar FeT concentrations, supporting the idea that Fe_{PRS} has been moved into the FeHR pool. It might be expected, given that the FeHR pool is defined by its reactivity towards sulphide on a diagenetic timescale, that the Fe_{carb}, Fe_{ox} and Fe_{mag} pools would react with S preferentially to Fe_{PRS}. However, the higher temperatures reached in the vicinity of the intrusion and the composition of any circulating hydrothermal fluids will have affected the stabilities of the various minerals involved in such reactions. It is also difficult to assess this by comparing concentrations of the Fe pools in S1 with S2, because it is difficult to separate these pools from Fe_{AVS}, as discussed above, and the depth plots shown in Figure 5.2 show generally similar profiles for Fe_{carb}, Fe_{ox} and Fe_{AVS}.

Fe_{AVS} is noticeably lacking in the Touirist Formation where samples are likely to be carbonate-rich (indicated by low Al and effervescence with HCl). One possibility is a lack of Fe to react with S containing fluids – FeT is lowest in this part of the core. In contrast, many carbonate-rich samples below the sill contain appreciable concentrations of Fe_{AVS}, and of FeT - comparable to the shales. However, low Fe_{AVS} could also be a result of the presence of calcite – in experiments to form magnetic minerals in Lower Jurassic argillites, Moreau et al. (2005) found that ferromagnetic iron sulphides were not present in samples containing more than 10% calcite. Magnetite, however, was formed at the expense of pyrite above 0.5% calcite. The Fe_{mag} profile in S1 shows increased concentrations (up to ~ 0.5 wt%) in a part of the Touirist Formation where Fe_{AVS} is very low – this is perhaps evidence of the metamorphic formation of magnetite in the presence of calcite.

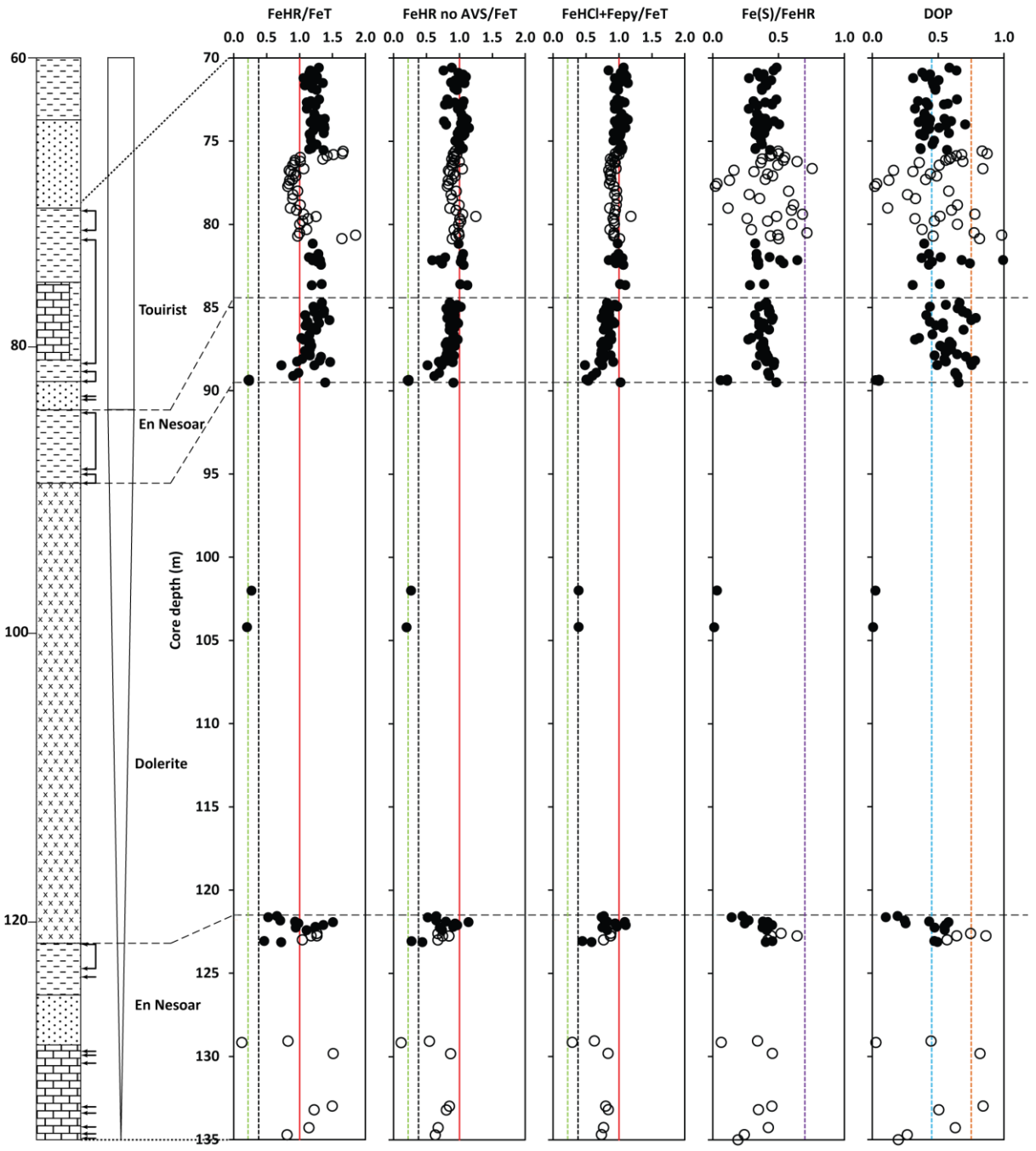

Figure 5.6 Depth profiles for Fe redox indicators in S1. See text for details on definitions of FeHR. The green dotted line represents FeHR/FeT=0.22, the black FeHR/FeT=0.38, the red FeHR/FeT=1, the purple FeP/FeHR=0.7, the blue DOP=0.45 and the orange DOP=0.75.

5.3.2 Trace metal patterns in S2 and S4

Figures 5.7 - 5.12 show plots of trace metal concentrations verses Al, TOC and Fe_{py} concentrations for S2 and S4. The aim of this section is to consider possible factors involving delivery and fixation mechanisms that have influenced the concentrations of trace metals in the sediments preserved in these two cores, in order for a comparison with S1.

A clear correlation between Cr and Al is evident in S4 (Figure 5.7d), especially in the I4 (En Nesoar) Formation, which contains the greatest range of Al and Cr concentrations. Correlations are also strong for the other two sampled formations in S4, and the slopes for the three formations are very similar, suggesting a consistent relationship between Al and Cr throughout the succession (although there is a shift to higher Al contents in the oldest I3 Formation). This suggests that Cr deposition is largely detrital. There is also evidence for a detrital Cr provenance in the Touirist (I5) Formtion in S2, with a similar gradient to that seen in S4, although the correlation is not as good (Figure 5.7a). Chromium is reportedly often mainly of detrital provenance, although, under anoxic conditions, Cr is reduced, forming cations that can complex with humic/fulvic acids or adsorb to Fe- and Mn-hydroxides, allowing export to the sediment (Tribovillard et al., 2006). Correlations of Cr with organic carbon concentrations have been observed, implying that organic matter was the main Cr host (Algeo and Maynard, 2004). However, it has been found that Cr enrichments in anoxic shale from the mid-Proterozoic are negligible, which is hypothesized to be the result of persistent oceanic Cr drawdown under pervasive anoxia (Reinhard et al., 2013). The correlation between Cr and Al for the En Nesoar (I4) Formation in S2 is, in contrast to S4 and the other formation from S2, very poor, owing to the enrichment in Cr in a number of samples, most of which are found towards the base of the formation. If these are removed, then the R^2 value improves slightly to 0.27. Although this is still a weak correlation, the data set is small, and the data points do fall on to the same trend as the samples from the overlying formation, so it is likely that those samples which are not enriched in Cr also show largely detrital Cr inputs. A weak covariation with TOC (Figure 5.7b) is apparent and the samples that do have higher Cr concentrations are also high in TOC (> 5 wt%). However, there are also samples with high concentrations of TOC that do not appear to be enriched in Cr. This could be explained by authigenic Cr enrichments only occurring when

additional Cr was available, probably following deposition (Calvert and Pedersen, 1993). Figure 5.7f suggests a good negative correlation between Cr and Fe_{py}, which is mostly likely the result of the dilution of the detrital Cr input by some exceptionally high pyrite concentrations.

Figure 5.8 shows a marked difference in the behaviour of copper between S2 and S4. Good to strong correlations between Cu and TOC concentrations exist in S2 (Figure 5.8b), but no such covariation is apparent in S4 (Figure 5.8e). However, where pyrite concentrations vary widely in S4, in the I4 (En Nesoar) Formation, a very strong correlation between Cu and Fe_{py} is evident. In the other formations in S4, and in S2, where Fe_{py} concentrations are much more restricted, such a correlation is either very weak or absent. Enrichments in Cu can occur when Cu is delivered to the sediment complexed with organic matter, and when it is scavenged from solution by Fe-Mn-oxyhydroxides (under oxic conditions). Under reducing conditions in the sediment, upon release from decaying organic matter and dissolved Fe-Mn-oxyhydroxides, Cu can then become incorporated into pyrite (Tribovillard et al., 2006). Under euxinic conditions, Cu is also removed from the water column in association with sulphide (Calvert and Pedersen, 1993, Little et al., 2015). Consequently, covariation with both TOC and Fe_{py} might be expected under the largely anoxic, sometimes sulphidic conditions recorded in S2 and S4. In S2, where TOC contents can be exceptionally high (up to nearly 40 wt%), Cu enrichments appear to be controlled by TOC. In S4, however, where TOC concentrations reach only 2.5 wt%, any enrichment in Cu seems to be almost entirely associated with high Fe_{py} in euxinic samples from one formation (I4/En Nesoar). An apparently good, negative correlation between Cu and Al in the I4 Formation in S4 is likely to reflect a dilution of the Al content by unusually high pyrite concentrations.

Molybdenum (Figure 5.9) presents a very similar picture to copper for both cores, with a covariation between TOC and Mo apparent in S2 and a fairly good correlation between Fe_{py} and Mo occurring in the I4 Formation of S4. Mo is known to be concentrated in the sediment under euxinic conditions. In modern oceans, Mo is abundant owing to its existence in the form of a low reactivity molybdate ion under oxic conditions (Scott and Lyons, 2012), but Helz et al. (1996) demonstrated that with sufficient hydrogen sulphide present (which they termed a

"geochemical switch"), molybdate is converted to particle-reactive thiomolybdates. Their experimental work showed that these ions can then be scavenged by Fe sulphide minerals and organic matter, allowing sequestration in the sediment under euxinic conditions. This can lead to high Mo concentrations (tens to hundreds of ppm) in modern environments and Phanerozoic shales (Lyons et al., 2009), although only muted enrichments are observed for much of the Precambrian, which is interpreted to be the result of persistent sulphidic sinks suppressing the size of the oceanic Mo reservoir (Scott et al., 2008). Given the link between Mo and sulphide concentrations, covariation between Mo and Fe_{py} might be expected – and such correlations have been reported (Helz et al. (1996) and references therein), but Chappaz et al. (2014) have, in work on both modern euxinic muds and recent and ancient black shales, demonstrated that pyrite is a relatively minor host phase for Mo. Strong correlations between TOC and Mo have however been frequently observed (e.g. Lyons et al. (2009)), and are taken to imply that most sedimentary Mo resides in organic matter (Algeo and Lyons, 2006). By analysing patterns of covariation between Mo and TOC in modern anoxic marine environments, Algeo and Lyons (2006) have demonstrated that availability of Mo in the basin of deposition also influences Mo enrichment in euxinic sediments. They found that decreases in $[Mo]_S$/TOC ratios correlated with increasing water mass restriction, which was inferred to be a result of removal of Mo from the water column without resupply to the water column from other sources. They also found that $[Mo]_S$ burial fluxes peaked under weakly sulphidic conditions, then decreased at higher H_2S concentrations. With slopes of 0.43 and 0.47, both the En Nesoar (I4) and Touirist (I5) formations in S2 show Mo/TOC ratios significantly lower (one to two orders of magnitude) than any of the data set presented by Algeo and Lyons (2006), perhaps indicative of the limited Mo availability expected during the mid-Proterozoic. It has previously been suggested by Gilleaudeau and Kah (2013b) that sequestration of Mo in proximal locations in the Mesoproterozic Taoudeni Basin led to a critical depletion in Mo in offshore waters, which may have had an impact on early eukaryote ecology.

Similarly to copper and molybdenum, in S2 there is a fairly good correlation between nickel and TOC, with some covariation between Ni and Fe_{py} also apparent in the En Nesoar (I4) Formation (Figure 5.10). In contrast to S2, there is no correlation between TOC and Ni in S4,

but a strong correlation between Fe_{py} and Ni is seen in the I4 (En Nesoar) Formation. Unlike for Cu and Mo, covariation between Fe_{py} and Ni is also apparent in the I3 and I5 (Touirist) formations. Delivery of Ni to the sediment is thought to occur mainly in association with organometallic complexes (Tribovillard et al., 2006), yet apparently sulphides are either a moderately important sink (Huerta-Diaz and Morse, 1992) or the main sink (Calvert and Pedersen, 1993) of Ni. It seems that Ni can become enriched in sediments as a result of scavenging of Ni by organic matter in the water column, which is then, under reducing conditions, incorporated into authigenic pyrite following organic matter breakdown after deposition (Tribovillard et al., 2006, Huerta-Diaz and Morse, 1992). Also, potentially important for the Taoudeni Basin during the Mesoproterozoic, is the finding that carbonated green rust could be an important Ni shuttle under ferruginous conditions (Zegeye et al., 2012). Correlations between Ni and TOC have previously been observed in both modern sediments and ancient shales (e.g. (Little et al., 2015, Algeo and Maynard, 2004)).

Covariation with TOC is again apparent in S2 for vanadium. Although the R^2 value for the Touirist (I5) Formation shown in Figure 5.11b suggests only a weak correlation, removal of the sample that appears to be unusually high in V in comparison to TOC for this formation produces a line of best fit with an R^2 value of 0.55, suggesting a fairly good correlation. In S4, there is no correlation between V and TOC, and apparently V and Fe_{py} correlate negatively in the I4 (En Nesoar) Formation. There is, however, a good correlation between V and Al in all three formations in S4. Such a correlation between V and Al, implying a mainly detrital provenance, is apparently rare (Tribovillard et al., 2006). Under oxic conditions, V exists as V(V) in the form of vanadate ions. Under mildly reducing conditions, V(V) is reduced to V(VI) ionic species, which may be removed to the sediment following formation of organometallic ligands, as well as through surface adsorption processes (Algeo and Maynard, 2004). Where H_2S is present in the water column, V is further reduced to V(III), which may be taken up by geoporphyrins or be precipitated as solid oxide or hydroxide phases. Algeo and Maynard (2004) found that in samples from non-sulfidic anoxic facies, V resided in an “organic fraction”, with lesser amounts in the “sulfidic” fraction, while in samples deposited under euxinic conditions, V was found to be mainly in the “sulfidic” fraction. They suggest that V was probably not taken

up in solid solution by Fe-sulphides, but was deposited as insoluble oxyhydroxides formed in the water column due to the presence of H_2S. They interpreted a strong correlation between V and TOC up to 10 wt% TOC as being the result of organometallic complexes being the main sink under non-sulphidic anoxic conditions, and increased enrichment and poor TOC-V correlations above 10 wt% TOC as signifying V drawdown in association with authigenic minerals formed due to presence of H_2S in the water column. Cox et al. (2016) found a very similar pattern in a study of a Mesoproterozoic succession (ca. 1.4 Ga), although their euxinic threshold is 4 wt% TOC. A strong correlation between V and Al in all formations from S4 indicates that, despite anoxic conditions, where, as seen in S2, V enrichments might be expected, V deposition in S4 was entirely detrital.

Figure 5.12f suggests that in the upper two formations studied in S4, there was a relationship between Zn and Fe_{py}. Noticeably, all Zn enriched samples in this core are euxinic (Figure 5.5). An R^2 value of 0.57 suggests a good correlation between Zn and Fe_{py} also exists in the Touirst (I5) Formation, although this is largely based on one sample. There is, in contrast to Cu, Mo, Ni and V, no evidence of covariation between Zn and TOC. It is thought that, in oxic waters, Zn is mainly present as complexes with humic and fulvic acids, whilst under anoxic conditions, dissolved Zn is rapidly precipitated as sulphide phases (Algeo and Maynard, 2004). Following delivery to the sediment, decay of organic matter by sulphate-reducing bacteria may release Zn, allowing subsequent uptake by authigenic Fe sulphides. Algeo and Maynard (2004) reported that, in non-sulphidic facies, Zn was found mainly in the "organic fraction", and the association between Zn and TOC was very strong, but in euxinic facies, Zn was found mainly in the "sulfidic" fraction, implying that under non-sulphidic conditions Zn was predominantly bound in organic complexes, and under euxinic conditions Zn was present in solid solution with Fe-sulfides. Little et al. (2015) found that covariations between Zn and TOC in samples from the Cariaco Basin and Peru Margin fell on the same trend, which they suggested implied that organic C was the only significant source of Zn to the sediment in all locations. They concluded that this trend could be explained entirely as being the result of direct uptake by plankton, without the need for secondary scavenging by organic C.

A lack of correlation between trace metals at low TOC concentrations (~ < 2 wt%) has previously been observed, and has been interpreted as being a result of largely detrital deposition under oxic-dysoxic conditions (Tribovillard et al., 2006, Algeo and Maynard, 2004). However, Fe speciation data suggests that, in the lower two formations at least, S4 records pervasively anoxic conditions, suggesting that lack of trace metal enrichment here is likely a result of low oceanic availability, due to effective stripping of trace metals from seawater here, or sequestration in more proximal locations (i.e. S2) – as previously suggested for Mo, V and Zn by Gilleaudeau and Kah (2015). Sulphidisation of organic matter may also be a factor – results presented in section 3.2.3 show a discrepancy between sulphide sulphur and total sulphur for the En Nesoar (I4) and Touirist (I5) Formations in S2, suggesting that a significant proportion of S in some samples resides in a phase that is not a Fe sulphide, likely organic S given the high TOC concentrations. This is not seen for S4, where almost all reduced sulphur appears to be found in pyrite.

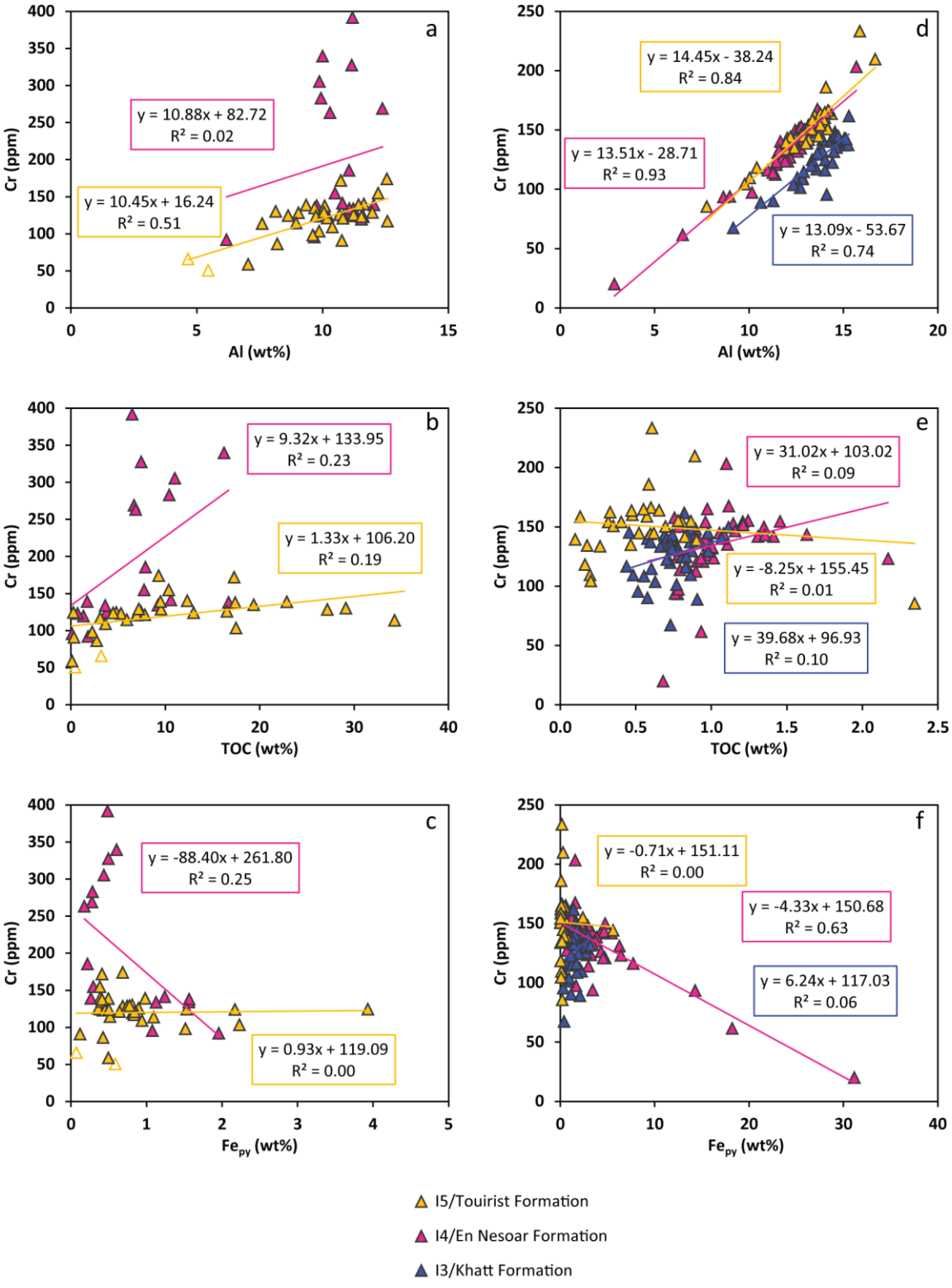
a
y = 10.88x + 82.72
R² = 0.02
y = 10.45x + 16.24
R² = 0.51
Cr (ppm)
Al (wt%)
d
y = 14.45x - 38.24
R² = 0.84
y = 13.51x - 28.71
R² = 0.93
y = 13.09x - 53.67
R² = 0.74
Cr (ppm)
Al (wt%)
b
y = 9.32x + 133.95
R² = 0.23
y = 1.33x + 106.20
R² = 0.19
Cr (ppm)
TOC (wt%)
e
y = 31.02x + 103.02
R² = 0.09
y = -8.25x + 155.45
R² = 0.01
y = 39.68x + 96.93
R² = 0.10
Cr (ppm)
TOC (wt%)
c
y = -88.40x + 261.80
R² = 0.25
y = 0.93x + 119.09
R² = 0.00
Cr (ppm)
Fepy (wt%)
f
y = -0.71x + 151.11
R² = 0.00
y = -4.33x + 150.68
R² = 0.63
y = 6.24x + 117.03
R² = 0.06
Cr (ppm)
Fepy (wt%)
I5/Touirist Formation
I4/En Nesoar Formation
I3/Khatt Formation

Figure 5.7 Crossplots of Cr with Al, TOC and Fe_{py} for S2 (a, b and c) and S4 (d, e and f), plotted by formation. Lines of best fit and equations are colour coded using the same key, shown beneath the plots. Open triangles indicate carbonate-rich samples.

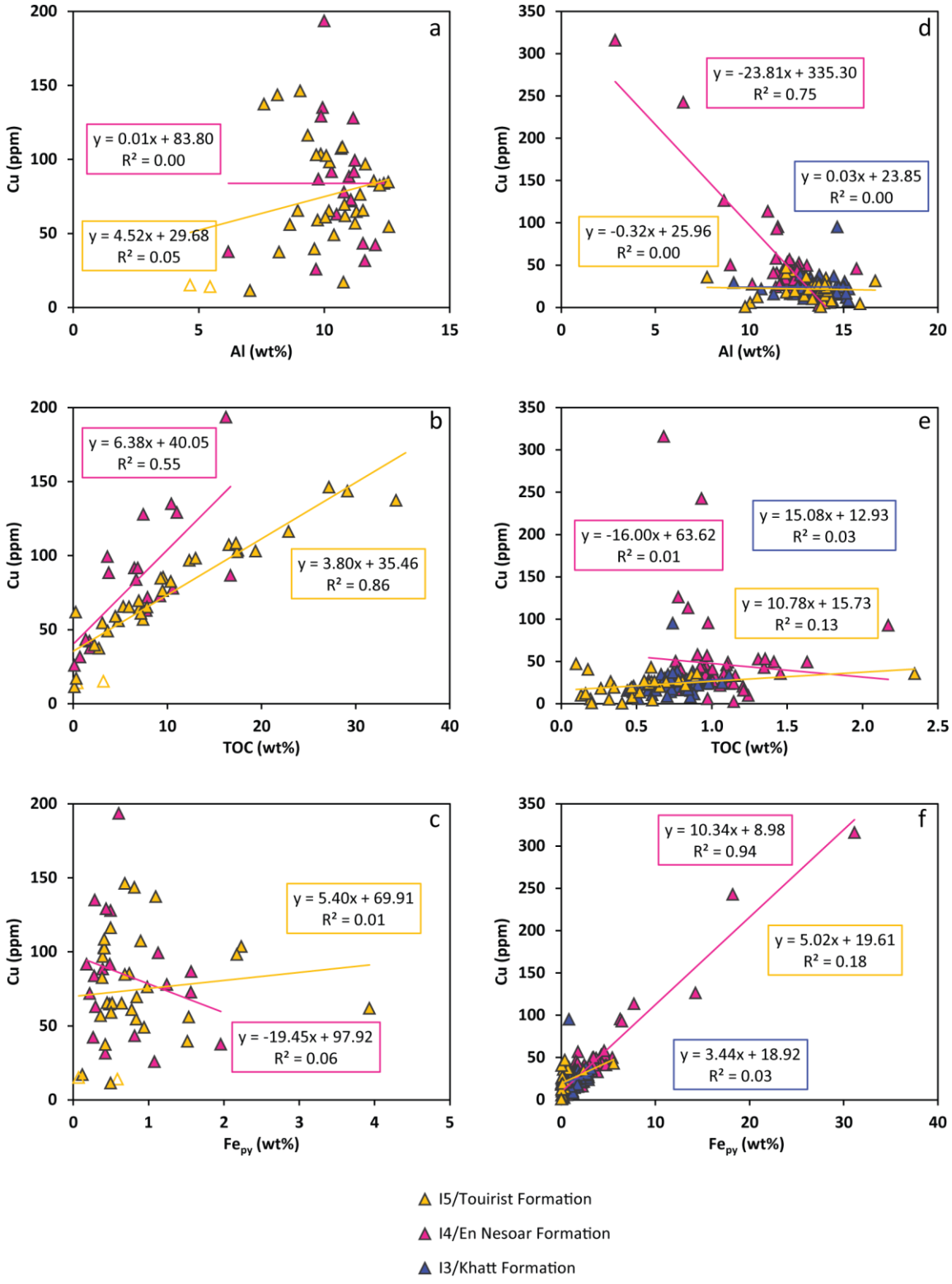
a
y = 0.01x + 83.80
R² = 0.00
y = 4.52x + 29.68
R² = 0.05
Cu (ppm)
Al (wt%)
d
y = -23.81x + 335.30
R² = 0.75
y = 0.03x + 23.85
R² = 0.00
y = -0.32x + 25.96
R² = 0.00
Cu (ppm)
Al (wt%)
b
y = 6.38x + 40.05
R² = 0.55
y = 3.80x + 35.46
R² = 0.86
Cu (ppm)
TOC (wt%)
e
y = -16.00x + 63.62
R² = 0.01
y = 15.08x + 12.93
R² = 0.03
y = 10.78x + 15.73
R² = 0.13
Cu (ppm)
TOC (wt%)
c
y = 5.40x + 69.91
R² = 0.01
y = -19.45x + 97.92
R² = 0.06
Cu (ppm)
Fe$_{py}$ (wt%)
f
y = 10.34x + 8.98
R² = 0.94
y = 5.02x + 19.61
R² = 0.18
y = 3.44x + 18.92
R² = 0.03
Cu (ppm)
Fe$_{py}$ (wt%)
I5/Touirist Formation
I4/En Nesoar Formation
I3/Khatt Formation

Figure 5.8 Crossplots of Cu with Al, TOC and Fe_{py} for S2 (a, b and c) and S4 (d, e and f), plotted by formation. Lines of best fit and equations are colour coded using the same key, shown beneath the plots. Open triangles indicate carbonate-rich samples.

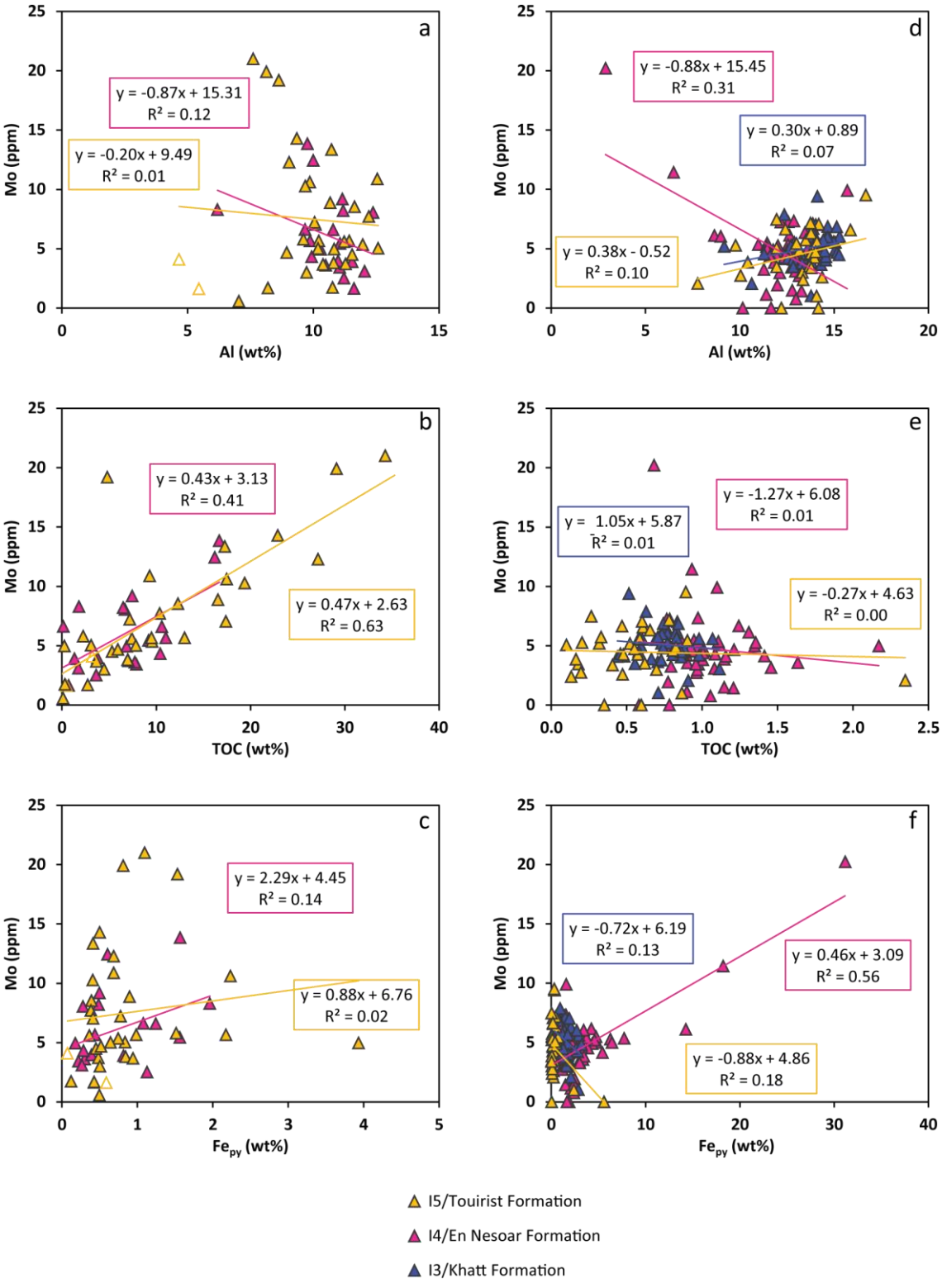
a
y = -0.87x + 15.31
R² = 0.12
y = -0.20x + 9.49
R² = 0.01
Mo (ppm)
Al (wt%)
d
y = -0.88x + 15.45
R² = 0.31
y = 0.30x + 0.89
R² = 0.07
y = 0.38x - 0.52
R² = 0.10
Mo (ppm)
Al (wt%)
b
y = 0.43x + 3.13
R² = 0.41
y = 0.47x + 2.63
R² = 0.63
Mo (ppm)
TOC (wt%)
e
y = -1.27x + 6.08
R² = 0.01
y = 1.05x + 5.87
R² = 0.01
y = -0.27x + 4.63
R² = 0.00
Mo (ppm)
TOC (wt%)
c
y = 2.29x + 4.45
R² = 0.14
y = 0.88x + 6.76
R² = 0.02
Mo (ppm)
Fepy (wt%)
f
y = -0.72x + 6.19
R² = 0.13
y = 0.46x + 3.09
R² = 0.56
y = -0.88x + 4.86
R² = 0.18
Mo (ppm)
Fepy (wt%)
I5/Touirist Formation
I4/En Nesoar Formation
I3/Khatt Formation

Figure 5.9 Crossplots of Mo with Al, TOC and Fe_{py} for S2 (a, b and c) and S4 (d, e and f), plotted by formation. Lines of best fit and equations are colour coded using the same key, shown beneath the plots. Open triangles indicate carbonate-rich samples.

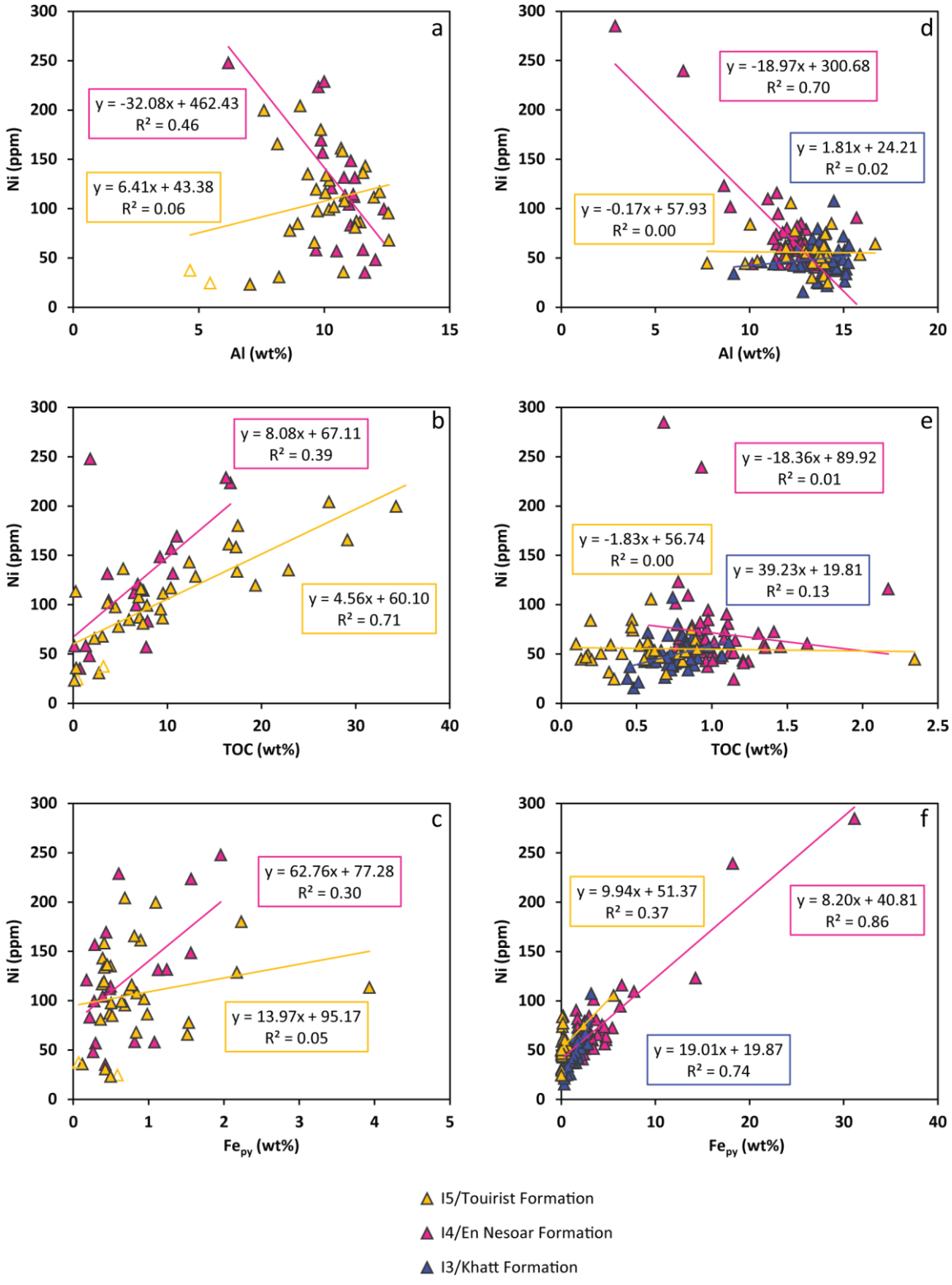
a
y = -32.08x + 462.43
R² = 0.46
y = 6.41x + 43.38
R² = 0.06
Ni (ppm)
Al (wt%)
d
y = -18.97x + 300.68
R² = 0.70
y = 1.81x + 24.21
R² = 0.02
y = -0.17x + 57.93
R² = 0.00
Ni (ppm)
Al (wt%)
b
y = 8.08x + 67.11
R² = 0.39
y = 4.56x + 60.10
R² = 0.71
Ni (ppm)
TOC (wt%)
e
y = -18.36x + 89.92
R² = 0.01
y = -1.83x + 56.74
R² = 0.00
y = 39.23x + 19.81
R² = 0.13
Ni (ppm)
TOC (wt%)
c
y = 62.76x + 77.28
R² = 0.30
y = 13.97x + 95.17
R² = 0.05
Ni (ppm)
Fepy (wt%)
f
y = 9.94x + 51.37
R² = 0.37
y = 8.20x + 40.81
R² = 0.86
y = 19.01x + 19.87
R² = 0.74
Ni (ppm)
Fepy (wt%)
I5/Touirist Formation
I4/En Nesoar Formation
I3/Khatt Formation

Figure 5.10 Crossplots of Ni with Al, TOC and Fe_{py} for S2 (a, b and c) and S4 (d, e and f), plotted by formation. Lines of best fit and equations are colour coded using the same key, shown beneath the plots. Open triangles indicate carbonate-rich samples.

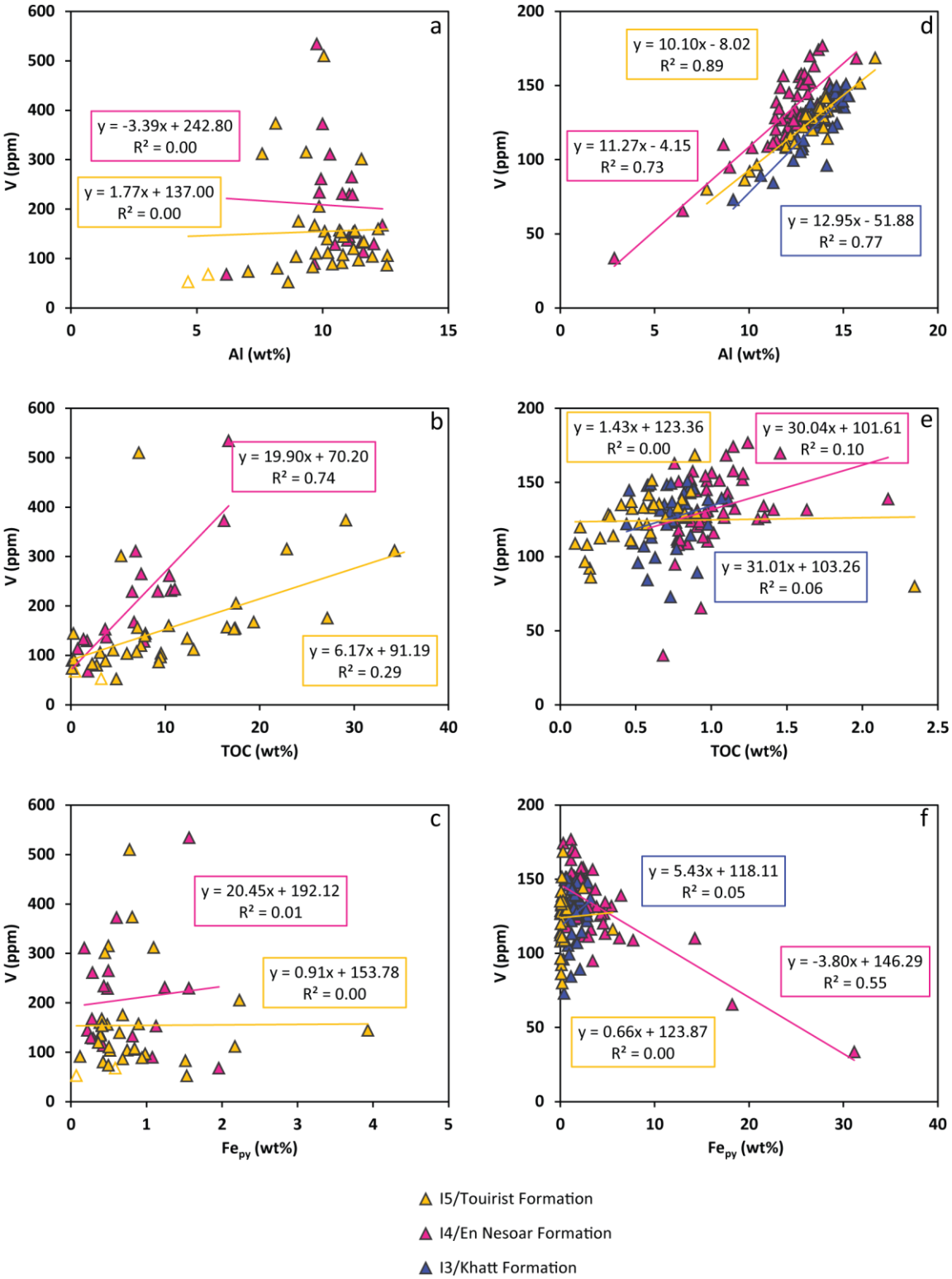
a
y = -3.39x + 242.80
R² = 0.00
y = 1.77x + 137.00
R² = 0.00
V (ppm)
Al (wt%)
d
y = 10.10x - 8.02
R² = 0.89
y = 11.27x - 4.15
R² = 0.73
y = 12.95x - 51.88
R² = 0.77
V (ppm)
Al (wt%)
b
y = 19.90x + 70.20
R² = 0.74
y = 6.17x + 91.19
R² = 0.29
V (ppm)
TOC (wt%)
e
y = 1.43x + 123.36
R² = 0.00
y = 30.04x + 101.61
R² = 0.10
y = 31.01x + 103.26
R² = 0.06
V (ppm)
TOC (wt%)
c
y = 20.45x + 192.12
R² = 0.01
y = 0.91x + 153.78
R² = 0.00
V (ppm)
Fepy (wt%)
f
y = 5.43x + 118.11
R² = 0.05
y = -3.80x + 146.29
R² = 0.55
y = 0.66x + 123.87
R² = 0.00
V (ppm)
Fepy (wt%)
I5/Touirist Formation
I4/En Nesoar Formation
I3/Khatt Formation

Figure 5.11 Crossplots of V with Al, TOC and Fe_{py} for S2 (a, b and c) and S4 (d, e and f), plotted by formation. Lines of best fit and equations are colour coded using the same key, shown beneath the plots. Open triangles indicate carbonate-rich samples.

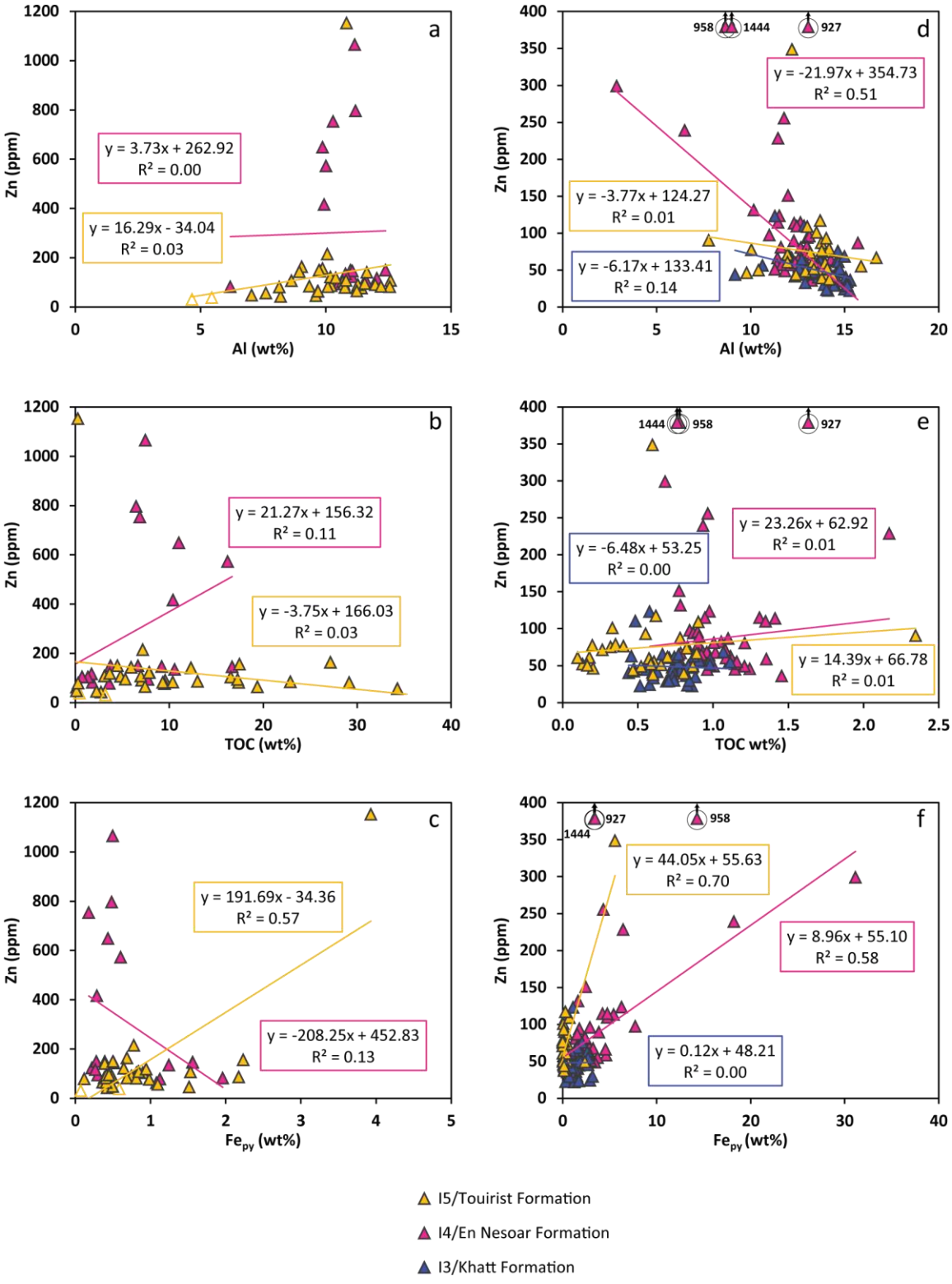
a
y = 3.73x + 262.92
R² = 0.00
y = 16.29x - 34.04
R² = 0.03
Zn (ppm)
Al (wt%)
d
958
1444
927
y = -21.97x + 354.73
R² = 0.51
y = -3.77x + 124.27
R² = 0.01
y = -6.17x + 133.41
R² = 0.14
Zn (ppm)
Al (wt%)
b
y = 21.27x + 156.32
R² = 0.11
y = -3.75x + 166.03
R² = 0.03
Zn (ppm)
TOC (wt%)
e
1444
958
927
y = 23.26x + 62.92
R² = 0.01
y = -6.48x + 53.25
R² = 0.00
y = 14.39x + 66.78
R² = 0.01
Zn (ppm)
TOC wt%)
c
y = 191.69x - 34.36
R² = 0.57
y = -208.25x + 452.83
R² = 0.13
Zn (ppm)
Fepy (wt%)
f
927
958
1444
y = 44.05x + 55.63
R² = 0.70
y = 8.96x + 55.10
R² = 0.58
y = 0.12x + 48.21
R² = 0.00
Zn (ppm)
Fepy (wt%)
I5/Touirist Formation
I4/En Nesoar Formation
I3/Khatt Formation

Figure 5.12 Crossplots of Zn with Al, TOC and Fe_{py} for S2 (a, b and c) and S4 (d, e and f), plotted by formation. Lines of best fit and equations are colour coded using the same key, shown beneath the plots. Open triangles indicate carbonate-rich samples.

5.3.3 Trace metal patterns in S1 compared to S2 and S4

Although Rooney et al. (2010) concluded that Re-Os ORS systematics have not been significantly affected by flash pyrolysis, this may not be the case for other trace elements. Indeed, figures 5.13 - 5.18 suggest that repartitioning of trace elements during hydrothermal fluid flow has occurred.

As in S2 and S4, S1 shows a strong correlation between Cr and Al in the Touirist (I5) Formation, with a gradient similar to those seen in S2 and S4, suggesting a mainly detrital control. Consistent with the conclusion that Cr concentrations depend upon detrital content, carbonate-rich samples also plot on this trend. However, Figure 5.13a suggests that the samples from the En Nesoar (I4) Formation from above the sill are enriched in Cr relative to the Tourist Formation. This coud be a result of authigenic enrichment of the precursory sediments, as seen in some samples in the same formation in S2. However, while the weak covariation between Cr and TOC seen in S2 (Figure 5.7b) can also be recognised in S1 in the Tourist Formation and in the En Nesoar Formation below the sill, it appears to be totally absent in the En Nesoar Formation below the sill (Figure 5.13b). Most samples from the En Nesoar Formation below the sill fall on the same trend as those from the Touirist Formation. Those that don't are those that are closest to the sill. This suggests that enrichments in Cr may be related to proximity of the sill, and a hydrothermal Cr input.

The other metals all show fairly good to good correlations with TOC in the Touirist Formation (figures 5.14 – 5.18), and in some cases in the En Nesoar Formation above or below the sill. Carbonate-rich samples tend to fall in the same trends within a formation, suggesting organic C is a more important factor in trace metal concentrations than carbonate contents. However, for similar TOC concentrations, the samples from the En Nesoar Formation, both above and below the sill, are depleted relative to the Touirist Formation, suggesting that metals were leached from organic matter close to the sill and repartitioned in association with organic matter further away. Higher concentrations of trace metals in S1 compared to S2, where similar covariations with TOC are seen, is consistent with this. Although it seems within the realms of possibility that, being more proximal, S1 may have been exposed to and drawn down higher

ocean metal concentrations and therefore could have become more enriched than S2 at the time of deposition, some particularly high concentrations, particularly of V and Zn, suggest an alternative source, namely hydrothermal fluids.

Cu, Mo, Ni, V and Zn also show some evidence of covariation with Fe_{py} in the Tourist Formation, but not on the whole in the En Nesoar Formation, suggesting an association between pyrite and trace metal that exists in the Touirist Formation does not exist in the En Nesoar Formation. This could perhaps be the result of Fe_{py} breakdown to produce pyrrhotite releasing trace metals that were either deposited with pyrite or had become associated with pyrite during early diagenesis. Alternatively, trace metals released during metamorphic alteration of the En Nesoar Formation may have become associated with pyrite in the Touirist Formation during repartitioning by hydrothermal fluids. Trace metals may also have been able to form metal sulphides with S released from the thermal decomposition of pyrite (Lambert, 1973).

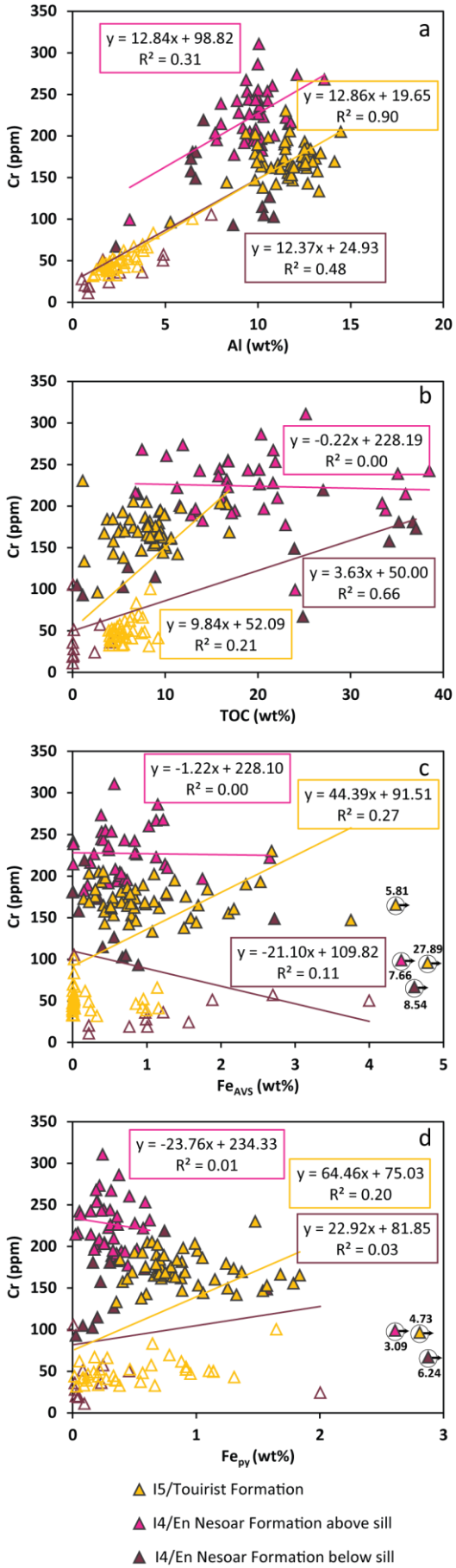
a
y = 12.84x + 98.82
R² = 0.31
y = 12.86x + 19.65
R² = 0.90
y = 12.37x + 24.93
R² = 0.48
Cr (ppm)
Al (wt%)
b
y = -0.22x + 228.19
R² = 0.00
y = 3.63x + 50.00
R² = 0.66
y = 9.84x + 52.09
R² = 0.21
Cr (ppm)
TOC (wt%)
c
y = -1.22x + 228.10
R² = 0.00
y = 44.39x + 91.51
R² = 0.27
y = -21.10x + 109.82
R² = 0.11
5.81
27.89
7.66
8.54
Cr (ppm)
Fe_AVS (wt%)
d
y = -23.76x + 234.33
R² = 0.01
y = 64.46x + 75.03
R² = 0.20
y = 22.92x + 81.85
R² = 0.03
4.73
3.09
6.24
Cr (ppm)
Fe_py (wt%)
I5/Touirist Formation
I4/En Nesoar Formation above sill
I4/En Nesoar Formation below sill

Figure 5.13 Crossplots of Cr with Al, TOC, Fe_{AVS} and Fe_{py} for S1 plotted by formation. Lines of best fit and equations are colour coded using the same key, shown beneath the plots. Open triangles indicate carbonate-rich samples.

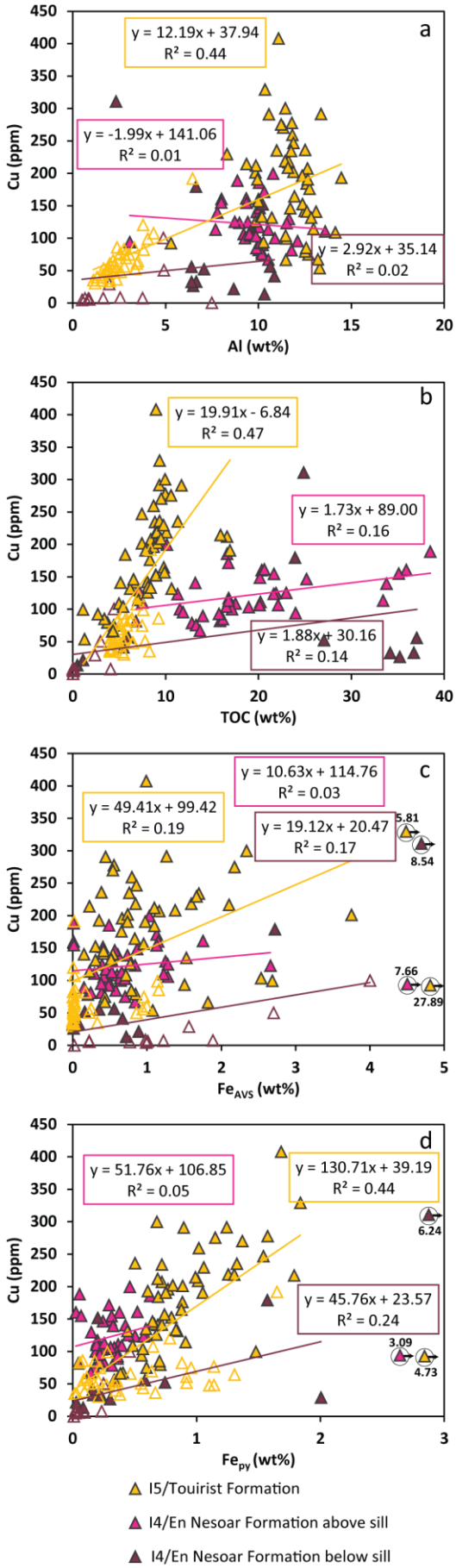
a
y = 12.19x + 37.94
R² = 0.44
y = -1.99x + 141.06
R² = 0.01
y = 2.92x + 35.14
R² = 0.02
Cu (ppm)
Al (wt%)
b
y = 19.91x - 6.84
R² = 0.47
y = 1.73x + 89.00
R² = 0.16
y = 1.88x + 30.16
R² = 0.14
Cu (ppm)
TOC (wt%)
c
y = 10.63x + 114.76
R² = 0.03
y = 49.41x + 99.42
R² = 0.19
y = 19.12x + 20.47
R² = 0.17
5.81
8.54
7.66
27.89
Cu (ppm)
Fe$_{AVS}$ (wt%)
d
y = 51.76x + 106.85
R² = 0.05
y = 130.71x + 39.19
R² = 0.44
6.24
y = 45.76x + 23.57
R² = 0.24
3.09
4.73
Cu (ppm)
Fe$_{py}$ (wt%)
I5/Touirist Formation
I4/En Nesoar Formation above sill
I4/En Nesoar Formation below sill

Figure 5.14 Crossplots of Cu with Al, TOC, Fe_{AVS} and Fe_{py} for S1 plotted by formation. Lines of best fit and equations are colour coded using the same key, shown beneath the plots. Open triangles indicate carbonate-rich samples.

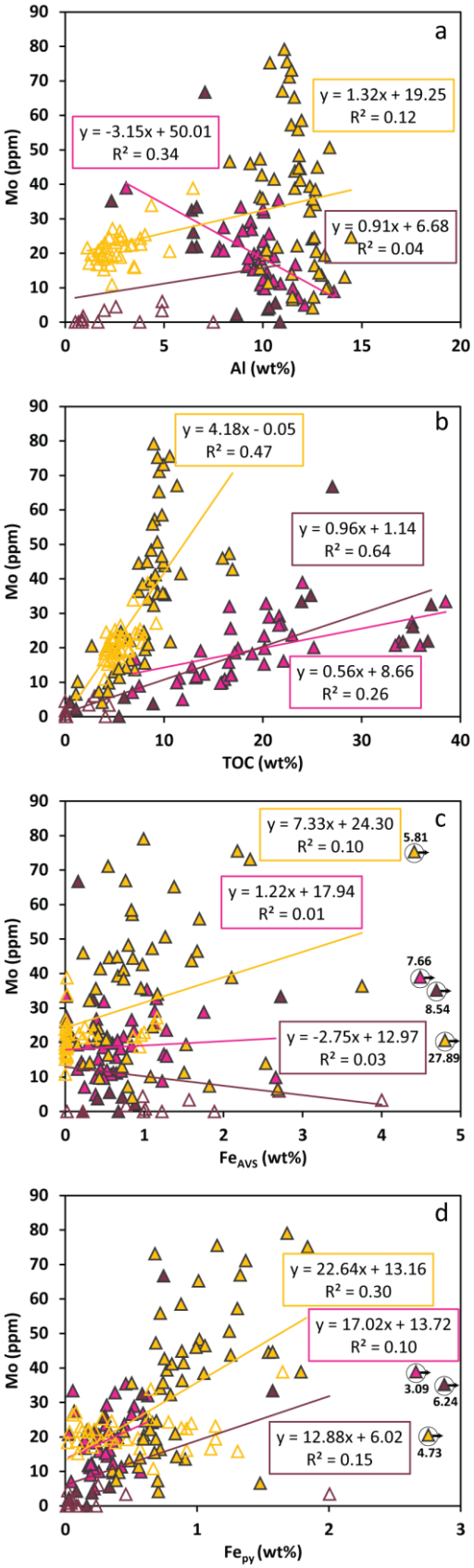
a
y = 1.32x + 19.25
R² = 0.12
y = -3.15x + 50.01
R² = 0.34
y = 0.91x + 6.68
R² = 0.04
Mo (ppm)
Al (wt%)
b
y = 4.18x - 0.05
R² = 0.47
y = 0.96x + 1.14
R² = 0.64
y = 0.56x + 8.66
R² = 0.26
Mo (ppm)
TOC (wt%)
c
y = 7.33x + 24.30
R² = 0.10
y = 1.22x + 17.94
R² = 0.01
y = -2.75x + 12.97
R² = 0.03
5.81
7.66
8.54
27.89
Mo (ppm)
Fe_AVS (wt%)
d
y = 22.64x + 13.16
R² = 0.30
y = 17.02x + 13.72
R² = 0.10
y = 12.88x + 6.02
R² = 0.15
3.09
6.24
4.73
Mo (ppm)
Fe_py (wt%)
I5/Touirist Formation
I4/En Nesoar Formation above sill
I4/En Nesoar Formation below sill

Figure 5.15 Crossplots of Mo with Al, TOC, Fe_{AVS} and Fe_{py} for S1 plotted by formation. Lines of best fit and equations are colour coded using the same key, shown beneath the plots. Open triangles indicate carbonate-rich samples.

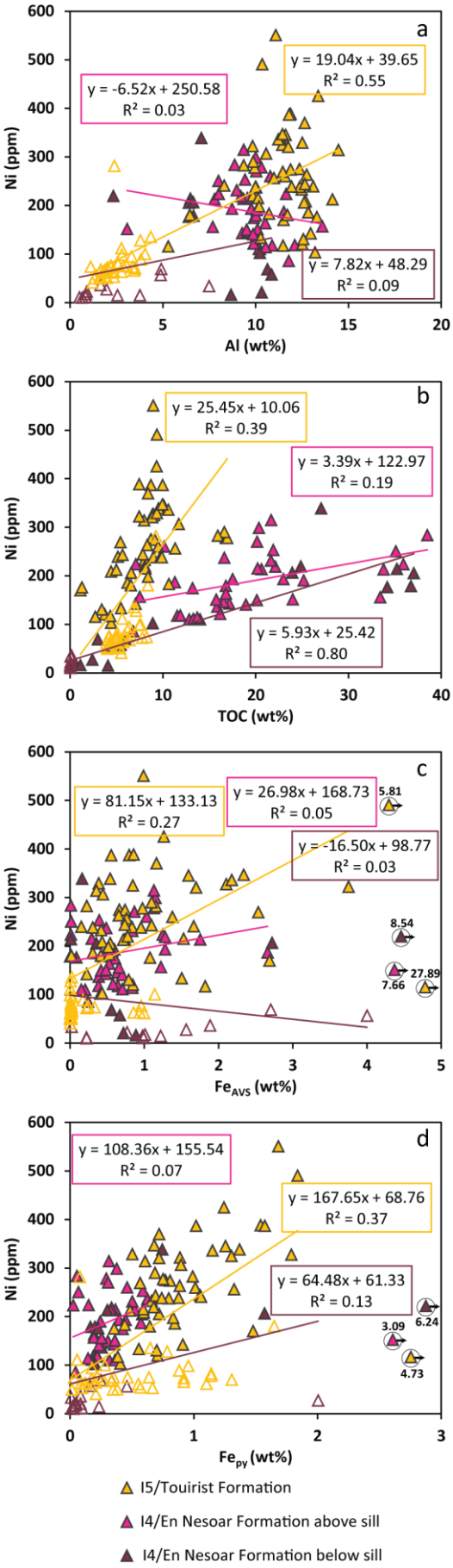
a
y = 19.04x + 39.65
R² = 0.55
y = -6.52x + 250.58
R² = 0.03
y = 7.82x + 48.29
R² = 0.09
Ni (ppm)
Al (wt%)
b
y = 25.45x + 10.06
R² = 0.39
y = 3.39x + 122.97
R² = 0.19
y = 5.93x + 25.42
R² = 0.80
Ni (ppm)
TOC (wt%)
c
y = 81.15x + 133.13
R² = 0.27
y = 26.98x + 168.73
R² = 0.05
y = -16.50x + 98.77
R² = 0.03
5.81
8.54
27.89
7.66
Ni (ppm)
Fe_AVS (wt%)
d
y = 108.36x + 155.54
R² = 0.07
y = 167.65x + 68.76
R² = 0.37
y = 64.48x + 61.33
R² = 0.13
6.24
3.09
4.73
Ni (ppm)
Fe_py (wt%)
I5/Touirist Formation
I4/En Nesoar Formation above sill
I4/En Nesoar Formation below sill

Figure 5.16 Crossplots of Ni with Al, TOC, Fe_{AVS} and Fe_{py} for S1 plotted by formation. Lines of best fit and equations are colour coded using the same key, shown beneath the plots. Open triangles indicate carbonate-rich samples.

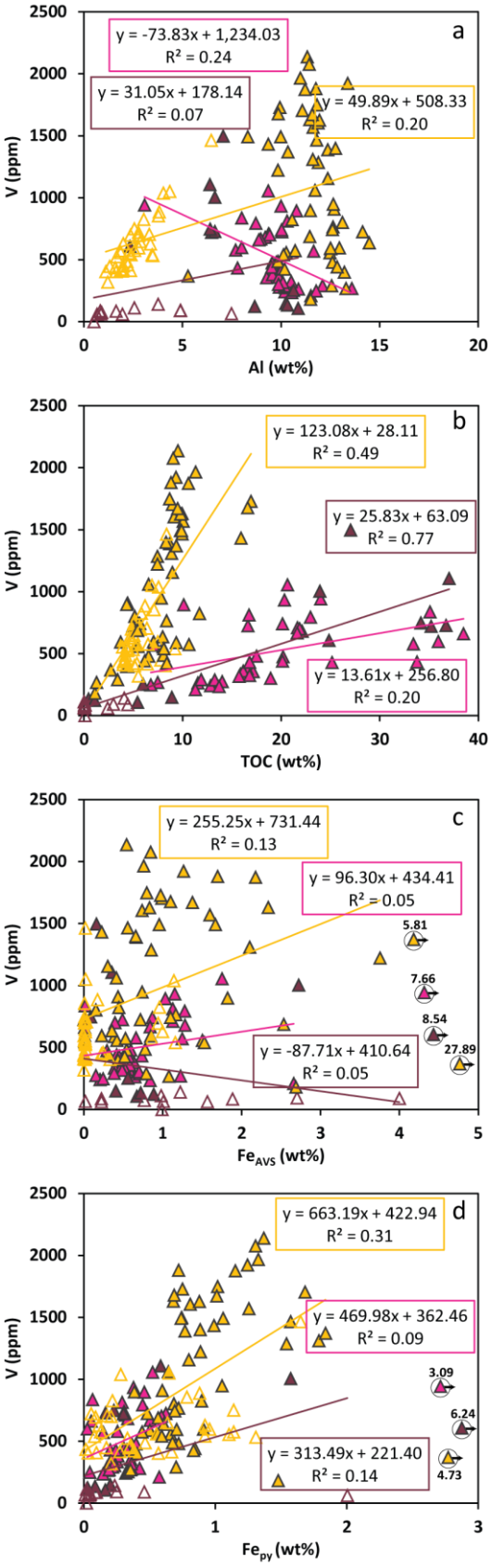
a
y = -73.83x + 1,234.03
R² = 0.24
y = 31.05x + 178.14
R² = 0.07
y = 49.89x + 508.33
R² = 0.20
V (ppm)
Al (wt%)
b
y = 123.08x + 28.11
R² = 0.49
y = 25.83x + 63.09
R² = 0.77
y = 13.61x + 256.80
R² = 0.20
V (ppm)
TOC (wt%)
c
y = 255.25x + 731.44
R² = 0.13
y = 96.30x + 434.41
R² = 0.05
y = -87.71x + 410.64
R² = 0.05
5.81
7.66
8.54
27.89
V (ppm)
Fe_AVS (wt%)
d
y = 663.19x + 422.94
R² = 0.31
y = 469.98x + 362.46
R² = 0.09
y = 313.49x + 221.40
R² = 0.14
3.09
6.24
4.73
V (ppm)
Fe_py (wt%)
I5/Touirist Formation
I4/En Nesoar Formation above sill
I4/En Nesoar Formation below sill

Figure 5.17 Crossplots of V with Al, TOC, Fe_{AVS} and Fe_{py} for S1 plotted by formation. Lines of best fit and equations are colour coded using the same key, shown beneath the plots. Open triangles indicate carbonate-rich samples.

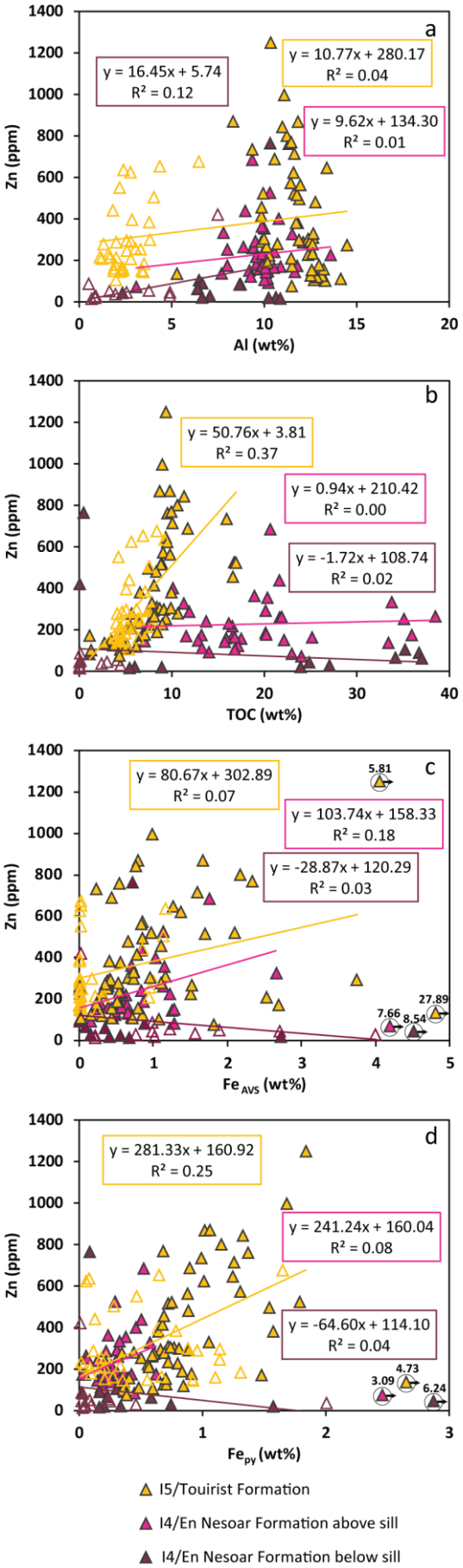
a
y = 16.45x + 5.74
R² = 0.12
y = 10.77x + 280.17
R² = 0.04
y = 9.62x + 134.30
R² = 0.01
Zn (ppm)
Al (wt%)
b
y = 50.76x + 3.81
R² = 0.37
y = 0.94x + 210.42
R² = 0.00
y = -1.72x + 108.74
R² = 0.02
Zn (ppm)
TOC (wt%)
c
y = 80.67x + 302.89
R² = 0.07
y = 103.74x + 158.33
R² = 0.18
y = -28.87x + 120.29
R² = 0.03
5.81
27.89
7.66
8.54
Zn (ppm)
Fe AVS (wt%)
d
y = 281.33x + 160.92
R² = 0.25
y = 241.24x + 160.04
R² = 0.08
y = -64.60x + 114.10
R² = 0.04
4.73
3.09
6.24
Zn (ppm)
Fe py (wt%)
I5/Touirist Formation
I4/En Nesoar Formation above sill
I4/En Nesoar Formation below sill

Figure 5.18 Crossplots of Zn with Al, TOC, Fe_{AVS} and Fe_{py} for S1 plotted by formation. Lines of best fit and equations are colour coded using the same key, shown beneath the plots. Open triangles indicate carbonate-rich samples.

5.4 Conclusions

The presence of large quantities of Fe_{AVS} in many samples from S1 has meant that FeHR/FeT and FeP/FeT ratios cannot be used to understand the partitioning of Fe in S1, as it is not clear to what extent Fe_{AVS} is dissolved during the sequential Fe extraction. DOP can be applied instead, but it inferring original depositional conditions from DOP ratios in S1 is not recommended because it is probable that the Fe_{AVS} pool consists of metamorphically derived pyrrhotite, and presence of metamorphically derived magnetite, produced at the expense of pyrite, is also likely.

Trace metal enrichments in S1 relative to S2 provides further evidence of metamorphic alteration. Evidence of repartitioning of Cu, Mi, Ni, V and Zn away from the dolerite contact suggests that these elements were remobilised by hydrothermal fluids, while Cr concentrations appear to be increased close to the intrusion.

A small dolerite sill was also found towards the base of S4, which could bring into question the use of this core for depositional redox reconstruction. However, a lack of Fe_{AVS} and little evidence of trace metal enrichment suggest that it is likely that the Fe-S-C systematics and trace metal contents of S4 have not been affected by hydrothermal fluid flow associated with the intrusion of dolerite.

Chapter 6

Conclusions

A reconstruction of ocean redox conditions in the Mesoproterozoic Taoudeni Basin suggests that redox varied both temporally and spatially. In the lower part of the succession, at the craton edge, euxinia dominated, with some ferruginous intervals. Towards the centre of the craton, where depositional environments were likely shallower, data from other studies indicates that the water column was likely ferruginous possibly with some oxic excursions. Euxinia continued to be prevalent in the deeper part of the basin during the deposition of the En Nesoar/I4 Formation, with more mixed, but mainly ferruginous conditions in shallower waters, suggesting a stratified water column. Ferruginous conditions persisted here in the Touirist/I5 Formation, but the deeper basin towards the craton edge seems largely to have become oxygenated, suggesting an oxygen minimum zone structure might be more likely than a stratified basin. Data from other studies indicating euxinia in the I5 Formation could also be explained by existence of an oxygen minimum zone causing heterogeneity in redox conditions along the edge of the craton. Following a drop in sea level, limited data from this study and data from other studies suggests the oxygen minimum zone likely persisted, but was probably reduced in extent.

Despite low total P contents, which might on their own be interpreted as mostly detrital, P speciation results reveal that much of the P buried in the Atar Group would have been bioavailable at the time of deposition. C to P ratios suggest that extensive remobilisation of P occurred in the shallower part of the basin, which would have enabled the continued high productivity implied by high TOC contents in S2. This P regeneration not only occurred during euxinic periods, but also under ferruginous and oxic conditions, likely as a result of high porewater sulphide concentrations stimulated by high TOC inputs. In contrast, in the deeper part of the basin, where preserved TOC concentrations are much lower, C to P ratios suggest efficient trapping of P in the sediment. Although under euxinic conditions there is some evidence of preferential release of P from organic matter, this is far less extensive than in S2.

High concentrations of pyrrhotite in S1 precludes the application of FeHR/FeT and FeP/FeHR for understanding Fe chemistry, and although DOP may be used instead, it is unlikely that this would provide accurate information on depositional conditions. Proximity of a ~ 30 m thick sill, presence of pyrrhotite and evidence of trace metal mobilisation and enrichments suggests contact metamorphism has occurred. Evidence of alteration stretches at least 20 m above the sill. The presence of a smaller sill in S4 does not seem to have affected this core in the same way.

Appendix A – S2, S3 and S4 data tables

Sample ID/ core depth	Formation	Description
S2 69.58	Aguelt El Mabha	Laminated greenish grey calcareous shale - lamination wavy
S2 79.51	Aguelt El Mabha	Reddish grey calcareous shale with cream lenticular bodies
S2 80.90	Aguelt El Mabha	Reddish brown calcareous shale with paler wavy and lenticular layers
S2 93.35	Aguelt El Mabha	Carbonate rich cream lenticular bodies interbedded with grey shale
S2 138.90	Touirist	Greenish grey pyritic shale, slightly calcareous
S2 139.00	Touirist	Laminated dark grey shale
S2 140.14	Touirist	Laminated black shale
S2 140.25	Touirist	Laminated black shale
S2 140.30	Touirist	Laminated black shale
S2 140.44	Touirist	Laminated dark grey shale
S2 140.52	Touirist	Laminated black shale
S2-8 140.77	Touirist	Powder - calcareous
S2 141.00	Touirist	Laminated dark grey calcareous shale
S2 141.08	Touirist	Laminated dark grey shale
S2-11 141.25	Touirist	Powder - calcareous
S2 141.25	Touirist	Laminated greenish grey calcareous shale
S2 141.48	Touirist	Laminated grey carbonate rich shale
S2 141.65	Touirist	Laminated greenish black shale
S2 141.80	Touirist	Greenish black shale with wavy and disrupted laminations
S2 141.90	Touirist	Laminated greenish black shale

Sample ID/ core depth	Formation	Description
S2-13 142.05	Touirist	Powder
S2 142.05	Touirist	Laminated dark greenish grey shale
S2 142.35	Touirist	Laminated dark greenish grey shale
S2 142.50	Touirist	Laminated greenish grey calcareous shale
S2 142.90	Touirist	Laminated dark greenish grey shale
S2 143.10	Touirist	Laminated black shale
S2 143.19	Touirist	Laminated black shale
S2-17 143.30	Touirist	Powder
S2 143.30	Touirist	Laminated dark greenish grey shale
S2 143.82	Touirist	Laminated greenish grey shale, slightly calcareous
S2 143.86	Touirist	Laminated black shale with paler lenticular bodies
S2 150.60	Touirist	Laminated dark greenish/brownish grey calcareous shale
S2 150.80	Touirist	Laminated dark greenish/brownish grey calcareous shale
S2 150.90	Touirist	Laminated dark greenish grey shale
S2 151.40	Touirist	Laminated light to dark greenish grey shale
S2 151.70	Touirist	Laminated green to dark greenish grey shale, some cross lamination
S2 169.65	Touirist	Carbonate rich dark grey shale
S2 185.45	En Nesoar	Laminated dark grey shale
S2 185.66	En Nesoar	Laminated greyish black silty shale
S2-20 187.60	En Nesoar	Powder - calcareous
S2-21 187.70	En Nesoar	Powder
S2 188.10	En Nesoar	Dark greenish grey silty shale
S2 188.20	En Nesoar	Laminated dark greenish grey silty shale
S2 188.30	En Nesoar	Laminated dark greenish grey silty shale, possible cross lamination

Sample ID/ core depth	Formation	Description
S2 188.40	En Nesoar	Laminated greenish grey silty shale, visible mica grains
S2 188.50	En Nesoar	Laminated grey shale
S2 188.60	En Nesoar	Laminated greenish grey calcareous shale
S2 200.8	En Nesoar	Laminated dark greenish grey silty shale, occasional mica grains
S2 201.00	En Nesoar	Laminated greenish grey to black shale, occasional mica grains
S2 202.15	En Nesoar	Laminated dark grey to black shale
S2-25 206.70	En Nesoar	Powder
S2 207.10	En Nesoar	Laminated greenish black silty shale, visible pyrite grain, some mica
S2-28 207.10	En Nesoar	Powder
S2-29 207.20	En Nesoar	Powder
S2 207.30	En Nesoar	Laminated dark grey to black silty shale, visible mica grains and pyrite grains
S2 207.70	En Nesoar	Laminated dark grey/brown shale
S3 59.18	Aguelt El Mabha	Laminated black fine sandstone, slightly calcareous
S3 59.33	Aguelt El Mabha	Grey micaceous fine sandstone, slightly calcareous
S3 60.01	Aguelt El Mabha	Laminated grey micaceous fine sandstone, slightly calcareous
S3 60.86	Aguelt El Mabha	Laminated grey micaceous siltstone, slightly calcareous
S3 60.97	Aguelt El Mabha	Grey micaceous silty shale, slightly calcareous
S3 61.27	Aguelt El Mabha	Laminated grey calcareous shale, some cross lamination
S3 61.88	Aguelt El Mabha	Laminated grey silty shale, some mica visible, slightly calcareous
S3 123.37	Aguelt El Mabha	Laminated grey shale
S3 123.54	Aguelt El Mabha	Laminted grey shale
S3 123.60	Aguelt El Mabha	Laminated dark grey shale
S3 124.24	Aguelt El Mabha	Laminated dark and pale grey shale
S3 170.73	Touirist	Powder

Sample ID/ core depth	Formation	Description
S3 179.80	Touirist	Powder - calcareous
S3 180.10	Touirist	Powder
S3 180.30	Touirist	Powder
S3 180.50	Touirist	Powder - calcareous
S3 180.70	Touirist	Powder - calcareous
S3 181.00	Touirist	Powder
S3 181.30	Touirist	Powder
S3 181.50	Touirist	Powder
S3 181.70	Touirist	Powder - calcareous
S3 181.80	Touirist	Powder
S3 181.90	Touirist	Powder - calcareous
S3 182.40	Touirist	Powder - calcareous
S3 182.50	Touirist	Powder
S3 182.60	Touirist	Powder - calcareous
S3 183.00	Touirist	Powder - calcareous
S4 74.17	I5	Laminated black shale, visible mica
S4 79.43	I5	Laminated dark grey to black shale
S4 79.56	I5	Black shale, visible mica
S4-13 79.66	I5	Powder
S4 79.66	I5	Fissile black shale, visible mica
S4 79.76	I5	Black shale with brownish orange grains - siderite/ankerite?
S4 79.95	I5	Black shale with brownish orange grains, > 1 wt% C_{carb} - siderite/ankerite?
S4 80.10	I5	Laminated black shale
S4-17 80.22	I5	Powder

Sample ID/ core depth	Formation	Description
S4 80.22	I5	Laminated black shale, visible mica
S4 80.34	I5	Laminated dark grey to black shale, visible mica
S4 80.45	I5	Dark grey to black shale, visible mica
S4 80.85	I5	Laminated black shale, visible mica
S4 81.00	I5	Laminated black shale, visible mica
S4 81.10	I5	Black shale, visible mica, visible pyrite
S4 81.22	I5	Laminated black shale, visible mica
S4 81.42	I5	Laminated black shale
S4 81.52	I5	Laminated black shale, visible mica
S4 81.64	I5	Black shale, visible mica
S4 81.76	I5	Black shale, visible mica
S4 81.94	I5	Laminated black shale, visible mica
S4 82.08	I5	Laminated black shale, occasional visible mica
S4 90.43	I5	Laminated dark greenish grey shale, visible mica
S4 90.52	I5	Laminated dark greenish grey shale, occasional visible mica
S4 90.57	I5	Dark grey shale, slightly calcareous, occasional visible mica
S4 90.77	I5	Laminated calcareous yellowish to dark grey shale with pale bluish grey lenses, visible mica
S4 90.89	I5	Laminated calcareous yellowish to dark grey shale with pale bluish grey lenses, visible mica
S4 91.00	I5	Dark grey calcareous shale with light greenish grey lenses, occasional visible mica
S4 91.08	I5	Grey calcareous shale
S4 91.16	I5	Dark grey shale, slightly calcareous, occasional visible mica
S4 109.71	I5	Dark grey to black calcareous shale, wavy laminations, visible mica
S4 120.24	I4	Laminated black shale, irregular pyrite layers, visible mica
S4 120.35	I4	Laminated black shale, irregular pyrite layers, visible mica

Sample ID/ core depth	Formation	Description
S4 120.51	I4	Laminated black shale with light grey lens, visible mica
S4 120.70	I4	Laminated black shale with light grey laminae, visible mica
S4 120.92	I4	Laminated black shale, visible mica
S4 121.21	I4	Laminated black shale, visible mica
S4 121.39	I4	Laminated black shale, visible mica
S4 122.66	I4	Laminated black shale, visible pyrite, visible mica
S4 122.78	I4	Laminated black shale, visible pyrite, visible mica
S4 122.88	I4	Laminated black shale, visible mica
S4 123.00	I4	Laminated black shale, visible mica
S4 123.10	I4	Laminated black shale, visible mica
S4 123.19	I4	Laminated black shale, lenses of pyrite, visible mica
S4 123.32	I4	Laminated black shale, pyrite layer, visible mica
S4 123.44	I4	Laminated black shale, visible mica
S4 123.58	I4	Laminated black shale, visible mica
S4 123.79	I4	Laminated dark grey to black shale, visible mica
S4 123.98	I4	Laminated black shale, visible mica
S4 128.06	I4	Laminated black shale with pyrite lenses, visible mica
S4 128.27	I4	Laminated black shale, visible pyrite, visible mica
S4 128.38	I4	Laminated black shale with light greenish grey layers, visible mica
S4 128.56 A	I4	Laminated black shale, visible mica, fragments of black in dark greenish yellow matrix - pyrite
S4 128.56 B	I4	As 128.56A, but with higher proportion of pyrite
S4 128.69	I4	Laminated black shale with light greenish grey layer, visible mica
S4 128.80 A	I4	Laminated black shale, visible mica
S4 128.80 B	I4	Laminated black shale with pyrite lenses, visible mica

Sample ID/ core depth	Formation	Description
S4 128.95	I4	Laminated black shale, visible pyrite, visible mica
S4 129.14	I4	Laminated black shale with light greenish grey layers, visible mica
S4 129.28	I4	Laminated black shale, occasional fine mica
S4 129.44	I4	Laminated black shale, occasional fine mica
S4 129.54	I4	Laminated black shale, visible pyrite concentrated in one band, occasional fine mica
S4 129.63	I4	Laminated dark grey to black shale, visible pyrite nodule, laminations curved around, occasional fine mica
S4 129.74	I4	Laminated black shale with lenses of pyrite, occasional fine mica
S4 129.94	I4	Laminated black shale with visible pyrite mostly concentrated in one band, occasional fine mica
S4 130.02	I4	Laminated black shale, visible pyrite, occasional fine mica
S4 130.04	I4	Laminated black shale, visible pyrite concentrated in one band
S4 132.17	I4	Laminated black shale, some cross-stratification, visible mica
S4 132.29	I4	Dark grey to black shale, visible mica
S4 132.56	I4	Laminated black shale, visible pyrite, visible mica
S4 132.75	I4	Laminated greenish grey to black shale, some cross stratification, visible pyrite, occasional fine mica
S4 132.91	I4	Laminated, fissile greenish grey to black shale, occasional fine mica
S4 133.73	I4	Fissile black shale, visible mica
S4 133.95	I4	Laminated black shale, visible mica
S4 134.17	I4	Laminated pale grey to black shale, visible mica
S4 134.37	I4	Laminated black shale with irregular, discontinuous light greenish grey layers, visible mica
S4 134.50	I4	Laminated black shale with irregular light greenish grey lenses and layers, visible pyrite
S4 134.65	I4	Laminated light greenish grey to greenish black shale, visible mica
S4 135.69	I4	Laminated black shale, visible mica
S4-2 135.81	I4	Powder
S4 135.81	I4	Laminated black shale with lenses of light greenish grey, visible mica

Sample ID/ core depth	Formation	Description
S4 136.18	I4	Laminated black shale, visible mica
S4 136.31	I4	Laminated light greenish grey to greenish black shale, visible mica
S4 136.46	I4	Laminated light greenish grey to greenish black shale, layers sometimes disrupted, visible mica
S4 136.57	I4	Laminated black shale with bands of light greenish grey, visible mica
S4 159.66 a	I3	Greenish black shale, visible mica
S4 159.66 b	I3	Greenish grey to black silty micaceous shale
S4 159.80	I3	Laminated dark greenish grey shale, some micaceous layers
S4 159.90	I3	Micaceous black silty shale with paler grey sandy wedge, lamination at various angles
S4 160.06	I3	Micaceous black silty shale with wavy laminations
S4 160.20	I3	Laminated, micaceous black shale
S4 160.30	I3	Laminated micaceous black shale containing light grey sand lenses draped with mud - flaser bedding
S4 160.40	I3	Micaceous black fine sandstone, some wavy lamination
S4 160.49	I3	Laminated, micaceous black silty shale
S4 160.72	I3	Laminated, micaceous black silty shale containing laminated fine sand body (gutter cast)
S4 160.86	I3	Laminated micaceous black shale, wavy laminations, some discontinuous
S4 161.08	I3	Micaceous black shale with light grey lenses
S4 161.16	I3	Micaceous black shale with wavy laminations and light greenish grey lenticular sand bodies
S4 161.29	I3	Laminated micaceous black shale
S4 161.39	I3	Laminated micaceous black silty shale, visible pyrite
S4 161.51	I3	Grey to dark grey micaceous shale, irregular laminations
S4 161.62	I3	Laminated dark grey shale
S4 161.69	I3	Greenish grey to black shale, visible mica, orangey brown lenses and layers - Fe carbonate? visible mica
S4 161.75	I3	Micaceous, dark greenish grey shale
S4 161.84	I3	Micaceous black silty shale

Sample ID/ core depth	Formation	Description
S4 161.91	I3	Micaceous dark greenish grey silty shale
S4 162.03	I3	Micaceous black silty shale, some lamination
S4-3 162.16	I3	Powder
S4-5 162.60	I3	Powder
S4 163.09	I3	Laminated, micaceous dark greenish grey to black silty shale
S4 163.32	I3	Micaceous black/light grey sandy shale, cross lamination, orangey brown lenses - Fe carbonate?
S4 163.40	I3	Laminated, micaceous black sandy shale
S4 165.20	I3	Laminated micaceous black shale with light grey sand lenses showing lenticular to flaser bedding
S4 165.50	I3	Laminated, micaceous black silty shale
S4 165.68	I3	Laminated, micaceous black silty shale
S4 165.80	I3	Laminated, micaceous light greenish grey to black silty/sandy shale
S4 165.98	I3	Laminated, micaceous black shale
S4 166.10	I3	Laminated, micaceous black shale
S4 166.26	I3	Laminated, micaceous dark grey to black shale, laminations wavy and irregular
S4 166.45	I3	Laminated, micaceous black shale with light grey silty/sandy lenses
S4 168.70	I3	Very micaceous light to dark greenish grey silty/sandy shale, irregular sand bodies with mud drapes
S4 169.11	I3	Laminated, very micaceous black silty shale
S4 169.35	I3	Very micaceous light bluish grey to black silty shale
S4 169.61	I3	Micaceous black shale
S4 169.78	I3	Laminated, micaceous dark greenish grey to black silty shale

Table A - 1 Sample descriptions for cores S2, S3 and S4. For most samples, the sample ID consists of the core name and depth. The exception is some samples from cores S2 and S4 that were received as powders, which have an additional number following the core name. Samples were split into A and B where there was a visible disparity in pyrite contents across the width of a core section.

Sample ID/ core depth	Formation	Total C (wt%)	TOC (wt%)	Inorganic C (wt%)	Total S (wt%)	Sulphide S (wt%)	$\delta^{34}S$ (‰)
S2 69.58	Aguelt El Mabha	4.33	0.05	4.28	0.00	0.01	24.44
S2 79.51	Aguelt El Mabha	3.31	0.04	3.27	0.00	0.00	
S2 80.90	Aguelt El Mabha	4.78	0.03	4.75	0.00	0.00	
S2 93.35	Aguelt El Mabha	8.06	0.03	8.03	0.02	0.00	
S2 138.90	Touirist	1.04	0.28	0.76	4.82	4.52	17.92
S2 139.00	Touirist	17.96	17.48	0.47	2.01	2.56	-11.82
S2 140.14	Touirist	28.17	27.18	0.99	1.69	0.79	-13.58
S2 140.25	Touirist	17.20	16.54	0.65	1.61	1.03	-12.53
S2 140.30	Touirist	12.40	12.32	0.08	0.68	0.45	-12.15
S2 140.44	Touirist	3.65	3.11	0.54	1.06	0.96	2.69
S2 140.52	Touirist	10.41	9.57	0.84	1.04	0.86	-19.63
S2-8 140.77	Touirist	8.99	4.82	4.17	1.83	1.76	-9.77
S2 141.00	Touirist	6.94	2.75	4.19	0.54	0.49	-9.41
S2 141.08	Touirist	9.83	9.51	0.31	1.28	1.13	-19.99
S2-11 141.25	Touirist	10.32	9.32	1.01	1.05	0.79	
S2 141.25	Touirist	4.78	2.26	2.52	1.81	1.74	-15.17
S2 141.48	Touirist	6.95	0.45	6.50	0.61	0.67	-4.54
S2 141.65	Touirist	31.93	34.30	0.00	2.18	1.26	-18.78
S2 141.80	Touirist	23.25	22.90	0.35	1.14	0.57	-16.61
S2 141.90	Touirist	28.53	29.15	0.00	1.91	0.93	-16.53
S2-13 142.05	Touirist	10.60	10.37	0.23	0.64	0.44	
S2 142.05	Touirist	7.11	7.06	0.05	0.67	0.56	-14.88
S2 142.35	Touirist	13.20	13.02	0.18	2.94	2.49	-20.08
S2 142.50	Touirist	4.45	0.13	4.33	0.47	0.57	-8.54

Sample ID/ core depth	Formation	Total C (wt%)	TOC (wt%)	Inorganic C (wt%)	Total S (wt%)	Sulphide S (wt%)	$\delta^{34}S$ (‰)
S2 142.90	Touirist	7.65	7.44	0.21	0.58	0.42	-12.16
S2 143.10	Touirist	19.41	19.39	0.03	0.85	0.47	-16.19
S2 143.19	Touirist	17.75	17.41	0.35	0.86	0.47	-13.92
S2-17 143.30	Touirist	18.15	17.29	0.85	0.86	0.47	
S2 143.30	Touirist	5.61	5.32	0.29	0.71	0.52	-3.78
S2 143.82	Touirist	0.99	0.32	0.67	0.16	0.14	7.28
S2 143.86	Touirist	7.20	6.98	0.22	1.26	0.97	-20.33
S2 150.60	Touirist	7.67	5.95	1.72	0.75	0.59	-7.60
S2 150.80	Touirist	5.90	4.49	1.41	0.70	0.58	-5.20
S2 150.90	Touirist	8.19	7.85	0.34	0.99	0.74	-12.83
S2 151.40	Touirist	4.09	3.66	0.43	1.13	1.08	-9.74
S2 151.70	Touirist	7.77	7.20	0.57	1.34	0.89	-9.42
S2 169.65	Touirist	10.63	3.22	7.41	0.16	0.09	-12.03
S2 185.45	En Nesoar	8.09	7.90	0.19	0.34	0.25	-15.31
S2 185.66	En Nesoar	8.36	7.75	0.61	0.45	0.34	-28.54
S2-20 187.60	En Nesoar	6.40	1.82	4.58	5.30	2.25	12.31
S2-21 187.70	En Nesoar	7.11	6.69	0.42	0.50	0.32	-6.78
S2 188.10	En Nesoar	2.02	1.75	0.28	0.67	0.30	-14.13
S2 188.20	En Nesoar	4.12	3.77	0.34	2.43	0.45	-8.25
S2 188.30	En Nesoar	3.87	3.63	0.23	1.47	1.30	-6.26
S2 188.40	En Nesoar	1.56	1.34	0.22	1.14	0.94	-9.13
S2 188.50	En Nesoar	0.99	0.73	0.27	0.54	0.49	-8.88
S2 188.60	En Nesoar	2.03	0.14	1.89	1.32	1.24	0.89
S2 200.8	En Nesoar	9.42	9.21	0.21	2.16	1.79	

Sample ID/ core depth	Formation	Total C (wt%)	TOC (wt%)	Inorganic C (wt%)	Total S (wt%)	Sulphide S (wt%)	$\delta^{34}S$ (‰)
S2 201.00	En Nesoar	10.90	10.59	0.30	1.75	1.43	-6.83
S2 202.15	En Nesoar	17.10	16.70	0.40	2.41	1.80	-8.66
S2-25 206.70	En Nesoar	16.75	16.22	0.53	1.16	0.69	-6.68
S2 207.10	En Nesoar	10.84	10.42	0.42	0.55	0.33	-10.73
S2-28 207.10	En Nesoar	6.86	6.49	0.37	1.36	0.56	
S2-29 207.20	En Nesoar	7.77	7.46	0.31	0.83	0.58	-14.25
S2 207.30	En Nesoar	11.35	11.03	0.32	0.80	0.50	-13.24
S2 207.70	En Nesoar	7.00	6.87	0.12	0.42	0.20	-11.82
S3 59.18	Aguelt El Mabha	0.90	0.28	0.62	0.00	0.01	
S3 59.33	Aguelt El Mabha	0.85	0.22	0.64	0.00	0.00	11.23
S3 60.01	Aguelt El Mabha	0.76	0.13	0.63	0.00	0.00	
S3 60.86	Aguelt El Mabha	1.06	0.10	0.96	0.00	0.00	
S3 60.97	Aguelt El Mabha	0.78	0.11	0.67	0.18	0.05	3.29
S3 61.27	Aguelt El Mabha	1.24	0.10	1.14	0.02	0.01	
S3 61.88	Aguelt El Mabha	0.92	0.11	0.81	0.02	0.00	
S3 123.37	Aguelt El Mabha	0.25	0.03	0.23	0.00	0.00	
S3 123.54	Aguelt El Mabha	0.29	0.03	0.26	0.02	0.00	
S3 123.60	Aguelt El Mabha	0.32	0.03	0.29	0.00	0.00	
S3 124.24	Aguelt El Mabha	0.24	0.02	0.22	0.10	0.00	
S3 170.73	Touirist	0.42	0.20	0.22	0.00	0.00	65.00
S3 179.80	Touirist	5.50	0.12	5.38	0.00	0.00	
S3 180.10	Touirist	0.69	0.37	0.32	0.00	0.01	8.37
S3 180.30	Touirist	0.63	0.06	0.57	0.00	0.00	
S3 180.50	Touirist	5.60	0.04	5.56	0.00	0.00	

Sample ID/ core depth	Formation	Total C (wt%)	TOC (wt%)	Inorganic C (wt%)	Total S (wt%)	Sulphide S (wt%)	$\delta^{34}S$ (‰)
S3 180.70	Touirist	5.36	0.03	5.33	0.00	0.02	4.42
S3 181.00	Touirist	0.58	0.17	0.41	0.00	0.02	-0.36
S3 181.30	Touirist	0.46	0.05	0.41	0.00	0.00	
S3 181.50	Touirist	1.36	0.80	0.56	0.80	0.56	4.43
S3 181.70	Touirist	5.20	0.04	5.17	0.00	0.00	
S3 181.80	Touirist	0.78	0.47	0.31	0.31	0.30	2.66
S3 181.90	Touirist	3.24	0.03	3.20	0.00	0.02	1.01
S3 182.40	Touirist	2.73	0.04	2.69	0.00	0.00	
S3 182.50	Touirist	0.50	0.14	0.37	0.51	0.43	1.31
S3 182.60	Touirist	1.61	0.08	1.53	0.00	0.03	0.88
S3 183.00	Touirist	3.89	0.04	3.85	0.00	0.00	
S4 74.17	I5	1.11	0.86	0.25	2.87	2.73	25.93
S4 79.43	I5	0.54	0.32	0.22	0.00	0.03	12.86
S4 79.56	I5	0.67	0.48	0.19	0.21	0.13	19.39
S4-13 79.66	I5	0.82	0.61	0.21	0.15	0.20	
S4 79.66	I5	0.73	0.47	0.26	0.34	0.23	-1.27
S4 79.76	I5	1.35	0.52	0.83	0.40	0.45	8.26
S4 79.95	I5	4.08	2.35	1.74	0.27	0.23	23.14
S4 80.10	I5	1.27	0.70	0.57	0.00	0.05	23.99
S4-17 80.22	I5	1.04	0.89	0.15	0.31	0.32	
S4 80.22	I5	1.02	0.80	0.21	0.19	0.19	18.22
S4 80.34	I5	0.55	0.33	0.22	0.06	0.08	-10.87
S4 80.45	I5	0.78	0.60	0.18	0.18	0.18	7.97
S4 80.85	I5	0.87	0.65	0.22	0.54	0.53	13.25

Sample ID/ core depth	Formation	Total C (wt%)	TOC (wt%)	Inorganic C (wt%)	Total S (wt%)	Sulphide S (wt%)	$\delta^{34}S$ (‰)
S4 81.00	I5	0.53	0.35	0.18	0.00	0.02	18.54
S4 81.10	I5	0.83	0.60	0.24	5.87	6.40	53.57
S4 81.22	I5	0.70	0.57	0.13	0.29	0.25	15.71
S4 81.42	I5	0.87	0.59	0.29	0.05	0.09	17.85
S4 81.52	I5	0.95	0.78	0.17	0.55	0.50	20.17
S4 81.64	I5	1.02	0.82	0.19	0.62	0.59	16.93
S4 81.76	I5	1.19	0.90	0.29	1.00	0.82	23.19
S4 81.94	I5	0.81	0.62	0.19	0.31	0.32	16.77
S4 82.08	I5	0.77	0.55	0.22	0.08	0.14	16.97
S4 90.43	I5	0.55	0.13	0.42	0.11	0.07	22.57
S4 90.52	I5	1.15	0.18	0.98	0.00	0.03	19.80
S4 90.57	I5	1.33	0.26	1.06	0.01	0.02	20.49
S4 90.77	I5	2.60	0.20	2.40	0.14	0.13	-6.44
S4 90.89	I5	3.29	0.20	3.09	0.11	0.11	-17.42
S4 91.00	I5	1.58	0.10	1.48	0.42	0.44	0.61
S4 91.08	I5	2.79	0.16	2.63	0.00	0.04	19.44
S4 91.16	I5	0.99	0.40	0.59	0.00	0.02	15.92
S4 109.71	I5	2.57	0.47	2.10	0.16	0.19	6.33
S4 120.24	I4	1.16	0.97	0.18	7.17	7.19	10.35
S4 120.35	I4	1.01	0.84	0.17	8.72	8.86	14.46
S4 120.51	I4	1.07	0.90	0.17	1.82	2.10	15.25
S4 120.70	I4	0.98	0.77	0.21	2.88	2.83	18.05
S4 120.92	I4	0.99	0.87	0.12	2.15	2.06	11.46
S4 121.21	I4	0.94	0.76	0.18	1.47	1.61	13.24

Sample ID/ core depth	Formation	Total C (wt%)	TOC (wt%)	Inorganic C (wt%)	Total S (wt%)	Sulphide S (wt%)	$\delta^{34}S$ (‰)
S4 121.39	I4	0.98	0.78	0.20	0.88	0.81	8.63
S4 122.66	I4	1.81	1.63	0.17	4.38	3.81	6.41
S4 122.78	I4	1.51	1.31	0.21	5.01	4.87	6.48
S4 122.88	I4	1.57	1.41	0.16	6.62	6.21	0.48
S4 123.00	I4	1.52	1.35	0.17	5.74	5.45	13.85
S4 123.10	I4	1.61	1.35	0.26	5.53	5.30	23.07
S4 123.19	I4	1.08	0.90	0.19	3.57	3.31	12.05
S4 123.32	I4	1.16	0.96	0.20	4.88	4.97	15.81
S4 123.44	I4	1.12	0.95	0.18	5.71	5.44	30.49
S4 123.58	I4	1.30	1.11	0.18	1.82	1.79	15.57
S4 123.79	I4	1.11	0.91	0.20	4.58	4.42	17.09
S4 123.98	I4	1.21	0.97	0.23	0.71	0.65	16.38
S4 128.06	I4	1.09	0.90	0.18	5.11	5.23	7.21
S4 128.27	I4	1.41	0.90	0.51	2.50	2.37	20.23
S4 128.38	I4	1.11	0.93	0.18	3.47	3.27	16.85
S4 128.56 A	I4	1.11	0.93	0.18	20.81	20.90	3.51
S4 128.56 B	I4	0.91	0.68	0.23	37.18	35.76	5.62
S4 128.69	I4	1.20	1.01	0.18	3.79	3.70	20.70
S4 128.80 A	I4	1.37	1.14	0.22	0.36	0.36	7.29
S4 128.80 B	I4	1.41	1.24	0.17	1.19	1.29	5.82
S4 128.95	I4	1.35	1.11	0.25	4.12	4.27	8.03
S4 129.14	I4	1.13	0.97	0.16	3.39	3.38	8.28
S4 129.28	I4	1.55	1.45	0.09	1.87	1.45	-0.70
S4 129.44	I4	1.36	1.21	0.15	1.70	1.70	3.20

Sample ID/ core depth	Formation	Total C (wt%)	TOC (wt%)	Inorganic C (wt%)	Total S (wt%)	Sulphide S (wt%)	$\delta^{34}S$ (‰)
S4 129.54	I4	1.42	1.21	0.21	2.56	2.59	3.27
S4 129.63	I4	1.32	1.14	0.17	3.14	2.77	10.19
S4 129.74	I4	1.17	1.05	0.12	2.63	2.74	10.41
S4 129.94	I4	1.06	2.17	0.00	5.89	7.38	7.64
S4 130.02	I4	1.26	1.00	0.26	3.88	3.94	13.59
S4 130.04	I4	1.09	0.78	0.32	17.06	16.38	15.34
S4 132.17	I4	1.07	0.88	0.19	2.45	2.55	9.80
S4 132.29	I4	1.04	0.58	0.46	2.42	2.15	16.79
S4 132.56	I4	1.03	0.87	0.17	2.87	2.51	17.45
S4 132.75	I4	1.11	0.78	0.32	2.40	2.43	14.60
S4 132.91	I4	1.02	0.76	0.26	1.30	1.31	15.65
S4 133.73	I4	1.26	0.96	0.30	1.39	1.35	13.94
S4 133.95	I4	1.29	0.97	0.32	2.25	2.04	13.08
S4 134.17	I4	1.04	0.76	0.28	5.10	3.94	13.96
S4 134.37	I4	1.08	0.78	0.30	1.99	1.89	12.67
S4 134.50	I4	1.29	1.00	0.28	1.50	1.57	12.03
S4 134.65	I4	1.07	0.79	0.28	3.86	3.43	17.45
S4 135.69	I4	1.27	0.97	0.30	1.72	1.77	10.57
S4-2 135.81	I4	1.29	1.10	0.20	1.69	1.80	
S4 135.81	I4	1.28	0.96	0.32	1.95	2.02	11.10
S4 136.18	I4	1.40	1.16	0.25	2.17	2.15	9.74
S4 136.31	I4	1.14	0.92	0.21	1.98	1.98	7.59
S4 136.46	I4	1.35	1.08	0.27	1.97	2.00	8.10
S4 136.57	I4	1.42	1.08	0.34	1.77	1.80	6.26

Sample ID/ core depth	Formation	Total C (wt%)	TOC (wt%)	Inorganic C (wt%)	Total S (wt%)	Sulphide S (wt%)	$\delta^{34}S$ (‰)
S4 159.66 a	I3	1.10	0.86	0.24	2.58	2.57	15.40
S4 159.66 b	I3	1.42	1.11	0.31	1.70	1.81	6.37
S4 159.80	I3	0.77	0.58	0.19	3.48	3.34	18.14
S4 159.90	I3	0.77	0.48	0.29	0.44	0.37	6.65
S4 160.06	I3	0.78	0.55	0.22	2.13	2.02	19.45
S4 160.20	I3	0.93	0.69	0.24	1.15	1.10	14.89
S4 160.30	I3	0.86	0.71	0.15	1.23	1.23	8.23
S4 160.40	I3	0.66	0.44	0.22	0.72	0.73	3.06
S4 160.49	I3	0.79	0.60	0.19	1.91	1.86	9.21
S4 160.72	I3	1.52	0.91	0.62	2.39	2.37	14.15
S4 160.86	I3	1.03	0.74	0.29	1.90	1.76	13.80
S4 161.08	I3	1.36	0.98	0.38	3.21	3.22	14.76
S4 161.16	I3	1.06	0.66	0.40	2.15	2.03	16.67
S4 161.29	I3	1.03	0.71	0.32	3.30	3.28	18.80
S4 161.39	I3	1.24	0.86	0.38	2.06	2.05	10.46
S4 161.51	I3	0.83	0.46	0.37	1.50	1.44	19.97
S4 161.62	I3	1.68	0.81	0.88	3.11	3.11	22.88
S4 161.69	I3	1.71	0.87	0.84	2.96	3.01	28.22
S4 161.75	I3	1.19	0.83	0.36	2.39	2.38	23.00
S4 161.84	I3	1.73	0.78	0.95	1.79	1.65	18.58
S4 161.91	I3	1.03	0.77	0.26	3.08	3.10	24.59
S4 162.03	I3	1.51	0.73	0.78	2.29	1.63	22.03
S4-3 162.16	I3	0.96	0.82	0.14	1.59	1.61	19.77
S4-5 162.60	I3	0.98	0.74	0.23	1.17	0.95	17.28

Sample ID/ core depth	Formation	Total C (wt%)	TOC (wt%)	Inorganic C (wt%)	Total S (wt%)	Sulphide S (wt%)	$\delta^{34}S$ (‰)
S4 163.09	I3	1.00	0.58	0.42	1.40	1.28	17.11
S4 163.32	I3	2.51	0.73	1.78	0.60	0.45	19.33
S4 163.40	I3	1.32	0.60	0.72	1.51	1.40	21.06
S4 165.20	I3	1.37	0.98	0.40	2.17	1.99	20.37
S4 165.50	I3	1.23	0.83	0.39	2.32	2.18	19.72
S4 165.68	I3	1.40	1.07	0.34	1.88	1.79	19.72
S4 165.80	I3	1.31	0.77	0.54	1.04	0.95	21.67
S4 165.98	I3	1.73	0.73	0.99	0.67	0.55	18.72
S4 166.10	I3	1.24	0.88	0.35	1.10	1.04	20.39
S4 166.26	I3	1.22	0.74	0.48	3.73	3.66	18.06
S4 166.45	I3	0.96	0.70	0.26	1.37	1.32	21.82
S4 168.70	I3	0.85	0.51	0.34	0.40	0.36	16.27
S4 169.11	I3	1.18	0.86	0.32	1.48	1.44	17.78
S4 169.35	I3	0.20	0.83	0.00	0.19	1.97	17.54
S4 169.61	I3	1.17	0.84	0.33	0.86	0.79	17.07
S4 169.78	I3	1.10	0.63	0.47	1.10	1.06	14.49

Table A - 2 Carbon and sulphur data for cores S2, S3 and S4. For most samples, the sample ID consists of the core name and depth. The exception is some samples from cores S2 and S4 that were received as powders, which have an additional number following the core name. Samples were split into A and B where there was a visible disparity in pyrite contents across the width of a core section.

Sample ID/ core depth	Formation	Al (wt%)	Cr (ppm)	Cu (ppm)	Mn (ppm)	Mo (ppm)	Ni (ppm)	P (ppm)	V (ppm)	Zn (ppm)
S2 69.58	Aguelt El Mabha	6.86	55	73	863	0.00	28	227	76	61
S2 79.51	Aguelt El Mabha	7.76	69	16	603	0.00	36	276	93	74
S2 80.90	Aguelt El Mabha	6.04	53	6	584	3.47	35	288	59	80
S2 93.35	Aguelt El Mabha	3.26	28	30	884	0.34	21	194	77	50
S2 138.90	Touirist	10.83	125	62	810	4.97	113	1223	145	1153
S2 139.00	Touirist	9.87	104	104	162	10.60	180	223	205	156
S2 140.14	Touirist	9.04	128	146	109	12.29	204	375	176	163
S2 140.25	Touirist	10.68	126	107	137	8.88	161	315	157	103
S2 140.30	Touirist	11.64	140	97	129	8.54	143	380	134	141
S2 140.44	Touirist	12.58	117	55	170	5.03	68	830	106	108
S2 140.52	Touirist	11.97	129	85	158	5.36	111	387	104	91
S2-8 140.77	Touirist	8.63	125	56	1970	19.20	78	409	52	107
S2 141.00	Touirist	8.20	86	37	1322	1.70	31	282	80	43
S2 141.08	Touirist	11.43	139	76	173	5.67	86	525	97	77
S2-11 141.25	Touirist	12.55	174	85	382	10.88	96	759	87	83
S2 141.25	Touirist	9.61	98	40	1000	5.80	66	429	83	46
S2 141.48	Touirist	5.45	51	14	2250	1.62	24	275	68	38
S2 141.65	Touirist	7.61	114	137	103	21.00	200	205	312	57
S2 141.80	Touirist	9.35	139	116	120	14.28	135	351	315	85
S2 141.90	Touirist	8.14	130	144	114	19.91	166	204	373	82
S2-13 142.05	Touirist	12.21	155	83	162	7.71	117	689	160	84
S2 142.05	Touirist	11.28	124	65	153	3.72	87	484	156	91
S2 142.35	Touirist	10.22	124	98	227	5.67	129	397	112	87

Sample ID/ core depth	Formation	Al (wt%)	Cr (ppm)	Cu (ppm)	Mn (ppm)	Mo (ppm)	Ni (ppm)	P (ppm)	V (ppm)	Zn (ppm)
S2 142.50	Touirist	7.05	59	11	1278	0.59	23	582	74	48
S2 142.90	Touirist	11.23	126	57	157	5.59	81	401	120	65
S2 143.10	Touirist	9.69	135	103	131	10.29	120	425	168	64
S2 143.19	Touirist	10.09	138	103	151	7.04	134	544	155	82
S2-17 143.30	Touirist	10.72	172	108	150	13.36	158	634	153	94
S2 143.30	Touirist	11.55	123	66	169	4.51	137	363	301	95
S2 143.82	Touirist	10.77	91	17	212	1.74	36	236	91	79
S2 143.86	Touirist	10.81	121	69	214	3.82	108	497	108	108
S2 150.60	Touirist	8.95	114	66	240	4.69	85	805	104	143
S2 150.80	Touirist	9.74	124	59	203	3.00	98	938	111	149
S2 150.90	Touirist	10.19	121	65	160	5.02	99	1247	140	122
S2 151.40	Touirist	10.39	109	49	206	3.69	102	847	89	119
S2 151.70	Touirist	10.06	129	61	215	7.22	116	878	510	215
S2 169.65	Touirist	4.66	66	15	423	4.11	38	192	53	31
S2 185.45	En Nesoar	11.05	185	72	149	3.43	83	619	145	123
S2 185.66	En Nesoar	10.50	155	63	178	3.61	57	340	128	94
S2-20 187.60	En Nesoar	6.18	92	38	808	8.29	248	337	68	83
S2-21 187.70	En Nesoar	12.38	269	84	120	8.05	100	336	167	150
S2 188.10	En Nesoar	12.04	139	42	195	3.11	48	399	129	116
S2 188.20	En Nesoar	10.99	124	88	145	3.97	104	241	137	149
S2 188.30	En Nesoar	11.23	134	99	173	2.52	131	259	153	78
S2 188.40	En Nesoar	11.55	120	43	174	3.89	58	300	133	103
S2 188.50	En Nesoar	11.62	123	32	224	1.66	35	283	113	105

Sample ID/ core depth	Formation	Al (wt%)	Cr (ppm)	Cu (ppm)	Mn (ppm)	Mo (ppm)	Ni (ppm)	P (ppm)	V (ppm)	Zn (ppm)
S2 188.60	En Nesoar	9.68	96	26	553	6.62	58	259	90	63
S2 200.8	En Nesoar	11.06	134	73	156	5.45	149	187	229	147
S2 201.00	En Nesoar	10.79	141	78	165	6.60	132	211	231	135
S2 202.15	En Nesoar	9.77	138	87	194	13.84	223	225	534	146
S2-25 206.70	En Nesoar	10.00	340	194	93	12.44	229	200	373	573
S2 207.10	En Nesoar	9.94	283	135	151	4.33	157	326	261	416
S2-28 207.10	En Nesoar	11.19	392	92	226	8.22	112	471	229	797
S2-29 207.20	En Nesoar	11.16	328	128	221	9.19	114	357	265	1065
S2 207.30	En Nesoar	9.87	306	129	139	5.67	169	300	234	649
S2 207.70	En Nesoar	10.29	263	92	130	4.94	121	264	311	754
S3 59.18	Aguelt El Mabha	8.37	68	15	748	4.54	40	195	80	129
S3 59.33	Aguelt El Mabha	8.70	70	17	769	2.78	34	210	82	121
S3 60.01	Aguelt El Mabha	9.68	92	17	817	1.84	34	248	94	116
S3 60.86	Aguelt El Mabha	9.49	89	35	1578	4.36	36	249	97	110
S3 60.97	Aguelt El Mabha	10.03	95	35	1142	2.21	34	265	104	126
S3 61.27	Aguelt El Mabha	8.90	80	23	1198	0.00	33	245	93	119
S3 61.88	Aguelt El Mabha	8.90	79	34	1016	1.75	38	234	93	119
S3 123.37	Aguelt El Mabha	10.78	104	55	221	0.00	37	242	115	160
S3 123.54	Aguelt El Mabha	10.89	104	33	251	1.78	42	258	120	152
S3 123.60	Aguelt El Mabha	10.54	102	26	288	0.00	38	267	116	122
S3 124.24	Aguelt El Mabha	10.82	107	27	242	4.51	44	255	122	127
S3 170.73	Touirist	10.86	117	13	201	8.69	43	277	91	133
S3 179.80	Touirist	6.34	70	7	1701	3.91	34	282	54	94

Sample ID/ core depth	Formation	Al (wt%)	Cr (ppm)	Cu (ppm)	Mn (ppm)	Mo (ppm)	Ni (ppm)	P (ppm)	V (ppm)	Zn (ppm)
S3 180.10	Touirist	11.85	127	8	271	9.77	54	460	118	300
S3 180.30	Touirist	12.53	144	4	807	4.81	64	513	116	173
S3 180.50	Touirist	5.88	71	8	2660	7.34	40	258	53	95
S3 180.70	Touirist	6.25	99	6	2299	12.21	47	304	56	120
S3 181.00	Touirist	11.71	128	4	557	8.03	63	440	111	175
S3 181.30	Touirist	12.30	125	50	634	3.55	61	551	109	155
S3 181.50	Touirist	12.78	164	12	672	10.02	89	465	128	145
S3 181.70	Touirist	6.55	69	5	4044	4.53	34	302	56	91
S3 181.80	Touirist	12.35	133	13	350	8.46	62	456	125	162
S3 181.90	Touirist	8.59	93	378	1130	0.00	47	383	75	122
S3 182.40	Touirist	10.20	113	5	1349	8.63	56	419	94	136
S3 182.50	Touirist	12.14	147	21	360	5.78	65	498	129	161
S3 182.60	Touirist	10.78	129	3	934	4.79	64	397	93	133
S3 183.00	Touirist	8.21	99	8	1623	5.89	51	350	77	120
S4 74.17	I5	14.06	155	34	49	1.00	75	258	144	49
S4 79.43	I5	13.95	154	5	49	5.21	32	229	129	75
S4 79.56	I5	14.02	160	14	41	4.26	74	245	132	45
S4-13 79.66	I5	15.87	233	4	45	6.56	53	316	151	55
S4 79.66	I5	14.36	164	8	52	2.60	85	263	137	42
S4 79.76	I5	12.90	145	14	129	5.19	59	316	122	49
S4 79.95	I5	7.75	85	36	469	2.07	45	8916	80	90
S4 80.10	I5	13.31	150	26	101	3.00	30	315	127	62
S4-17 80.22	I5	16.68	210	31	38	9.52	64	291	169	67

Sample ID/ core depth	Formation	Al (wt%)	Cr (ppm)	Cu (ppm)	Mn (ppm)	Mo (ppm)	Ni (ppm)	P (ppm)	V (ppm)	Zn (ppm)
S4 80.22	I5	13.77	154	26	43	4.60	43	220	139	39
S4 80.34	I5	13.49	162	26	53	5.73	59	192	127	101
S4 80.45	I5	14.18	166	26	44	7.06	55	228	133	38
S4 80.85	I5	13.77	164	20	45	6.31	47	249	136	51
S4 81.00	I5	14.16	151	19	43	0.00	25	243	114	79
S4 81.10	I5	12.19	144	43	67	0.00	106	219	116	349
S4 81.22	I5	13.95	159	23	42	4.26	62	243	122	60
S4 81.42	I5	14.07	186	24	46	5.57	52	242	142	52
S4 81.52	I5	13.74	155	27	44	7.16	50	245	133	87
S4 81.64	I5	13.16	142	22	59	4.88	52	215	129	73
S4 81.76	I5	13.00	139	36	93	5.44	55	255	130	109
S4 81.94	I5	13.68	145	27	63	3.52	54	235	135	117
S4 82.08	I5	14.01	165	27	47	4.73	44	239	133	93
S4 90.43	I5	13.35	159	10	81	2.38	45	251	120	52
S4 90.52	I5	11.95	134	41	121	3.47	49	215	108	61
S4 90.57	I5	11.95	134	18	102	7.47	51	219	112	71
S4 90.77	I5	10.03	109	6	171	2.75	84	229	92	77
S4 90.89	I5	9.77	104	1	212	5.27	44	234	86	46
S4 91.00	I5	11.95	139	47	160	5.06	60	350	109	61
S4 91.08	I5	10.41	118	12	218	3.85	47	329	97	50
S4 91.16	I5	13.78	154	1	65	3.37	50	244	135	76
S4 109.71	I5	12.40	135	19	493	6.64	77	240	111	44
S4 120.24	I4	11.51	131	96	96	5.28	95	206	110	124

Sample ID/ core depth	Formation	Al (wt%)	Cr (ppm)	Cu (ppm)	Mn (ppm)	Mo (ppm)	Ni (ppm)	P (ppm)	V (ppm)	Zn (ppm)
S4 120.35	I4	10.98	116	113	62	5.35	109	269	109	98
S4 120.51	I4	13.07	139	24	53	3.56	51	262	129	79
S4 120.70	I4	11.98	124	41	54	1.93	80	217	112	151
S4 120.92	I4	13.01	139	30	49	4.23	79	252	124	94
S4 121.21	I4	12.57	132	19	42	7.26	57	217	123	53
S4 121.39	I4	12.17	127	16	66	7.24	44	208	118	67
S4 122.66	I4	13.05	143	49	133	3.56	60	173	132	927
S4 122.78	I4	12.63	142	53	105	6.13	71	169	125	115
S4 122.88	I4	12.30	142	50	95	4.14	73	201	132	114
S4 123.00	I4	12.44	150	43	81	4.98	61	211	134	110
S4 123.10	I4	12.02	143	53	94	5.27	56	226	127	59
S4 123.19	I4	13.11	148	27	72	4.19	58	232	144	96
S4 123.32	I4	11.76	126	43	58	4.90	76	195	127	256
S4 123.44	I4	11.45	121	41	54	5.47	64	200	113	115
S4 123.58	I4	13.62	167	24	58	5.05	51	244	138	63
S4 123.79	I4	12.29	138	33	62	4.52	66	388	131	90
S4 123.98	I4	14.26	165	6	67	5.33	37	278	151	64
S4 128.06	I4	11.42	121	58	58	5.19	74	194	120	66
S4 128.27	I4	11.40	112	24	343	1.12	48	261	128	57
S4 128.38	I4	12.06	123	30	52	4.56	52	244	122	69
S4 128.56 A	I4	6.48	62	243	44	11.43	239	147	65	239
S4 128.56 B	I4	2.87	20	316	34	20.21	285	68	33	299
S4 128.69	I4	11.91	124	34	47	4.54	62	227	116	68

Sample ID/ core depth	Formation	Al (wt%)	Cr (ppm)	Cu (ppm)	Mn (ppm)	Mo (ppm)	Ni (ppm)	P (ppm)	V (ppm)	Zn (ppm)
S4 128.80 A	I4	13.68	151	2	51	3.85	24	227	174	45
S4 128.80 B	I4	13.89	155	10	55	6.68	42	235	177	45
S4 128.95	I4	12.55	135	49	43	5.36	81	241	143	55
S4 129.14	I4	12.74	134	33	38	3.43	85	251	131	54
S4 129.28	I4	13.23	155	36	63	3.14	57	247	170	36
S4 129.44	I4	13.26	154	21	68	1.43	44	223	152	49
S4 129.54	I4	12.65	152	16	70	4.67	41	185	156	81
S4 129.63	I4	12.77	153	24	79	1.49	51	213	158	52
S4 129.74	I4	12.97	145	21	76	0.76	46	177	151	82
S4 129.94	I4	11.45	123	93	100	4.98	116	173	139	229
S4 130.02	I4	11.81	132	41	187	3.82	52	236	156	49
S4 130.04	I4	8.64	93	126	378	6.11	123	218	110	958
S4 132.17	I4	12.93	151	37	110	4.20	61	203	158	59
S4 132.29	I4	11.66	140	28	371	0.00	59	242	148	57
S4 132.56	I4	12.76	146	21	78	5.30	53	227	152	49
S4 132.75	I4	12.92	150	25	122	5.01	66	247	151	50
S4 132.91	I4	13.45	158	24	107	6.36	40	296	163	47
S4 133.73	I4	13.14	154	24	73	2.71	43	241	154	44
S4 133.95	I4	12.12	140	57	159	2.96	61	233	145	57
S4 134.17	I4	8.98	94	50	181	6.04	101	179	95	1444
S4 134.37	I4	10.15	97	27	118	0.00	44	171	108	132
S4 134.50	I4	11.59	133	27	163	4.40	43	235	134	81
S4 134.65	I4	11.27	114	41	90	3.26	69	184	111	51

Sample ID/ core depth	Formation	Al (wt%)	Cr (ppm)	Cu (ppm)	Mn (ppm)	Mo (ppm)	Ni (ppm)	P (ppm)	V (ppm)	Zn (ppm)
S4 135.69	I4	12.85	143	31	139	7.33	56	435	131	60
S4-2 135.81	I4	15.69	203	46	167	9.90	91	359	168	87
S4 135.81	I4	12.73	140	34	130	3.44	65	244	129	69
S4 136.18	I4	13.00	147	33	104	4.11	64	230	132	55
S4 136.31	I4	12.53	138	44	106	4.89	82	223	124	65
S4 136.46	I4	12.36	140	32	160	4.28	73	6173	126	60
S4 136.57	I4	12.94	144	36	106	3.08	65	255	129	71
S4 159.66 a	I3	12.56	110	25	22	4.21	60	226	114	53
S4 159.66 b	I3	13.26	150	34	101	3.03	62	254	138	54
S4 159.80	I3	14.98	140	24	25	5.59	71	313	148	24
S4 159.90	I3	12.83	109	21	21	4.10	16	223	109	110
S4 160.06	I3	12.83	108	23	31	3.48	42	232	107	45
S4 160.20	I3	15.06	143	30	26	5.52	26	296	135	29
S4 160.30	I3	14.30	140	21	22	3.65	39	244	148	31
S4 160.40	I3	13.58	117	16	22	4.08	25	229	122	40
S4 160.49	I3	15.05	137	24	23	4.91	58	288	149	40
S4 160.72	I3	10.62	89	22	75	2.05	46	207	89	57
S4 160.86	I3	13.90	142	17	26	6.30	37	211	128	30
S4 161.08	I3	13.60	129	26	29	4.20	56	218	122	59
S4 161.16	I3	13.79	133	35	26	3.89	53	239	131	65
S4 161.29	I3	13.77	134	35	37	1.02	69	218	125	61
S4 161.39	I3	14.54	148	15	27	4.03	42	243	147	47
S4 161.51	I3	14.56	145	17	35	4.32	37	286	145	63

Sample ID/ core depth	Formation	Al (wt%)	Cr (ppm)	Cu (ppm)	Mn (ppm)	Mo (ppm)	Ni (ppm)	P (ppm)	V (ppm)	Zn (ppm)
S4 161.62	I3	13.34	125	29	473	4.24	69	283	129	45
S4 161.69	I3	13.70	130	38	264	4.49	67	262	129	63
S4 161.75	I3	14.63	142	26	37	6.28	52	264	136	76
S4 161.84	I3	13.87	132	20	346	7.10	49	260	132	42
S4 161.91	I3	13.63	131	30	31	6.01	79	237	129	55
S4 162.03	I3	13.30	120	14	225	3.79	51	267	130	48
S4-3 162.16	I3	15.28	162	22	51	6.02	62	286	143	36
S4-5 162.60	I3	14.66	143	95	53	6.87	39	257	124	61
S4 163.09	I3	11.28	90	16	80	4.54	44	212	84	123
S4 163.32	I3	9.17	67	29	1218	5.19	34	1853	73	44
S4 163.40	I3	12.89	115	11	493	5.52	42	253	113	33
S4 165.20	I3	14.73	145	24	27	5.58	58	194	138	51
S4 165.50	I3	14.02	125	29	22	7.02	62	209	126	50
S4 165.68	I3	14.97	140	25	27	5.57	48	245	139	68
S4 165.80	I3	12.70	101	38	245	5.23	42	249	105	65
S4 165.98	I3	14.63	135	17	536	5.97	39	378	149	36
S4 166.10	I3	15.14	141	12	37	4.68	39	274	146	34
S4 166.26	I3	14.48	132	37	21	4.80	107	237	137	30
S4 166.45	I3	14.42	122	9	25	5.74	46	225	122	29
S4 168.70	I3	14.11	95	6	60	9.40	21	649	96	22
S4 169.11	I3	15.25	137	8	23	4.48	45	230	143	22
S4 169.35	I3	14.02	116	18	21	5.67	58	193	127	23
S4 169.61	I3	15.13	143	17	45	6.84	34	301	151	29

Sample ID/ core depth	Formation	Al (wt%)	Cr (ppm)	Cu (ppm)	Mn (ppm)	Mo (ppm)	Ni (ppm)	P (ppm)	V (ppm)	Zn (ppm)
S4 169.78	I3	12.35	104	16	20	7.87	42	203	99	42

Table A - 3 Total element data for cores S2, S3 and S4. For most samples, the sample ID consists of the core name and depth. The exception is some samples from cores S2 and S4 that were received as powders, which have an additional number following the core name. Samples were split into A and B where there was a visible disparity in pyrite contents across the width of a core section.

Sample ID/ core depth	Formation	Fe_{carb} (wt%)	Fe_{ox} (wt%)	Fe_{mag} (wt%)	Fe_{AVS} (wt%)	Fe_{py} (wt%)	FeT (wt%)	FeHR/FeT	FeP/FeHR	FeT/Al
S2 69.58	Aguelt El Mabha	0.51	0.09	0.25	nd	0.00	2.91	0.29	0.01	0.42
S2 79.51	Aguelt El Mabha	0.07	1.12	0.28	nd	0.00	4.22	0.35	0.00	0.54
S2 80.90	Aguelt El Mabha	0.05	1.45	0.27	nd	0.00	4.11	0.43	0.00	0.68
S2 93.35	Aguelt El Mabha	0.05	0.03	0.02	0.004	0.00	1.11	0.08	0.05	0.34
S2 138.90	Touirist	0.76	0.07	0.09	0.017	3.93	6.11	0.80	0.81	0.56
S2 139.00	Touirist	0.41	0.07	0.07	0.002	2.23	3.13	0.89	0.80	0.32
S2 140.14	Touirist	0.24	0.04	0.06	nd	0.69	2.57	0.40	0.67	0.28
S2 140.25	Touirist	0.29	0.05	0.07	0.002	0.90	3.05	0.43	0.69	0.29
S2 140.30	Touirist	0.29	0.06	0.09	nd	0.39	2.52	0.33	0.47	0.22
S2 140.44	Touirist	0.33	0.06	0.10	0.002	0.84	3.16	0.42	0.63	0.25
S2 140.52	Touirist	0.43	0.07	0.11	nd	0.75	3.09	0.44	0.55	0.26
S2-8 140.77	Touirist	0.52	0.09	0.13	nd	1.53	3.23	0.70	0.68	0.37
S2 141.00	Touirist	0.35	0.08	0.12	nd	0.43	2.22	0.44	0.44	0.27
S2 141.08	Touirist	0.48	0.09	0.14	0.004	0.98	3.58	0.47	0.58	0.31
S2-11 141.25	Touirist	0.42	0.09	0.17	nd	0.69	2.91	0.47	0.50	0.23
S2 141.25	Touirist	0.82	0.08	0.13	nd	1.52	3.70	0.69	0.60	0.38
S2 141.48	Touirist	0.27	0.03	0.07	0.002	0.59	1.94	0.50	0.61	0.36
S2 141.65	Touirist	0.40	0.05	0.08	0.002	1.10	2.89	0.57	0.67	0.38
S2 141.80	Touirist	0.32	0.06	0.12	nd	0.50	2.53	0.40	0.50	0.27
S2 141.90	Touirist	0.25	0.04	0.09	nd	0.81	2.97	0.40	0.68	0.37
S2-13 142.05	Touirist	0.36	0.10	0.23	nd	0.38	2.74	0.39	0.36	0.22
S2 142.05	Touirist	0.40	0.08	0.18	nd	0.48	3.14	0.36	0.43	0.28
S2 142.35	Touirist	0.66	0.08	0.16	nd	2.17	4.84	0.63	0.71	0.47

Sample ID/ core depth	Formation	Fe_{carb} (wt%)	Fe_{ox} (wt%)	Fe_{mag} (wt%)	Fe_{AVS} (wt%)	Fe_{py} (wt%)	FeT (wt%)	FeHR/FeT	FeP/FeHR	FeT/Al
S2 142.50	Touirist	0.27	0.05	0.10	nd	0.50	1.99	0.46	0.55	0.28
S2 142.90	Touirist	0.37	0.07	0.16	nd	0.36	3.03	0.32	0.38	0.27
S2 143.10	Touirist	0.33	0.05	0.13	nd	0.41	2.69	0.34	0.44	0.28
S2 143.19	Touirist	0.40	0.07	0.16	nd	0.41	2.97	0.35	0.39	0.29
S2-17 143.30	Touirist	0.33	0.09	0.21	nd	0.41	2.70	0.39	0.39	0.25
S2 143.30	Touirist	0.50	0.09	0.19	nd	0.45	3.26	0.37	0.37	0.28
S2 143.82	Touirist	0.30	0.06	0.14	nd	0.12	2.39	0.26	0.19	0.22
S2 143.86	Touirist	0.59	0.08	0.19	nd	0.84	3.65	0.47	0.49	0.34
S2 150.60	Touirist	0.42	0.09	0.18	nd	0.52	3.19	0.38	0.43	0.36
S2 150.80	Touirist	0.38	0.10	0.17	nd	0.50	3.24	0.36	0.44	0.33
S2 150.90	Touirist	0.45	0.09	0.18	nd	0.64	3.55	0.38	0.48	0.35
S2 151.40	Touirist	0.46	0.09	0.17	nd	0.94	3.87	0.43	0.57	0.37
S2 151.70	Touirist	0.43	0.08	0.16	nd	0.78	3.63	0.40	0.54	0.36
S2 169.65	Touirist	0.88	0.05	0.02	0.009	0.07	1.97	0.52	0.08	0.42
S2 185.45	En Nesoar	0.20	0.06	0.06	nd	0.22	2.56	0.21	0.41	0.23
S2 185.66	En Nesoar	0.23	0.07	0.06	nd	0.30	2.76	0.24	0.46	0.26
S2-20 187.60	En Nesoar	0.45	0.08	0.12	nd	1.96	6.75	0.39	0.75	1.09
S2-21 187.70	En Nesoar	0.19	0.07	0.08	nd	0.28	2.23	0.28	0.45	0.18
S2 188.10	En Nesoar	0.24	0.07	0.09	nd	0.27	3.27	0.20	0.40	0.27
S2 188.20	En Nesoar	0.36	0.10	0.06	nd	0.39	3.99	0.23	0.43	0.36
S2 188.30	En Nesoar	0.55	0.15	0.07	0.002	1.13	3.88	0.49	0.60	0.35
S2 188.40	En Nesoar	0.29	0.07	0.06	0.005	0.81	3.07	0.40	0.66	0.27
S2 188.50	En Nesoar	0.33	0.08	0.11	nd	0.43	3.35	0.28	0.45	0.29

Sample ID/ core depth	Formation	Fe_{carb} (wt%)	Fe_{ox} (wt%)	Fe_{mag} (wt%)	Fe_{AVS} (wt%)	Fe_{py} (wt%)	FeT (wt%)	FeHR/FeT	FeP/FeHR	FeT/Al
S2 188.60	En Nesoar	0.53	0.08	0.11	nd	1.08	3.88	0.46	0.60	0.40
S2 200.8	En Nesoar	0.35	0.06	0.05	nd	1.56	3.78	0.54	0.77	0.34
S2 201.00	En Nesoar	0.35	0.06	0.05	nd	1.24	3.47	0.49	0.73	0.32
S2 202.15	En Nesoar	0.25	0.03	0.00	nd	1.57	3.04	0.61	0.85	0.31
S2-25 206.70	En Nesoar	0.20	0.04	0.02	0.001	0.60	1.90	0.46	0.70	0.19
S2 207.10	En Nesoar	0.20	0.06	0.04	nd	0.29	2.26	0.26	0.49	0.23
S2-28 207.10	En Nesoar	0.15	0.05	0.06	nd	0.49	2.72	0.27	0.65	0.24
S2-29 207.20	En Nesoar	0.17	0.05	0.05	0.012	0.50	2.38	0.32	0.67	0.21
S2 207.30	En Nesoar	0.22	0.05	0.02	nd	0.44	2.21	0.33	0.59	0.22
S2 207.70	En Nesoar	0.15	0.05	0.04	nd	0.18	2.43	0.17	0.43	0.24
S3 59.18	Aguelt El Mabha	0.45	0.12	0.56	nd	0.00	5.19	0.22	0.00	0.62
S3 59.33	Aguelt El Mabha	0.40	0.10	0.41	nd	0.00	4.65	0.19	0.00	0.53
S3 60.01	Aguelt El Mabha	0.40	0.11	0.40	nd	0.00	3.98	0.23	0.00	0.41
S3 60.86	Aguelt El Mabha	0.43	0.10	0.32	nd	0.00	4.68	0.18	0.00	0.49
S3 60.97	Aguelt El Mabha	0.34	0.08	0.26	nd	0.04	4.12	0.18	0.06	0.41
S3 61.27	Aguelt El Mabha	0.44	0.10	0.39	nd	0.01	4.66	0.20	0.01	0.52
S3 61.88	Aguelt El Mabha	0.51	0.12	0.56	nd	0.00	5.44	0.22	0.00	0.61
S3 123.37	Aguelt El Mabha	0.31	0.73	0.46	nd	0.00	5.82	0.26	0.00	0.54
S3 123.54	Aguelt El Mabha	0.45	0.79	0.62	nd	0.00	6.52	0.28	0.00	0.60
S3 123.60	Aguelt El Mabha	0.32	1.20	0.49	nd	0.00	6.23	0.32	0.00	0.59
S3 124.24	Aguelt El Mabha	0.37	0.63	0.54	nd	0.00	6.04	0.25	0.00	0.56
S3 170.73	Touirist	0.18	0.06	0.15	nd	0.00	3.95	0.10	0.01	0.36
S3 179.80	Touirist	0.19	0.24	0.14	nd	0.00	2.87	0.20	0.00	0.45

Sample ID/ core depth	Formation	Fe_{carb} (wt%)	Fe_{ox} (wt%)	Fe_{mag} (wt%)	Fe_{AVS} (wt%)	Fe_{py} (wt%)	FeT (wt%)	FeHR/FeT	FeP/FeHR	FeT/Al
S3 180.10	Touirist	0.15	0.06	0.11	nd	0.01	3.44	0.10	0.02	0.29
S3 180.30	Touirist	0.29	0.07	0.13	nd	0.00	4.12	0.12	0.00	0.33
S3 180.50	Touirist	0.29	0.67	0.36	nd	0.00	3.96	0.33	0.00	0.67
S3 180.70	Touirist	0.29	0.05	0.11	nd	0.01	2.31	0.20	0.03	0.37
S3 181.00	Touirist	0.27	0.07	0.15	nd	0.02	4.03	0.13	0.04	0.34
S3 181.30	Touirist	0.28	0.22	0.32	nd	0.00	5.21	0.16	0.00	0.42
S3 181.50	Touirist	0.31	0.07	0.14	nd	0.49	4.13	0.24	0.48	0.32
S3 181.70	Touirist	0.23	0.04	0.11	nd	0.00	2.66	0.14	0.00	0.41
S3 181.80	Touirist	0.19	0.07	0.13	nd	0.26	3.87	0.17	0.41	0.31
S3 181.90	Touirist	0.28	0.09	0.22	nd	0.02	3.72	0.17	0.03	0.43
S3 182.40	Touirist	0.28	0.06	0.14	nd	0.00	3.53	0.14	0.00	0.35
S3 182.50	Touirist	0.23	0.08	0.16	nd	0.37	4.24	0.20	0.44	0.35
S3 182.60	Touirist	0.26	0.07	0.15	nd	0.03	3.74	0.14	0.06	0.35
S3 183.00	Touirist	0.29	0.45	0.26	nd	0.00	4.18	0.24	0.00	0.51
S4 74.17	I5	0.38	0.07	0.04	nd	2.38	4.10	0.70	0.83	0.29
S4 79.43	I5	0.16	0.05	0.23	nd	0.03	2.88	0.16	0.06	0.21
S4 79.56	I5	0.22	0.06	0.18	nd	0.12	2.61	0.22	0.20	0.19
S4-13 79.66	I5	0.15	0.04	0.21	nd	0.17	2.88	0.20	0.30	0.18
S4 79.66	I5	0.20	0.04	0.24	nd	0.20	3.08	0.22	0.29	0.21
S4 79.76	I5	1.51	0.13	0.82	nd	0.39	6.21	0.46	0.14	0.48
S4 79.95	I5	3.66	0.20	3.70	nd	0.20	19.55	0.40	0.03	2.52
S4 80.10	I5	0.89	0.07	0.51	nd	0.04	4.57	0.33	0.03	0.34
S4-17 80.22	I5	0.15	0.05	0.19	nd	0.28	2.95	0.23	0.42	0.18

Sample ID/ core depth	Formation	Fe_{carb} (wt%)	Fe_{ox} (wt%)	Fe_{mag} (wt%)	Fe_{AVS} (wt%)	Fe_{py} (wt%)	FeT (wt%)	FeHR/FeT	FeP/FeHR	FeT/Al
S4 80.22	I5	0.18	0.05	0.22	nd	0.17	2.86	0.22	0.27	0.21
S4 80.34	I5	0.26	0.06	0.35	nd	0.07	3.53	0.21	0.09	0.26
S4 80.45	I5	0.24	0.08	0.32	nd	0.16	3.06	0.26	0.20	0.22
S4 80.85	I5	0.20	0.05	0.25	nd	0.46	3.23	0.30	0.48	0.23
S4 81.00	I5	0.16	0.05	0.27	nd	0.01	2.73	0.18	0.03	0.19
S4 81.10	I5	0.36	0.06	0.24	nd	5.57	8.65	0.72	0.89	0.71
S4 81.22	I5	0.17	0.05	0.26	nd	0.22	3.00	0.23	0.31	0.21
S4 81.42	I5	0.13	0.05	0.22	nd	0.08	2.67	0.18	0.17	0.19
S4 81.52	I5	0.21	0.05	0.21	nd	0.43	3.06	0.30	0.48	0.22
S4 81.64	I5	0.27	0.05	0.26	nd	0.52	3.70	0.30	0.47	0.28
S4 81.76	I5	0.41	0.05	0.31	nd	0.71	4.31	0.35	0.48	0.33
S4 81.94	I5	0.28	0.07	0.33	nd	0.28	3.86	0.25	0.29	0.28
S4 82.08	I5	0.19	0.06	0.28	nd	0.12	2.94	0.22	0.19	0.21
S4 90.43	I5	0.23	0.06	0.30	nd	0.06	3.77	0.17	0.10	0.28
S4 90.52	I5	0.41	0.08	0.54	nd	0.03	4.98	0.21	0.03	0.42
S4 90.57	I5	0.37	0.08	0.46	nd	0.02	4.35	0.21	0.02	0.36
S4 90.77	I5	0.36	0.03	0.15	nd	0.11	2.52	0.26	0.17	0.25
S4 90.89	I5	0.62	0.05	0.21	nd	0.10	3.09	0.32	0.10	0.32
S4 91.00	I5	0.49	0.08	0.37	nd	0.38	4.33	0.30	0.29	0.36
S4 91.08	I5	0.54	0.07	0.38	nd	0.03	1.84	0.55	0.03	0.18
S4 91.16	I5	0.12	0.03	0.13	nd	0.02	2.50	0.12	0.05	0.18
S4 109.71	I5	0.69	0.03	0.02	nd	0.16	2.35	0.39	0.18	0.19
S4 120.24	I4	0.84	0.08	0.15	nd	6.26	8.99	0.82	0.85	0.78

Sample ID/ core depth	Formation	Fe_{carb} (wt%)	Fe_{ox} (wt%)	Fe_{mag} (wt%)	Fe_{AVS} (wt%)	Fe_{py} (wt%)	FeT (wt%)	FeHR/FeT	FeP/FeHR	FeT/Al
S4 120.35	I4	1.05	0.07	0.19	nd	7.71	10.75	0.84	0.86	0.98
S4 120.51	I4	0.38	0.05	0.17	nd	1.83	4.19	0.58	0.75	0.32
S4 120.70	I4	0.73	0.06	0.19	nd	2.46	5.55	0.62	0.71	0.46
S4 120.92	I4	0.65	0.08	0.18	nd	1.79	4.55	0.59	0.66	0.35
S4 121.21	I4	0.28	0.04	0.14	nd	1.40	3.88	0.48	0.75	0.31
S4 121.39	I4	0.31	0.05	0.18	nd	0.71	4.00	0.31	0.57	0.33
S4 122.66	I4	0.40	0.08	0.10	nd	3.32	5.23	0.74	0.85	0.40
S4 122.78	I4	0.66	0.10	0.11	nd	4.24	6.53	0.78	0.83	0.52
S4 122.88	I4	0.79	0.10	0.11	nd	5.41	7.89	0.81	0.84	0.64
S4 123.00	I4	1.34	0.12	0.17	nd	4.75	7.39	0.86	0.74	0.59
S4 123.10	I4	0.60	0.11	0.11	nd	4.62	6.82	0.80	0.85	0.57
S4 123.19	I4	0.35	0.06	0.13	nd	2.89	5.40	0.63	0.84	0.41
S4 123.32	I4	0.54	0.07	0.16	nd	4.33	7.21	0.71	0.85	0.61
S4 123.44	I4	0.62	0.08	0.15	nd	4.74	7.44	0.75	0.85	0.65
S4 123.58	I4	0.43	0.05	0.11	nd	1.56	3.88	0.56	0.72	0.28
S4 123.79	I4	0.50	0.07	0.14	nd	3.85	6.32	0.72	0.84	0.51
S4 123.98	I4	0.23	0.05	0.14	nd	0.57	3.08	0.32	0.58	0.22
S4 128.06	I4	0.71	0.11	0.22	nd	4.55	7.72	0.72	0.81	0.68
S4 128.27	I4	0.95	0.09	0.64	nd	2.06	6.89	0.54	0.55	0.60
S4 128.38	I4	0.38	0.06	0.19	nd	2.85	5.99	0.58	0.82	0.50
S4 128.56 A	I4	2.66	0.17	0.32	nd	18.21	21.81	0.98	0.85	3.37
S4 128.56 B	I4	2.70	0.10	0.29	nd	31.15	36.12	0.95	0.91	12.59
S4 128.69	I4	0.61	0.08	0.24	nd	3.22	6.18	0.67	0.78	0.52

Sample ID/ core depth	Formation	Fe_{carb} (wt%)	Fe_{ox} (wt%)	Fe_{mag} (wt%)	Fe_{AVS} (wt%)	Fe_{py} (wt%)	FeT (wt%)	FeHR/FeT	FeP/FeHR	FeT/Al
S4 128.80 A	I4	0.20	0.05	0.21	nd	0.32	2.93	0.26	0.41	0.21
S4 128.80 B	I4	0.23	0.04	0.19	nd	1.12	3.75	0.42	0.71	0.27
S4 128.95	I4	0.61	0.08	0.18	nd	3.72	6.43	0.71	0.81	0.51
S4 129.14	I4	0.41	0.05	0.16	nd	2.95	5.55	0.64	0.83	0.44
S4 129.28	I4	0.34	0.06	0.10	nd	1.26	3.95	0.45	0.71	0.30
S4 129.44	I4	0.35	0.05	0.11	nd	1.48	4.08	0.48	0.75	0.31
S4 129.54	I4	0.28	0.04	0.11	nd	2.25	4.81	0.56	0.84	0.38
S4 129.63	I4	0.38	0.05	0.13	nd	2.41	5.09	0.58	0.81	0.40
S4 129.74	I4	0.29	0.04	0.14	nd	2.39	5.30	0.54	0.84	0.41
S4 129.94	I4	0.68	0.06	0.19	nd	6.42	10.53	0.70	0.87	0.92
S4 130.02	I4	0.56	0.09	0.26	nd	3.43	6.63	0.65	0.79	0.56
S4 130.04	I4	1.15	0.19	0.27	nd	14.27	18.61	0.85	0.90	2.15
S4 132.17	I4	0.46	0.07	0.20	nd	2.22	5.10	0.58	0.75	0.39
S4 132.29	I4	0.80	0.17	0.32	nd	1.87	5.93	0.53	0.59	0.51
S4 132.56	I4	0.30	0.04	0.16	nd	2.19	5.32	0.51	0.81	0.42
S4 132.75	I4	0.47	0.05	0.20	nd	2.12	5.35	0.53	0.74	0.41
S4 132.91	I4	0.31	0.06	0.19	nd	1.14	4.35	0.39	0.67	0.32
S4 133.73	I4	0.27	0.04	0.13	nd	1.17	4.01	0.40	0.73	0.31
S4 133.95	I4	0.44	0.05	0.20	nd	1.78	5.01	0.49	0.72	0.41
S4 134.17	I4	0.94	0.09	0.37	nd	3.43	8.01	0.60	0.71	0.89
S4 134.37	I4	0.57	0.10	0.32	nd	1.65	5.29	0.50	0.63	0.52
S4 134.50	I4	0.36	0.05	0.22	nd	1.37	4.61	0.43	0.69	0.40
S4 134.65	I4	0.76	0.07	0.33	nd	2.99	7.06	0.59	0.72	0.63

Sample ID/ core depth	Formation	Fe_{carb} (wt%)	Fe_{ox} (wt%)	Fe_{mag} (wt%)	Fe_{AVS} (wt%)	Fe_{py} (wt%)	FeT (wt%)	FeHR/FeT	FeP/FeHR	FeT/Al
S4 135.69	I4	0.54	0.07	0.30	nd	1.54	4.95	0.49	0.63	0.39
S4-2 135.81	I4	0.47	0.08	0.25	nd	1.57	4.63	0.51	0.66	0.30
S4 135.81	I4	0.59	0.07	0.27	nd	1.76	4.85	0.55	0.65	0.38
S4 136.18	I4	0.53	0.07	0.23	nd	1.87	4.81	0.56	0.69	0.37
S4 136.31	I4	0.48	0.07	0.26	nd	1.73	4.98	0.51	0.68	0.40
S4 136.46	I4	0.46	0.06	0.41	nd	1.74	5.02	0.53	0.65	0.41
S4 136.57	I4	0.41	0.06	0.23	nd	1.57	4.68	0.49	0.69	0.36
S4 159.66 a	I3	0.36	0.03	0.01	nd	2.24	3.02	0.87	0.85	0.24
S4 159.66 b	I3	0.37	0.05	0.18	nd	1.58	4.22	0.51	0.73	0.32
S4 159.80	I3	0.46	0.03	0.02	nd	2.91	3.81	0.90	0.85	0.25
S4 159.90	I3	0.13	0.02	0.01	nd	0.32	1.00	0.49	0.67	0.08
S4 160.06	I3	0.31	0.03	0.04	nd	1.76	2.75	0.78	0.82	0.21
S4 160.20	I3	0.25	0.02	0.02	nd	0.96	1.94	0.64	0.77	0.13
S4 160.30	I3	0.28	0.02	0.02	nd	1.07	1.96	0.71	0.77	0.14
S4 160.40	I3	0.20	0.01	0.02	nd	0.63	1.43	0.60	0.74	0.11
S4 160.49	I3	0.35	0.03	0.01	nd	1.62	2.53	0.80	0.81	0.17
S4 160.72	I3	0.60	0.09	0.14	nd	2.07	3.48	0.83	0.71	0.33
S4 160.86	I3	0.26	0.03	0.02	nd	1.54	2.72	0.68	0.83	0.20
S4 161.08	I3	0.47	0.03	0.04	nd	2.81	3.84	0.87	0.84	0.28
S4 161.16	I3	0.40	0.03	0.02	nd	1.77	2.67	0.83	0.80	0.19
S4 161.29	I3	0.63	0.04	0.07	nd	2.86	4.07	0.88	0.79	0.30
S4 161.39	I3	0.33	0.03	0.02	nd	1.78	2.76	0.78	0.82	0.19
S4 161.51	I3	0.22	0.03	0.04	nd	1.26	2.45	0.63	0.81	0.17

Sample ID/ core depth	Formation	Fe_{carb} (wt%)	Fe_{ox} (wt%)	Fe_{mag} (wt%)	Fe_{AVS} (wt%)	Fe_{py} (wt%)	FeT (wt%)	FeHR/FeT	FeP/FeHR	FeT/Al
S4 161.62	I3	0.94	0.10	0.60	nd	2.71	6.01	0.72	0.62	0.45
S4 161.69	I3	1.11	0.08	0.59	nd	2.63	5.75	0.77	0.60	0.42
S4 161.75	I3	0.32	0.04	0.05	nd	2.07	3.27	0.76	0.84	0.22
S4 161.84	I3	0.96	0.06	0.59	nd	1.43	4.67	0.65	0.47	0.34
S4 161.91	I3	0.53	0.04	0.04	nd	2.70	3.79	0.87	0.81	0.28
S4 162.03	I3	0.87	0.08	0.44	nd	1.42	4.48	0.63	0.51	0.34
S4-3 162.16	I3	0.31	0.04	0.06	nd	1.40	2.69	0.68	0.77	0.18
S4-5 162.60	I3	0.29	0.03	0.08	nd	0.83	2.20	0.55	0.68	0.15
S4 163.09	I3	0.53	0.04	0.14	nd	1.12	2.38	0.77	0.61	0.21
S4 163.32	I3	2.81	0.09	1.14	nd	0.39	7.53	0.59	0.09	0.82
S4 163.40	I3	0.76	0.08	0.48	nd	1.22	4.00	0.63	0.48	0.31
S4 165.20	I3	0.31	0.02	0.02	nd	1.73	2.86	0.73	0.83	0.19
S4 165.50	I3	0.44	0.03	0.01	nd	1.90	2.82	0.85	0.80	0.20
S4 165.68	I3	0.16	0.01	0.01	nd	1.56	2.57	0.67	0.90	0.17
S4 165.80	I3	0.50	0.02	0.39	nd	0.83	3.11	0.56	0.48	0.25
S4 165.98	I3	1.29	0.05	0.77	nd	0.48	4.40	0.59	0.18	0.30
S4 166.10	I3	0.14	0.01	0.02	nd	0.91	1.89	0.57	0.84	0.12
S4 166.26	I3	0.51	0.03	0.01	nd	3.18	3.97	0.94	0.85	0.27
S4 166.45	I3	0.21	0.04	0.02	nd	1.15	2.17	0.66	0.80	0.15
S4 168.70	I3	0.07	0.01	0.02	nd	0.31	1.02	0.40	0.76	0.07
S4 169.11	I3	0.31	0.02	0.01	nd	1.25	1.98	0.80	0.78	0.13
S4 169.35	I3	0.21	0.02	0.01	nd	1.72	2.52	0.78	0.88	0.18
S4 169.61	I3	0.11	0.01	0.01	nd	0.69	1.57	0.52	0.84	0.10

Sample ID/ core depth	Formation	Fe_{carb} (wt%)	Fe_{ox} (wt%)	Fe_{mag} (wt%)	Fe_{AVS} (wt%)	Fe_{py} (wt%)	FeT (wt%)	FeHR/FeT	FeP/FeHR	FeT/Al
S4 169.78	I3	0.15	0.01	0.02	nd	0.93	1.55	0.71	0.84	0.13

Table A - 4 Fe pools and redox indicators for cores S2, S3 and S4. For most samples, the sample ID consists of the core name and depth. The exception is some samples from cores S2 and S4 that were received as powders, which have an additional number following the core name. Samples were split into A and B where there was a visible disparity in pyrite contents across the width of a core section.

Sample ID/ core depth	Formation	P_{Fe} (ppm)	P_{auth} (ppm)	P_{det} (ppm)	P_{org} (ppm)	P_{res} (ppm)	P_{sum} (ppm)	Total P (ppm)
S2 80.90	Aguelt El Mabha	1.30	138.49	79.70	51.64	28.60	299.73	288.07
S2 93.35	Aguelt El Mabha	7.59	102.83	63.89	21.27	9.74	205.33	193.52
S2 138.90	Touirist	12.76	307.96	422.94	126.86	63.30	933.83	1222.93
S2 139.00	Touirist	0.16	37.82	36.27	95.18	35.40	204.83	223.41
S2 140.25	Touirist	0.00	52.41	61.15	116.72	41.85	272.13	315.10
S2 140.44	Touirist	0.05	245.29	238.75	134.95	54.44	673.48	829.99
S2 140.52	Touirist	4.69	66.27	96.76	119.54	49.18	336.45	386.63
S2 141.00	Touirist	0.14	110.75	78.47	90.12	29.05	308.53	282.42
S2 141.08	Touirist	0.84	144.64	136.26	123.75	54.11	459.60	525.26
S2 141.48	Touirist	0.00	85.35	72.63	49.89	22.74	230.61	274.68
S2 141.80	Touirist	0.24	75.48	64.77	118.25	41.56	300.30	350.74
S2-13 142.05	Touirist	0.10	142.70	191.78	128.23	63.33	526.14	689.28
S2 142.50	Touirist	3.62	161.63	282.48	63.15	116.93	627.81	582.32
S2-17 143.30	Touirist	0.05	114.99	183.80	140.91	51.91	491.66	633.63
S2 143.30	Touirist	0.25	78.69	78.30	95.65	66.39	319.28	363.43
S2 143.86	Touirist	3.17	108.87	164.82	101.86	119.20	497.92	497.26
S2 150.60	Touirist	0.28	187.15	335.06	84.46	49.32	656.27	804.91
S2 150.90	Touirist	8.71	341.88	473.67	103.80	54.90	982.96	1246.60
S2 151.40	Touirist	0.05	243.57	301.90	86.50	58.41	690.43	847.23
S2 151.70	Touirist	2.00	269.22	282.31	125.22	57.58	736.33	877.87
S2 185.45	En Nesoar	0.10	216.17	143.69	116.37	52.12	528.44	618.71
S2 185.66	En Nesoar	0.14	67.20	111.25	97.04	45.55	321.18	339.60
S2 188.10	En Nesoar	0.00	87.66	106.42	113.80	56.46	364.34	399.41

Sample ID/ core depth	Formation	P_{Fe} (ppm)	P_{auth} (ppm)	P_{det} (ppm)	P_{org} (ppm)	P_{res} (ppm)	P_{sum} (ppm)	Total P (ppm)
S2 188.20	En Nesoar	0.10	35.22	53.49	104.58	55.19	248.58	240.85
S2 188.30	En Nesoar	3.50	11.53	51.05	97.12	57.06	220.28	259.33
S2 188.60	En Nesoar	0.78	10.12	70.23	88.43	48.76	218.32	259.05
S2 200.8	En Nesoar	0.00	26.81	9.23	120.14	55.48	211.66	186.62
S2 201.00	En Nesoar	6.58	29.30	12.88	112.27	56.09	217.12	211.31
S2 202.15	En Nesoar	0.15	33.88	31.55	104.56	52.03	222.16	224.73
S2-25 206.70	En Nesoar	0.17	23.25	15.17	81.16	46.66	166.42	199.98
S2 207.70	En Nesoar	1.20	50.80	58.28	95.59	48.09	253.96	263.92
S3 59.18	Aguelt El Mabha	0.14	26.29	47.88	64.62	40.99	179.92	195.08
S3 59.33	Aguelt El Mabha	0.00	28.52	50.78	68.11	44.34	191.76	210.36
S3 60.01	Aguelt El Mabha	0.00	27.06	63.70	91.36	52.03	234.14	247.62
S3 60.86	Aguelt El Mabha	1.24	29.47	60.54	94.10	40.95	226.30	249.19
S3 60.97	Aguelt El Mabha	0.00	27.08	58.67	102.19	52.44	240.37	264.93
S3 61.27	Aguelt El Mabha	0.00	42.01	61.11	90.89	44.62	238.63	244.78
S3 61.88	Aguelt El Mabha	2.09	30.08	62.55	92.35	43.84	230.91	234.25
S3 170.73	Touirist	0.00	27.88	24.90	102.82	57.39	213.00	277.32
S3 179.80	Touirist	0.00	51.05	124.67	49.03	22.87	247.62	282.06
S3 180.10	Touirist	5.64	69.57	145.93	114.73	40.33	376.20	459.66
S3 180.70	Touirist	0.00	115.26	117.29	64.65	17.93	315.12	303.84
S3 181.00	Touirist	0.00	40.92	184.43	94.71	40.55	360.61	440.32
S3 181.30	Touirist	6.95	23.77	152.09	179.54	49.45	411.79	551.15
S3 181.70	Touirist	4.73	72.77	107.83	58.10	18.10	261.53	301.88
S3 181.80	Touirist	0.00	35.12	189.42	104.04	39.89	368.47	455.71

Sample ID/ core depth	Formation	P_{Fe} (ppm)	P_{auth} (ppm)	P_{det} (ppm)	P_{org} (ppm)	P_{res} (ppm)	P_{sum} (ppm)	Total P (ppm)
S3 181.90	Touirist	8.04	85.19	146.45	77.84	27.10	344.62	382.97
S3 182.40	Touirist	0.00	53.77	156.05	109.40	31.91	351.13	419.50
S3 182.50	Touirist	0.00	42.72	211.09	97.40	40.69	391.90	497.86
S3 182.60	Touirist	0.00	48.87	151.40	110.26	36.12	346.65	397.42
S4 74.17	I5	1.78	24.79	19.27	132.13	70.61	248.58	258.14
S4 79.43	I5	1.99	46.31	9.47	154.42	63.44	275.63	229.01
S4 79.66	I5	0.00	50.67	14.12	157.89	61.79	284.47	262.82
S4 79.76	I5	0.42	51.48	66.83	147.33	52.62	318.67	315.56
S4 80.22	I5	2.86	59.40	8.03	142.33	56.99	269.61	219.55
S4 80.34	I5	0.00	17.84	4.57	163.22	54.70	240.33	192.29
S4 81.00	I5	0.00	34.92	10.23	154.80	54.19	254.15	242.71
S4 81.10	I5	11.10	20.53	5.83	117.38	74.18	229.03	219.45
S4 81.42	I5	1.66	42.98	10.79	154.97	57.48	267.88	242.39
S4 90.43	I5	13.57	41.50	21.78	142.94	59.27	279.06	250.58
S4 90.57	I5	0.00	62.95	32.74	124.33	43.61	263.64	218.67
S4 91.08	I5	2.38	53.33	77.21	121.23	50.72	304.86	329.47
S4 91.16	I5	4.05	33.22	20.07	123.77	48.78	229.89	243.55
S4 109.71	I5	1.05	42.16	38.79	106.09	38.73	226.82	240.36
S4 120.24	I4	0.28	22.12	2.25	102.88	59.69	187.21	206.07
S4 120.51	I4	0.32	33.32	4.35	130.04	69.02	237.05	262.42
S4 122.66	I4	1.99	17.44	5.76	87.16	48.06	160.41	172.93
S4 123.10	I4	0.20	15.58	3.96	91.12	81.57	192.43	226.24
S4 123.44	I4	0.15	22.97	2.69	86.93	84.95	197.68	199.88

Sample ID/ core depth	Formation	P_{Fe} (ppm)	P_{auth} (ppm)	P_{det} (ppm)	P_{org} (ppm)	P_{res} (ppm)	P_{sum} (ppm)	Total P (ppm)
S4 128.06	I4	0.18	24.91	6.54	77.62	71.94	181.19	194.30
S4 128.27	I4	1.75	19.42	24.27	151.57	53.75	250.76	260.61
S4 128.95	I4	0.65	19.04	2.12	140.85	57.75	220.40	241.33
S4 129.28	I4	0.09	17.54	1.69	132.78	69.01	221.11	247.12
S4 129.94	I4	0.00	18.42	2.71	97.72	51.85	170.71	172.77
S4 130.02	I4	0.91	23.62	3.38	134.80	55.47	218.19	236.15
S4 132.75	I4	0.05	26.54	7.05	150.05	56.48	240.18	247.22
S4 133.73	I4	0.05	29.12	3.02	141.75	19.02	192.96	241.19
S4 134.37	I4	0.14	28.62	9.33	105.03	43.52	186.64	170.98
S4 134.65	I4	0.03	31.47	5.01	106.96	36.75	180.22	183.67
S4 135.81	I4	0.36	35.36	14.17	146.37	54.46	250.71	243.77
S4 159.66 a	I3	0.98	10.75	7.26	131.01	41.97	191.98	225.96
S4 159.80	I3	1.54	21.88	9.24	176.81	55.09	264.56	313.39
S4 160.20	I3	0.24	16.71	5.43	158.96	72.09	253.43	296.25
S4 160.40	I3	4.74	23.06	8.45	127.04	44.86	208.15	228.55
S4 160.86	I3	0.10	18.85	3.83	126.36	52.74	201.88	210.70
S4 161.16	I3	0.05	17.41	7.97	124.66	52.30	202.39	238.87
S4 161.51	I3	0.00	28.39	5.15	163.39	69.12	266.04	285.93
S4 161.62	I3	0.30	11.82	22.38	156.80	60.81	252.12	282.93
S4 161.91	I3	0.15	18.37	8.82	134.90	56.76	219.00	237.47
S4 162.03	I3	0.10	41.45	19.35	141.04	28.71	230.66	267.08
S4 163.09	I3	0.18	26.64	15.18	96.56	63.55	202.12	212.00
S4 163.32	I3	9.09	31.10	1943.02	90.75	77.72	2151.68	1853.37

Sample ID/ core depth	Formation	P_{Fe} (ppm)	P_{auth} (ppm)	P_{det} (ppm)	P_{org} (ppm)	P_{res} (ppm)	P_{sum} (ppm)	Total P (ppm)
S4 163.40	I3	0.27	24.24	26.81	127.03	68.52	246.87	252.95
S4 165.20	I3	2.15	21.57	6.57	111.09	67.23	208.61	193.89
S4 165.98	I3	0.28	34.67	60.14	195.20	78.34	368.64	378.17
S4 166.26	I3	1.44	13.58	15.81	128.75	67.21	226.79	237.08
S4 168.70	I3	3.05	157.35	220.63	136.07	59.31	576.41	648.65
S4 169.61	I3	0.10	23.14	15.40	139.53	50.44	228.61	301.38

Table A - 5 P pools for selected samples from cores S2, S3 and S4. For most samples, the sample ID consists of the core name and depth. The exception is some samples from cores S2 and S4 that were received as powders, which have an additional number following the core name. Samples were split into A and B where there was a visible disparity in pyrite contents across the width of a core section.

Appendix B – S1 data tables

Sample Id/core depth	Formation	Description	TOC (wt%)	Sulphide S (wt%)
S1 70.58	Touirist	Laminated black shale, visible iron sulphide	1.11	3.24
S1 70.75	Touirist	Black shale	1.27	1.02
S1 70.89	Touirist	Flaky black shale, visible iron sulphide	4.42	0.93
S1 70.98	Touirist	Black shale, visible iron sulphide	8.97	2.50
S1 71.05	Touirist	Black shale, visible iron sulphide	8.70	1.62
S1 71.12	Touirist	Black shale	7.45	2.26
S1 71.21	Touirist	Black shale	5.14	0.87
S1 71.34	Touirist	Black shale, visible iron sulphide	8.90	3.26
S1 71.47	Touirist	Black shale, visible iron sulphide	10.08	2.36
S1-12 71.51	Touirist	Powder	9.33	2.15
S1 71.65	Touirist	Flaky black shale, splitting along wavy foliations, visible iron sulphide	9.96	2.12
S1 71.81	Touirist	Laminated, flaky black shale, visible iron sulphide	4.97	0.97
S1 71.92	Touirist	Laminated black shale, visible iron sulphide	8.39	1.49
S1 78.50	Touirist	Black shale, visible iron sulphide	9.36	5.44
S1 72.60	Touirist	Laminated black shale, visible iron sulphide	9.53	1.88
S1 72.67	Touirist	Black shale	9.06	1.98
S1 72.75	Touirist	Black shale, visible iron sulphide	10.60	2.57
S1 72.80	Touirist	Black shale	8.84	1.80
S1 72.85	Touirist	Black shale, visible iron sulphide	8.70	1.26
S1 73.05	Touirist	Laminated black shale	9.35	0.80

Sample Id/core depth	Formation	Description	TOC (wt%)	Sulphide S (wt%)
S1 73.35	Touirist	Black shale	9.15	1.35
S1 73.60	Touirist	Black shale	8.03	1.00
S1-17 73.65	Touirist	Powder	7.98	0.90
S1 73.65	Touirist	Black shale	5.66	1.42
S1-18 73.70	Touirist	Powder	8.33	1.39
S1 73.80	Touirist	Black shale	9.95	2.12
S1 73.85	Touirist	Black shale	8.96	1.09
S1 73.92	Touirist	Black shale	9.81	1.49
S1 73.99	Touirist	Black shale with some visible irregular patches of carbonate, visible iron sulphide	7.45	3.17
S1 74.07	Touirist	Black shale with patchy lens of bluish white carbonate	9.50	1.95
S1 74.13	Touirist	Black shale	11.33	1.96
S1 74.20	Touirist	Black shale, visible iron sulphide	7.84	1.63
S1 74.26	Touirist	Black shale	6.57	1.14
S1 74.36	Touirist	Black shale	4.41	0.71
S1 74.52	Touirist	Black shale with lenses of bluish white carbonate	5.50	1.50
S1 74.57	Touirist	Black shale	7.05	1.17
S1 74.67	Touirist	Black shale, visible iron sulphide	6.17	1.15
S1 74.97	Touirist	Black shale, visible iron sulphide, minor pale grey sheets of carbonate	3.73	1.30
S1 75.19	Touirist	Black shale, visible iron sulphide	3.42	1.26
S1 75.42	Touirist	Black shale, visible iron sulphide	11.71	1.28
S1 75.48	Touirist	Black shale	6.56	0.97
S1 75.53	Touirist	Laminated black shale interbedded with fine layers of carbonate, visible iron sulphide	9.77	2.17
S1 75.60	Touirist	Laminated carbonate rich black shale	5.40	0.63
S1 75.75	Touirist	Laminated interbedded black shale and bluish grey carbonate	4.61	0.70

Sample Id/core depth	Formation	Description	TOC (wt%)	Sulphide S (wt%)
S1 75.80	Touirist	Laminated carbonate rich black shale	5.83	0.80
S1 75.88	Touirist	Laminated carbonate rich black shale	7.58	0.98
S1 75.97	Touirist	Laminated carbonate rich black shale, visible iron sulphide	6.21	1.11
S1 76.07	Touirist	Laminated carbonate rich black shale, visible iron sulphide	5.73	0.64
S1 76.15	Touirist	Black shale and laminated carbonate rich black shale, separated by visible iron sulphide	8.38	1.90
S1 76.22	Touirist	Laminated carbonate rich black shale, visible iron sulphide	5.08	1.31
S1 76.29	Touirist	Laminated carbonate rich black shale, visible iron sulphide	4.41	0.39
S1 76.44	Touirist	Laminated carbonate rich black shale	5.08	0.74
S1 76.65	Touirist	Laminated carbonate rich black shale	3.91	1.28
S1 76.75	Touirist	Laminated carbonate rich black shale	4.82	0.24
S1 76.83	Touirist	Laminated black shale with lighter carbonate rich bands	6.89	0.75
S1 76.97	Touirist	Laminated carbonate rich black shale	4.08	0.40
S1 77.09	Touirist	Carbonate rich black shale, visible iron sulphide	4.38	0.63
S1 77.30	Touirist	Carbonate rich black shale, visible iron sulphide	7.12	0.90
S1 77.35	Touirist	Laminated carbonate rich black shale	6.39	0.22
S1 77.56	Touirist	Laminated carbonate rich black shale, calcite vein ~ perpendicular to lamination	5.64	0.07
S1 77.71	Touirist	Laminated carbonate rich shale, with calcite vein	4.01	0.02
S1 78.00	Touirist	Carbonate rich black shale, visible iron sulphide	5.13	0.66
S1 78.21	Touirist	Laminated carbonate rich black shale	6.41	0.33
S1 78.45	Touirist	Carbonate rich black shale, calcite veins	5.53	0.24
S1 78.83	Touirist	Laminated carbonate rich black shale, visible iron sulphide	4.48	1.06
S1 79.02	Touirist	Laminated carbonate rich black shale	4.31	0.11
S1 79.15	Touirist	Laminated carbonate rich black shale, visible iron sulphide	7.48	1.10
S1 79.39	Touirist	Laminated carbonate rich black shale, visible iron sulphide	5.00	1.51

Sample Id/core depth	Formation	Description	TOC (wt%)	Sulphide S (wt%)
S1 79.52	Touirist	Laminated carbonate rich black shale, visible iron sulphide	3.99	0.77
S1 79.65	Touirist	Laminated carbonate rich black shale, visible iron sulphide	4.18	0.54
S1 79.80	Touirist	Carbonate rich black shale, visible iron sulphide	4.24	0.55
S1 79.99	Touirist	Carbonate rich black shale, visible iron sulphide	4.83	1.06
S1 80.31	Touirist	Carbonate rich black shale	7.79	0.32
S1 80.51	Touirist	Carbonate rich black shale, visible iron sulphide	6.51	1.32
S1 80.64	Touirist	Carbonate rich black shale	9.23	0.76
S1 80.70	Touirist	Carbonate rich black shale, visible iron sulphide	5.37	0.45
S1 80.86	Touirist	Carbonate rich black shale	8.26	0.22
S1 81.15	Touirist	Flaky black shale	10.65	0.81
S1 81.77	Touirist	Flaky black shale	8.08	1.22
S1 81.97	Touirist	Black shale	8.11	1.55
S1 82.02	Touirist	Black shale	8.40	1.25
S1 82.15 A	Touirist	Laminated black shale, visible iron sulphide	4.35	1.49
S1 82.15 B	Touirist	Laminated black shale, visible iron sulphide - roughly a third of sample	2.71	21.44
S1 82.24	Touirist	Black shale	9.90	1.40
S1 82.34	Touirist	Black shale	5.43	2.10
S1 82.43	Touirist	Black shale	16.93	1.42
S1 83.59	Touirist	Black shale	16.61	1.42
S1 83.65	Touirist	Black shale	15.93	1.27
S1 84.71	En Nesoar	Laminated black shale, visible iron sulphide	7.07	0.89
S1 84.83	En Nesoar	Laminated black shale	10.13	1.12
S1 84.94	En Nesoar	Laminated black shale, minor white veining (no reaction to HCl)	16.63	1.00
S1 85.05	En Nesoar	Black shale, some white veining (no reaction to HCl)	16.76	0.98

Sample Id/core depth	Formation	Description	TOC (wt%)	Sulphide S (wt%)
S1 85.19	En Nesoar	Black shale	20.35	1.09
S1 85.25	En Nesoar	Black shale	20.15	0.85
S1 85.34	En Nesoar	Black shale	20.64	1.60
S1 85.45	En Nesoar	Laminated black shale, minor calcite veining	20.20	0.59
S1 85.62	En Nesoar	Black shale, minor calcite veining	21.67	1.01
S1 85.75	En Nesoar	Black shale, minor calcite veining	22.12	1.12
S1 85.85	En Nesoar	Laminated black shale, minor calcite veining	21.90	0.90
S1 85.94	En Nesoar	Laminated black shale	21.64	1.06
S1 86.07	En Nesoar	Black shale	15.88	0.51
S1 86.20	En Nesoar	Laminated black shale	17.51	0.80
S1 86.33	En Nesoar	Laminated black shale	22.98	1.25
S1 86.62	En Nesoar	Laminated black shale	13.21	0.83
S1 86.82	En Nesoar	Laminated black shale	12.84	0.48
S1 86.92	En Nesoar	Laminated black shale	14.02	0.50
S1 87.05	En Nesoar	Laminated black shale	11.55	0.58
S1 87.19	En Nesoar	Laminated black shale	13.28	0.61
S1 87.29	En Nesoar	Laminated black shale	17.17	0.68
S1 87.36	En Nesoar	Laminated black shale	16.54	0.66
S1 87.50	En Nesoar	Black shale	16.16	0.58
S1 87.60	En Nesoar	Black shale, minor white veining (no reaction to HCl)	20.14	0.59
S1 87.70	En Nesoar	Black shale, minor white veining (no reaction to HCl)	16.79	0.49
S1 87.80	En Nesoar	Black shale, minor white veining (no reaction to HCl)	16.80	0.52
S1 87.87	En Nesoar	Black shale	15.74	0.69
S1 87.95	En Nesoar	Laminated black shale, minor white veining (no reaction to HCl)	18.94	0.67

Sample Id/core depth	Formation	Description	TOC (wt%)	Sulphide S (wt%)
S1-1 88.09	En Nesoar	Powder	11.89	0.47
S1 88.19	En Nesoar	Black shale	13.71	0.65
S1 88.24	En Nesoar	Black shale, minor white veining (no reaction to HCl)	33.79	0.80
S1-3 88.27	En Nesoar	Powder	11.30	2.18
S1-5 88.46	En Nesoar	Powder	7.50	0.92
S1 88.46	En Nesoar	Laminated black shale	6.80	0.19
S1-19 88.92	En Nesoar	Powder	25.18	0.60
S1-21 89.10	En Nesoar	Powder	33.43	0.67
S1-22 89.33	En Nesoar	Powder	38.50	0.07
S1-23 89.36	En Nesoar	Powder	35.93	0.03
S1-24 89.40	En Nesoar	Powder	35.10	0.08
S1-25 89.50	En Nesoar	Powder	24.01	7.94
S1 102.00		Dolerite	0.02	0.07
S1 104.20		Dolerite	0.04	0.02
S1 121.56	En Nesoar	Black shale, shows contact with dolerite (not included in crushed sample)	35.21	0.35
S1 121.63	En Nesoar	Black shale	36.72	0.19
S1 121.82	En Nesoar	Black shale	34.18	0.31
S1 121.89	En Nesoar	Black shale	37.05	0.87
S1 121.92	En Nesoar	Black shale	24.86	12.08
S1 122.00	En Nesoar	Black shale	27.06	0.95
S1 122.10	En Nesoar	Black shale	23.93	3.37
S1 122.20	En Nesoar	Laminated black shale	5.99	0.71
S1 122.25	En Nesoar	Laminated black shale	8.91	0.46
S1 122.40	En Nesoar	Black shale	5.45	0.57

Sample Id/core depth	Formation	Description	TOC (wt%)	Sulphide S (wt%)
S1 122.60	En Nesoar	Laminated dark grey to black calcareous shale	4.45	2.82
S1 122.75 A	En Nesoar	Laminated white to dark grey carbonate rich shale	2.98	1.84
S1 122.75 B	En Nesoar	Laminated white to dark grey carbonate rich shale, visible iron sulphide	2.40	3.20
S1 122.99	En Nesoar	Laminated bluish grey to black carbonate rich shale	4.08	0.97
S1 123.06	En Nesoar	Laminated bluish grey to greenish black shale, visible iron sulphide, slightly calcareous	0.48	0.51
S1 123.12	En Nesoar	Laminated bluish grey to greenish black shale, visible iron sulphide, slightly calcareous	1.10	0.54
S1 129.07	En Nesoar	White to bluish/greenish grey stromatolitic carbonate	0.02	0.58
S1 129.15	En Nesoar	White to dark greenish grey stromatolitic carbonate	0.05	0.02
S1 129.82	En Nesoar	White to dark greenish grey stromatolite	0.05	0.50
S1 132.98	En Nesoar	White to dark greenish grey stromatolitic carbonate	0.03	0.63
S1 133.20	En Nesoar	White to dark greenish grey brecciated carbonate	0.11	0.59
S1 134.27	En Nesoar	White to dark greenish grey brecciated carbonate	0.14	1.18
S1 134.70	En Nesoar	White to dark greenish grey brecciated stromatolitic carbonate	0.08	0.16
S1 135.00	En Nesoar	White to bluish/greenish grey stromatolitic carbonate	0.04	0.24

Table B - 1 Sample descriptions and carbon and sulphur data for core S1. For most samples, the sample ID consists of the core name and depth. The exception is some samples that were received as powders, which have an additional number following the core name. Samples were split into A and B where there was a visible disparity in pyrite contents across the width of a core section.

Sample Id/core depth	Formation	Al (wt%)	Cr (ppm)	Cu (ppm)	Mn (ppm)	Mo (ppm)	Ni (ppm)	P (ppm)	V (ppm)	Zn (ppm)
S1 70.58	Touirist	11.50	230	99	355	6.5	170	663	182	171
S1 70.75	Touirist	13.29	133	54	192	10.1	176	435	269	102
S1 70.89	Touirist	12.69	143	75	147	20.5	208	254	909	106
S1 70.98	Touirist	11.08	166	408	204	79.1	551	587	1703	996
S1 71.05	Touirist	11.82	153	259	205	48.3	387	339	1748	867
S1 71.12	Touirist	11.88	147	247	223	44.5	388	375	1286	495
S1 71.21	Touirist	13.10	173	141	180	19.4	239	354	802	125
S1 71.34	Touirist	11.61	156	217	236	38.8	327	550	1309	523
S1 71.47	Touirist	11.61	150	219	231	43.8	345	473	1569	713
S1-12 71.51	Touirist	13.37	179	291	198	50.6	425	441	1922	645
S1 71.65	Touirist	11.80	153	278	200	44.7	387	331	1465	380
S1 71.81	Touirist	14.14	169	109	156	13.0	213	514	724	110
S1 71.92	Touirist	12.63	162	207	163	34.1	370	351	765	309
S1 78.50	Touirist	11.33	169	270	206	71.1	338	971	2137	761
S1 72.60	Touirist	10.35	165	329	230	75.2	490	904	1370	1249
S1 72.67	Touirist	11.43	173	218	204	57.2	325	477	2076	572
S1 72.75	Touirist	11.22	161	275	228	75.5	336	732	1874	800
S1 72.80	Touirist	11.76	165	234	204	55.9	321	425	1880	516
S1 72.85	Touirist	12.36	168	196	204	39.4	275	350	1389	303
S1 73.05	Touirist	12.51	193	236	188	35.7	329	378	589	253
S1 73.35	Touirist	11.88	164	202	217	41.1	274	387	1605	298
S1 73.60	Touirist	12.48	165	142	190	24.1	233	460	556	293
S1-17 73.65	Touirist	14.46	205	193	192	24.6	314	484	636	273
S1 73.65	Touirist	12.60	170	184	219	24.6	243	711	743	278

Sample Id/core depth	Formation	Al (wt%)	Cr (ppm)	Cu (ppm)	Mn (ppm)	Mo (ppm)	Ni (ppm)	P (ppm)	V (ppm)	Zn (ppm)
S1-18 73.70	Touirist	12.75	182	176	216	44.9	263	665	1399	480
S1 73.80	Touirist	11.45	190	300	234	73.1	347	922	1630	768
S1 73.85	Touirist	12.37	176	152	219	32.2	238	454	1156	227
S1 73.92	Touirist	11.94	162	165	268	58.5	239	760	1627	563
S1 73.99	Touirist	9.84	147	201	315	36.4	322	433	1222	291
S1 74.07	Touirist	11.58	195	208	216	65.2	260	826	1671	623
S1 74.13	Touirist	10.98	142	235	247	67.0	256	2069	1966	842
S1 74.20	Touirist	12.65	186	191	207	38.5	244	738	947	329
S1 74.26	Touirist	12.61	174	141	217	16.4	206	882	481	233
S1 74.36	Touirist	13.20	157	67	247	9.7	103	557	400	156
S1 74.52	Touirist	10.26	138	94	687	11.3	133	532	558	223
S1 74.57	Touirist	12.96	169	114	223	13.6	142	584	596	177
S1 74.67	Touirist	12.84	184	131	251	14.2	185	757	441	119
S1 74.97	Touirist	12.51	184	79	279	4.1	120	763	593	126
S1 75.19	Touirist	12.56	167	85	350	7.3	130	2012	290	153
S1 75.42	Touirist	10.56	198	291	248	41.5	307	698	823	687
S1 75.48	Touirist	11.71	206	146	330	22.1	180	781	1061	381
S1 75.53	Touirist	8.31	144	230	526	46.5	241	705	1492	869
S1 75.60	Touirist	1.81	46	50	909	21.6	63	298	574	440
S1 75.75	Touirist	1.99	39	60	1221	23.0	62	674	629	287
S1 75.80	Touirist	3.03	52	75	1119	22.2	77	829	826	256
S1 75.88	Touirist	4.03	66	99	1131	25.3	100	636	1038	503
S1 75.97	Touirist	3.82	62	82	835	22.6	89	545	886	300
S1 76.07	Touirist	2.78	42	56	1129	18.8	63	392	696	206

Sample Id/core depth	Formation	Al (wt%)	Cr (ppm)	Cu (ppm)	Mn (ppm)	Mo (ppm)	Ni (ppm)	P (ppm)	V (ppm)	Zn (ppm)
S1 76.15	Touirist	6.46	100	192	1331	38.8	180	519	1463	675
S1 76.22	Touirist	2.55	50	77	1378	23.1	82	518	750	296
S1 76.29	Touirist	1.65	45	53	1204	20.7	68	468	523	215
S1 76.44	Touirist	2.86	57	69	728	25.2	75	358	647	395
S1 76.65	Touirist	2.26	51	48	755	16.5	61	633	554	160
S1 76.75	Touirist	2.35	44	55	1528	19.1	64	535	699	152
S1 76.83	Touirist	4.35	83	107	795	33.9	135	514	1050	653
S1 76.97	Touirist	1.31	40	40	895	19.5	50	751	447	277
S1 77.09	Touirist	1.87	37	50	951	19.6	61	708	558	149
S1 77.30	Touirist	3.78	70	120	732	24.3	128	453	856	385
S1 77.35	Touirist	3.31	67	85	1102	22.3	94	365	706	253
S1 77.56	Touirist	2.76	62	83	878	26.4	112	409	720	623
S1 77.71	Touirist	1.58	44	35	606	18.4	50	434	435	232
S1 78.00	Touirist	1.63	48	44	546	16.6	54	535	404	213
S1 78.21	Touirist	1.87	41	48	423	19.0	67	318	417	161
S1 78.45	Touirist	1.21	34	30	289	17.0	41	973	319	207
S1 78.83	Touirist	3.45	52	61	419	16.1	66	472	540	144
S1 79.02	Touirist	1.94	33	38	396	15.2	53	458	408	179
S1 79.15	Touirist	2.78	47	74	512	23.9	99	392	596	290
S1 79.39	Touirist	3.50	43	64	372	15.8	70	404	533	183
S1 79.52	Touirist	2.36	33	36	337	10.9	53	791	413	164
S1 79.65	Touirist	2.22	39	57	426	24.5	75	811	460	146
S1 79.80	Touirist	2.17	52	66	362	19.3	75	1256	486	551
S1 79.99	Touirist	3.37	55	52	481	22.4	73	402	627	150

Sample Id/core depth	Formation	Al (wt%)	Cr (ppm)	Cu (ppm)	Mn (ppm)	Mo (ppm)	Ni (ppm)	P (ppm)	V (ppm)	Zn (ppm)
S1 80.31	Touirist	2.00	49	51	509	21.4	72	501	448	213
S1 80.51	Touirist	2.57	50	48	550	19.4	78	605	575	246
S1 80.64	Touirist	2.39	41	86	770	27.1	282	392	539	636
S1 80.70	Touirist	1.97	33	33	362	18.4	51	1216	423	106
S1 80.86	Touirist	1.11	32	35	429	21.5	74	353	404	215
S1 81.15	Touirist	10.71	161	131	207	21.7	183	588	574	279
S1 81.77	Touirist	9.84	179	126	245	15.5	220	610	487	414
S1 81.97	Touirist	10.12	176	135	241	19.4	215	1573	541	265
S1 82.02	Touirist	10.18	163	133	209	20.9	198	705	425	189
S1 82.15 A	Touirist	11.48	184	66	236	7.4	117	991	898	75
S1 82.15 B	Touirist	5.28	96	92	322	20.5	115	478	367	136
S1 82.24	Touirist	9.98	189	157	275	35.8	238	1125	1492	304
S1 82.34	Touirist	11.45	193	104	232	14.0	269	906	687	210
S1 82.43	Touirist	9.94	169	191	236	42.7	277	563	1728	522
S1 83.59	Touirist	9.85	202	212	198	47.3	290	661	1678	456
S1 83.65	Touirist	9.35	203	214	215	46.0	282	515	1432	734
S1 84.71	En Nesoar	11.64	214	130	190	16.7	224	392	570	144
S1 84.83	En Nesoar	10.78	260	199	187	35.3	260	282	895	400
S1 84.94	En Nesoar	10.03	232	185	135	31.9	237	201	724	174
S1 85.05	En Nesoar	10.30	223	171	205	25.6	278	658	813	525
S1 85.19	En Nesoar	10.00	286	160	162	32.8	299	247	933	355
S1 85.25	En Nesoar	10.03	226	149	129	23.4	270	247	740	186
S1 85.34	En Nesoar	9.34	197	161	202	28.9	213	538	1056	684
S1 85.45	En Nesoar	9.54	226	111	149	19.7	215	499	476	177

Sample Id/core depth	Formation	Al (wt%)	Cr (ppm)	Cu (ppm)	Mn (ppm)	Mo (ppm)	Ni (ppm)	P (ppm)	V (ppm)	Zn (ppm)
S1 85.62	En Nesoar	9.36	267	154	141	29.2	314	220	710	260
S1 85.75	En Nesoar	9.20	210	106	118	16.1	219	188	681	150
S1 85.85	En Nesoar	9.42	253	125	137	26.9	253	222	701	261
S1 85.94	En Nesoar	8.97	228	124	171	26.6	231	238	667	438
S1 86.07	En Nesoar	10.01	245	82	149	9.9	137	305	334	159
S1 86.20	En Nesoar	9.75	194	108	152	19.8	193	257	479	156
S1 86.33	En Nesoar	8.72	177	125	173	23.6	193	217	794	84
S1 86.62	En Nesoar	9.90	194	140	150	11.3	174	367	279	174
S1 86.82	En Nesoar	10.19	189	78	147	14.4	110	695	242	148
S1 86.92	En Nesoar	10.22	182	89	122	12.3	110	226	274	91
S1 87.05	En Nesoar	10.88	200	100	133	11.1	118	374	263	169
S1 87.19	En Nesoar	10.18	196	75	128	11.7	111	299	288	112
S1 87.29	En Nesoar	9.27	191	100	101	18.5	143	209	354	122
S1 87.36	En Nesoar	9.56	205	104	112	15.8	146	197	380	217
S1 87.50	En Nesoar	9.88	208	85	111	10.8	122	281	360	231
S1 87.60	En Nesoar	9.51	244	106	88	15.2	150	184	441	291
S1 87.70	En Nesoar	10.01	255	117	92	12.3	179	193	430	106
S1 87.80	En Nesoar	10.52	254	113	103	12.0	163	214	324	164
S1 87.87	En Nesoar	10.09	236	92	86	9.6	151	199	317	141
S1 87.95	En Nesoar	9.86	243	103	89	18.2	141	205	302	362
S1-1 88.09	En Nesoar	12.10	273	95	113	4.9	118	316	291	286
S1 88.19	En Nesoar	10.53	242	67	135	19.1	114	257	235	240
S1 88.24	En Nesoar	7.78	195	139	128	21.7	213	179	432	333
S1-3 88.27	En Nesoar	11.51	222	123	125	9.9	187	376	210	327

Sample Id/core depth	Formation	Al (wt%)	Cr (ppm)	Cu (ppm)	Mn (ppm)	Mo (ppm)	Ni (ppm)	P (ppm)	V (ppm)	Zn (ppm)
S1-5 88.46	En Nesoar	13.59	268	110	162	8.9	157	519	269	225
S1 88.46	En Nesoar	11.78	216	81	135	7.0	85	342	248	173
S1-19 88.92	En Nesoar	10.05	311	146	91	20.1	190	236	428	163
S1-21 89.10	En Nesoar	7.69	203	113	112	20.6	156	168	579	137
S1-22 89.33	En Nesoar	8.87	242	188	305	33.4	283	250	662	263
S1-23 89.36	En Nesoar	8.00	214	160	449	20.7	223	207	598	174
S1-24 89.40	En Nesoar	8.00	239	155	750	27.4	250	254	836	252
S1-25 89.50	En Nesoar	3.08	99	94	474	38.9	151	1520	942	71
S1 102.00		8.12	152	131	1455	0.0	84	748	283	94
S1 104.20		8.13	240	127	1419	3.1	98	603	285	91
S1 121.56	En Nesoar	6.47	181	26	286	26.1	214	200	721	105
S1 121.63	En Nesoar	6.64	181	33	434	21.9	179	218	727	90
S1 121.82	En Nesoar	6.39	158	32	228	21.8	176	324	748	66
S1 121.89	En Nesoar	6.39	173	56	256	32.5	205	404	1107	62
S1 121.92	En Nesoar	2.33	67	311	520	35.1	219	683	608	42
S1 122.00	En Nesoar	7.06	219	52	311	66.7	338	1441	1497	28
S1 122.10	En Nesoar	6.63	149	179	227	33.3	207	642	1005	20
S1 122.20	En Nesoar	10.63	127	56	52	5.5	68	316	253	21
S1 122.25	En Nesoar	10.23	115	152	191	3.7	102	263	148	19
S1 122.40	En Nesoar	10.86	102	41	96	0.0	57	483	107	15
S1 122.60	En Nesoar	4.88	50	100	1106	3.3	56	265	90	30
S1 122.75 A	En Nesoar	4.90	57	50	1193	6.0	69	240	93	45
S1 122.75 B	En Nesoar	1.96	24	29	997	3.4	27	124	61	36
S1 122.99	En Nesoar	3.76	36	7	1569	0.0	15	399	141	54

Sample Id/core depth	Formation	Al (wt%)	Cr (ppm)	Cu (ppm)	Mn (ppm)	Mo (ppm)	Ni (ppm)	P (ppm)	V (ppm)	Zn (ppm)
S1 123.06	En Nesoar	10.32	105	13	2766	4.2	21	372	135	764
S1 123.12	En Nesoar	8.66	93	22	2167	2.2	16	322	123	83
S1 129.07	En Nesoar	2.55	36	8	2460	4.4	15	192	112	46
S1 129.15	En Nesoar	7.48	105	0	1893	0.0	33	278	65	420
S1 129.82	En Nesoar	0.89	19	5	1659	1.7	22	177	73	27
S1 132.98	En Nesoar	0.86	19	6	1579	0.8	17	289	64	19
S1 133.20	En Nesoar	0.50	28	5	3021	0.0	10	112	0	86
S1 134.27	En Nesoar	1.63	51	8	2639	0.0	36	216	86	51
S1 134.70	En Nesoar	0.66	20	7	2065	0.0	10	174	61	14
S1 135.00	En Nesoar	0.83	11	6	2243	0.0	12	192	87	26

Table B - 2 Total element data for core S1. For most samples, the sample ID consists of the core name and depth. The exception is some samples that were received as powders, which have an additional number following the core name. Samples were split into A and B where there was a visible disparity in pyrite contents across the width of a core section.

Sample Id/core depth	Formation	Fe_{carb} (wt%)	Fe_{ox} (wt%)	Fe_{mag} (wt%)	Fe_{AVS} (wt%)	Fe_{py} (wt%)	Fe_{HCl} (wt%)	FeT (wt%)
S1 70.58	Touirist	2.22	2.11	0.09	2.69	1.48	5.64	6.64
S1 70.75	Touirist	1.26	0.36	0.04	1.08	0.35	1.89	2.66
S1 70.89	Touirist	1.03	0.87	0.11	0.43	0.60	2.12	2.63
S1 70.98	Touirist	2.34	1.77	0.12	0.99	1.68	4.40	5.59
S1 71.05	Touirist	1.71	1.35	0.07	0.80	1.02	3.20	4.08
S1 71.12	Touirist	2.10	2.08	0.13	0.85	1.54	4.39	5.31
S1 71.21	Touirist	1.02	1.03	0.15	0.15	0.68	2.01	2.86
S1 71.34	Touirist	2.31	2.42	0.16	2.10	1.79	5.95	7.13
S1 71.47	Touirist	2.21	1.76	0.13	1.60	1.26	4.96	6.12
S1-12 71.51	Touirist	2.12	0.95	0.69	1.26	1.24	4.02	4.63
S1 71.65	Touirist	1.82	1.19	0.08	0.55	1.57	3.00	4.83
S1 71.81	Touirist	1.40	0.56	0.04	0.71	0.48	2.02	2.69
S1 71.92	Touirist	2.08	0.98	0.09	1.16	0.72	3.23	4.00
S1 78.50	Touirist	4.49	3.42	0.26	5.81	1.84	10.09	12.22
S1 72.60	Touirist	2.27	1.94	0.06	0.54	1.37	4.13	5.28
S1 72.67	Touirist	1.76	1.43	0.05	0.85	1.30	3.98	4.86
S1 72.75	Touirist	2.85	1.21	0.04	2.18	1.15	4.67	6.22
S1 72.80	Touirist	2.07	0.84	0.01	1.69	0.72	3.72	4.66
S1 72.85	Touirist	1.67	1.04	0.05	0.66	0.77	2.61	3.38
S1 73.05	Touirist	1.52	0.80	0.04	0.38	0.50	2.24	2.92
S1 73.35	Touirist	1.79	1.21	0.06	0.74	0.81	3.10	3.76
S1 73.60	Touirist	1.20	0.63	0.04	0.42	0.66	1.90	2.34
S1-17 73.65	Touirist	1.17	0.57	0.12	0.35	0.61	1.86	2.31
S1 73.65	Touirist	1.91	0.74	0.05	1.10	0.69	2.58	3.25

Sample Id/core depth	Formation	Fe_{carb} (wt%)	Fe_{ox} (wt%)	Fe_{mag} (wt%)	Fe_{AVS} (wt%)	Fe_{py} (wt%)	Fe_{HCl} (wt%)	FeT (wt%)
S1-18 73.70	Touirist	1.28	1.00	0.28	0.66	0.88	2.63	3.09
S1 73.80	Touirist	1.90	1.44	0.10	2.34	0.68	4.37	5.37
S1 73.85	Touirist	1.30	1.03	0.03	0.30	0.80	2.32	2.96
S1 73.92	Touirist	2.00	1.09	0.04	0.83	0.88	3.09	3.91
S1 73.99	Touirist	2.88	1.54	0.12	3.75	0.89	5.69	6.80
S1 74.07	Touirist	2.46	0.87	0.02	1.38	1.01	3.27	4.19
S1 74.13	Touirist	2.22	1.61	0.06	0.76	1.33	3.72	4.66
S1 74.20	Touirist	1.64	0.93	0.06	0.74	1.05	2.49	3.21
S1 74.26	Touirist	1.52	0.78	0.03	0.54	0.72	2.20	2.95
S1 74.36	Touirist	1.06	0.58	0.06	0.43	0.41	1.66	2.11
S1 74.52	Touirist	2.19	0.92	0.07	1.50	0.56	2.98	3.83
S1 74.57	Touirist	1.23	1.10	0.04	0.22	0.91	2.21	3.04
S1 74.67	Touirist	1.10	0.95	0.15	0.31	0.84	2.10	2.89
S1 74.97	Touirist	1.55	1.07	0.07	0.85	0.71	2.61	3.60
S1 75.19	Touirist	1.41	0.98	0.10	0.79	0.70	2.57	3.17
S1 75.42	Touirist	1.78	0.94	0.05	0.44	0.90	2.77	3.47
S1 75.48	Touirist	1.09	1.06	0.06	0.41	0.64	2.24	2.85
S1 75.53	Touirist	2.10	1.32	0.11	1.67	1.06	3.75	4.59
S1 75.60	Touirist	0.85	0.12	0.02	0.85	0.13	1.05	1.19
S1 75.75	Touirist	0.98	0.10	0.03	0.99	0.11	1.16	1.35
S1 75.80	Touirist	1.14	0.25	0.05	0.96	0.22	1.51	1.73
S1 75.88	Touirist	1.42	0.33	0.11	1.14	0.28	1.94	2.31
S1 75.97	Touirist	0.52	0.18	0.17	0.17	0.88	0.89	1.91
S1 76.07	Touirist	1.32	0.26	0.13	0.94	0.09	1.68	2.02

Sample Id/core depth	Formation	Fe_{carb} (wt%)	Fe_{ox} (wt%)	Fe_{mag} (wt%)	Fe_{AVS} (wt%)	Fe_{py} (wt%)	Fe_{HCl} (wt%)	FeT (wt%)
S1 76.15	Touirist	0.57	0.34	0.53	0.02	1.65	1.35	3.33
S1 76.22	Touirist	0.35	0.19	0.10	0.01	1.14	0.54	1.79
S1 76.29	Touirist	0.23	0.27	0.11	0.02	0.33	0.65	1.04
S1 76.44	Touirist	0.27	0.27	0.12	0.01	0.64	0.65	1.47
S1 76.65	Touirist	0.25	0.07	0.04	0.02	1.10	0.23	1.40
S1 76.75	Touirist	0.35	0.48	0.29	0.01	0.21	1.14	1.59
S1 76.83	Touirist	0.41	0.55	0.50	0.02	0.65	1.53	2.46
S1 76.97	Touirist	0.22	0.22	0.04	0.00	0.35	0.44	0.91
S1 77.09	Touirist	0.29	0.30	0.08	0.00	0.55	0.58	1.30
S1 77.30	Touirist	0.32	0.51	0.36	0.01	0.78	1.18	2.23
S1 77.35	Touirist	0.35	0.54	0.53	0.03	0.18	1.50	1.91
S1 77.56	Touirist	0.47	0.82	0.50	0.00	0.06	1.84	2.21
S1 77.71	Touirist	0.23	0.31	0.24	0.00	0.02	0.89	0.98
S1 78.00	Touirist	0.22	0.17	0.04	0.01	0.57	0.44	1.04
S1 78.21	Touirist	0.27	0.41	0.11	0.03	0.27	0.86	1.21
S1 78.45	Touirist	0.16	0.18	0.03	0.00	0.21	0.43	0.65
S1 78.83	Touirist	0.30	0.21	0.08	0.02	0.92	0.53	1.51
S1 79.02	Touirist	0.21	0.29	0.22	0.00	0.09	0.72	0.95
S1 79.15	Touirist	0.27	0.23	0.14	0.00	0.96	0.64	1.68
S1 79.39	Touirist	0.39	0.15	0.07	0.02	1.31	0.40	1.83
S1 79.52	Touirist	0.27	0.32	0.12	0.00	0.67	0.63	1.10
S1 79.65	Touirist	0.87	0.61	0.20	0.24	0.35	1.49	2.02
S1 79.80	Touirist	0.34	0.28	0.06	0.02	0.46	0.57	1.12
S1 79.99	Touirist	0.29	0.22	0.11	0.02	0.92	0.53	1.56

Sample Id/core depth	Formation	Fe_{carb} (wt%)	Fe_{ox} (wt%)	Fe_{mag} (wt%)	Fe_{AVS} (wt%)	Fe_{py} (wt%)	Fe_{HCl} (wt%)	FeT (wt%)
S1 80.31	Touirist	0.63	0.28	0.02	0.22	0.17	0.87	1.21
S1 80.51	Touirist	0.31	0.12	0.03	0.01	1.14	0.35	1.61
S1 80.64	Touirist	1.12	0.13	0.02	1.16	0.08	1.18	1.36
S1 80.70	Touirist	0.21	0.23	0.07	0.02	0.38	0.49	0.94
S1 80.86	Touirist	0.33	0.02	0.00	0.33	0.03	0.41	0.44
S1 81.15	Touirist	1.44	0.43	0.16	0.53	0.44	2.02	2.51
S1 81.77	Touirist	1.93	0.89	0.09	0.78	0.67	2.71	3.40
S1 81.97	Touirist	1.86	0.80	0.13	1.53	0.59	3.49	4.31
S1 82.02	Touirist	1.63	0.99	0.09	0.51	0.83	2.78	3.42
S1 82.15 A	Touirist	1.58	0.43	0.09	1.82	0.38	2.87	3.60
S1 82.15 B	Touirist	10.97	4.39	2.82	27.89	4.73	28.13	38.85
S1 82.24	Touirist	2.17	0.94	0.10	0.95	0.74	3.01	3.86
S1 82.34	Touirist	2.11	0.47	0.09	2.53	0.57	3.62	4.39
S1 82.43	Touirist	2.09	1.06	0.10	0.97	0.75	3.27	3.76
S1 83.59	Touirist	1.96	0.75	0.08	1.10	0.69	2.80	3.42
S1 83.65	Touirist	1.36	1.61	0.09	0.22	0.99	2.97	3.61
S1 84.71	En Nesoar	1.68	0.27	0.09	1.25	0.15	1.96	2.56
S1 84.83	En Nesoar	1.77	0.45	0.08	1.03	0.46	2.21	2.85
S1 84.94	En Nesoar	1.35	0.61	0.07	0.49	0.62	1.93	2.61
S1 85.05	En Nesoar	1.33	0.49	0.09	1.13	0.29	1.90	2.73
S1 85.19	En Nesoar	1.55	0.44	0.07	1.15	0.38	1.86	2.62
S1 85.25	En Nesoar	1.14	0.34	0.06	0.87	0.31	1.40	2.21
S1 85.34	En Nesoar	2.22	0.70	0.12	1.75	0.52	2.64	3.89
S1 85.45	En Nesoar	0.91	0.41	0.06	0.29	0.37	1.24	1.88

Sample Id/core depth	Formation	Fe_{carb} (wt%)	Fe_{ox} (wt%)	Fe_{mag} (wt%)	Fe_{AVS} (wt%)	Fe_{py} (wt%)	Fe_{HCl} (wt%)	FeT (wt%)
S1 85.62	En Nesoar	1.36	0.28	0.08	1.13	0.31	1.52	2.48
S1 85.75	En Nesoar	1.48	0.41	0.08	1.28	0.33	1.82	2.47
S1 85.85	En Nesoar	1.08	0.65	0.07	0.39	0.59	1.66	2.48
S1 85.94	En Nesoar	1.48	0.58	0.09	0.84	0.50	2.01	2.69
S1 86.07	En Nesoar	0.80	0.30	0.07	0.39	0.25	1.08	1.66
S1 86.20	En Nesoar	1.16	0.41	0.08	0.59	0.40	1.45	2.20
S1 86.33	En Nesoar	1.64	0.54	0.12	1.28	0.45	2.05	3.22
S1 86.62	En Nesoar	1.26	0.55	0.11	0.61	0.42	1.83	2.57
S1 86.82	En Nesoar	0.75	0.44	0.06	0.20	0.32	1.15	1.73
S1 86.92	En Nesoar	0.88	0.46	0.05	0.15	0.36	1.22	1.79
S1 87.05	En Nesoar	0.95	0.29	0.10	0.65	0.18	1.23	1.86
S1 87.19	En Nesoar	1.08	0.25	0.08	0.70	0.18	1.28	2.00
S1 87.29	En Nesoar	1.12	0.28	0.07	0.48	0.36	1.27	1.95
S1 87.36	En Nesoar	1.05	0.45	0.07	0.64	0.26	1.43	2.15
S1 87.50	En Nesoar	0.89	0.25	0.08	0.58	0.22	1.11	1.73
S1 87.60	En Nesoar	0.69	0.33	0.11	0.42	0.31	0.96	1.72
S1 87.70	En Nesoar	0.72	0.26	0.08	0.44	0.20	0.96	1.54
S1 87.80	En Nesoar	0.78	0.20	0.06	0.52	0.19	0.92	1.52
S1 87.87	En Nesoar	1.01	0.44	0.07	0.48	0.36	1.43	2.05
S1 87.95	En Nesoar	1.03	0.20	0.06	0.70	0.23	1.08	1.68
S1-1 88.09	En Nesoar	0.56	0.23	0.12	0.38	0.22	0.88	1.46
S1 88.19	En Nesoar	1.06	0.14	0.07	0.84	0.15	1.12	1.73
S1 88.24	En Nesoar	1.17	0.29	0.08	0.73	0.33	1.58	2.70
S1-3 88.27	En Nesoar	2.30	0.81	0.56	2.66	0.57	3.76	4.73

Sample Id/core depth	Formation	Fe_{carb} (wt%)	Fe_{ox} (wt%)	Fe_{mag} (wt%)	Fe_{AVS} (wt%)	Fe_{py} (wt%)	Fe_{HCl} (wt%)	FeT (wt%)
S1-5 88.46	En Nesoar	1.23	0.26	0.15	1.22	0.19	1.69	2.50
S1 88.46	En Nesoar	0.39	0.11	0.07	0.24	0.04	0.54	1.19
S1-19 88.92	En Nesoar	0.56	0.27	0.29	0.56	0.24	1.04	1.96
S1-21 89.10	En Nesoar	0.65	0.27	0.29	0.66	0.26	1.16	2.36
S1-22 89.33	En Nesoar	0.21	0.07	0.24	0.01	0.06	1.23	2.52
S1-23 89.36	En Nesoar	0.20	0.06	0.28	0.01	0.02	1.36	2.57
S1-24 89.40	En Nesoar	0.26	0.11	0.27	0.01	0.07	1.62	3.14
S1-25 89.50	En Nesoar	6.51	3.78	1.20	7.66	3.09	13.35	16.02
S1 102.00		0.72	0.28	1.05	0.01	0.06	3.01	7.85
S1 104.20		0.51	0.26	0.76	0.00	0.02	3.01	7.77
S1 121.56	En Nesoar	0.53	0.27	0.27	0.01	0.30	1.32	2.10
S1 121.63	En Nesoar	0.37	0.17	0.44	0.00	0.16	1.45	2.18
S1 121.82	En Nesoar	0.40	0.20	0.23	0.08	0.23	1.04	1.62
S1 121.89	En Nesoar	0.75	0.44	0.34	0.35	0.58	1.59	2.65
S1 121.92	En Nesoar	13.22	5.80	1.53	8.55	6.24	19.39	23.50
S1 122.00	En Nesoar	1.04	1.13	0.64	0.16	0.74	2.83	3.79
S1 122.10	En Nesoar	2.35	2.46	0.42	2.72	1.57	6.16	7.01
S1 122.20	En Nesoar	0.74	0.38	0.08	0.56	0.33	1.30	1.69
S1 122.25	En Nesoar	0.59	0.26	0.15	0.41	0.20	1.08	1.71
S1 122.40	En Nesoar	0.78	0.36	0.07	0.67	0.16	1.35	1.84
S1 122.60	En Nesoar	2.62	1.22	0.28	4.00	0.46	5.51	6.79
S1 122.75 A	En Nesoar	2.43	0.78	0.47	2.70	0.25	4.36	5.26
S1 122.75 B	En Nesoar	1.45	0.39	0.16	1.56	2.00	2.13	4.75
S1 122.99	En Nesoar	1.32	0.46	0.24	1.22	0.23	2.33	3.34

Sample Id/core depth	Formation	Fe_{carb} (wt%)	Fe_{ox} (wt%)	Fe_{mag} (wt%)	Fe_{AVS} (wt%)	Fe_{py} (wt%)	Fe_{HCl} (wt%)	FeT (wt%)
S1 123.06	En Nesoar	0.61	0.19	0.17	0.72	0.08	1.62	3.83
S1 123.12	En Nesoar	0.91	0.16	0.29	0.88	0.03	1.82	3.16
S1 129.07	En Nesoar	1.29	0.38	0.27	0.98	0.02	2.22	3.57
S1 129.15	En Nesoar	0.19	0.08	0.14	0.02	0.01	1.02	3.52
S1 129.82	En Nesoar	0.76	0.20	0.02	0.77	0.05	0.95	1.19
S1 132.98	En Nesoar	0.89	0.28	0.12	1.01	0.04	1.21	1.56
S1 133.20	En Nesoar	1.69	0.15	0.05	0.99	0.02	1.98	2.38
S1 134.27	En Nesoar	2.15	0.40	0.14	1.88	0.08	3.04	4.08
S1 134.70	En Nesoar	0.67	0.08	0.03	0.22	0.03	0.91	1.28
S1 135.00	En Nesoar	1.23	0.08	0.03	0.22	0.10	1.51	1.94

Table B - 3 Fe pools for core S1. For most samples, the sample ID consists of the core name and depth. The exception is some samples that were received as powders, which have an additional number following the core name. Samples were split into A and B where there was a visible disparity in pyrite contents across the width of a core section.

Sample Id/core depth	Formation	FeHR/FeT	FeHR no AVS/FeT	$Fe_{HCl}+Fe_{py}/FeT$	Fe(S)/FeHR	DOP
S1 70.58	Touirist	1.29	0.89	1.07	0.48	0.58
S1 70.75	Touirist	1.16	0.76	0.84	0.46	0.64
S1 70.89	Touirist	1.15	0.99	1.03	0.34	0.38
S1 70.98	Touirist	1.23	1.06	1.09	0.39	0.44
S1 71.05	Touirist	1.21	1.02	1.03	0.37	0.43
S1 71.12	Touirist	1.26	1.10	1.12	0.36	0.40
S1 71.21	Touirist	1.06	1.01	0.94	0.28	0.31
S1 71.34	Touirist	1.23	0.94	1.08	0.44	0.50
S1 71.47	Touirist	1.14	0.88	1.02	0.41	0.46
S1-12 71.51	Touirist	1.35	1.08	1.14	0.40	0.48
S1 71.65	Touirist	1.08	0.97	0.95	0.41	0.46
S1 71.81	Touirist	1.19	0.93	0.93	0.37	0.48
S1 71.92	Touirist	1.26	0.97	0.99	0.38	0.48
S1 78.50	Touirist	1.29	0.82	0.98	0.48	0.64
S1 72.60	Touirist	1.17	1.07	1.04	0.31	0.35
S1 72.67	Touirist	1.11	0.93	1.09	0.40	0.41
S1 72.75	Touirist	1.19	0.84	0.93	0.45	0.57
S1 72.80	Touirist	1.15	0.78	0.95	0.45	0.54
S1 72.85	Touirist	1.24	1.05	1.00	0.34	0.42
S1 73.05	Touirist	1.11	0.98	0.94	0.27	0.32
S1 73.35	Touirist	1.23	1.03	1.04	0.34	0.40
S1 73.60	Touirist	1.26	1.08	1.09	0.37	0.42
S1-17 73.65	Touirist	1.21	1.06	1.07	0.34	0.39
S1 73.65	Touirist	1.38	1.04	1.01	0.40	0.55

Sample Id/core depth	Formation	FeHR/FeT	FeHR no AVS/FeT	$Fe_{HCl}+Fe_{py}/FeT$	Fe(S)/FeHR	DOP
S1-18 73.70	Touirist	1.33	1.11	1.14	0.38	0.44
S1 73.80	Touirist	1.20	0.77	0.94	0.47	0.60
S1 73.85	Touirist	1.17	1.06	1.05	0.32	0.35
S1 73.92	Touirist	1.24	1.02	1.02	0.35	0.43
S1 73.99	Touirist	1.35	0.80	0.97	0.51	0.71
S1 74.07	Touirist	1.37	1.04	1.02	0.42	0.56
S1 74.13	Touirist	1.28	1.12	1.08	0.35	0.41
S1 74.20	Touirist	1.38	1.15	1.10	0.40	0.51
S1 74.26	Touirist	1.22	1.04	0.99	0.35	0.43
S1 74.36	Touirist	1.20	1.00	0.98	0.33	0.41
S1 74.52	Touirist	1.37	0.98	0.92	0.39	0.58
S1 74.57	Touirist	1.15	1.08	1.03	0.32	0.36
S1 74.67	Touirist	1.16	1.06	1.02	0.34	0.39
S1 74.97	Touirist	1.18	0.94	0.92	0.37	0.47
S1 75.19	Touirist	1.26	1.01	1.03	0.37	0.46
S1 75.42	Touirist	1.18	1.05	1.06	0.33	0.37
S1 75.48	Touirist	1.14	1.00	1.01	0.32	0.37
S1 75.53	Touirist	1.36	1.00	1.05	0.44	0.57
S1 75.60	Touirist	1.66	0.94	0.99	0.50	0.83
S1 75.75	Touirist	1.65	0.91	0.95	0.50	0.87
S1 75.80	Touirist	1.51	0.96	1.00	0.45	0.68
S1 75.88	Touirist	1.42	0.92	0.96	0.43	0.64
S1 75.97	Touirist	1.01	0.92	0.93	0.55	0.59
S1 76.07	Touirist	1.35	0.89	0.87	0.38	0.58

Sample Id/core depth	Formation	FeHR/FeT	FeHR no AVS/FeT	$Fe_{HCl}+Fe_{py}/FeT$	Fe(S)/FeHR	DOP
S1 76.15	Touirist	0.93	0.93	0.90	0.54	0.56
S1 76.22	Touirist	1.01	1.00	0.94	0.64	0.69
S1 76.29	Touirist	0.92	0.90	0.94	0.36	0.36
S1 76.44	Touirist	0.90	0.89	0.87	0.49	0.51
S1 76.65	Touirist	1.06	1.05	0.96	0.76	0.84
S1 76.75	Touirist	0.84	0.84	0.85	0.16	0.16
S1 76.83	Touirist	0.87	0.86	0.88	0.31	0.31
S1 76.97	Touirist	0.91	0.91	0.86	0.42	0.44
S1 77.09	Touirist	0.94	0.94	0.87	0.45	0.49
S1 77.30	Touirist	0.89	0.89	0.88	0.40	0.40
S1 77.35	Touirist	0.85	0.83	0.87	0.13	0.12
S1 77.56	Touirist	0.84	0.84	0.86	0.03	0.03
S1 77.71	Touirist	0.82	0.82	0.92	0.02	0.02
S1 78.00	Touirist	0.97	0.96	0.97	0.58	0.58
S1 78.21	Touirist	0.90	0.87	0.93	0.28	0.27
S1 78.45	Touirist	0.89	0.89	0.97	0.36	0.33
S1 78.83	Touirist	1.01	1.00	0.96	0.61	0.65
S1 79.02	Touirist	0.86	0.86	0.86	0.12	0.12
S1 79.15	Touirist	0.95	0.95	0.95	0.60	0.60
S1 79.39	Touirist	1.06	1.05	0.93	0.68	0.78
S1 79.52	Touirist	1.25	1.25	1.18	0.48	0.51
S1 79.65	Touirist	1.13	1.01	0.91	0.26	0.32
S1 79.80	Touirist	1.04	1.02	0.92	0.42	0.47
S1 79.99	Touirist	1.00	0.99	0.93	0.60	0.65

Sample Id/core depth	Formation	FeHR/FeT	FeHR no AVS/FeT	$Fe_{HCl}+Fe_{py}/FeT$	Fe(S)/FeHR	DOP
S1 80.31	Touirist	1.11	0.92	0.86	0.29	0.38
S1 80.51	Touirist	1.00	0.99	0.93	0.72	0.77
S1 80.64	Touirist	1.85	1.00	0.93	0.49	0.98
S1 80.70	Touirist	0.97	0.95	0.92	0.44	0.46
S1 80.86	Touirist	1.64	0.89	1.01	0.50	0.81
S1 81.15	Touirist	1.20	0.99	0.98	0.32	0.39
S1 81.77	Touirist	1.28	1.06	0.99	0.33	0.43
S1 81.97	Touirist	1.14	0.79	0.95	0.43	0.52
S1 82.02	Touirist	1.19	1.03	1.06	0.33	0.37
S1 82.15 A	Touirist	1.20	0.69	0.90	0.51	0.68
S1 82.15 B	Touirist	1.31	0.59	0.85	0.64	0.99
S1 82.24	Touirist	1.27	1.02	0.97	0.35	0.45
S1 82.34	Touirist	1.32	0.74	0.95	0.54	0.74
S1 82.43	Touirist	1.32	1.06	1.07	0.35	0.43
S1 83.59	Touirist	1.33	1.01	1.02	0.39	0.51
S1 83.65	Touirist	1.18	1.12	1.10	0.28	0.31
S1 84.71	En Nesoar	1.34	0.85	0.82	0.41	0.66
S1 84.83	En Nesoar	1.33	0.97	0.94	0.39	0.56
S1 84.94	En Nesoar	1.21	1.02	0.98	0.35	0.44
S1 85.05	En Nesoar	1.22	0.81	0.80	0.43	0.65
S1 85.19	En Nesoar	1.37	0.93	0.86	0.43	0.68
S1 85.25	En Nesoar	1.22	0.83	0.77	0.43	0.69
S1 85.34	En Nesoar	1.37	0.92	0.81	0.43	0.72
S1 85.45	En Nesoar	1.08	0.93	0.85	0.32	0.41

Sample Id/core depth	Formation	FeHR/FeT	FeHR no AVS/FeT	$Fe_{HCl}+Fe_{py}/FeT$	Fe(S)/FeHR	DOP
S1 85.62	En Nesoar	1.27	0.82	0.74	0.46	0.78
S1 85.75	En Nesoar	1.45	0.93	0.87	0.45	0.75
S1 85.85	En Nesoar	1.12	0.96	0.91	0.35	0.44
S1 85.94	En Nesoar	1.30	0.98	0.93	0.39	0.53
S1 86.07	En Nesoar	1.09	0.86	0.80	0.35	0.48
S1 86.20	En Nesoar	1.20	0.93	0.84	0.38	0.54
S1 86.33	En Nesoar	1.25	0.85	0.77	0.43	0.69
S1 86.62	En Nesoar	1.15	0.91	0.88	0.35	0.46
S1 86.82	En Nesoar	1.03	0.91	0.85	0.29	0.35
S1 86.92	En Nesoar	1.06	0.98	0.89	0.27	0.32
S1 87.05	En Nesoar	1.16	0.81	0.76	0.38	0.59
S1 87.19	En Nesoar	1.15	0.79	0.73	0.38	0.60
S1 87.29	En Nesoar	1.18	0.93	0.83	0.36	0.51
S1 87.36	En Nesoar	1.15	0.85	0.78	0.36	0.53
S1 87.50	En Nesoar	1.16	0.82	0.77	0.40	0.60
S1 87.60	En Nesoar	1.08	0.84	0.74	0.39	0.57
S1 87.70	En Nesoar	1.11	0.82	0.75	0.38	0.56
S1 87.80	En Nesoar	1.15	0.81	0.73	0.41	0.64
S1 87.87	En Nesoar	1.15	0.92	0.87	0.36	0.47
S1 87.95	En Nesoar	1.32	0.91	0.78	0.42	0.71
S1-1 88.09	En Nesoar	1.04	0.77	0.75	0.40	0.55
S1 88.19	En Nesoar	1.30	0.82	0.73	0.44	0.78
S1 88.24	En Nesoar	0.96	0.69	0.70	0.41	0.56
S1-3 88.27	En Nesoar	1.46	0.90	0.92	0.47	0.75

Sample Id/core depth	Formation	FeHR/FeT	FeHR no AVS/FeT	$Fe_{HCl}+Fe_{py}/FeT$	Fe(S)/FeHR	DOP
S1-5 88.46	En Nesoar	1.22	0.73	0.75	0.46	0.75
S1 88.46	En Nesoar	0.72	0.52	0.49	0.33	0.49
S1-19 88.92	En Nesoar	0.98	0.69	0.66	0.42	0.63
S1-21 89.10	En Nesoar	0.90	0.62	0.60	0.43	0.65
S1-22 89.33	En Nesoar	0.23	0.23	0.51	0.11	0.05
S1-23 89.36	En Nesoar	0.22	0.22	0.54	0.06	0.02
S1-24 89.40	En Nesoar	0.23	0.23	0.54	0.11	0.05
S1-25 89.50	En Nesoar	1.39	0.91	1.03	0.48	0.65
S1 102.00		0.27	0.27	0.39	0.03	0.02
S1 104.20		0.20	0.20	0.39	0.01	0.01
S1 121.56	En Nesoar	0.66	0.65	0.77	0.23	0.19
S1 121.63	En Nesoar	0.52	0.52	0.74	0.14	0.10
S1 121.82	En Nesoar	0.70	0.65	0.78	0.27	0.25
S1 121.89	En Nesoar	0.93	0.80	0.82	0.38	0.43
S1 121.92	En Nesoar	1.50	1.14	1.09	0.42	0.58
S1 122.00	En Nesoar	0.98	0.94	0.94	0.24	0.25
S1 122.10	En Nesoar	1.36	0.97	1.10	0.45	0.56
S1 122.20	En Nesoar	1.24	0.91	0.97	0.43	0.55
S1 122.25	En Nesoar	0.94	0.70	0.75	0.38	0.47
S1 122.40	En Nesoar	1.11	0.74	0.82	0.41	0.55
S1 122.60	En Nesoar	1.26	0.68	0.88	0.52	0.75
S1 122.75 A	En Nesoar	1.26	0.75	0.88	0.44	0.64
S1 122.75 B	En Nesoar	1.17	0.84	0.87	0.64	0.86
S1 122.99	En Nesoar	1.04	0.67	0.77	0.42	0.57

Sample Id/core depth	Formation	FeHR/FeT	FeHR no AVS/FeT	$Fe_{HCl}+Fe_{py}/FeT$	Fe(S)/FeHR	DOP
S1 123.06	En Nesoar	0.46	0.28	0.45	0.45	0.47
S1 123.12	En Nesoar	0.72	0.44	0.59	0.40	0.49
S1 129.07	En Nesoar	0.82	0.55	0.63	0.34	0.44
S1 129.15	En Nesoar	0.12	0.12	0.29	0.06	0.03
S1 129.82	En Nesoar	1.51	0.87	0.84	0.45	0.82
S1 132.98	En Nesoar	1.49	0.85	0.80	0.45	0.84
S1 133.20	En Nesoar	1.22	0.80	0.84	0.35	0.50
S1 134.27	En Nesoar	1.14	0.68	0.77	0.42	0.63
S1 134.70	En Nesoar	0.81	0.64	0.73	0.24	0.26
S1 135.00	En Nesoar	0.85	0.74	0.82	0.19	0.20

Table B - 4 Redox indicators for core S1. For most samples, the sample ID consists of the core name and depth. The exception is some samples that were received as powders, which have an additional number following the core name. Samples were split into A and B where there was a visible disparity in pyrite contents across the width of a core section.

References

ALGEO, T. J. & LYONS, T. W. 2006. Mo-total organic carbon covariation in modern anoxic marine environments: Implications for analysis of paleoredox and paleohydrographic conditions. *Paleoceanography,* 21**,** PA1016.

ALGEO, T. J. & MAYNARD, J. B. 2004. Trace-element behavior and redox facies in core shales of Upper Pennsylvanian Kansas-type cyclothems. *Chemical Geology,* 206**,** 289-318.

ANDERSON, L. D., DELANEY, M. L. & FAUL, K. L. 2001. Carbon to phosphorus ratios in sediments: Implications for nutrient cycling. *Global Biogeochemical Cycles,* 15**,** 65-79.

ANDERSON, T. F. & RAISWELL, R. 2004. Sources and mechanisms for the enrichment of highly reactive iron in euxinic Black Sea sediments. *American Journal of Science,* 304**,** 203-233.

ANDREWS, M. S. & RIPLEY, E. M. 1989. Mass transfer and sulfur fixation in the contact aureole of the Duluth Complex, Dunka Road Cu-Ni deposit, Minnesota. *The Canadian Mineralogist,* 27**,** 293-310.

ARNAUD, E., HALVERSON, G. P. & SHIELDS-ZHOU, G. The geological record of Neoproterozoic glaciations. 2011. Geological Society of London.

ARTHUR, M. A. & SAGEMAN, B. B. 1994. Marine black shales: depositional mechanisms and environments of ancient deposits. *Annual Review of Earth and Planetary Sciences,* 22**,** 499-551.

BEGHIN, J., GUILBAUD, R., POULTON, S. W., GUENELI, N., BROCKS, J. J., STORME, J.-Y., BLANPIED, C. & JAVAUX, E. J. 2017a. A palaeoecological model for the late Mesoproterozoic – early Neoproterozoic Atar/El Mreïti Group, Taoudeni Basin, Mauritania, northwestern Africa. *Precambrian Research,* 299**,** 1-14.

BEGHIN, J., STORME, J.-Y., BLANPIED, C., GUENELI, N., BROCKS, J. J., POULTON, S. W. & JAVAUX, E. J. 2017b. Microfossils from the late Mesoproterozoic – early Neoproterozoic Atar/El Mreïti Group, Taoudeni Basin, Mauritania, northwestern Africa. *Precambrian Research,* 291**,** 63-82.

BENAN, C. A. & DEYNOUX, M. 1998. Facies analysis and sequence stratigraphy of Neoproterozoic platform deposits in Adrar of Mauritania, Taoudeni Basin, West Africa. *Geologische Rundschau,* 87**,** 283-302.

BENITEZ-NELSON, C. R. 2000. The biogeochemical cycling of phosphorus in marine systems. *Earth-Science Reviews,* 51**,** 109-135.

BERNER, R. A. 1970. Sedimentary pyrite formation. *American Journal of Science,* 268**,** 1-23.

BERNER, R. A. 1973. Phosphate removal from sea water by adsorption on volcanogenic ferric oxides. *Earth and Planetary Science Letters,* 18**,** 77-86.

BERNER, R. A. 1984. Sedimentary pyrite formation: An update. *Geochimica et Cosmochimica Acta,* 48**,** 605-615.

BERNER, R. A. & RAISWELL, R. 1983. Burial of organic carbon and pyrite sulfur in sediments over phanerozoic time: a new theory. *Geochimica et Cosmochimica Acta,* 47**,** 855-862.

BERNER, R. A. & RAISWELL, R. 1984. C/S method for distinguishing freshwater from marine sedimentary rocks. *Geology,* 12**,** 365-368.

BERTRAND-SARFATI, J. & MOUSSINE-POUCHKINE, A. 1985. Evolution and environmental conditions of Conophyton--jacutophyton associations in the atar dolomite (upper proterozoic, Mauritania). *Precambrian Research,* 29**,** 207-234.

BERTRAND-SARFATI, J. & MOUSSINE-POUCHKINE, A. 1988. Is cratonic sedimentation consistent with available models? An example from the Upper Proterozoic of the West African craton. *Sedimentary Geology,* 58**,** 255-276.

BERTRAND-SARFATI, J. & MOUSSINE-POUCHKINE, A. 1992. Formation et comblement d'une dépression intraplateforme engendrée par la croissance d'un biostrome stromatolitique, Protérozoique supérieur, Sahara algérien. *Compte Rendus de l'Académie des Sciences (Paris),* 315**,** 837-843.

BERTRAND-SARFATI, J., MOUSSINE-POUCHKINE, A., AFFATON, P., TROMPETTE, R. & BELLION, Y. 1991. Cover Sequences of the West African Craton. *In:* DALLMEYER, R. D. & LÉCORCHÉ, J. P. (eds.) *The West African Orogens and Circum-Atlantic Correlatives.* Springer Berlin Heidelberg.

BERTRAND-SARFATI, J. & TROMPETTE, R. 1976. Use of Stromatolites for Intrabasinal Correlation: Example from the Late Proterozoic of the Northwestern Margin of the Taoudenni Basin. *In:* WALTER, M. R. (ed.) *Developments in Sedimentology*. Elsevier.

BJERRUM, C. J. & CANFIELD, D. E. 2002. Ocean productivity before about 1.9 Gyr ago limited by phosphorus adsorption onto iron oxides. *Nature,* 417**,** 159-162.

BOESEN, C. & POSTMA, D. 1988. Pyrite formation in anoxic environments of the Baltic. *American Journal of Science,* 288**,** 575-603.

BRASIER, M. D. & LINDSAY, J. F. 1998. A billion years of environmental stability and the emergence of eukaryotes: new data from northern Australia. *Geology,* 26**,** 555-558.

BRONNER, G., ROUSSEL, J., TROMPETTE, R. & CLAUER, N. 1980. Genesis and geodynamic evolution of the Taoudeni cratonic basin (Upper Precambrian and Paleozoic), Western Africa. *In:* BALLY, A. W., BENDER, P. L., MCGETCHIN, T. R. & WALCOTT, R. I. (eds.) *Dynamics of Plate Interiors.* American Geophysical Union.

BUICK, R., DES MARAIS, D. J. & KNOLL, A. H. 1995. Stable isotopic compositions of carbonates from the Mesoproterozoic Bangemall group, northwestern Australia. *Chemical Geology,* 123**,** 153-171.

CALVERT, S. E. & PEDERSEN, T. F. 1993. Geochemistry of Recent oxic and anoxic marine sediments: Implications for the geological record. *Marine Geology,* 113**,** 67-88.

CALVERT, S. E. & PEDERSEN, T. F. 1996. Sedimentary geochemistry of manganese; implications for the environment of formation of manganiferous black shales. *Economic Geology,* 91**,** 36-47.

CANFIELD, D. E. 1989a. Reactive iron in marine sediments. *Geochimica et Cosmochimica Acta,* 53**,** 619-632.

CANFIELD, D. E. 1989b. Sulfate reduction and oxic respiration in marine sediments: implications for organic carbon preservation in euxinic environments. *Deep Sea Research Part A. Oceanographic Research Papers,* 36**,** 121-138.

CANFIELD, D. E. 1994. Factors influencing organic carbon preservation in marine sediments. *Chemical Geology,* 114**,** 315-329.

CANFIELD, D. E. 2005. The early history of atmospheric oxygen: Homage to Robert A. Garrels. *Annual Review of Earth and Planetary Sciences,* 33**,** 1-36.

CANFIELD, D. E., LYONS, T. W. & RAISWELL, R. 1996. A model for iron deposition to euxinic Black Sea sediments. *American Journal of Science,* 296**,** 818-834.

CANFIELD, D. E., NGOMBI-PEMBA, L., HAMMARLUND, E. U., BENGTSON, S., CHAUSSIDON, M., GAUTHIER-LAFAYE, F., MEUNIER, A., RIBOULLEAU, A., ROLLION-BARD, C., ROUXEL, O., ASAEL, D., PIERSON-WICKMANN, A.-C. & EL ALBANI, A. 2013. Oxygen dynamics in the aftermath of the Great Oxidation of Earth's atmosphere. *Proceedings of the National Academy of Sciences of the United States of America,* 110**,** 16736-16741.

CANFIELD, D. E., RAISWELL, R. & BOTTRELL, S. H. 1992. The reactivity of sedimentary iron minerals toward sulfide. *American Journal of Science,* 292**,** 659-683.

CANFIELD, D. E. & TESKE, A. 1996. Late Proterozoic rise in atmospheric oxygen concentration inferred from phylogenetic and sulphur-isotope studies. *Nature,* 382**,** 127-132.

CANFIELD, D. E., ZHANG, S., WANG, H., WANG, X., ZHAO, W., SU, J., BJERRUM, C. J., HAXEN, E. R. & HAMMARLUND, E. U. 2018. A Mesoproterozoic iron formation. *Proceedings of the National Academy of Sciences,* 115**,** E3895-E3904.

CHAPPAZ, A., LYONS, T. W., GREGORY, D. D., REINHARD, C. T., GILL, B. C., LI, C. & LARGE, R. R. 2014. Does pyrite act as an important host for molybdenum in modern and ancient euxinic sediments? *Geochimica et Cosmochimica Acta,* 126**,** 112-122.

CLARKSON, M. O., POULTON, S. W., GUILBAUD, R. & WOOD, R. A. 2014. Assessing the utility of Fe/Al and Fe-speciation to record water column redox conditions in carbonate-rich sediments. *Chemical Geology,* 382**,** 111-122.

CLAUER, N. 1976. *Chimie isotopique du strontium des milieux sédimentaires. Application á la géochronologie de la couverture du craton ouest africain*.

CLAUER, N. 1981. Rb--Sr and K--Ar dating of Precambrian clays and glauconies. *Precambrian Research,* 15**,** 331-352.

CLAUER, N., CABY, R., JEANNETTE, D. & TROMPETTE, R. 1982. Geochronology of sedimentary and metasedimentary Precambrian rocks of the West African craton. *Precambrian Research,* 18**,** 53-71.

CORNWELL, J. C. & MORSE, J. W. 1987. The characterization of iron sulfide minerals in anoxic marine sediments. *Marine Chemistry,* 22**,** 193-206.

COX, G. M., JARRETT, A., EDWARDS, D., CROCKFORD, P. W., HALVERSON, G. P., COLLINS, A. S., POIRIER, A. & LI, Z.-X. 2016. Basin redox and primary productivity within the Mesoproterozoic Roper Seaway. *Chemical Geology,* 440**,** 101-114.

CRAIG, J., BIFFI, U., GALIMBERTI, R. F., GHORI, K. A. R., GORTER, J. D., HAKHOO, N., LE HERON, D. P., THUROW, J. & VECOLI, M. 2013. The palaeobiology and geochemistry of Precambrian hydrocarbon source rocks. *Marine and Petroleum Geology,* 40**,** 1-47.

CREVELING, J. R., JOHNSTON, D. T., POULTON, S. W., KOTRC, B., MÄRZ, C., SCHRAG, D. P. & KNOLL, A. H. 2014. Phosphorus sources for phosphatic Cambrian carbonates. *Geological Society of America Bulletin,* 126**,** 145-163.

DAIDU, F., YUAN, W. & MIN, L. 2013. Classifications, sedimentary features and facies associations of tidal flats. *Journal of Palaeogeography,* 2**,** 66-80.

DELANEY, M. L. 1998. Phosphorus accumulation in marine sediments and the oceanic phosphorus cycle. *Global Biogeochem. Cycles,* 12**,** 563-572.

DEYNOUX, M., AFFATON, P., TROMPETTE, R. & VILLENEUVE, M. 2006. Pan-African tectonic evolution and glacial events registered in Neoproterozoic to Cambrian cratonic and foreland basins of West Africa. *Journal of African Earth Sciences,* 46**,** 397-426.

DOTT JR, R. & BOURGEOIS, J. 1982. Hummocky stratification: significance of its variable bedding sequences. *Geological Society of America Bulletin,* 93**,** 663-680.

FEELY, R. A., TREFRY, J. H., LEBON, G. T. & GERMAN, C. R. 1998. The relationship between P/Fe and V/Fe ratios in hydrothermal precipitates and dissolved phosphate in seawater. *Geophysical Research Letters,* 25**,** 2253-2256.

FEELY, R. A., TREFRY, J. H., MASSOTH, G. J. & METZ, S. 1991. A comparison of the scavenging of phosphorus and arsenic from seawater by hydrothermal iron oxyhydroxides in the Atlantic and Pacific Oceans. *Deep Sea Research Part A. Oceanographic Research Papers,* 38**,** 617-623.

FILIPPELLI, G. M. 1997. Controls on phosphorus concentration and accumulation in oceanic sediments. *Marine Geology,* 139**,** 231-240.

FILIPPELLI, G. M. & DELANEY, M. L. 1996. Phosphorus geochemistry of equatorial Pacific sediments. *Geochimica et Cosmochimica Acta,* 60**,** 1479-1495.

FILIPPELLI, G. M., DELANEY, M. L. & WILLIAMS, C. F. 1995. *Phosphorus geochemistry, diagenesis, and mass balances of the Miocene Monterey Formation at Shell Beach, California*.

FÖLLMI, K. B., BADERTSCHER, C., DE KAENEL, E., STILLE, P., JOHN, C. M., ADATTE, T. & STEINMANN, P. 2005. Phosphogenesis and organic-carbon preservation in the Miocene Monterey Formation at Naples Beach, California—The Monterey hypothesis revisited. *Geological Society of America Bulletin,* 117**,** 589-619.

FREI, R., GAUCHER, C., POULTON, S. W. & CANFIELD, D. E. 2009. Fluctuations in Precambrian atmospheric oxygenation recorded by chromium isotopes. *Nature,* 461**,** 250-253.

FROELICH, P. N., BENDER, M. L., LUEDTKE, N. A., HEATH, G. R. & DEVRIES, T. 1982. The Marine Phosphorus Cycle. *American Journal of Science,* 282**,** 474-511.

GILLEAUDEAU, G. J. & KAH, L. C. 2013a. Carbon Isotope Records in a Mesoproterozoic Epicratonic Sea: Carbon Cycling in a Low-Oxygen World. *Precambrian Research,* 228**,** 85-101.

GILLEAUDEAU, G. J. & KAH, L. C. 2013b. Oceanic molybdenum drawdown by epeiric sea expansion in the Mesoproterozoic. *Chemical Geology,* 356**,** 21-37.

GILLEAUDEAU, G. J. & KAH, L. C. 2015. Heterogeneous redox conditions and a shallow chemocline in the Mesoproterozoic ocean: Evidence from carbon–sulfur–iron relationships. *Precambrian Research,* 257**,** 94-108.

GILLETT, S. L. 2003. Paleomagnetism of the Notch Peak contact metamorphic aureole, revisited: Pyrrhotite from magnetite+pyrite under submetamorphic conditions. *Journal of Geophysical Research,* 108**,** 2446.

GIRARD, J.-P., DEYNOUX, M. & NAHON, D. 1989. Diagenesis of the upper Proterozoic siliciclastic sediments of the Taoudeni Basin (West Africa) and relation to diabase emplacement. *JOURNAL OF SEDIMENTARY RESEARCH,* 59**,** 233-248.

GUILBAUD, R., POULTON, S. W., BUTTERFIELD, N. J., ZHU, M. & SHIELDS-ZHOU, G. A. 2015. A global transition to ferruginous conditions in the early Neoproterozoic oceans. *Nature Geoscience,* 8**,** 466-470.

HALL, A. 1986. Pyrite-pyrrhotine redox reactions in nature. *Mineral. Mag,* 50**,** 223-229.

HARTNETT, H. E., KEIL, R. G., HEDGES, J. I. & DEVOL, A. H. 1998. Influence of oxygen exposure time on organic carbon preservation in continental margin sediments. *Nature,* 391**,** 572-575.

HELZ, G. R., MILLER, C. V., CHARNOCK, J. M., MOSSELMANS, J. F. W., PATTRICK, R. A. D., GARNER, C. D. & VAUGHAN, D. J. 1996. Mechanism of molybdenum removal from the sea and its concentration in black shales: EXAFS evidence. *Geochimica et Cosmochimica Acta,* 60**,** 3631-3642.

HOLLAND, H. D. 1984. *The chemical evolution of the atmosphere,* Princeton, NJ, Princeton University Press.

HOLLAND, H. D. 2006. The oxygenation of the atmosphere and oceans. *Philosophical Transactions of the Royal Society B: Biological Sciences,* 361**,** 903-915.

HU, G., DAM-JOHANSEN, K., WEDEL, S. & HANSEN, J. P. 2006. Decomposition and oxidation of pyrite. *Progress in Energy and Combustion Science,* 32**,** 295-314.

HUCKRIEDE, H. & MEISCHNER, D. 1996. Origin and environment of manganese-rich sediments within black-shale basins. *Geochimica et Cosmochimica Acta,* 60**,** 1399-1413.

HUERTA-DIAZ, M. A. & MORSE, J. W. 1992. Pyritization of trace metals in anoxic marine sediments. *Geochimica et Cosmochimica Acta,* 56**,** 2681-2702.

INGALL, E. & JAHNKE, R. 1994. Evidence for enhanced phosphorus regeneration from marine sediments overlain by oxygen depleted waters. *Geochimica et Cosmochimica Acta,* 58**,** 2571-2575.

INGALL, E. & JAHNKE, R. 1997. Influence of water-column anoxia on the elemental fractionation of carbon and phosphorus during sediment diagenesis. *Marine Geology,* 139**,** 219-229.

INGALL, E. D., BUSTIN, R. M. & VAN CAPPELLEN, P. 1993. Influence of water column anoxia on the burial and preservation of carbon and phosphorus in marine shales. *Geochimica et Cosmochimica Acta,* 57**,** 303-316.

INGALL, E. D. & VAN CAPPELLEN, P. 1990. Relation between sedimentation rate and burial of organic phosphorus and organic carbon in marine sediments. *Geochimica et Cosmochimica Acta,* 54**,** 373-386.

JAHNKE, R. A., EMERSON, S. R., ROE, K. K. & BURNETT, W. C. 1983. The present day formation of apatite in Mexican continental margin sediments. *Geochimica et Cosmochimica Acta,* 47**,** 259-266.

JAVAUX, E. J. & LEPOT, K. 2018. The Paleoproterozoic fossil record: Implications for the evolution of the biosphere during Earth's middle-age. *Earth-Science Reviews,* 176**,** 68-86.

JOHNSTON, D. T., POULTON, S. W., DEHLER, C., PORTER, S., HUSSON, J., CANFIELD, D. E. & KNOLL, A. H. 2010. An emerging picture of Neoproterozoic ocean chemistry: Insights from the Chuar Group, Grand Canyon, USA. *Earth and Planetary Science Letters,* 290**,** 64-73.

JONES, C., NOMOSATRYO, S., CROWE, S. A., BJERRUM, C. J. & CANFIELD, D. E. 2015. Iron oxides, divalent cations, silica, and the early earth phosphorus crisis. *Geology,* 43**,** 135-138.

JØRGENSEN, B. B. 1982. Mineralization of organic matter in the sea bed—the role of sulphate reduction. *Nature,* 296**,** 643-645.

KAH, L. C. & BARTLEY, J. K. 2011. Protracted oxygenation of the Proterozoic biosphere. *International Geology Review,* 53**,** 1424-1442.

KAH, L. C., BARTLEY, J. K. & STAGNER, A. F. 2009. Reinterpreting a Proterozoic enigma: Conophyton–Jacutophyton stromatolites of the Mesoproterozoic Atar Group, Mauritania. *International Association of Sedimentology Special Publication,* 41**,** 277-295.

KAH, L. C., BARTLEY, J. K. & TEAL, D. A. 2012. Chemostratigraphy of the Late Mesoproterozoic Atar Group, Taoudeni Basin, Mauritania: Muted isotopic variability, facies correlation, and global isotopic trends. *Precambrian Research,* 200–203**,** 82-103.

KAH, L. C., LYONS, T. W. & FRANK, T. D. 2004. Low marine sulphate and protracted oxygenation of the Proterozoic biosphere. *Nature,* 431**,** 834-838.

KAJIWARA, Y., SASAKI, A. & MATSUBARA, O. 1981. Kinetic sulfur isotope effects in the thermal decomposition of pyrite. *Geochemical Journal,* 15**,** 193-197.

KONHAUSER, K. O., LALONDE, S. V., AMSKOLD, L. & HOLLAND, H. D. 2007. Was There Really an Archean Phosphate Crisis? *Science,* 315**,** 1234.

KROM, M. D. & BERNER, R. A. 1981. The diagenesis of phosphorus in a nearshore marine sediment. *Geochimica et Cosmochimica Acta,* 45**,** 207-216.

LAHONDÈRE, D., THIÉBLEMONT, D., GOUJOU, J. C., ROGER, J., MOUSSINE-POUCHKINE, A., LE MÉTOUR, J., COCHERIE, A. & GUERROT, C. 2003. Notice explicative des cartes géologiques et gîtologiques à 1/200 000 et 1/500 000 du Nord de la Mauritanie. *Vol. 1DMG, Ministère des Mines et de l'Industrie, Nouakchott*.

LAMBERT, I. B. 1973. Post-depositional availability of sulphur and metals and formation of secondary textures and structures in stratiform sedimentary sulphide deposits. *Journal of the Geological Society of Australia,* 20**,** 205-215.

LI, C., LOVE, G. D., LYONS, T. W., FIKE, D. A., SESSIONS, A. L. & CHU, X. L. 2010. A Stratified Redox Model for the Ediacaran Ocean. *Science,* 328**,** 80-83.

LITTLE, S. H., VANCE, D., LYONS, T. W. & MCMANUS, J. 2015. Controls on trace metal authigenic enrichment in reducing sediments: Insights from modern oxygen-deficient settings. *American Journal of Science,* 315**,** 77-119.

LOTTAROLI, F., CRAIG, J. & THUSU, B. 2009. Neoproterozoic-Early Cambrian (Infracambrian) hydrocarbon prospectivity of North Africa: a synthesis. *Geological Society, London, Special Publications,* 326**,** 137-156.

LYONS, T. W., ANBAR, A. D., SEVERMANN, S., SCOTT, C. & GILL, B. C. 2009. Tracking Euxinia in the Ancient Ocean: A Multiproxy Perspective and Proterozoic Case Study. *Annual Review of Earth and Planetary Sciences,* 37**,** 507-534.

LYONS, T. W., REINHARD, C. T. & PLANAVSKY, N. J. 2014. The rise of oxygen in Earth's early ocean and atmosphere. *Nature,* 506**,** 307-315.

LYONS, T. W. & SEVERMANN, S. 2006. A critical look at iron paleoredox proxies: New insights from modern euxinic marine basins. *Geochimica et Cosmochimica Acta,* 70**,** 5698-5722.

LYONS, T. W., WERNE, J. P., HOLLANDER, D. J. & MURRAY, R. W. 2003. Contrasting sulfur geochemistry and Fe/Al and Mo/Al ratios across the last oxic-to-anoxic transition in the Cariaco Basin, Venezuela. *Chemical Geology,* 195**,** 131-157.

MARTÍN-MONGE, A., BAUDINO, R., GAIRIFO-FERREIRA, L. M., TOCCO, R., BADALÌ, M., OCHOA, M., HARYONO, S., SORIANO, S., EL HAFIZ, N., HERNÁN-GÓMEZ, J., CHACÓN, B., BRISSON, I., GRAMMATICO, G., VARADÉ, R. & ABDALLAH, H. 2016. An unusual Proterozoic petroleum play in Western Africa: the Atar Group carbonates (Taoudeni Basin, Mauritania). *Geological Society, London, Special Publications,* 438**,** 119-157.

MÄRZ, C., POULTON, S. W., BECKMANN, B., KÜSTER, K., WAGNER, T. & KASTEN, S. 2008. Redox sensitivity of P cycling during marine black shale formation: Dynamics of sulfidic and anoxic, non-sulfidic bottom waters. *Geochimica et Cosmochimica Acta,* 72**,** 3703-3717.

MOREAU, M. G., ADER, M. & ENKIN, R. J. 2005. The magnetization of clay-rich rocks in sedimentary basins: low-temperature experimental formation of magnetic carriers in natural samples. *Earth and Planetary Science Letters,* 230**,** 193-210.

MORT, H. P., SLOMP, C. P., GUSTAFSSON, B. G. & ANDERSEN, T. J. 2010. Phosphorus recycling and burial in Baltic Sea sediments with contrasting redox conditions. *Geochimica et Cosmochimica Acta,* 74**,** 1350-1362.

MOUSSINE-POUCHKINE, A. & BERTRAND-SARFATI, J. 1997. Tectonosedimentary subdivisions in the neoproterozoic to Early Cambrian cover of the taoudenni Basin (Algeria-Mauritania-Mali). *Journal of African Earth Sciences,* 24**,** 425-443.

NICOLL, G., STRAATHOF, G., TAIT, J., LO, K., EL MOCTAR DAHMADA, M., BERNDT, J. & KEY, R. Provenance analysis and tectonic setting of the Neoproterozoic sediments within the Taoudeni Basin, Northern Mauritania. EGU General Assembly Conference Abstracts, 2010. 7094.

PEDERSEN, T. & CALVERT, S. 1990. Anoxia vs. Productivity: What Controls the Formation of Organic-Carbon-Rich Sediments and Sedimentary Rocks?(1). *AAPG Bulletin,* 74**,** 454-466.

PELOVSKI, Y. & PETKOVA, V. 1999. Investigation on thermal decomposition of pyrite part I. *Journal of thermal analysis and calorimetry,* 56**,** 95-99.

PIPER, D. & CALVERT, S. 2009. A marine biogeochemical perspective on black shale deposition. *Earth-Science Reviews,* 95**,** 63-96.

PLANAVSKY, N. J. 2014. The elements of marine life. *Nature Geoscience,* 7**,** 855-856.

PLANAVSKY, N. J., MCGOLDRICK, P., SCOTT, C. T., LI, C., REINHARD, C. T., KELLY, A. E., CHU, X., BEKKER, A., LOVE, G. D. & LYONS, T. W. 2011. Widespread iron-rich conditions in the mid-Proterozoic ocean. *Nature,* 477**,** 448-451.

PLANAVSKY, N. J., REINHARD, C. T., WANG, X., THOMSON, D., MCGOLDRICK, P., RAINBIRD, R. H., JOHNSON, T., FISCHER, W. W. & LYONS, T. W. 2014. Low

Mid-Proterozoic atmospheric oxygen levels and the delayed rise of animals. *Science,* 346**,** 635-638.

PLANAVSKY, N. J., ROUXEL, O. J., BEKKER, A., LALONDE, S. V., KONHAUSER, K. O., REINHARD, C. T. & LYONS, T. W. 2010. The evolution of the marine phosphate reservoir. *Nature,* 467**,** 1088-1090.

PLANAVSKY, N. J., SLACK, J. F., CANNON, W. F., O'CONNELL, B., ISSON, T. T., ASAEL, D., JACKSON, J. C., HARDISTY, D. S., LYONS, T. W. & BEKKER, A. 2018. Evidence for episodic oxygenation in a weakly redox-buffered deep mid-Proterozoic ocean. *Chemical Geology,* 483**,** 581-594.

POULTON, S. W. 2017. Biogeochemistry: Early phosphorus redigested. *Nature Geoscience,* 10**,** 75-76.

POULTON, S. W. & CANFIELD, D. E. 2005. Development of a sequential extraction procedure for iron: implications for iron partitioning in continentally derived particulates. *Chemical Geology,* 214**,** 209-221.

POULTON, S. W. & CANFIELD, D. E. 2011. Ferruginous Conditions: A Dominant Feature of the Ocean through Earth's History. *Elements,* 7**,** 107-112.

POULTON, S. W., FRALICK, P. W. & CANFIELD, D. E. 2004. The transition to a sulphidic ocean ~ 1.84 billion years ago. *Nature,* 431**,** 173-177.

POULTON, S. W., FRALICK, P. W. & CANFIELD, D. E. 2010. Spatial variability in oceanic redox structure 1.8 billion years ago. *Nature Geoscience,* 3**,** 486-490.

POULTON, S. W., HENKEL, S., MÄRZ, C., URQUHART, H., FLÖGEL, S., KASTEN, S., SINNINGHE DAMSTÉ, J. S. & WAGNER, T. 2015. A continental-weathering control on orbitally driven redox-nutrient cycling during Cretaceous Oceanic Anoxic Event 2. *Geology,* 43**,** 963-966.

POULTON, S. W. & RAISWELL, R. 2002. The low-temperature geochemical cycle of iron: From continental fluxes to marine sediment deposition. *American Journal of Science,* 302**,** 774-805.

RAISWELL, R., BUCKLEY, F., BERNER, R. A. & ANDERSON, T. F. 1988. Degree of pyritization of iron as a paleoenvironmental indicator of bottom-water oxygenation. *Journal of Sedimentary Research,* 58**,** 812-819.

RAISWELL, R. & CANFIELD, D. E. 1998. Sources of iron for pyrite formation in marine sediments. *American Journal of Science,* 298**,** 219-245.

RAISWELL, R. & CANFIELD, D. E. 2012. The Iron Biogeochemical Cycle Past and Present. *Geochemical Perspectives,* 1**,** 1-2.

RAISWELL, R., CANFIELD, D. E. & BERNER, R. A. 1994. A comparison of iron extraction methods for the determination of degree of pyritisation and the recognition of iron-limited pyrite formation. *Chemical Geology,* 111**,** 101-110.

RAISWELL, R., NEWTON, R., BOTTRELL, S. H., COBURN, P. M., BRIGGS, D. E. G., BOND, D. P. G. & POULTON, S. W. 2008. Turbidite depositional influences on the

diagenesis of Beecher's Trilobite Bed and the Hunsrück Slate; sites of soft tissue pyritization. *American Journal of Science,* 308**,** 105-129.

RAISWELL, R., NEWTON, R. & WIGNALL, P. B. 2001. An Indicator of Water-Column Anoxia: Resolution of Biofacies Variations in the Kimmeridge Clay (Upper Jurassic, U.K.). *Journal of Sedimentary Research,* 71**,** 286-294.

REDFIELD, A. C. 1963. The influence of organisms on the composition of seawater. *The Sea,* 2**,** 26-77.

REINECK, H.-E. & WUNDERLICH, F. 1968. Classification and origin of flaser and lenticular bedding. *Sedimentology,* 11**,** 99-104.

REINHARD, C. T., PLANAVSKY, N. J., GILL, B. C., OZAKI, K., ROBBINS, L. J., LYONS, T. W., FISCHER, W. W., WANG, C., COLE, D. B. & KONHAUSER, K. O. 2017. Evolution of the global phosphorus cycle. *Nature,* 541**,** 386-389.

REINHARD, C. T., PLANAVSKY, N. J., ROBBINS, L. J., PARTIN, C. A., GILL, B. C., LALONDE, S. V., BEKKER, A., KONHAUSER, K. O. & LYONS, T. W. 2013. Proterozoic ocean redox and biogeochemical stasis. *Proceedings of the National Academy of Sciences,* 110**,** 5357-5362.

RICKARD, D. & LUTHER, G. W. 2007. Chemistry of Iron Sulfides. *Chemical Reviews,* 107**,** 514-562.

RICKARD, D. & MORSE, J. W. 2005. Acid volatile sulfide (AVS). *Marine Chemistry,* 97**,** 141-197.

RIMMER, S. M., THOMPSON, J. A., GOODNIGHT, S. A. & ROBL, T. L. 2004. Multiple controls on the preservation of organic matter in Devonian–Mississippian marine black shales: geochemical and petrographic evidence. *Palaeogeography, Palaeoclimatology, Palaeoecology,* 215**,** 125-154.

ROONEY, A. D., SELBY, D., HOUZAY, J. P. & RENNE, P. R. 2010. Re-Os geochronology of a Mesoproterozoic sedimentary succession, Taoudeni basin, Mauritania: Implications for basin-wide correlations and Re-Os organic-rich sediments systematics. *Earth and Planetary Science Letters,* 289**,** 486-496.

RUTTENBERG, K. 1993. Reassessment of the oceanic residence time of phosphorus. *Chemical Geology,* 107**,** 405-409.

RUTTENBERG, K. C. 1992. Development of a sequential extraction method for different forms of phosphorus in marine sediments. *Limnology and Oceanography,* 37**,** 1460-1482.

RUTTENBERG, K. C. & BERNER, R. A. 1993. Authigenic apatite formation and burial in sediments from non-upwelling, continental margin environments. *Geochimica et Cosmochimica Acta,* 57**,** 991-1007.

SAGEMAN, B. B., MURPHY, A. E., WERNE, J. P., VER STRAETEN, C. A., HOLLANDER, D. J. & LYONS, T. W. 2003. A tale of shales: the relative roles of production, decomposition, and dilution in the accumulation of organic-rich strata, Middle–Upper Devonian, Appalachian basin. *Chemical Geology,* 195**,** 229-273.

SCOTT, C. & LYONS, T. W. 2012. Contrasting molybdenum cycling and isotopic properties in euxinic versus non-euxinic sediments and sedimentary rocks: Refining the paleoproxies. *Chemical Geology,* 324–325**,** 19-27.

SCOTT, C., LYONS, T. W., BEKKER, A., SHEN, Y., POULTON, S. W., CHU, X. & ANBAR, A. D. 2008. Tracing the stepwise oxygenation of the Proterozoic ocean. *Nature,* 452**,** 456-459.

SHEMESH, A. 1990. Crystallinity and diagenesis of sedimentary apatites. *Geochimica et Cosmochimica Acta,* 54**,** 2433-2438.

SHEN, Y. N., CANFIELD, D. E. & KNOLL, A. H. 2002. Middle proterozoic ocean chemistry: Evidence from the McArthur Basin, northern Australia. *American Journal of Science,* 302**,** 81-109.

SHIELDS-ZHOU, G. & OCH, L. 2011. The case for a Neoproterozoic oxygenation event: geochemical evidence and biological consequences. *GSA Today,* 21**,** 4-11.

SLOMP, C. P., EPPING, E. H. G., HELDER, W. & RAAPHORST, W. V. 1996a. A key role for iron-bound phosphorus in authigenic apatite formation in North Atlantic continental platform sediments. *Journal of Marine Research,* 54**,** 1179-1205.

SLOMP, C. P., THOMSON, J. & DE LANGE, G. J. 2002. Enhanced regeneration of phosphorus during formation of the most recent eastern Mediterranean sapropel (S1). *Geochimica et Cosmochimica Acta,* 66**,** 1171-1184.

SLOMP, C. P., THOMSON, J. & DE LANGE, G. J. 2004. Controls on phosphorus regeneration and burial during formation of eastern Mediterranean sapropels. *Marine Geology,* 203**,** 141-159.

SLOMP, C. P., VAN DER GAAST, S. J. & VAN RAAPHORST, W. 1996b. Phosphorus binding by poorly crystalline iron oxides in North Sea sediments. *Marine Chemistry,* 52**,** 55-73.

SPERLING, E. A., ROONEY, A. D., HAYS, L., SERGEEV, V. N., VOROB'EVA, N. G., SERGEEVA, N. D., SELBY, D., JOHNSTON, D. T. & KNOLL, A. H. 2014. Redox heterogeneity of subsurface waters in the Mesoproterozoic ocean. *Geobiology,* 12**,** 373-386.

TEAL, D. J. & KAH, L. C. 2005. Using C-isotopes to constrain interbasinal stratigraphic correlations, Mesoproterozoic Atar Group, Mauritania. *Geological Society of America, Abstracts with Programs* 37**,** 45.

TRACY, R. J. & ROBINSON, P. 1988. Silicate-sulfide-oxide-fluid reactions in granulite-grade pelitic rocks, central Massachusetts. *American Journal of Science,* 288**,** 45-74.

TRIBOVILLARD, N., ALGEO, T. J., LYONS, T. & RIBOULLEAU, A. 2006. Trace metals as paleoredox and paleoproductivity proxies: An update. *Chemical Geology,* 232**,** 12-32.

TROMPETTE, R. 1969. Les stromatolites du “Précambrien supérieur” de l'Adrar de Mauritanie (Sahara occidental). *Sedimentology,* 13**,** 123-154.

TROMPETTE, R. 1973. *Le Précambrien supérieur et le Paléozoïque inférieur de l'Adrar de Mauritanie (bordure occidentale du bassin de Taoudeni, Afrique de l'Ouest), un exemple de sédimentation de craton. Étude stratigraphique et sédimentologique-TOME 2 (Séries 2 et 3).* Université de Provence-Aix-Marseille I.

TROMPETTE, R. 1994. *Geology of western Gondwana (2000-500 Ma): Pan-Africa-Brasiliano aggregation of South America and Africa*.

TSANDEV, I., REED, D. C. & SLOMP, C. P. 2012. Phosphorus diagenesis in deep-sea sediments: Sensitivity to water column conditions and global scale implications. *Chemical Geology,* 330–331**,** 127-139.

TUREKIAN, K. K. & WEDEPOHL, K. H. 1961. Distribution of the Elements in Some Major Units of the Earth's Crust. *Geological Society of America Bulletin,* 72**,** 175-192.

TYRRELL, T. 1999. The relative influences of nitrogen and phosphorus on oceanic primary production. *Nature,* 400**,** 525-531.

TYSON, R. V. 2005. The "productivity versus preservation" controversy: cause, flaws, and resolution. *Special Publication-SEPM,* 82**,** 17.

VAN CAPPELLEN, P. & INGALL, E. D. 1994. Benthic phosphorus regeneration, net primary production, and ocean anoxia: A model of the coupled marine biogeochemical cycles of carbon and phosphorus. *Paleoceanography,* 9**,** 677-692.

VAN CAPPELLEN, P. & INGALL, E. D. 1996. Redox Stabilization of the Atmosphere and Oceans by Phosphorus-Limited Marine Productivity. *Science,* 271**,** 493-496.

VERATI, C., BERTRAND, H. & FÉRAUD, G. 2005. The farthest record of the Central Atlantic Magmatic Province into West Africa craton: Precise $^{40}Ar/^{39}Ar$ dating and geochemistry of Taoudenni basin intrusives (northern Mali). *Earth and Planetary Science Letters,* 235**,** 391-407.

VILLENEUVE, M. 2005. Paleozoic basins in West Africa and the Mauritanide thrust belt. *Journal of African Earth Sciences,* 43**,** 166-195.

VILLENEUVE, M. & CORNÉE, J. J. 1994. Structure, evolution and palaeogeography of the West African craton and bordering belts during the Neoproterozoic. *Precambrian Research,* 69**,** 307-326.

WHEAT, C. G., FEELY, R. A. & MOTTL, M. J. 1996. Phosphate removal by oceanic hydrothermal processes: An update of the phosphorus budget in the oceans. *Geochimica et Cosmochimica Acta,* 60**,** 3593-3608.

WIJSMAN, J. W. M., MIDDELBURG, J. J. & HEIP, C. H. R. 2001. Reactive iron in Black Sea Sediments: implications for iron cycling. *Marine Geology,* 172**,** 167-180.

YALLUP, C., EDMONDS, M. & TURCHYN, A. V. 2013. Sulfur degassing due to contact metamorphism during flood basalt eruptions. *Geochimica et Cosmochimica Acta,* 120**,** 263-279.

YAMAMOTO, M. 1984. Sulfur isotope effects in the thermal breakdown of pyrite. *Earth and Planetary Science Letters,* 69**,** 335-340.

ZEGEYE, A., BONNEVILLE, S., BENNING, L. G., STURM, A., FOWLE, D. A., JONES, C., CANFIELD, D. E., RUBY, C., MACLEAN, L. C., NOMOSATRYO, S., CROWE, S. A. & POULTON, S. W. 2012. Green rust formation controls nutrient availability in a ferruginous water column. *Geology*, 40**,** 599-602.

ZHANG, S., WANG, X., WANG, H., BJERRUM, C. J., HAMMARLUND, E. U., COSTA, M. M., CONNELLY, J. N., ZHANG, B., SU, J. & CANFIELD, D. E. 2016. Sufficient oxygen for animal respiration 1,400 million years ago. *Proceedings of the National Academy of Sciences*, 113**,** 1731-1736.